Modelling dilution and transport processes from marine outfall discharges.

Claudia Fernanda Castro Faccetti

Submitted in accordance with the requirements for the Degree of

Doctor of Philosophy

The University of Leeds

School of Civil Engineering

July 2020

Intelectual property and publication statements.

The candidate confirms that the work submitted is her own, except where work which has formed part of jointly authored publications has been included. The contribution of the candidate and the other authors to this work has been explicitly indicated below. The candidate confirms that appropriate credit has been given within the thesis where reference has been made to the work of others.

The work presented in Chapters 4, 5 and 6 of this thesis has appeared in publication as follows:

Castro-Faccetti, C.: Borman, D., Sleigh, P.A., Khan, A, Eljaiek-Urzola, M. 2019. Three-dimensional CFD modelling of mixing and dispersion from marine outfall discharges. In: Proceedings of the 38th IAHR World Congress, Panama city, Panama. 1st-6th September.

I was responsible for the execution of the modelling work, data processing, analysis and preparation of the manuscript. D. Borman, P.A. Sleigh, A. Khan contributed in the editing of the manuscript. M. Eljaiek-Urzola was responsible for providing field data.

Acknowledgements.

First of all, I would like to thank my supervisors, Dr Andrew Sleigh, Dr Duncan Borman and Dr Amirul Khan, for their valuable help and instruction on the development of this thesis. Special thanks are given to Dr Duncan Borman, for being infinitely caring and supporting when it was most needed.

I would also like to thank the regional government of Bolívar, Colombia and the Fundación Ceiba for funding this project and giving me the opportunity to embark in this journey.

I am also thankful for my colleagues at the University of Leeds, fellow PhD students and members of staff, all from whom I learned greatly in the years of my study. Special thanks to my dear friend Sura, who sat next to my desk for most of my PhD years and made my days a lot happier.

My gratitude is due to my dear friends from the Environmental Research Group at the University of Cartagena for their support and collaboration, and to ACUACAR for providing field data from the Cartagena marine outfall. Special thanks to Dr Edgar Quiñones for his continuous support and for being the great role model that inspired me to study a PhD.

I would also like to thank Dr Phillip Roberts and Dr Tobias Bleninger for providing field and modelling data from their research on the Cartagena marine outfall, which was of great help for meeting the final objective of this project.

I am immensely grateful to my closest friends from Colombia and from my time in Leeds, for always being there for me when I needed them. Special thanks to María Alejandra, my dear friends from Instituto Cervantes and my therapist (who is in my heart a friend), Emma.

I feel immense gratitude to my extended family, my parents, Arnol and Vilma, and my *little* brother, Javier, who have always believed in me, much more than I have ever done, and for whom I try to better myself every day. I would have never completed my thesis without you.

I am immensely grateful to my love, my partner in life, Edward, for supporting me every day of this journey since he arrived in my life.

Last, but not least, I would like to thank myself: for not giving up even when it was most tempting, for overcoming all the challenges encountered and becoming a better Claudia. The lessons learned are the most valuable part of this time and they will remain in me forever.

Abstract

Municipal, industrial and desalination wastewater is commonly discharged into coastal waters. Marine outfalls are a common wastewater disposal system used in coastal areas, consisting on a pipe or tunnel, or the combination of both, that ends in a diffuser. The aim of the diffuser is to mix the effluent in the receiving waters.

Accurate prediction of mixing and dispersion in the near field of marine outfall discharges is important to prevent pollutants present in wastewater from affecting the water quality of the receiving environment. Traditionally, marine discharges have been modelled using empirical or entrainment models. Computational Fluid Dynamics (CFD) approaches have rarely been used to model this situation, despite their great potential.

This thesis aimed to assess how coupling CFD near field models with far field circulation models can be implemented to improve predictive capability of dilution and pollutant fate and transport in the near and far field of marine outfalls with multiport diffusers.

The present work includes the description and validation of a CFD modelling methodology for the simulation of the near field of single and multiple ports discharges at laboratory scale. A mesh adaption approach was used to capture geometric and flow detail around the discharge port while reducing computational resource requirements. Predictions of flow trajectory, velocity and dilution generally show good agreement with available experimental data. This approach demonstrates improved predictive capability for velocity and dilution when compared against conventional buoyant jet entrainment models. The dynamics of merging between plumes were successfully captured by RANS based k-ε and k-σ models.

Further studies were conducted focusing on the simulation of a real-life marine outfall located in the city of Cartagena, Colombia. The sensitivity of the outfall performance to a variety of parameters, including port alignment and other discharge and ambient conditions was assessed. The level of dilution obtained by the outfall showed great sensitivity to port alignment and Roberts Froude number. A framework for the implementation of the CFD methodology implemented here to other marine outfalls is presented.

The CFD near field model results obtained for the Cartagena marine outfall were successfully coupled to the far field circulation model Delft3D by inputting a near field discharge flow vertical profile into the far field model. Time-dependent and other complex processes such as tidal forcing, density stratification and wind effects were ignored to isolate the individual parameters of interest for their analysis. The far field model showed little sensitivity to the coupling model used under the conditions studied.

The overall aim of this thesis was achieved and a framework for the application of CFD near field models and its subsequent coupling with far field circulation models was proposed. RANS turbulence models produce reliable predictions of single and multiple port buoyant jet discharges from marine outfalls. The computational cost of this modelling method was reduced by implementing solution-based mesh adaption.

Time-dependent processes and variations in the discharge and ambient conditions would be the next step in understanding the behaviour of near and far field models of marine outfalls.

Table of contents.

List of figures.

List of tables.

Nomenclature.

Symbols

α	Entrainment coefficient
A_T	Area of plume element
A_p	Projected area of entrainment
A_{cyl}	Cylinder entrainment term
A_g	Growth entrainment term
A_{cur}	Current entrainment term
B	line source buoyancy flux
B	point source buoyancy flux
b_c	Plume radius
C	Local pollutant concentration
C_0	Souce pollutant concentration
D	Plume diameter
$D_{i,m}$	Scalar mass diffusion coefficient
$D_{i,T}$	Turbulent diffusion coefficient
E	Turbulent dissipation
F_0	Densimetric Froude number
F	Roberts Froude number
g	Gravity
g_0'	Modified acceleration due to gravity
H	Water depth
$\vec{J}_i$	Mass diffusion of a scalar i
K	Turbulence kinetic energy
k_{xm}, k_{zm} *and* k_{xr}	Experimental coefficients for the position of the maximum height and return point.
L	Diffuser length
l_b	Buoyancy to stratification length scale ratio for line plumes
l_B	Buoyancy to stratification length scale ratio for point plumes
l_M	Momentum to buoyancy length scale ratio for point plumes
l_m	Momentum to buoyancy length scale ratio for line plumes
M	Source momentum flux for point plumes
M	Source momentum flux for line plumes
M	Dynamic viscosity
μ_T	Turbulent viscosity
N	Number of ports in a diffuser
N	Buoyancy frequency
P	Pressure
Q_0	Volumetric flow rate
Q	Volumetric flow rate per unit diffuser length
S	Port spacing
S_n	Dilution in the end of the near field
T	Time
u_0	Port discharge velocity
u_a	Ambient current velocity
x, y, z	Cartesian coordinates
x_n	Length of the near field
Ω	Turbulent frequency

1 INTRODUCTION.

Due to the economic benefits resulting from ocean navigation, fisheries, tourism and recreation, human settlements are often more concentrated in coastal areas than elsewhere (United Nations, 2008; Neumann, et al., 2015). Around 44% of the world's population lives within 150 km of the sea, and most of the world's megacities are located in the coast zone (UN Atlas of the Oceans, 2016; Neumann, et al., 2015). However, the concentration of human settlements in these areas put the seas and oceans under increasing pressure from pollution (United Nations, 2008). Municipal, industrial and agricultural waste and run-off account for as much as 80% of all marine pollution (United Nations Environment Programme, 2015). Excessive nutrients from sewage outfalls and agricultural runoff, generate low oxygen (hypoxic) areas known as dead zones, where most marine life cannot survive, resulting in the collapse of some ecosystems. Currently, there are close to 500 dead zones covering more than 245,000 km^2 globally (UNESCO-IOC, 2015).

Marine outfalls are a wastewater disposal system commonly used in coastal areas. This system (also known as ocean outfall, sea outfall or simply outfall) consists of a pipeline or tunnel, or the combination of both, that terminates in a diffuser, whose purpose is to efficiently mix the effluent in the receiving water (Roberts, 2013). Increasingly, marine outfalls are being used for the disposal of wastewater. By 2000, there was a total of 99 constructed marine outfalls in the Latin American & Caribbean Region according to a survey conducted by the Pan American Health Organization and the Panamerican Center for Sanitary Engineering and Environmental Sciences. An update to this survey in 2006 found a total of 134 constructed marine outfalls of 500 meters or grater length in this region (see Table 1-1) (Panamerican Health Organization, 2006). The widespread use of marine outfalls responds to their capacity for the dilution of the organics, nutrients, and other pollutants present in wastewater given an appropriate design, which makes them a cost-efficient alternative for wastewater management (Salas, 2000). However, proper analysis of social, public health, environmental, regulatory, and economic factors should be done prior opting for this disposal alternative (Tate, et al., 2016).

In terms of the environmental and public health aspects, understanding the effects of marine outfalls in the water quality of the receiving water body is important. Pollutants present in domestic and industrial waters such as organic matter, nutrients, pathogenic organisms, toxic chemicals, metals, and solids may compromise the quality of coastal waters. Water quality regulations worldwide emphasize in the need to ensure that the concentrations of such pollutants is within acceptable levels. The World Health Organization *Guidelines for Safe Recreational Water Environments (2003)* prioritize the protection of human health, establishing enterococci/faecal streptococci as the main indicator organism correlated with the risk of illness for swimmers in marine waters. In the Latin America & Caribbean Region, the *Cartagena Convention and Protocols* provide the legal framework concerning environmental issues namely, oil spills, specially protected areas and wildlife, and land-based sources of marine pollution. Regarding the latter, regulations establish limit concentrations of pollutants for two types of marine waters: class I and class II (see Table 1-2). Class I includes waters in the Convention area that are particularly sensitive to the impact of wastewaters such as waters containing coral reefs, seagrass beds, or mangroves; critical breeding, nursery or forage areas for aquatic and terrestrial life; areas that provide habitat for species protected under the Protocol Concerning Specially Protected Areas and Wildlife (SPAW Protocol); protected areas listed in the SPAW Protocol; and waters used for

recreation. On the other hand, Class II waters are defined as "those less sensitive to the impacts of domestic wastewater and where humans or living resources that are likely to be adversely affected by the discharges are not exposed to such discharges" (United Nations, 1999). Other standards for water quality indicators exist at international, national and local level, varying widely depending on their supporting criteria, be they epidemiological, aesthetic, or ecological (Roberts, et al., 2010).

Mathematical models comprise an important tool for the design and monitoring of discharges via marine outfalls, simulating the mixing and dispersion processes that take place in the near and far field of the point of discharge (Zhao, et al., 2011); whereby, helping designers and operators to ensure that concentrations of specific pollutants resulting from such discharges have little negative impact in the marine environment and public health.

Due to the different time and space scales of the processes that govern mixing of outfall discharges in the marine environment, it is common to use different models to simulate the near and far field of a marine outfall. Widely used near field models are based on empirical and integral formulations. These models have the disadvantage of overlooking or simplifying important aspects of near field mixing including boundary interactions and merging between adjacent plumes. Additionally, the initial zone where the flow is not yet established is usually assumed to have similar characteristics to other regions of the plume. In entrainment models, the assumption of self-similarity of velocity, buoyancy and tracer concentration profiles along the trajectory of the buoyant jet is rather unrealistic. Existing software packages such as VISUAL PLUMES, VISJET and CORMIX, are only applicable for regular diffuser configurations with equally spaced ports.

CFD models have been scarcely applied to simulate jet, plume and buoyant jet from outfall discharges. Real-life effluent discharges from multiport diffusers have been modelled with CFD techniques (Davis, et al., 2004; Tang, et. al., 2008; Blumberg, et. al., 1996); nonetheless, additional research is required to reduce the computational cost of using these modelling techniques. The problem of coupling between CFD near field models and far field circulation models has not been addressed in the literature yet.

Table 1-1. Number of marine outfalls in some countries in Latin America & the Caribbean.

COUNTRY	CONSTRUCTED	PLANNED	TOTAL
Venezuela	39	-	39
Chile	39	-	39
Brazil	22	-	22
Puerto Rico	12	-	12
Mexico	9	-	9
Peru	-	2	2
Colombia	3	-	3
Uruguay	1	2	3
Argentina	1	1	2
Martinique	1	-	1
Ecuador	1	-	1
Bermuda	1	-	1
Costa Rica	1	-	1
Paraguay	2	-	2
Dominican Republic	1	-	1
Dominique	1	-	1
Total	134	5	139

Source: Panamerican Health Organization (2006).

Table 1-2. Effluent limits based on a monthly average defined by the Protocol for land-based sources of marine pollution in the Cartagena Convention region.

Parameter	**Effluent limit**	
	Class I	Class II
Total suspended solids	30 mg/l*	150 mg/l*
Biochemical Oxygen Demand (BOD5)	30 mg/l	150 mg/l
Ph	5-10 pH units	5-10 pH units
Fat, oils and Grease	15 mg/l	50 mg/l
Faecal coliforms (Parties may meet effluent limitations either for faecal coliform or for E. coli (freshwater) and enterococci (saline water)).	200 mpn/100 ml or; E.Coli: 126 organisms/100 ml; enterococci: 35 organisms/100 ml.	-
Floatables	Not visible	Not visible
*** Does not include algae from treatment ponds**		

Source: United Nations (1999).

1.1 AIMS AND OBJECTIVES.

The aim of this research is to assess how coupling CFD near field models with far field circulation models can be implemented to improve predictive capability of dilution and pollutant fate and transport in the near and far field of marine outfalls with multiport diffusers.

In order to achieve this aim, four main objectives were established:

I. To develop a RANS modelling methodology to simulate near field mixing and dilution of marine outfalls.
II. To validate the developed RANS methodology using experimental data at laboratory scale available in the literature.
III. To simulate mixing and dilution in the near field of a real-life scale marine outfall, using the Cartagena marine outfall as a case study.
IV. To assess different approaches for coupling the near field RANS model of Cartagena with a far field circulation model.

1.2 STRUCTURE OF THE THESIS.

Chapter 2: Understanding marine outfalls.

This chapter includes an introduction to marine outfalls and their governing processes. A review of the modelling methodologies that have been used to simulate dilution and transport processes from marine outfall discharges is detailed, including the advantages and disadvantages of the different modelling methods discussed.

Chapter 3: Methodology for CFD modelling of buoyant jets.

Chapter 3 summarises the equations that govern turbulent flows, which are solved numerically using CFD methods. The approach undertaken to reduce the computational cost of meshing is assessed using two-dimensional pure and buoyant jets. Based on this assessment, a methodology for meshing three-dimensional buoyant jets is presented.

Chapter 4: Near field modelling of single port discharges.

Chapter 4 presents the simulation of single port dense discharges at inclination angles between 15° and 45°. Different RANS turbulence models and turbulent Schmidt numbers were implemented to assess the sensitivity of the solution to the turbulence parameters used. Based on the results obtained, three main parameters were compared with available experimental data to validate the modelling methodology proposed, namely buoyant jet trajectory, velocity and dilution.

Chapter 5: Coalescing axisymmetric turbulent plumes.

In this chapter, further validation of the modelling is presented, focusing on the interaction between adjacent plumes with equal and unequal sources of buoyancy. Sensitivity to turbulence model is further studied and comparisons with available experimental data are discussed.

Chapter 6: Multiple port discharges from Tee-shaped risers at real-life scale. Case study: Cartagena de Indias, Colombia.

Chapter 6 discusses the application of the realizable k-ε turbulence model to predict the behaviour of a real-life marine outfall located in the city of Cartagena, Colombia. Sensitivity of the outfall behaviour to a variety of discharge and ambient conditions is discussed. A methodology is proposed for the application of the RANS turbulence models to other real-life marine outfalls.

Chapter 7: Coupling near and far field models. Case study: Cartagena de Indias, Colombia.

This chapter presents the coupling of the CFD near field model developed in Chapter VI with the far field circulation model Delft3D. Different coupling techniques, discharge and ambient conditions are studied. A methodology for the application of the presented coupling approach to other real-life marine outfalls is outlined.

Chapter 8: Conclusions.

Chapter 8 discusses the main findings of this thesis and suggests areas for further research.

2 UNDERSTANDING MARINE OUTFALLS.

A marine outfall (also known as ocean outfall, sea outfall or simply outfall) is a wastewater treatment and disposal system, consisting of a pipeline or tunnel, or the combination of both, that ends in a diffuser whose purpose is to mix the effluent in the receiving water (Roberts, 2013). Typically, outfalls are used to dispose the effluent of a municipal wastewater treatment plant or brine from a desalination plant (Tate, et al., 2016). Outfall settings vary depending on the type of water to be disposed. Outfalls discharging effluents from sewage treatment plants generally discharge onto coastal waters with a gradual slope (usually less than 1%) in order to make the horizontal flow prevail over the vertical one. Most outfalls range from 1 km to 5 km long and discharge at depths ranging from 20 to 70 m into the water (Roberts, 2013). The overall system, including the outfall and the region where rapid mixing and dilution occurs (known as near field), can be considered a treatment plant. This is due to the reduction in pollutant concentrations that results from the dilution. For instance, a dilution rate of 100:1 represents a reduction in the concentration of any pollutant by 99%, which exceeds significantly the removal capabilities of conventional treatment plants (Roberts, 2013).

The main components of a marine outfall are listed below and can be seen in Figure 2-1.

- **Manifold:** The part of the outfall from which there are a series of offtakes (risers).
- **Risers:** Vertical structures whose purpose is transferring the wastewater from the outfall to the outlet nozzles. They can be tens of meters in length.
- **Diffuser:** Comprises the section of the outfall that includes the manifold and the risers.
- **Nozzles:** Outlets located on top of each riser. There can be up to 8 outlet nozzles attached to a riser. Locating more than eight nozzles per riser is not favourable since the plumes from adjacent nozzles may interfere with each other and reduce effective dilution. In order to prevent the seawater to ingress into the pipeline, it is common to fit outlet nozzles with non-return check valves.

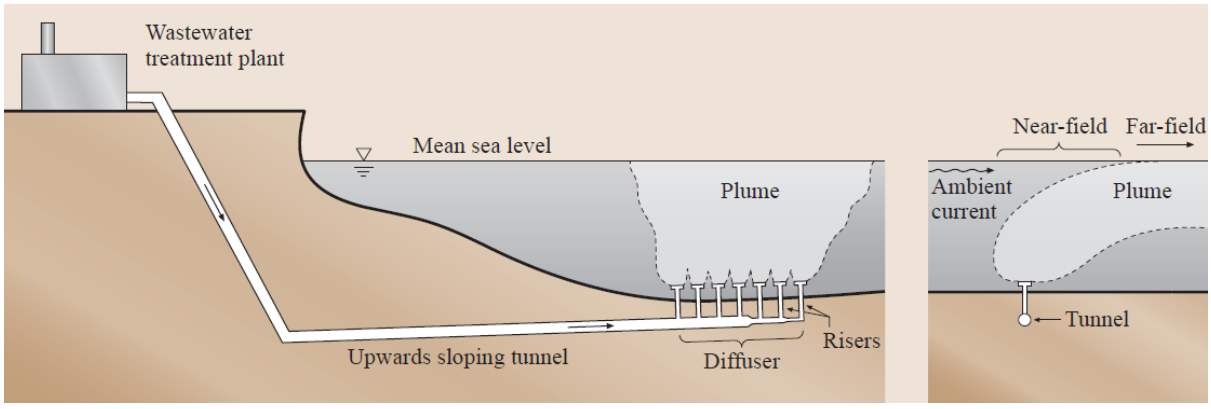

Figure 2-1. Schematic of a typical wastewater treatment plant outfall. Source: Tate, et. al. (2016).

Sewage has a density close to that of freshwater; hence, it is very buoyant in seawater. For this reason, once the effluent from a wastewater treatment plant outfall is discharged into seawater, the jets tend to rise towards the surface. Based on their proximity, jets may merge with their neighbours as they rise. The turbulence and entrainment of the jets causes rapid mixing and dilution in a region that is often called *near field*. The density stratification of the ocean may trap the rising plumes below the surface where they stop rising and begin to spread laterally, forming a *wastefield*. This wastefield is advected by the ocean currents and diffused by oceanic turbulence in a region called *far field*. Dilution rates are much slower in the far field than in the near field. Finally, large scale flushing, upwelling, sedimentation, chemical and biological decay processes remove contaminants and prevent long term accumulation of pollutants (Roberts, 2013). This processes occur at different length and time scales, with transitions between phases as shown in Figure 2-2. The main regions where these processes take place are: near field, far field, and long-term flushing, as defined below.

- **Near field:** In this region, mixing is caused by the buoyancy and momentum of the discharge. This region is located between 10 to 1,000 m from the diffuser and 1-10 minutes after the effluent is released.
- **Far field:** Comprises the region where the mixing is mainly due to advection by ocean currents and diffusion by oceanic turbulence. These processes take place over distances of 100 m to 10 km and times of 1 to 20 hours.
- **Long-term flushing region:** Large scale flushing, upwelling and downwelling, and sedimentation are the main processes that contribute to pollutant removal. This region is located between 10 to 100 km from the diffuser and times of 1 to 100 days and longer.

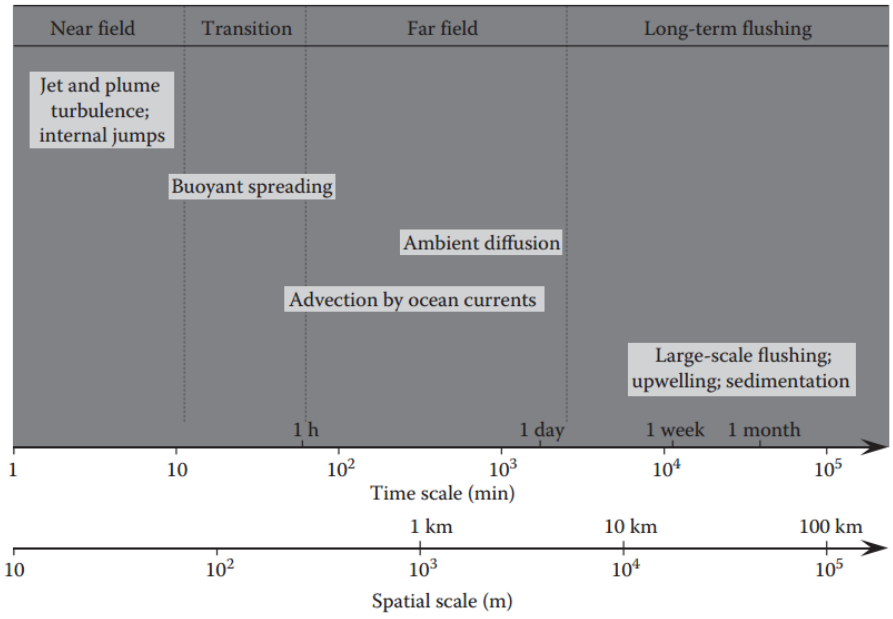

Figure 2-2. Approximate time and length scales of main processes governing marine outfalls. Source: Roberts (2013).

Modelling is an important tool for designing marine outfalls and monitoring their impact on the receiving water body. To simulate the processes that govern mixing and dispersion of outfall effluents, it is usually necessary to use different types of models for near and far field simulation.

The following subsections give an overall description of the types of models that can be used for near and far field modelling.

2.1 NEAR FIELD MODELS.

Most of the dilution of the discharged wastewater occurs in the near field. Such dilution depends on the buoyancy and momentum of the discharge; hence, the engineer can configure the outfall design to maximize the dilution in this zone. On the other hand, far field processes are dominated by the natural dynamics of the receiving water body; therefore, the engineer has little control over dilution in this region. For this reason, when it comes to designing marine outfalls, near field modelling is the most important part of the simulation.

For the prediction of near field mixing it is necessary to understand the dynamics of jets, plumes, and buoyant jets. A jet is a flow that is driven by the source of momentum only; a plume is driven by the source of buoyancy only; and a buoyant jet is driven by both momentum and buoyancy. Discharges from marine outfalls are buoyant jets; however, buoyancy usually dominates over momentum fluxes and they can be approximated as plumes (Roberts, 2013). A near field model simulates the hydrodynamics and dilution of buoyant jets. In this subsection, three different types of near field models are presented: empirical models, entrainment models, and computational fluid dynamics (CFD) models.

2.1.1 Empirical models.

Empirical solutions (or length-scale approaches) are commonly used to develop expressions of the governing plume parameters. This approach uses dimensionless analysis to form dimensionless groups. These dimensionless groups are then used to scale the results of laboratory studies to full-sized field processes (Zhao, et al., 2011).

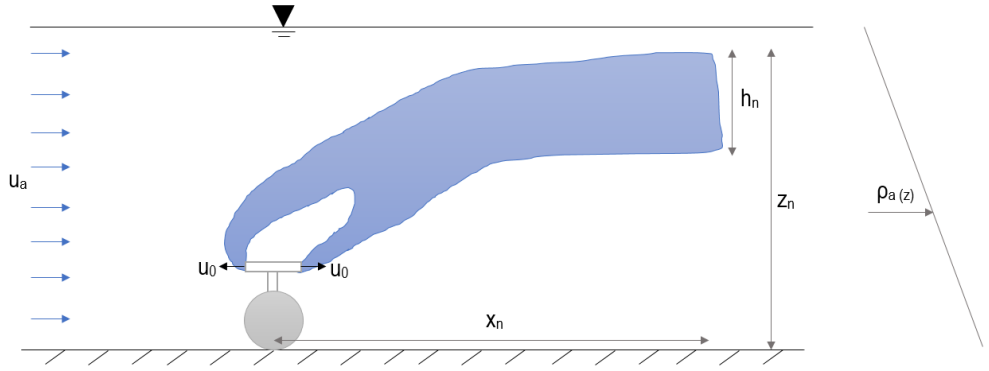

Figure 2-3. Schematic of a typical multiple port diffuser with Tee-shaped risers discharging into a stratified flowing environment.

One of the most commonly used empirical solutions is the RSB model developed by Roberts, et al. (1989a, 1989b, 1989c). This model has been updated with subsequent experimental work (Tian & Roberts, 2003) and renamed NRFIELD. NRFIELD model is part of the latest version of U.S. Environmental Protection Agency (EPA) mixing zone modelling application VISUAL PLUMES

(2003). This model describes the performance of a multiport diffuser with Tee-shaped risers, each having two ports, as shown in Figure 2-3. The effluent issues horizontally at a velocity u_0 from from ports with a d diameter, spaced a distance s apart. A current velocity, u_a, flows at an angle Θ to the diffuser axis. In the RSB model, near field plume properties such as rise height and dilution are predicted based on the analysis of the source kinematic fluxes of volume, Q_j ($L^3\ t^{-1}$, where L is length; t, time); momentum, M ($L^4\ t^{-2}$); and buoyancy ($L^4\ t^{-3}$):

$$Q_0 = \frac{\pi}{4} d^2 u_0 \quad \textbf{(2.1)}$$

$$M = u_j Q_0 = \frac{\pi}{4} d^2 u_0^2 \quad \textbf{(2.2)}$$

$$B = g_0' Q_j \quad \textbf{(2.3)}$$

where $g_0' = g\left(\frac{\Delta\rho}{\rho}\right)$, the modified acceleration due to gravity (Boussinesq assumption), g is the acceleration due to gravity, ρ is a reference density, and $\Delta\rho$ is the density difference between the effluent and seawater. If the density stratification is linear, it can be characterised by the buoyancy frequency, N (t^{-1}):

$$N = \sqrt{\left(-\frac{g}{\rho}\right)\left(\frac{d\rho_a}{dz}\right)} = \sqrt{\left(-\frac{g}{\rho}\right)\left(\frac{\Delta\rho_a}{H}\right)} \quad \textbf{(2.4)}$$

where ρ_a is the ambient density at height z and $\Delta\rho_a$ is the density difference over the water depth, H. The relative importance of buoyancy and inertial forces on the buoyant jet is expressed by the densimetric Froude number, F_0:

$$F_0 = \frac{u_0}{\sqrt{g_0' d}} \quad \textbf{(2.5)}$$

Based on a dimensional analysis, NRFIELD uses length scales, in order to characterize flow according to the relationship between variables such as momentum, buoyancy and density stratification; whereby, simplifying its analysis.

$$l_B = \frac{B^{1/4}}{N^{3/4}} \quad \textbf{(2.6)}$$

$$l_M = \frac{M^{3/4}}{B^{1/2}} \quad \textbf{(2.7)}$$

The length scale l_B (L, length) is proportional to the maximum rise height for a buoyancy driven plume in a stationary fluid with linear density stratification. l_M (L, length) characterizes the distance over which the source momentum flux is important relative to the buoyancy flux: for distances much less than l_M, the flow is dominated by momentum (behaves like a jet); and for distances greater than l_M, the flow is dominated by buoyancy (behaves like a plume). Based on this analysis, it can be concluded that given enough depth, a buoyant jet will always turn into a plume were the effect of source momentum flux is neglected.

For unstratified stagnant waters, the main relationships used to classify the flow are spacing to water depth and the momentum to buoyancy length scale. Tian, et. al. (2004a) found in a series of Laser Induced Fluorescence (LIF) experiments that for buoyant jets discharging in stagnant

environments, s/H ratios higher than 1 correspond to point plume behaviour and values lower than 0.3 correspond to line plume behaviour. Brookes (1980) determined the ranges in which buoyancy prevails over momentum, as shown in Table 2-1. Various studies have found that most real-life marine outfalls operate such that they are mainly driven by buoyancy, being their source of momentum negligible (Roberts et. al., 1989a; Fischer et. al. 1979).

Table 2-1. Classification of plumes exiting in an unstratified stagnant environment.

Classification	**Unstratified stagnant environment**		
According to spacing (Tian et. al., 2004a)	**s/H < 0.3**	**0.3 < s/H ≤ 1**	**s/H > 1**
	Line plume	In transition from line to point plume	Point plume
According to momentum to buoyancy length scale (Brooks, 1980)	**l_M/H < 0.2 or l_m< 0.25**		
	Buoyancy dominates over momentum		

When buoyant jets discharge in an unstratified flowing environment, the relationship between ambient current and buoyancy, given by the Roberts Froude number, becomes the main parameter for flow classification. The Roberts Froude number is given by the following equation:

$$F = \frac{u^3}{b} \tag{2.8}$$

In the presence of a current, Roberts et. al. (1979) found that a line plume behaviour occurs for s/H higher or equal to 0.5. However, even for s/H values as high as 4.5, the plumes merged before reaching the surface and cannot be classified as point plumes. This is due to the presence of a current, which delays the plumes' rise to the surface; whereby, providing more time for plume merging. This indicates that in the presence of a current, line plume equations are widely applicable for marine outfall modelling.

For line plumes, Roberts et. al. (1979) identified mainly three types of flow regimes, as listed in Table 2-1. When the Roberts Froude number is below 0.2, the plume quickly rises, and an upstream wedge is formed near the surface. For Froude numbers between 0.2 to 1, Roberts et. al. (1979) observed a phenomenon called forced entrainment. In the forced entrainment regime, the plumes mix over the water depth and get attached to the lower boundary. For Froude numbers higher than 1, the study did not observe an upstream wedge and a forced entrainment regime prevailed.

Table 2-2. Classification of plumes exiting in an unstratified coflowing environment. Based on Tian et. al. (2004b).

Classification	**Unstratified in flowing environment**		
According to Roberts Froude number for a line plume (Roberts, 1979)	**F < 0.2**	**0.2 < F < 1**	**F > 1**
	Plume and upstream wedge	Forced entrainment and upstream wedge	Forced entrainment, no upstream wedge
According to spacing (Tian et. al., 2004b)	**s/H ≤ 0.5**	**s/H up to 4.5**	
	Line plume	In transition from line to point plume	
According to momentum to buoyancy length scale (Brooks, 1980)	**l_M/H < 0.2 or l_m< 0.25**		
	Buoyancy dominates over momentum		

For a line source, the volume, momentum and buoyancy fluxes are better described per unit length of diffuser, rather than fluxes per individual port. Therefore, line source fluxes of volume, q ($L^2\ t^{-1}$; where L is length; t, time); momentum, m ($L^3\ t^{-2}$); and buoyancy, b ($L^3\ t^{-3}$) are defined as:

$$q = Q_T/L \quad \textbf{(2.9)}$$

$$m = u_j q \quad \textbf{(2.10)}$$

$$b = g_0' q \quad \textbf{(2.11)}$$

where Q_T is the total flowrate discharged by the outfall and L is the length of the diffuser.

NRFIELD defines equations to determine dilution, near field length, plume rise height and layer thickness. These equations have been produced for different scenarios including multiple buoyant jets in unstratified and stratified environments in the presence or absence of flowing currents. Such equations are the result of decades of extensive research using dimensionless analysis with the source fluxes as independent variables combined with length scales and experimental data (Frick, et al., 2003). Some of NRFIELD equations for the cases of multiple jets in stratified and unstratified stationary environment are shown in Table 2-3.

In the presence of a flowing current, the dilution and rise height are defined in NRFIELD as a function of the Roberts Froude number and the angle of the current relative to the diffuser axis, Θ. On the other hand, the length of the near field (x_n) is defined as independent of Θ. Increasing Froude numbers (i.e. higher current speeds) generate higher dilution while reducing rise height.

Other empirical models that have been widely used are part of the CORMIX simulation and decision support system. The CORMIX system contains three semiempirical models: CORMIX1, for submerged single-port discharges; CORMIX2, for submerged multiport discharges; and CORMIX3 for buoyant surface discharges.

CORMIX classifies the possible flow regimes for wastewater discharges into several categories based on the following factors: depth, stratification, crossflow velocity, and density of the receiving waters; the flow rate and density of the effluent; and the design patterns of the diffuser (Yeh, et al., 2011). Similar to other empirical models such as NRFIELD, CORMIX classifies flow regimes in terms of length scale ratios that define the relative importance of the aforementioned factors. These length scales ratios are compared with empirical constants. According to the flow classification, CORMIX selects the combination of equations that best describe the behaviour of the flow in study.

Table 2-3. Equations for predicting near field behaviour for point and line plumes in stationary environments. Source: Roberts, et. al. (2010)

Unstratified	**Point plume (s/H > 1)**	**Line plume (s/H < 0.3)**
Dilution (S_n)	$\frac{S_n Q_j}{B^{1/3} H^{5/3}} = 0.26$	$\frac{S_n q}{b^{1/3} H} = 0.49$
Length of near field (x_n)	$\frac{x_n}{H} = 2.8$	$\frac{x_n}{H} = 0.9$
Layer thickness (h_n)	$\frac{h_n}{H} = 0.11$	$\frac{h_n}{H} = 0.36$
Rise height	H	H
Stratified	**Point plume ($s/l_B > 3$)**	**Line plume ($s/l_B < 0.5$)**
Dilution	$\frac{S_n Q_j N^{5/4}}{B^{3/4}} = 0.90$	$\frac{S_n q N}{b^{2/3}} = 0.86$
Length of near field	$\frac{x_n}{l_B} = 4.1$	$\frac{x_n}{l_b} = 2.3$
Layer thickness	$\frac{h_n}{l_B} = 1.6$	$\frac{h_n}{l_B} = 1.5$
Rise height (z_m)	$\frac{z_m}{l_B} = 3.5$	$\frac{z_m}{l_B} = 2.5$

Compared to NRFIELD, CORMIX simulates a wider range of diffuser configurations, with varying angles of discharge. Three major types of diffuser configurations are considered: unidirectional, where all ports point in the same direction perpendicular to the diffuser axis; staged diffusers, where all the ports point in the same direction parallel to the diffuser axis; and finally, alternating diffuser, where ports are arranged in an alternating fashion and point in different directions (Doneker & Jirka, 2007; Akar & Jirka, 1991).

Flow classification with CORMIX requires the use of six different length scales: firstly, *discharge geometric scale*, the distance over which the port has effect on the flow, relating volume and momentum flux; *plume/crossflow length scale*, which measures the effect of crossflow on the plume behaviour relating buoyancy flux and current velocity; *jet/crossflow length scale*, the distance to the position where the flow becomes affected by the current velocity, relating momentum and current velocity; *jet/plume length scale*, stating the distance from momentum dominated flow to buoyancy dominated flow; *jet/stratification length scale*, relating momentum and density stratification; and finally, *plume/stratification length scale*, relating buoyancy and density stratification (Akar & Jirka, 1991; Doneker & Jirka, 1990). For instance, in a single plume in a linearly stratified environment, the flow is initially classified as jet-like or plume-like according to the ratio between the jet/crossflow and plume/crossflow length scales. Subsequently, other length scale ratios are incorporated to the analysis, to classify the flow according to the relative importance of buoyancy or stratification over crossflow velocity (Akar & Jirka, 1991). The final flow classification will depend on the ports alignment, water depth, among other factors. It is important to note that not only empirical models are used in CORMIX. Once a flow is classified, entrainment, length scale and passive diffusion modelling methods are used to predict the flow behaviour. A similar analysis is applied to a variety of scenarios.

CORMIX1, CORMIX2 and CORMIX3, consider 70, 62, and 11 distinct flow classifications, respectively (Doneker & Jirka, 2007).

Both NRFIELD and CORMIX models have been applied to a variety of real-life scenarios (Carvalho, et al., 2013; Yeh, et al., 2011; Maia, et al., 2011). Roberts (1999) used NRFIELD to simulate the behaviour of the Sand Island ocean outfall discharging in Mamala Bay, Hawai. More than 20,000 simulations were run for a modelling period of almost a year, varying current and density stratification conditions. The results found good agreement with field studies that mapped the plume with natural tracers such as salinity and turbidity. However, the patchy nature of the wastefield in the vertical and horizontal direction that was observed in the field measurements was not predicted by the NRFIELD model. Similarly, Carvalho, et al. (2002) used fluorescent dye tracers at low concentrations to model stratified and unstratified conditions in the Ipanema Beach, Rio de Janeiro, ocean outfall, and compared its results to those of NRFIELD and CORMIX, finding overall, a good agreement between observed and predicted results for dilution, height minimum dilution and spreading layer thickness; nonetheless, coinciding with Roberts (1999), the models did not predict the patchiness of the wastefield. This is likely to result from the assumption that plume properties vary smoothly in space. Other studies have used NRFIELD for design and verification of proposed outfall configurations in locations such as Florianópolis, Brazil; Boston, USA; Cartagena, Colombia, among many others (Carvalho, et al., 2013; Roberts & Carvalho, 2000; Roberts & Snyder, 1993).

2.1.2 Entrainment models.

Entrainment models were firstly suggested by Morton et. al. (1956) and have been found to be of great utility for predicting the jet and plume type flows typical of outfall discharge. These methods are also known as buoyant jet type integral models. In this type of models, the governing equations of motion and turbulent transport are integrated over the buoyant jet cross-sections.

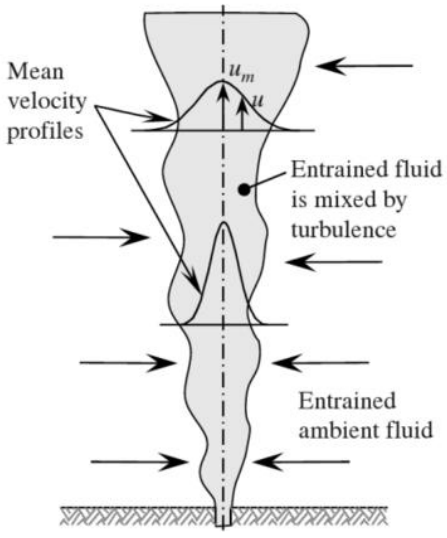

Figure 2-4. Entrainment in a simple plume. Source: Roberts et. al. (2010).

Entrainment is the process by which the buoyant jet incorporates ambient material into itself. Several mechanisms are involved in the entrainment process: aspirated, forced, and turbulent (or

eddy diffusion) entrainment. Aspirated entrainment (also known as Taylor entrainment) is shear entrainment, present even in the absent of current. Forced entrainment is due to the effect of the current which advects mass into the buoyant jet. Aspirated and forced entrainment are the main mechanisms considered for the formulation of near field models since diffusion entrainment is relevant only in the far field, where the other two entrainment mechanisms have been diminished (Baumgartner, et al., 1994).

The Taylor entrainment hypothesis (Morton, et al., 1956) states that the rate of entrainment at the buoyant jet edge is proportional to some characteristic velocity at that height (usually the centreline or average velocity) and the profiles of mean velocity and mean buoyancy force are similar at all heights. Hence, the fluid is entrained into the turbulent jet zone at the plume radius b_c, with a mean velocity u_e that is proportional to the mean centreline velocity, u_m (see Figure 2-4). This can be expressed as:

$$u_e = \alpha u_m \tag{2.12}$$

where α is the entrainment coefficient which differs for jets and plumes.

Entrainment models can be formulated using a Eulerian or Lagrangian approach, depending on whether the conservation equations are solved on a fixed control volume or a moving control volume. Both approaches give similar results when given similar assumptions.

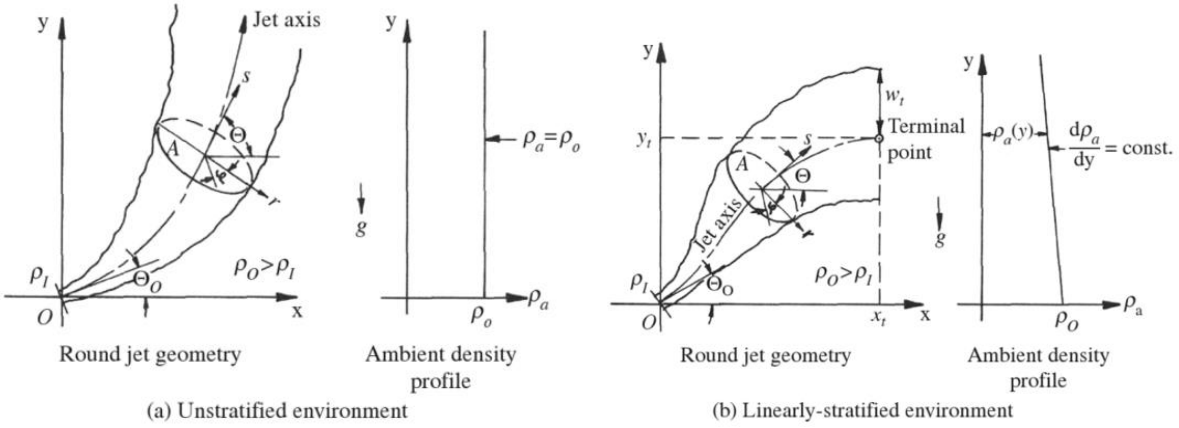

Figure 2-5. Definition sketch for two-dimensional buoyant jet discharge. Source: Roberts et. al. (2010).

Fan and Brooks (1969) developed one of the earliest Eulerian entrainment models for inclined round and slot buoyant jets in unstratified and linearly-stratified stagnant ambient. This model was based on the following assumptions: 1) the fluids are incompressible; 2) the variation of density is neglected for inertia terms but included in gravity terms (Boussinesq approximation); 3) the density of the fluid is a linear function of the temperature or salinity content; 4) flow is fully turbulent; therefore, there is not Reynolds number dependence; 5) longitudinal turbulent transport is small compared to longitudinal convective transport; 6) pressure is hydrostatic throughout the flow field; 7) the effect of curvature is neglected; and 8) the velocity, density deficiency respect to the ambient density, and concentration profiles are similar at all cross sections normal to the jet trajectory and follow a Gaussian distribution. Based on this assumptions, the velocity profile in a round jet (see Figure 2-5) is given by:

$$u = u_m(s)e^{-r^2/{b_c}^2} \tag{2.13}$$

where u_m is the local velocity at radial distance r from the jet centreline, $u_m(s)$ is the maximum centreline velocity at distance *s* along the buoyant jet trajectory, and b_c is the characteristic length defined by the velocity profile. Commonly, $\sqrt{2}\, b_c$ is the nominal half width of the buoyant jet (radius). Hence, the continuity equation is:

$$\frac{d}{ds}\int_0^\infty \int_0^{2\pi} u \cdot r \cdot dr \cdot d\varphi = 2\pi\alpha b_c u_m \tag{2.14}$$

Integrating and substituting, the continuity equation becomes:

$$\frac{d}{ds}\left(u_m {b_c}^2\right) = 2\alpha u_m b_c \tag{2.15}$$

Similar analyses were conducted for the conservation of horizontal and vertical components of momentum, density deficiency, and tracer. The horizontal momentum conservation is defined as:

$$\frac{d}{ds}\left(\frac{u^2 {b_c}^2}{2}\cos\theta\right) = 0 \tag{2.16}$$

The rate of change of the vertical momentum flux is equal to the buoyancy force acting on the buoyant jet, which leads to the following equation (using the Boussinesq approximation):

$$\frac{d}{ds}\left(\frac{u^2 {b_c}^2}{2}\sin\theta\right) = g\lambda^2 {b_c}^2 \frac{\rho_0 - \rho}{\rho_0} \tag{2.17}$$

where λb_c is the characteristic length of the momentum profile and λ is the turbulent Schmidt number which is assumed to be constant and somewhat larger than 1.

The density deficiency conservation is given by:

$$\frac{d}{ds}\left(u\, {b_c}^2 \cdot (\rho_0 - \rho)\right) = 0 \tag{2.18}$$

Finally, the continuity of a tracer substance present in the source flow is expressed by:

$$\frac{d}{ds}\left(c\, u\, {b_c}^2\right) = 0 \tag{2.19}$$

where *c* is the tracer concentration.

These equations, along with the equation of geometry of the centreline are solved numerically along the buoyant jet, predicting its trajectory, width, and dilution ratios, in a uniform or density stratified environment without ambient currents.

A more complete Eulerian integral model is Corjet (Jirka, 2004), which is part of the commercial software package, CORMIX. Corjet calculates the entrainment in a cylindrical coordinate system considering the contributions of two types of shearing mechanisms: 1) streamwise shear, in which the excess buoyant jet velocity above the component of the ambient velocity parallel to the jet trajectory causes entrainment at the jet periphery; 2) azimuthal shear in which the component of the ambient flow normal to the buoyant jet trajectory passes around and interacts with the cylindrical jet element, causing entrainment predominantly in the lee and an internal double vortex circulation (Figure 2-6). The equations of the conversation of mass, momentum, buoyancy and scalar quantities are integrated. Gaussian profiles are assumed for the velocity, buoyancy, passive and active scalar concentrations along the plume trajectory. CorJet considers both single and multiple buoyant jets issuing from single port and multiport diffusers in an *unbounded*

stratified ambient crossflow. The term unbounded refers to conditions in which the spatial scale of the buoyant jet motion is much less than the ambient dimension (Jirka, 2004). Likewise, most entrainment models ignore the effect of the interactions with the ambient boundary, representing one of their major disadvantages (Zhao, et al., 2011; Jirka, 2004).

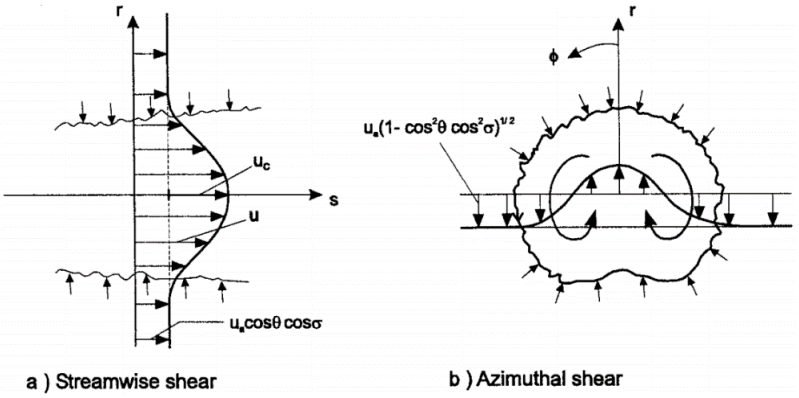

Figure 2-6. Shear mechanisms leading to entrainment across the laminar-turbulent interface of buoyant jets. Source: Jirka (2004).

Lagrangian entrainment models have also been widely used. Some popular Lagrangian entrainment models include JETLAG (Lee & Cheung, 1990) and UM3 (Baumgartner, et al., 1994). JETLAG is the model solved by the software package VISJET and UM3 is part of U.S. EPA mixing zone software VISUAL PLUMES. Both UM3 and JETLAG are based on the Taylor entrainment hypothesis and the Projected Area Entrainment hypothesis (PAE). The unknown buoyant jet trajectory is analysed as a series of plume elements with the shape of a section of a bent cone. The changes in the properties of the plume such as average velocity, pollutant concentration, temperature and salinity, width and thickness are evaluated at discrete time steps, integrating the continuity, horizontal and vertical momentum, and energy equations over time along the buoyant jet trajectory.

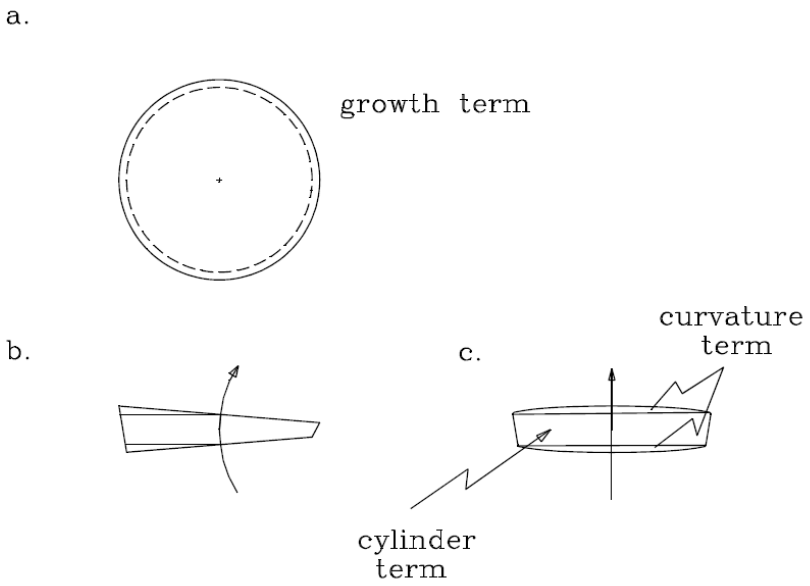

Figure 2-7. The projected area entrainment components: **a)** the growth area; **b)** side view of the element; and **c)** cylinder and curvature area. Source: Baumgartner, et al. (1994).

Models based on the PAE hypothesis such as JETLAG and UM3 state that the forced entrainment of fluid through the projected area of the buoyant jet is composed of three terms: the first term represents the forced entrainment due to the projected area normal to the current flow (assuming a cylindrical shape); the second is the correction due to the growth of the plume radius; and the third is the correction due to the curvature of the buoyant jet trajectory (see Figure 2-7). An additional term, encompassing the entire peripheral area accounts for the Taylor entrainment. The complete entrainment equation is then defined as a sum of the forced and Taylor entrainment:

$$\frac{dm}{dt} = \rho \vec{A}_p \vec{u}_a + \rho A_T \vec{u}_e \qquad \textbf{(2.20)}$$

where dm is the incremental amount of mass entrained in the time increment dt, A_p is the projected area, u_a is the ambient current speed normal to the projected area, and ρ is the local ambient density, A_T area of the plume element in contact with the ambient fluid and u_e is the Taylor aspiration speed ($\vec{u}_e = \alpha u_m$, and u_m is the average or "top hat" element velocity). A_T is simply the peripheral area of the element, defined as:

$$A_T = 2\pi b_c h \qquad \textbf{(2.21)}$$

where b is the element radius and h is the length of the element, which changes according to the difference in velocity of the leading and trailing faces of the element (see

Figure **2-8**). The reduction of this area due to merging are included in UM3 model. However, JETLAG does not model merging and each buoyant jet is calculated independently.

The projected area A_p is the sum of the cylinder, growth and curvature terms. The entrainment in the area normal to the current flow (cylinder term, A_{cyl}), assuming that in a crossflow situation, as is common in buoyant jets, only the upstream portion of the area (half a circumference) has flow going through it.

$$A_{cyl} = 2 b_c h \qquad \textbf{(2.22)}$$

The growth term (A_g) of the projected area is defined as:

$$A_g = \pi b_c \, \Delta b_c \qquad \textbf{(2.23)}$$

where $\Delta b = b_c h / \Delta s$, being Δb_c the difference in radius over the leading and trailing faces of the element and Δs is the distance along the centreline.

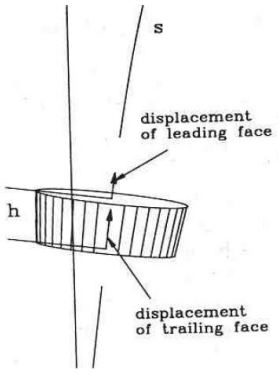

Figure 2-8. Buoyant jet element with the shape of a section of bent cone. Source: Baumgartner, et al. (1994).

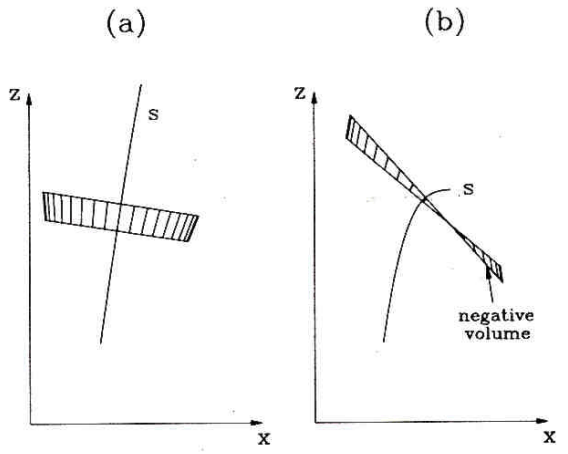

Figure 2-9. a) The plume in a region of weak trajectory curvature; **b)** strong trajectory curvature. Source: Baumgartner, et al. (1994).

The change in direction of the average plume element velocity, in other words the curvature of the centreline, causes the element of the plume to be deformed into a wedge shape (see Figure 2-9). Hence, the curvature term of the projected area will depend on the local jet orientation angles. Assuming that the plume has an elevation angle θ in the xz plane, the curvature term (A_{cur}) is:

$$A_{cur} = \frac{\pi h {b_c}^2 \cos\theta}{2\Delta s} \qquad \textbf{(2.24)}$$

Hence, the continuity equation is written as:

$$\frac{dm}{dt} = \rho u_e (2\pi b_c h) + \rho \vec{u}_a \left(2 b_c h + \frac{\pi {b_c}^2 h}{\Delta s} + \frac{\pi {b_c}^2 \cos\theta \; h}{2\,\Delta s}\right) \qquad \textbf{(2.25)}$$

The conservation of momentum

$$\frac{dm\vec{u}_a}{dt} = \vec{u}_a \frac{dm}{t} + m \frac{(\rho_a - \rho)}{\rho} \vec{g} \qquad \textbf{(2.26)}$$

where m is the mass of the plume element ($m = \rho\pi b^2 h$), ρ_a and ρ are the ambient and average element densities, respectively, and $\vec{g}$ is the gravity vector.

JETLAG, as other early developed models, does not consider the effect of plume merging; hence, the model is indifferent to diffuser port spacing and the buoyant jets are simulated independently (Palomar, et al., 2012a; Lee & Cheung, 1990). However, UM3 includes merging in its formulation, applying a correction to the Taylor and forced entrainment by reducing the entrainment area due to the interference between buoyant jets from adjacent ports (Baumgartner, et al., 1994).

Both JETLAG and UM3, differing with Corjet and other Eulerian models, assume that the velocity and pollutant concentrations have a uniform or "top hat" profile, and the radius of the buoyant jet element is calculated as a function of its mass:

$$b_c = \sqrt{\frac{m}{\pi \rho h}} \tag{2.27}$$

Although assuming a "top hat" profile is acceptable for the dynamic properties of the buoyant jet, centreline concentrations of pollutants are of interest for environmental protection and using average values can represent the underestimation of the pollutant effect on the environment. For this reason, UM3 assumes a 3/2 power profile for pollutant concentrations, which closely matches the Gaussian profile but has definite boundaries, which better suits the plume element used in the formulation of the model. When the 3/2 profile is used, a scaling factor ϕ is applied to a centreline value to determine the corresponding one at a distance r from the centre of the plume.

$$\phi = \left(1 - \left(\frac{r}{b_c}\right)^{3/2}\right)^2 \tag{2.28}$$

Boundary conditions for solving entrainment models include the initial plume radius (port radius), discharge velocity, effluent temperature, pollutant concentrations and ambient conditions. The general procedure for solving Lagrangian entrainment models is: 1) a time step is provided; 2) the entrainment equations are used to calculate the amount of mass entraining the buoyant jet at that time step; 3) the equations of motion and concentration of active and passive scalars (temperature, salinity, pollutants) are integrated; 4) the new time step is established and the cycle is repeated (Baumgartner, et al., 1994).

Table 2-4. *Comparison of software packages based on entrainment models.*

Software package	VISJET	UM3	Corjet
Access	Commercial package	Open access	Commercial package
Application	Positively and negatively buoyant effluents from single and multiport discharges.		
Modelling approach	Lagrangian Governing equations of fluid motion are not directly integrated, but an approximation is made evaluating the changes in the properties of subsequent plume elements over time, considering the effect of entrainment.		Eulerian Governing equations of fluid motion and scalar transport are integrated through the buoyant jet cross-sections.
Assumptions	Unbounded environment. Self-similarity in cross-sectional velocity, buoyancy, and scalars profiles.		
	"Top hat" (uniform) profile.		Gaussian profiles.
	Results are referred to average values of the cross-section.	Results are referred to average values of the cross-section, except for pollutant concentrations for which centreline concentrations are calculated using a 3/2 power profile.	Results are referred to centreline values.
	Entrainment is caused by two mechanisms: streamwise and azimuthal shear.	Two types of entrainment mechanisms: Taylor and forced entrainment. Forced entrainment is calculated using the projected area entrainment (PAE) hypothesis, which determines the amount of mass incorporated into the buoyant jet due to a cross (transverse) current.	
	Merging is not simulated; hence, buoyant jets from adjacent ports modelled independently.	Merging between adjacent buoyant jets is considered reducing the entrainment area due to the interference between plumes.	Merging between adjacent buoyant jets is considered assuming an equivalent slot diffuser.
	The buoyant jet radius is determined for each buoyant jet element, using the entrained mass as independent variable for its calculation. Velocity and scalar concentrations are uniform over the buoyant jet diameter.	The buoyant jet radius is determined for each buoyant jet element, using the entrained mass as independent variable for its calculation. Velocity and scalar concentrations are uniform over the buoyant jet diameter.	The buoyant jet radius is assumed to be at a distance $\sqrt{2}b$ from the centreline. The model assumes that at the radius, the concentration of scalars is 25% and velocity is 14% of the centreline values.

<table>
<tr><td></td><td colspan="2">The initial zone of flow establishment (ZOFE) is assumed to agree with the assumptions made for all regions along the buoyant jet trajectory.</td><td>The ZOFE is considered a transition region that lacks self-similarity; hence, the formulation for this zone is not based on the integration of the governing equations but rather on experimental observations.</td></tr>
<tr><td rowspan="2">Capabilities</td><td colspan="3">The model takes into account discharge parameters (flow rate, density, concentration of pollutants, temperature, etc.), diffuser geometry (port diameter, port height and depth, port spacing, discharge angle, etc.) and ambient conditions (currents, density, etc.).
Different values for density, temperature, salinity, current velocity and direction can be inputted to the software along the water column, enabling the mode to simulate buoyant jets in stratified environments.
The software is user-friendly and can be run by non-expert users.
The software is fast and renders instant calculations.</td></tr>
<tr><td>Since every buoyant jet is modelled independently, it is possible to input different configurations for each diffuser outlet.</td><td colspan="2">Merging between buoyant jets from adjacent ports can be modelled.</td></tr>
<tr><td rowspan="5">Limitations</td><td colspan="3">Interactions with boundaries (surface and bottom) are not considered since it is assumed that the jets are in an unbounded environment. The simulation usually stops when the jet impacts the surface, which is considered the end of the near field.</td></tr>
<tr><td>Merging is not modelled, making port spacing irrelevant to the design.</td><td colspan="2">All diffuser ports should have the same characteristics (diameter, height, flow rate, and discharge angle) and equal spacing.</td></tr>
<tr><td colspan="2">Unrealistic assumption of self-similarity in the ZOFE.</td><td rowspan="2">No graphics available for the evolution of variables such as velocity, scalar concentrations, dilution, etc.</td></tr>
<tr><td>No graphics available for the evolution of variables such as velocity, scalar concentrations, dilution, etc.</td><td rowspan="2">Low quality graphics.</td></tr>
<tr><td>Time series data files of discharge and ambient conditions cannot be inputted for sequential modelling.</td><td>Time series data files of discharge and ambient conditions cannot be inputted for sequential modelling.</td></tr>
</table>

References	Etemad-Shahidi & Azimi (2007) found agreement between laboratory results and VISJET predictions for experiments simulating the conditions of two real scale outfalls discharging thermal effluents from power plants. The error between modelled and observed dilution values was below ±20% most of the times. Lai et. al. (2011) simulated in the laboratory the performance of rosette-type buoyant jets (2-8 ports arranged circumferentially), finding a good agreement for dilution values obtained by the VISJET model and experimental results using laser-induced fluorescence (LIF) technique. An additional comparison was done to results of LIF study conducted by Roberts & Synder (1993a) for a 8-jet rosette riser in a nonlinearly stratified environment, corresponding to a physical model of a section of the Boston outfall, finding a very similar trend for the relationship between dilution and number of ports. In general, existing studies using VISJET have obtained good results for dilution values; however, results for buoyant jet geometry parameters (rise height, spreading layer thickness, etc.) are less accurate.	Roberts & Tian (2003) used a physical model with a three-dimensional LIF system to study the discharge of a multiport diffuser in a 12 m deep water. The study found good agreement between UM3 predicted and measured buoyant jet variables including dilution, length of the near field, layer thickness and rise height. Carvalho, et. al. (2002) found very similar results for dilution measurements in the near field of the Ipanema Beach Outfall, using a fluorescent dye as a tracer. Muhammetoglu, et. al. (2012) coupled UM3 model with Brooks dispersion model to study near and far field dilution in Antalya Bay, Turkey, finding good agreement with measured total and faecal coliform concentrations in the near and far field. In general, existing studies using UM3 have obtained good results for dilution values; however, results for buoyant jet geometry parameters (rise height, spreading layer thickness, etc.) are less accurate.	Jirka (2004), Corjet author, validated the model with experimental results from literature for a variety of regimes, including pure jets, vertical and horizontal buoyant jets in co-flow and cross-flow.

Source: Author. Based on Palomar et. al. (2011); Jirka (2004); Baumgartner, et. al. (1994); and Lee & Cheung (1990).

In summary, entrainment models, also known as buoyant jet type integral methods, are a useful tool for near field modelling. However, their simplicity leads to limitations that should be considered when applying these types of models (Roberts et. al., 2010; Zhao, et. al., 2011; Palomar, et.al., 2012). Some of these limitations lie on their assumption of an 'unbounded' environment, which implies that these models are not suitable for situations in which the boundary interactions can terminate or alter the buoyant jet motion (Zhao et. al., 2011; Jirka, 2004). The entrainment coefficient is assumed to be constant; however, it always varies along the trajectory of the buoyant jet. Moreover, their limited capacity to model merging between buoyant jets from multiport diffusers is a disadvantage. A complete comparison of the three most used integral models, VISJET, UM3 and Corjet, is given in Table 2-4, including their main application, assumptions, capabilities, limitations, and studies available in literature that have validated these models with measurements from physical models and real life outfall discharges.

2.1.3 Computational fluid dynamics (CFD).

CFD modelling is being increasingly applied to solve problems in fluid dynamics and heat transfer. However, little has been done on the use of CFD models for simulating initial mixing of outfall and diffuser discharges.

CFD modelling of turbulent flows is applied through three main approaches: Direct Numerical Simulation (DNS), Large Eddie Simulations (LES), and Reynolds-averaged Navier-Stokes equations (RANS). In the DNS approach, the Navier-Stokes equations are solved over scales that are small enough to solve the whole spectrum of turbulence, from the largest eddies to the smallest Kolmogorov microscales (where viscosity dominates and turbulent energy is dissipated as heat). Due to the high cost of DNS models for simulating high Reynolds number flows, their use is limited to flows of low Reynolds numbers. A more affordable approach is LES, in which the Navier-Stokes equations are directly solved for the large eddies but small eddies are modelled with a sub-grid. However, LES are still costly and unpractical for high Reynolds numbers. The most widely used approach is RANS, in which flow quantities are decomposed in time-averaged and fluctuating components to solve the Navier-Stokes equations. A wide range of RANS models are available to solve all turbulent length scales, being the eddy viscosity k-ε models the most commonly used since they provide a good level of accuracy at reasonable numerical effort. In the eddy viscosity k-ε turbulence model, the local mean state of turbulence can be characterized by the turbulent kinetic energy k and its rate of dissipation ε (Roberts et. al., 2010; Versteeg & Malalasekera, 2007) .

As aforementioned, the applicability of CFD models to jet and plume-type flows from marine outfalls has been scarcely researched. This is due to the geometrical complexity of multiport diffusers and the disparity between the size of a typical diffuser and the length scale of the receiving water body in which the diffuser is located (Zhao et. al. 2011; Roberts et. al., 2010; Tang, et al., 2008). Other factors adding to its complexity are buoyancy effects, plume merging, flowing currents, among others. An early attempt on applying CFD to buoyant jets was made by Hwang, et al. (1995) and Hwang & Chiang (1995), who used three-dimensional RANS k-ε turbulence models to investigate the effect of ambient density stratification on a buoyant jet in cross-flow, obtaining satisfactory correlations between the models and experimental data.

Far field circulation models have been applied to near field simulations, in order to determinate the capacity of circulation models to describe near field behaviour (Blumberg, et al., 1996; Zhang

& Adams, 1999). Blumberg, et al. (1996) applied a model based on the three-dimmensional circulation model (ECOM) to the near field of the Boston sewage outfall in the Massachussets Bay. The results were compared to the predictions of ULINE near field model (part of previous versions of VISUAL PLUMES, predecesor of NRFIELD), finding that 65% of the time the circulation model predicts lower plume height rise than the near field model and 70% of the time, a lower dilution. The discrepancies between both models result from the spatial resolution of the far field model, which is rather coarse compared to the domain of the initial mixing processes. Furthermore, the circulation model is designed for far field simulation where the hydrostatic approximation is valid; whereas in the near field, buoyancy dominates and the details of the outfall design are important.

The LES approach has been applied to simulate the initial mixing of effluent from a real outfall on seabed (Nakayama & Nizamani, 2016). The model was formulated on a fixed rectangular grid in which boundaries are approximated by Inmmersed Boundary method (IB). The Smagorinsky model was used to define the eddy diffusivity and eddy viscosity, which express the subgrid effects of unresolved fluctuations of velocity and the concentration fields. The model is initially validated by calculating a basic buoyant wall jet to be later applied to simulate a real case of marine water disposal. Although there are limitations related to the extent of the simulation region and the duration of the simulation period, the LES model has good potential for near field modelling that can be improved as computer performance is improved.

RANS models have also been used for modelling the near field of outfalls. Davis, et. al. (2004) used ANSYS CFX 5.6 and FLUENT 6.1 for modelling three case studies: first, a controlled discharge in a laboratory through a simple line diffuser; second, a deep ocean discharge from a 14 port diffuser in an unstratified environment; and third, the discharge of a dense fluid from multiple risers with multiple ports into a shallow river. The CFD model results were compared with those of popular near field models such as VISUAL PLUMES (UM and DKHW) and CORMIX. For the first case study, the model was also compared to experimental data, finding a close agreement with experimental data for both plume trajectory and concentration of tracers. The CFD model had the advantage of simulating more closely the actual discharge conditions for the second and third case studies, since the version of VISUAL PLUMES used for this study could not simulate ports on both sides of a diffuser and CORMIX could not run for few ports. Furthermore, for the third case study, the CFD model could more accurately simulate the buoyant jet interactions with the bottom, including the slower mixing once the negatively buoyant jets touch the bottom.

To overcome the difficulties that arise from the different length scales between the diffuser diamater and the characteristic lenghts of the receiving water bodies, Tang, et al. (2008) developed a RANS model using a domain decomposition method with multilevel embbeded overset grids (Chimera grids). This method divides a complex domain into subdomains that can arbitrarily overlap with each other and are discretised using structured, body-fitted, curvilinear grids. Turbulence was resolved using a simple mixing length approach. The model was validated using experimental data of negatively buoyant wall jet flows. Results obtained for single and multiple port discharges were very similar to those of commonly used models CORMIX and NRFIELD. However, these results were only conducted in steady-state conditions and the source of buoyancy was solely based on temperature variations. On the other hand, Robinson et. al. (2015) used a mesh optimisation algorithm to solve the RANS k-ε equations for an angled dense jet. The model updated the mesh every 10 time-steps depending on the curvature of velocity, salinity, turbulent energy and turbulent dissipation. Results obtained are in good agreement with experimental values; however, this study did not examine the capacity of CFD models to simulate

other complex processes that take place in full-scale marine outfalls such as merging between buoyant jets.

In recent years, as desalination plants have become the preferred option for meeting potable water demands in water-scarce regions, including countries such as Saudi Arabia, Israel, United Arab Emirates, USA, amongst others, the interest in understanding the dynamics of inclined brine discharges has grown. Extensive experimental research at laboratory scale has been conducted on inclined dense jets, measuring trajectories, velocity and dilution from discharges at varied inclination angles. However, there is limited available studies on the performance of CFD models for the simulation of brine discharges. Most of the research conducted so far has focused mainly on the computationally expensive Large Eddy Simulations (LES) models (Zhang, et al., 2016; Zhang, et al., 2017). Zhang et. al. (2016) modelled brine discharges with an angle of 45° using LES methods. They found good agreement for trajectory and dilution predictions. Similarly, Zhang et. al. (2017) predicted trajectory and dilution for negatively buoyant jets with discharge angles of 45° and 60° with bottom impact, obtaining favourable results. However, the simulation of a single case for a brine discharge using LES is between 7 and 20 days, which makes this method unfeasible for the simulation of multiple port discharges at a real-life scale with today's computational power.

Despite the demostrated potential of CFD models for the simulation of near field behaviour, it is important to keep in mind that the mixing processes in this zone of outfall diffusers are dominated by complex and highly unsteady dynamics, resulting from the instabilities of port jets and their interactions with each other and the ambient flow. Unsteady simulations increase the computational cost as they require finer meshes (Tang, et al., 2008). Moreover, outfall design may involve running thousands of simulations with different oceanographic and discharge conditions. For this reason, empirical and entrainment models continue to be the most widely used for near field modelling; however, the higher accuracy of CFD models should not be ignored when it comes to simulations of complex diffuser geometries (Roberts et. al., 2010; Davis, et. al., 2004).

2.2 FAR FIELD MODELS.

Although environmental guidelines are usually applied at the end of the near field, far field simulations are required when discharging into relatively shallow water, when mixing in near field is incomplete or when evaluating potential impacts on sites remote from the outfall such as bathing areas or protected ecosystems. Far field simulations include hydrodynamics and water quality components (Tate, et al., 2016). These components are further described in the following subsections.

2.2.1 Hydrodynamic models.

Hydrodynamic models of coastal circulation are suitable to predict the fate and transport of coastal discharges. These models require more extensive data input than near field models, including currents, bathymetry, winds, density stratification, tides and their spatial and temporal variability (Tate, et al., 2016; Zhao et. al. 2011; Roberts et. al. 2010). Most of these models are two dimensional and use hydrostatic and Boussinesq approximation. The equations of continuity, momentum, and thermodynamics are solved using finite difference (FDM), finite elements (FEM) or finite volume methods (FVM). A variety of turbulence closure sub-models are applied, including k-ε, k-w, Smagorinsky, among others (Roberts et. al., 2010). More sophisticated three-dimensional methods are needed for waters deeper than 30 m since high density stratification

cause the currents to be strongly sheared, flowing at different speeds and directions over depth, processes that would not be evident with two-dimensional models. Similarly, in areas with low stratification where the plume always reaches the surface, the effect of wind in the pollutants distribution is underestimated with two-dimensional models; hence, three-dimensional models are required for better results (Bedri, et al., 2011). However, due to the extensive current and density data required for three-dimensional models, this are rarely used for small outfall projects.

Far field circulation models are applicable to oceans, coastal waters, lakes, rivers, and estuaries. Circulation models can be easily coupled with water quality models, and many other them such as TELEMAC, DELFT and MIKE have water quality and particle tracking extensions. The advantage of circulation models is their use of terrain-following coordinates, which enables the incorporation of the topography smoothly, normalizing the vertical coordinate by the fluid depth. One of the most commonly used terrain following coordinates are known as σ-coordinates (Roberts, 2010; MIT, 2004). Table 2-5 compares three of the most up-to-date widely validated far field circulation models.

2.2.2 Water quality models.

The transport of dissolved constituents in the far field is mainly lead by two mechanisms: advection and diffusion. Advection is the transport mechanism driven by the fluid's bulk motion (ocean current); whereas, diffusion is the movement of a substance from a region of higher concentration to a region of lower concentration. The mass conservation equation – also known as advection-diffusion equation- is stated below:

$$\frac{\partial c}{\partial t} + u\frac{\partial c}{\partial x} + v\frac{\partial c}{\partial y} + w\frac{\partial c}{\partial z} = \frac{\partial}{\partial x}\left(\varepsilon_x \frac{\partial c}{\partial x}\right) + \frac{\partial}{\partial y}\left(\varepsilon_y \frac{\partial c}{\partial y}\right) + \frac{\partial}{\partial z}\left(\varepsilon_z \frac{\partial c}{\partial z}\right) \pm S + W \qquad \textbf{(2.28)}$$

where c is the concentration of the constituent; S is the production of species due to chemical or biological processes; W is a source term; u, v and w are the velocities in x, y and z directions, respectively; and ε_x, ε_y and ε_z are the diffusion coefficients in x, y and z directions, respectively.

This equation can be solved using Eulerian or Lagrangian methods. In the Eulerian methods, the advection-diffusion equation is solved in a fixed grid. The diffusion coefficients and current data are obtained from the hydrodynamic model. Alternatively, the Lagrangian method follows individual particles or puff as they move through space and time, obtaining current data from a hydrodynamic model or from a recording device (e.g. Acoustic Doppler Current Profiler).

2.2.3 Model coupling.

The independent modelling of the near and far field implies the need for coupling between models. Such coupling implies the transfer of different parameters such as volume, momentum and pollutant concentrations from one field to the other. Two types of coupling systems exist: passive and active. In the passive coupling approach, the effect of the discharge in the ocean hydrodynamics are neglected and only continuity principles are applied. In other words, only the pollutant concentrations at the end of the near field are transferred to the far field. This assumption is acceptable for the majority of marine outfalls since the discharge flow is insignificant as compared with the ocean currents. However, for marine outfalls with very large flows or thermal discharges, the effect of the discharge in the hydrodynamics of the receiving water body cannot be neglected and an active or two-way coupling is required, were not only the principles of mass conservation are considered but also momentum conservation (Roberts, et al., 2010; Blenninger, 2006; Chin & Roberts, 1985).

Table 2-5. Comparison of far field circulation models.

Name	Description	Considerations	Assumptions	Turbulence closure model	Applications/Extensions	Availability	References
Telemac 2D/3D	FEM. Solves the Reynolds-Averaged Navier-Stokes equations using an unstructured grid. *By Artelia,* **BundesAnstalt für Wasserbau, Centre d'Etudes Techniques Maritimes et Fluviales, Daresbury Laboratory, Electricité de France R&D,** *and* **HR Wallingford.**	• Wave propagation. • Bed friction. • Water-atmosphere exchanges: wind, precipitation, evaporation, temperature, and atmospheric pressure. • Source and sink terms. • Flood and drying. • Coriolis force.	• Boussinesq approximation. • Hydrostatic and non-hydrostatic assumption.	Different models can be used for horizontal and vertical turbulence. • Constant viscosity. • Mixing length (only for vertical turbulence): Prandtl, Nezu and Nakagawam Quetin and Tsanis. • Smagorinsky formulation. • k-ε model.	• Passive tracer transport. • Active tracer transport (temperature, salinity, and some types of sediments). • Sediment transport and bed evolution (SISYPHE and SEDI-3D modules). • Water quality: coupling with TELEMAC module SUBIEF-3D or with DELWAQ by DELTARES. • Wave propagation with the module TOMAWAC.	Open source.	Bedri, et. al. (2011) used TELEMAC-3D coupled with SUBIEF-3D to assess the impact of E. Coli emission on bathing the water quality of Dublin Bay (Ireland). Bedri, et. al. (2013) and Bedri, et. al. (2015) used TELEMAC-3D to model E. Coli distributions for different discharge scenarios, using the advection-diffusion equation for transport and the Mancini formula for bacterial die-off.
MIKE	FVM. Solves the Reynolds-Averaged Navier-Stokes equations using dynamical nesting. Graphical user interface. *By DHI.*	• Bed friction. • Water-atmosphere exchanges: wind, precipitation, evaporation, temperature, and atmospheric pressure.	• Boussinesq approximation. • Hydrostatic assumption.	• Constant viscosity. • Smagorinsky formulation. • k-model. • k- ε model. • k- ε in the vertical component and Smagorinsky	• Active tracer transport (temperature and salinity). • Passive tracer transport. • Sediment transport and bed evolution (Mud Transport module). • Water quality and ecological modelling	Commercial package.	Pritchard, et. al. (2013) used Mike 21 (2D model) to determine the impact of a wastewater plume in Northern Ireland, using nitrogen, phosphorous, temperature and

		• Source and sink terms. • Flood and drying. • Coriolis force.		for the horizontal component.	using the Eco Lab module.		salinity as plume tracers.
Delft3D	FVM. Solves the Reynolds-Averaged Navier-Stokes equations using staggered grids. Graphical user interface. *By DELTARES.*	• Bed friction. • Water-atmosphere exchanges: wind, precipitation, evaporation, temperature, and atmospheric pressure. • Source and sink terms. • Flood and drying. • Coriolis force.	• Shallow water approximation. • Boussinesq approximation.	• Constant viscosity. • Algebraic closure model. • Prandtl mixing length model. • k-L model. • k- ε model.	• Active tracer transport (temperature and salinity). • Passive tracer transport. • Water quality modelling: D-Water quality module for far field and D-Waq module for mid-field and particle tracking. • Ecological modelling with Delft3D- ECO module. • Sediment transport with Delft3D- SED module. • Wave propagation with Delft3D-WAVE. • Tidal analysis with Delft3D-TIDE.	Open source.	Baptistelli (2015) used Delft3D Flow to model the hydrodynamics of Santos Bay, Brazil. Based on the hydrodynamic model, the dilution of a 4.5 long marine outfall was calculated for the area of study. Roberts (2005) used Delft3D and Delft3D-WAQ to model bacterial fate and transport in the Cartagena outfall, coupled with the near field model NRFIELD.

2.3 SUMMARY.

This chapter presented the general theory on the marine outfalls and the processes that govern their near and far field. The modelling methods that have been used for the simulation of the near field of marine outfalls were described, identifying their advantages and disadvantages. These methods are namely empirical, entrainment and CFD techniques. The latter has been scarcely used for the simulation of marine outfall discharges, despite their great potential.

Likewise, the governing equations and most popular far field circulation models were described, detailing their features and previous applications on real-life marine outfalls.

3 METHODOLOGY FOR CFD MODELLING OF BUOYANT JETS.

In this chapter, the CFD methodology used for the modelling of two and three-dimensional single and multiple jets and buoyant jets is described. This methodology includes the equations governing the modelled flows and the detail assessment of different potential meshing approaches.

The Computational Fluid Dynamics (CFD) models were applied using the commercial software package *Ansys Fluent version 18.2* (Ansys Inc., 2018). This software package has been selected since it has been widely validated for a variety of applications including turbulent flows, which are the focus of this research. Furthermore, Ansys Fluent enables the use of High Performance Computing (HPC), allowing the application of parallel processing to accelerate the modelling process.

3.1 GOVERNING EQUATIONS.

3.1.1 Continuity, momentum, energy and turbulence.

The CFD simulation of the buoyant jet flows in this study is based on the time-averaged solution of the equations of fluid motion, known as the Reynolds-Averaged Navier-Stokes (RANS) equations. These equations reduce the computational effort of directly solving the instantaneous quantities in turbulent flows, by reducing them into a mean and a fluctuating component. This reduction is applied to quantities such as velocity, pressure, energy, and other scalars. An instantaneous velocity, u_i, is hence described as:

$$u_i = \overline{u_\iota} + u_i \tag{3.1}$$

where $\overline{u_\iota}$ and u_i' are the mean and fluctuating components, respectively. The mass and momentum conservation equations are hence described as

$$\frac{\partial \rho}{\partial t} + \frac{\partial}{\partial x_i}(\rho \overline{u_i}) = 0 \tag{3.2}$$

$$\rho\left(\frac{D\overline{u_i}}{Dt}\right) = -\frac{\partial p}{\partial x_i} + \frac{\partial}{\partial x_j}\left(\mu \frac{\partial \overline{u_i}}{\partial x_i} - \rho \overline{u_i' u_j'}\right) \tag{3.3}$$

where ρ is density, p is static pressure and μ is the dynamic viscosity of the fluid. The term $\rho\overline{u_i' u_j'}$ represents the effects of turbulence, generally referred to as Reynold stresses. In order to close Eq. (5), the Reynold stresses, must be modelled, a problem that is often called turbulence closure.

One of the approaches used to obtain turbulence closure is the Boussinesq hypothesis, which states that the momentum transfer caused by turbulent eddies can be modelled with an eddy viscosity, μ_t.

In this research, two different types of turbulence models based on the Boussinesq hypothesis are used: k –ε and k-σ models. These types of models have the advantage of having relatively low computational cost.

In the k – ε models, two additional transport equations are solved: the equation for the turbulence kinetic energy, k, and the equation for the turbulence dissipation,ε. For modelling the inclined dense jets described in this chapter, three different types of k – ε models are used: standard k – ε, proposed by Launder and Spalding (1974); RNG k – ε, a modification to the standard k – ε proposed by Choudhury (1993); and realizable k – ε, a more recent modification to the standard k – ε proposed by Shih et. al. (1995).

The standard k – ε model solves the turbulence closure model with two additional transport equations for turbulent kinetic energy and turbulent dissipation, as follows

$$\frac{\partial}{\partial t}(\rho k) + \frac{\partial}{\partial x_i}(\rho k u_i) = \frac{\partial}{\partial x_j}\left[\left(\mu + \frac{\mu_t}{\sigma_k}\right)\frac{\partial k}{\partial x_j}\right] + G_k + G_b - \rho\varepsilon - Y_M \qquad \textbf{(3.4)}$$

$$\frac{\partial}{\partial t}(\rho \varepsilon) + \frac{\partial}{\partial x_i}(\rho \varepsilon u_i) = \frac{\partial}{\partial x_j}\left[\left(\mu + \frac{\mu_t}{\sigma_\varepsilon}\right)\frac{\partial \varepsilon}{\partial x_j}\right] + C_{1\varepsilon}\frac{\varepsilon}{k}(G_k + C_{3\epsilon}G_b) - C_{2\varepsilon}\rho\frac{\varepsilon^2}{k} \qquad \textbf{(3.5)}$$

where $G_k$is the generation of turbulence kinetic energy due to the mean velocity gradients, G_b is the generation of turbulence kinetic energy due to buoyancy, $C_{1\varepsilon}$, $C_{2\varepsilon}$ and $C_{3\varepsilon}$ are constants, σ_k and σ_ε are turbulent Prandtl numbers for k and ε.

For the standard k – ε, the turbulent viscosity, μ_t, is calculated as a function of k and ε, as follows

$$\mu_t = \rho C_\mu \frac{k^2}{\varepsilon} \qquad \textbf{(3.6)}$$

where $C_\mu$is a constant.

For the standard k – ε models, these constants have the following values:

$$C_{1\varepsilon} = 1.44, C_{2\varepsilon} = 1.92, C_\mu = 0.09, \sigma_k = 1.0, \sigma_\varepsilon = 1.3 \qquad \textbf{(3.7)}$$

The RNG k – ε model is a modification to the standard k – ε model, which is based on a statistical technique named renormalization group theory. Contrary to the standard model which uses constant values, RNG k – ε proposes analytical formulas for the effective viscosity and Prandtl number. Whereby, this model takes into account the effect of varying Reynolds numbers. Additional terms are added to equations 3.9 and 3.10 to account for the effect of strain rate. For this reason, RNG models have been found to better simulate low-Reynolds-number and near-wall flows. Constant values of $C_{1\varepsilon}$ and $C_{2\varepsilon}$ are 1.42 and 1.68.

A more recent modification to the standard k – ε model is the realizable method. According to this model, C_μ from equation 3.11 is no longer a constant as in the standard and RNG models, but rather a function of the mean strain and rotation rates, the angular velocity of the system rotation, the turbulence kinetic energy, k, and the turbulence dissipation rate, ε. It also includes a new model equation for the turbulence dissipation rate, based on the dynamic equation of the mean-square vorticity fluctuation. As a result of these modifications, realizable k - ε has been found to perform better for free flows, separated flows and flows with complex secondary flow features. In particular, it has been found that the realizable k-ε model can accurately predict the spread of round axisymmetric jets, contrary to the standard k-ε model, which overpredicts this feature by about 40%, a problem that is known as the round-jet anomaly (Pope, 1978).

Other types of turbulence models tested in this research are the k – ω models. In this approach, two transport equations are solved: an equation for the turbulence kinetic energy, k, and an equation for the specific dissipation rate, ω. The specific dissipation rate is the ratio of turbulence dissipation, ε, to turbulence kinetic energy, k. The standard k – ω model was proposed by Wilcox (1998). However, for the purpose of this research, only a modified version of the standard k – ω model, the shear-stress transport (SST) k – ω model is used. This is due to its better accuracy for wider class of flows since it blends the accuracy of the k – ω model in the near wall region with the advantage of the k - ε in the free stream areas. The transport equations for the k – ω SST model are:

$$\frac{\partial}{\partial t}(\rho k) + \frac{\partial}{\partial x_i}(\rho k u_i) = \frac{\partial}{\partial x_j}\left(\left(\mu + \frac{\mu_t}{\sigma_k}\right)\frac{\partial k}{\partial x_j}\right) + \tilde{G}_k - Y_k \qquad \textbf{(3.8)}$$

$$\frac{\partial}{\partial t}(\rho \omega) + \frac{\partial}{\partial x_i}(\rho \omega u_i) = \frac{\partial}{\partial x_j}\left(\left(\mu + \frac{\mu_t}{\sigma_\omega}\right)\frac{\partial \omega}{\partial x_j}\right) + G_\omega - Y_\omega + D_\omega \qquad \textbf{(3.9)}$$

where $\tilde{G}_k$ is the generation of turbulence kinetic energy due to mean velocity gradients, G_ω is the generation of ω, Y_k and Y_ω are the dissipation of k and ω due to turbulence and D_ω is a cross-diffusion term.

The different turbulence models described here were implemented for different the simulation of scenarios of single and multiple port discharges.

3.1.2 Species transport and equation of state.

The transport of the scalars present in the fluid is modelled using the advection-diffusion equation, defined by

$$\frac{\partial}{\partial t}(\rho Y_i) + \nabla \cdot (\rho u_i Y_i) = -\nabla \cdot \vec{J}_i \qquad \textbf{(3.10)}$$

where Y_i is the local mass fraction of the scalar i and $\vec{u}$ is the velocity and $\vec{J}_i$ is the mass diffusion of the scalar, defined as

$$\vec{J}_i = \left(\rho D_{i,m} + \frac{\mu_t}{Sc_t}\right)\nabla Y_i - D_{T,i}\frac{\nabla T}{T} \qquad \textbf{(3.11)}$$

In this equation, $D_{i,m}$ is the mass diffusion coefficient of the scalar in the mixture, $D_{T,i}$ is the thermal diffusion coefficient, and Sc_t is the dimensionless turbulent Schmidt number. The Schmidt number is a ratio between turbulent viscosity and turbulent diffusivity. To assess the sensitivity of the model to turbulent Schmidt number and determine the most appropriate value for the type of flow in study, various values have been used, ranging from 0.6 to 1.4. The molecular diffusivity of scalars in the flow is negligible (diffusivity coefficients in the order of 10^{-9} m^2/s) when compared to turbulent diffusion values. Hence, the prevailing source of diffusion is turbulence.

The seawater state equation was implemented to account for the effect of salinity and temperature on the density of the water and salt mixture. This equation, also known as UNESCO formulation (UNESCO, 1980), is defined as

$$\rho = 999.84 + 6.79 \cdot 10^{-2}T - 9.10 \cdot 10^{-3}T^2 + 10^{-4}T^3 - 1.12 \cdot 10^{-6}T^4 + 6.54 \cdot 10^{-9}T^5 + (8.25 \cdot 10^{-1} - 4.09 \cdot 10^{-3}T + 7.64 \cdot 10^{-5}T^2 - 8.25 \cdot 10^{-7}T^3 + 5.39 \cdot 10^{-9}T^4)\, s + (-5.72 \cdot 10^{-3} + 1.02 \cdot 10^{-4}T - 1.65 \cdot 10^{-6}T^2)s^{3/2} + 4.83 \cdot 10^{-4}s^2 \quad \textbf{(3.12)}$$

where T is the temperature in °C and s is the salinity in ppt. This equation is only applicable in waters with temperatures in the range of 0 to 40° C and maximum salinity of 43 ppt. The seawater state equation was included in Ansys Fluent 18.1 as a User Defined Function (UDF).

3.2 MESHING METHODOLOGY.

Initial attempts on meshing were based on using structured uniform meshes. However, during this process, it was found that to achieve a mesh independent solution, very large meshes were required, although most of the important processes were taking place in a small portion of the domain.

To tackle this issue, a mesh adaption approach was tested. In order to reduce the computational cost of such testing, this mesh adaption approach was designed modelling two-dimensional pure and buoyant jets. Based on these two-dimensional cases, the computational cost of using structured uniform meshes was compared against that of using a mesh adaption approach. The resulting methodology was then revised for the single and multiple port buoyant jet discharges modelled in the following chapters.

Jets and buoyant jets can be identified by a region of relatively high velocity and scalars. It is easy to predict the trajectory of a pure jet, since the trajectory of the flow depends solely on the initial discharge angle; hence, we can easily create a mesh with the appropriate refinement in the areas where the main processes are taking place. However, the same cannot be said about buoyant jets. Before running the model, the trajectory that the buoyant jet will follow is unknown; hence, an initial mesh is required to conduct a first run of the simulation. Based on the initial results, the mesh can be refined in the areas of highest velocity or scalar concentration. In the following subsection, mesh refinement is evaluated for pure jets and buoyant jets, to identify the most appropriate strategy for mesh adaption.

3.2.1 Two-dimensional pure jets.

Consider the case of a slot water jet ejecting into a stagnant environment of homogeneous density. The slot length (d) is 0.2 m and the jet discharge velocity (u_0) is 0.5 m/s. The receiving water body is a square of 50 m side. Figure 3-1 shows a schematic of the modelling domain. In this domain, the top, bottom and right lateral boundaries were modelled as non-slip wall boundary conditions. The left lateral boundary was simulated as a pressure-outlet and the discharging slot as an inlet. A summary of the boundary conditions is presented in Table 3-1.

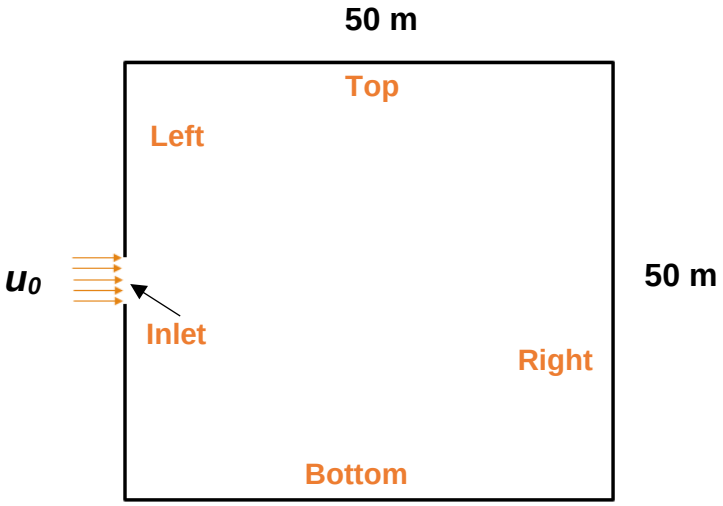

Figure 3-1. Problem specification of two-dimensional pure jet.

Table 3-1. Description of boundary conditions for the two-dimensional pure jet case.

Case	Boundary	Boundary type	Momentum			Thermal	Turbulence	
			x-velocity (m/s)	y-velocity (m/s)	Gauge pressure (Pa)	Temperature (°C)	Turbulent intensity (%)	Hydraulic diameter (m)
Pure jet	Top	No slip wall	0	0	N/A	Zero heat flux	N/A	N/A
	Bottom	No slip wall	0	0	N/A	Zero heat flux	N/A	N/A
	Right	Pressure oulet	N/A	N/A	0	N/A	N/A	N/A
	Left	No slip wall	0	0	N/A	Zero heat flux	N/A	N/A
	Inlet	Velocity inlet	0.5	0	N/A	Zero heat flux	5%	0.2

For the simulation of this scenario, structured meshes were designed so that the size of the elements would grow gradually as we move away from the discharge, in the x and y direction (see Figure 3-2). As a reference for comparison, the scenario was initially tested for a total of six structured meshes (see Table 3-2), and mesh sizes ranged from 1.5 x 10^3 elements to 4.1 x 10^5 elements.

Table 3-2. Size of structured meshes.

Mesh	Total elements
0	1,566
1	6,435
2	25,740
3	102,960
4	219,780
5	411,840

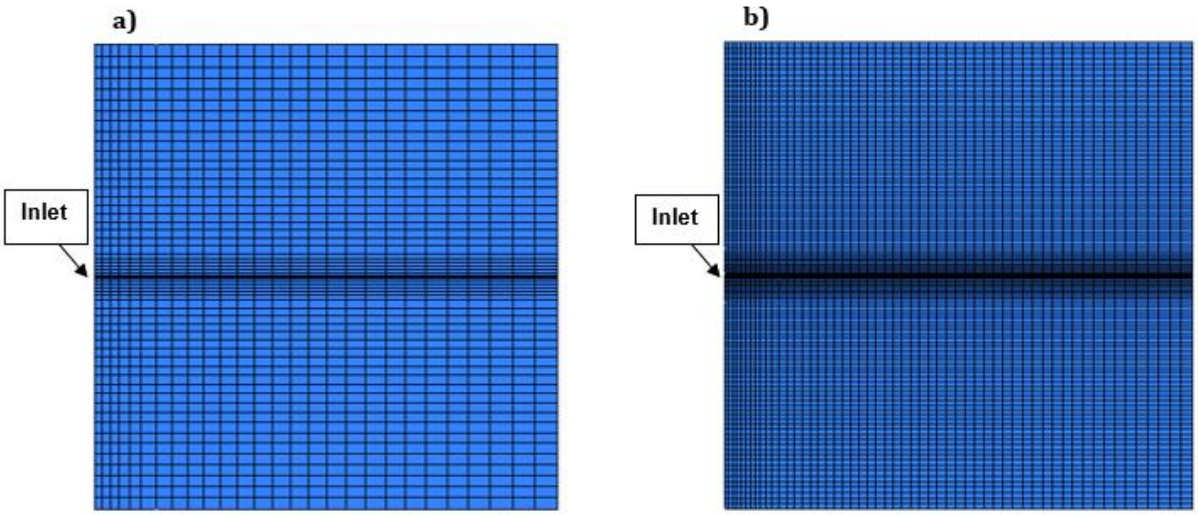

Figure 3-2. Comparison of sizes of initial structured meshes: a) Mesh 0; b) Mesh 1.

Turbulence was modelled using the RANS standard k- ε model. Since buoyancy is not relevant for the case of a pure jet, the energy equation was not solved. This case was modelled assuming a steady-state.

In order to identify whether the solution had reached mesh independence, the local concentrations along the centreline of the jet were plotted for the different meshes tested. Mesh independence was reached at mesh 4, with a total number of elements of 2.2 x 104 elements, as can be observed in Figure 3-3, where mesh 4 and mesh 5 provide the same results for centreline velocity vs. downstream distance.

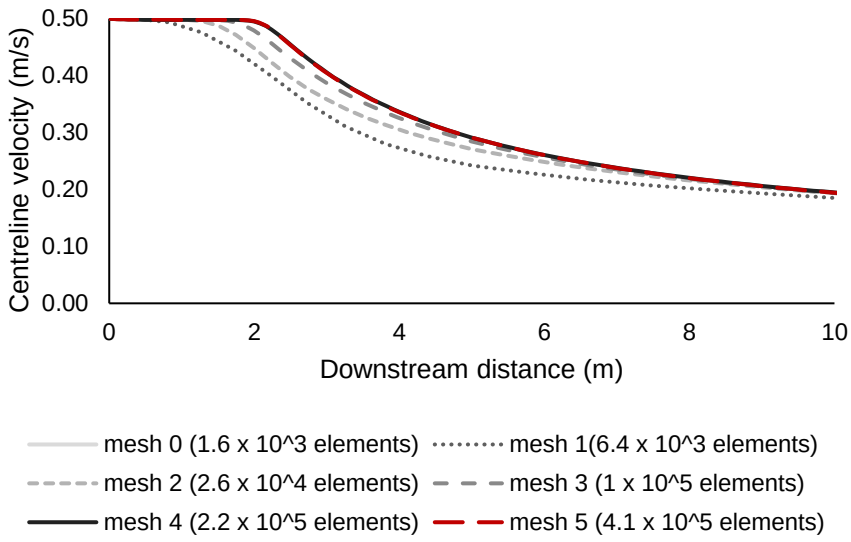

Figure 3-3. Centreline velocity vs. downstream distance results for a pure jet using structured meshes.

Figure 3-4 shows the mesh independent contours of velocity magnitude. The centreline of the jet in this figure divides the jet in two symmetrical parts and it is at this location that local concentrations are compared for the different meshing approaches tested.

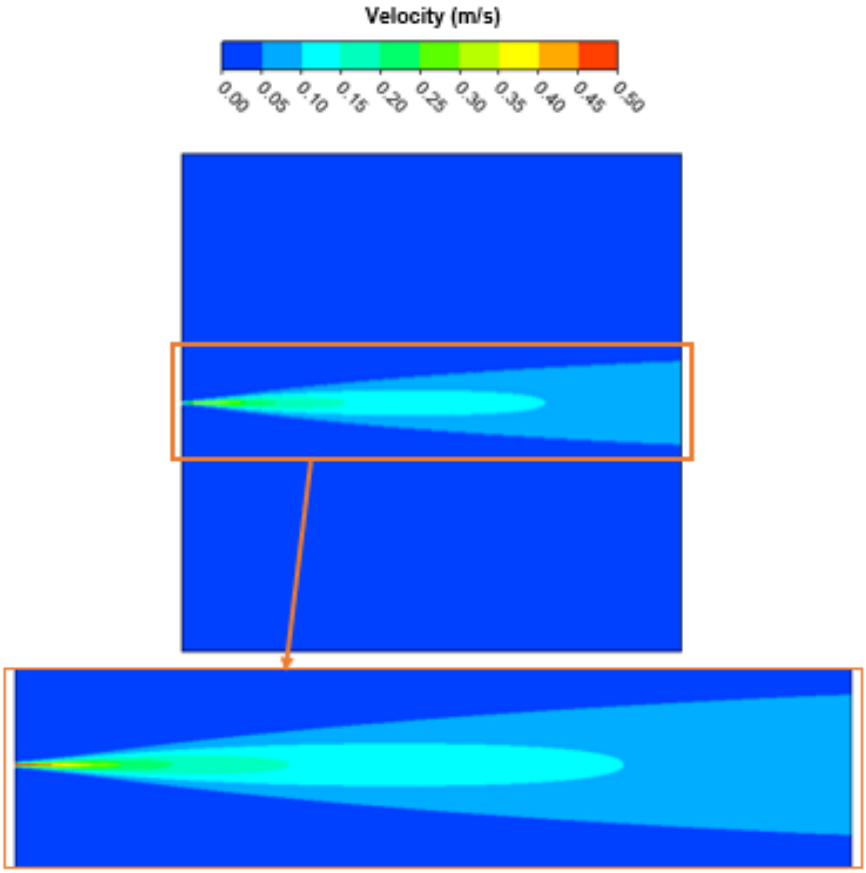

Figure 3-4. Contours of velocity magnitude in the pure jet case.

Once mesh independence was achieved for a structured mesh, mesh adaption was conducted based on the results of the two smallest meshes, mesh 0 and mesh 1, to evaluate the accuracy of using this approach and whether this method reduces the number of cells necessary to achieve mesh independence.

3.2.1.1 Adaption from coarse mesh.

As has been previously stated, smaller cells are required in the areas where velocity is higher in the domain. In this case, isovalue adaption of velocity was conducted from the results of mesh 0, refining those cells where velocity was higher than the 10% of the maximum velocity in the domain (jet discharge velocity). Once refinement was conducted in these areas, an additional adaption was conducted, to ensure that the volume change ratio in adjacent cells was maximum 2. For each adaption, Ansys Fluent 18.2 divides each 2D cell marked for refinement into 4 cells, obtaining 3 times the initial number of cells in the regions adapted.

Two methods for refinement were used: 1) conducting one isovalue and volume change adaption at a time, running the model after each adaption, and conducting additional refinement from the results of the adapted mesh; 2) conducting more than one isovalue adaption at a time, from the initial results obtained from the structured mesh.

Method 1: Adapt, run, adapt.

Table 3-3 shows the number of cells corresponding to each adaption conducted to mesh 0. After each adaption, the model was run, and the subsequent adaption was based on the results of the previous one.

Table 3-3. Number of cells for each mesh adaption using method 1.

Mesh	No. of cells refined	No. of new cells (relative to previous adaption)	Total number of cells
0 – no adaption	---	---	1,566
0 – adaption 1	488	1,464	3,030
0 – adaption 2	1,556	4,674	7,704
0 – adaption 3	5,706	17,118	24,822
0 – adaption 4	19,734	59,202	84,024

Results show that mesh independence is achieved after the third adaption, with a mesh of 2.5 x 10^4 elements (see Figure 3-5 and Figure 3-6**Figure 3-5.** Mesh 0 after third adaption with method 1.). This implies that by using mesh adaption, the size of the mesh required for accuracy is ten times smaller than that of a structured mesh for this case.

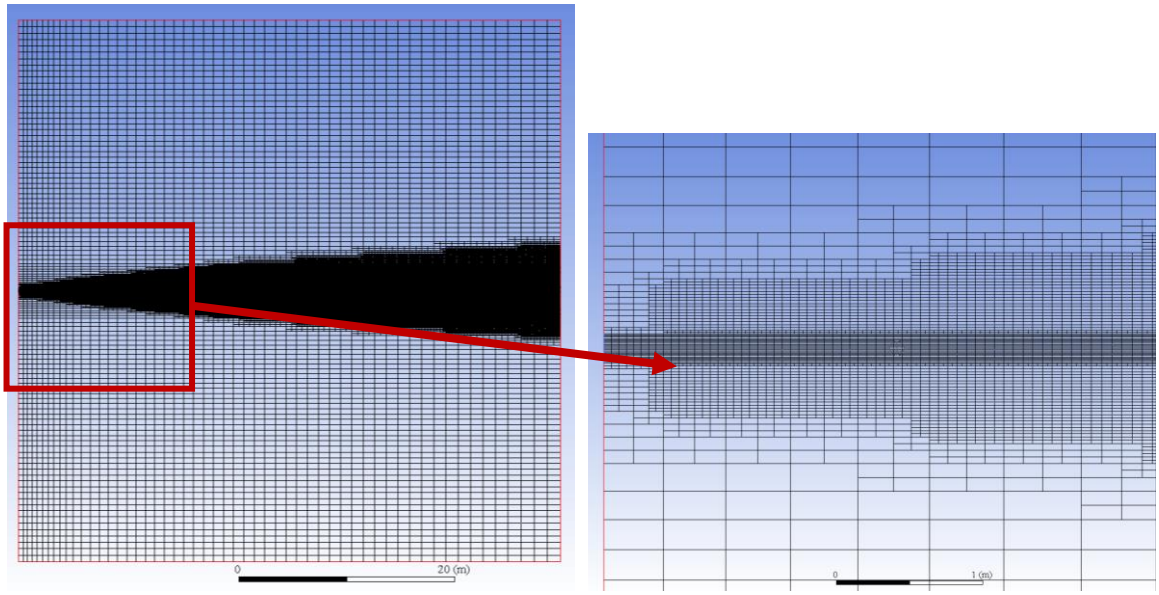

Figure 3-5. Mesh 0 after third adaption with method 1.

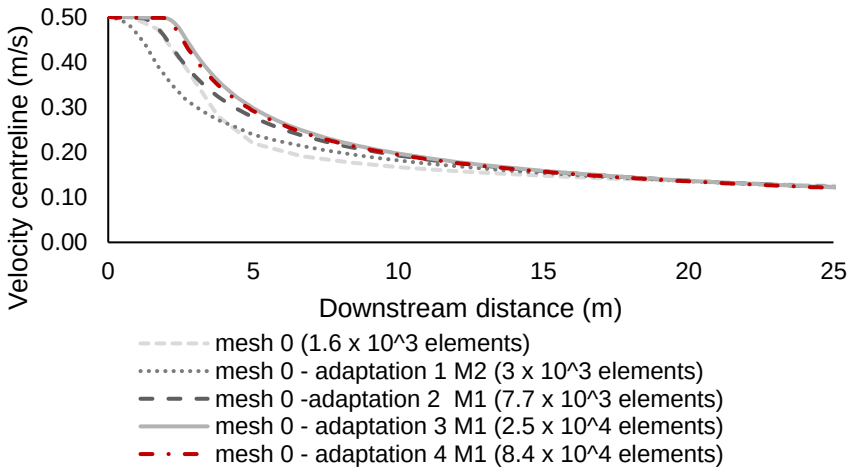

Figure 3-6. Centreline velocity vs. downstream distance results for a pure jet using different mesh adaptions based on method 1.

Method 2: Adapt all, run.

Although method 1 provided favourable results, running the model after each adaption implies additional computational time that is comparable to using a structured mesh. For this reason, a second adaption method was evaluated. With this method, the model was adapted based on the initial results obtained for mesh 0, with no intermediate runs. The number of cells corresponding to each adaption are shown in Table 3-4.

Table 3-4. Number of cells for each mesh adaption using method 2.

Mesh	No. of new cells (relative to mesh 0)	Total number of cells
0 – no adaption	---	1,566
0 – adaption 1	1,464	3,030
0 – adaption 2	6,270	7,836
0 – adaption 3	23,898	25,464

Like for method 1, mesh independence was obtained for the third adaption with a very similar mesh size, although slightly larger (about additional 1,000 elements). This implies that method 2 is the most appropriate for adaption, since it implies a shorter running time compared to method 1 where intermediate runs are necessary. However, more rigour is required for method 2, since the initial mesh should always be good enough to locate the regions of higher velocity accurately; whereby, ensuring that refinement is conducted in the correct areas.

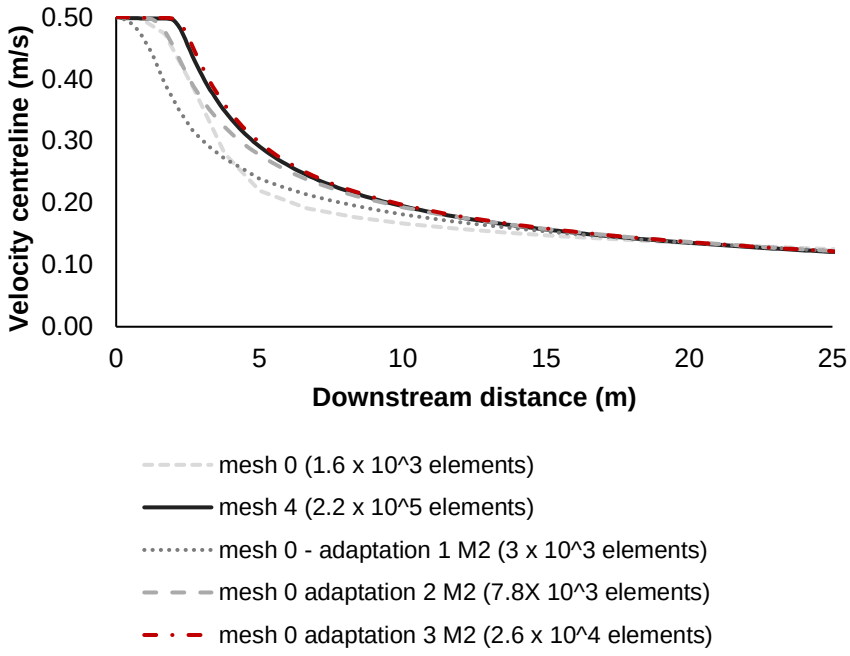

Figure 3-7. Centreline velocity vs. downstream distance for a pure jet using different mesh adaptions based on method 2.

3.2.1.2 Adaption from finer mesh.

Adaption was conducted from mesh 1 using method 2. The purpose of this exercise was to evaluate if using a finer mesh influences the number of adaptions required and the total number of cells necessary to obtain mesh independence. Although results using mesh 0 were favourable, it is important to keep in mind that once buoyancy is added to the jet, a finer mesh will be necessary above the point of discharge, and mesh 0 may be too coarse to accurately resolve it. Table 3-5 shows a summary of the adapted mesh sizes using mesh 1.

Table 3-5. Number of cells for each mesh adaption from mesh 1.

Mesh	No. of cells refined	No. of new cells (relative to mesh 0)	Total number of cells
1 – no adaption	---	---	6,435
1 – adaption 1	1,589	4,767	11,202
1 – adaption 2	7,101	21,639	28,074
1 – adaption 3	28,217	85,839	92,274
1 – adaption 4	110,891	335,565	342,000

Results show that mesh independence is obtained at the third adaption (see Figure 3-8), although the second adaption provides results that are close enough to the mesh independent solution. However, for a pure jet, using mesh 1 does not improve considerably the adaption process, and independence is achieved for a mesh almost four times larger than that necessary when refinement is conducted from mesh 0.

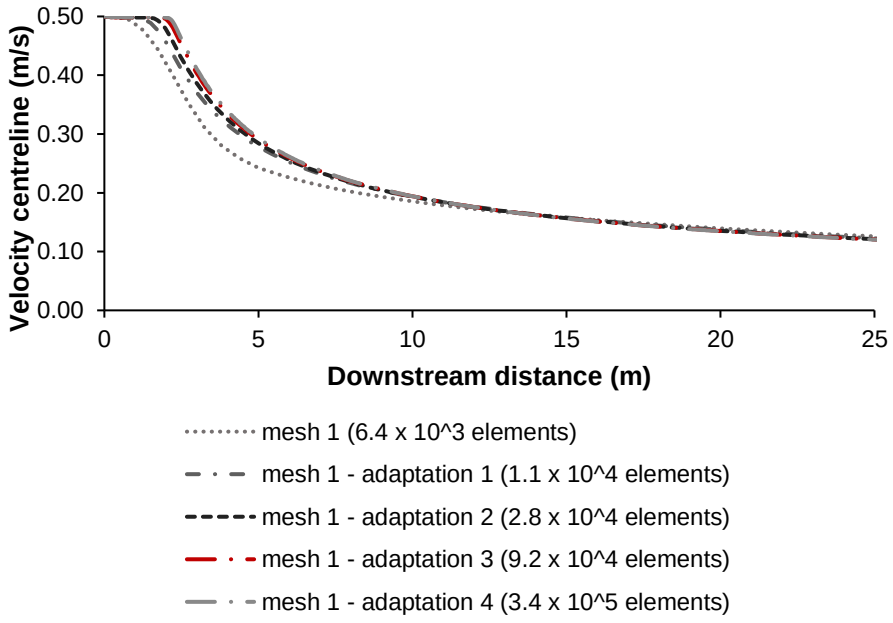

Figure 3-8. Centreline velocity vs. downstream distance for different mesh adaptions from mesh 1.

3.2.2 Two-dimensional buoyant jets.

Once the mesh adaption approach was tested for a pure jet, the same rationale was applied for the case of a buoyant jet. This case consisted of a water jet ejecting through a slot into a stagnant environment of homogeneous density at temperature 20°C. The slot length (d) is 0.2 m and the jet discharge velocity (u) is 0.5 m/s at temperature 25°C. The receiving water body is a square of 50 m side. A schematic of the model domain can be seen in Figure 3-1.

Initially, the buoyant jet was modelled using the structured meshes described in the previous section (except for mesh 0). A summary of the boundary conditions used is presented in ***Table 3-6***. The flow was modelled by solving the RANS equations. Turbulence closure was achieved by using the standard k- ε model. Water density was assumed constant in all solved equations except for the buoyancy term (Boussinesq approximation).

Figure 3-9 shows the contours of velocity and temperature in the domain of the buoyant jet case. Results of velocity and temperature profiles at different locations were compared to evaluate mesh independence. Mesh independence was achieved for mesh 3, corresponding to 102,960 elements (see Figure 3-10 and Figure 3-11).

Mesh adaption was conducted using method 2, which means all refinements were done from the initial results with no intermediate runs, since this methodology was proved to be accurate and less time consuming than method 1.

Table 3-6. Description of boundary conditions for the two-dimensional pure jet case.

Case	Boundary	Boundary type	Momentum			Thermal	Turbulence	
			x-velocity (m/s)	y-velocity (m/s)	Gauge pressure (Pa)	Temperature (°C)	Turbulent intensity (%)	Hydraulic diameter (m)
Buoyant jet	Top	No slip wall	0	0	N/A	Zero heat flux	N/A	N/A
	Bottom	No slip wall	0	0	N/A	Zero heat flux	N/A	N/A
	Right	Pressure oulet	N/A	N/A	0	N/A	N/A	N/A
	Left	No slip wall	0	0	N/A	Zero heat flux	N/A	N/A
	Inlet	Velocity inlet	0.5	0	N/A	25	5%	0.2

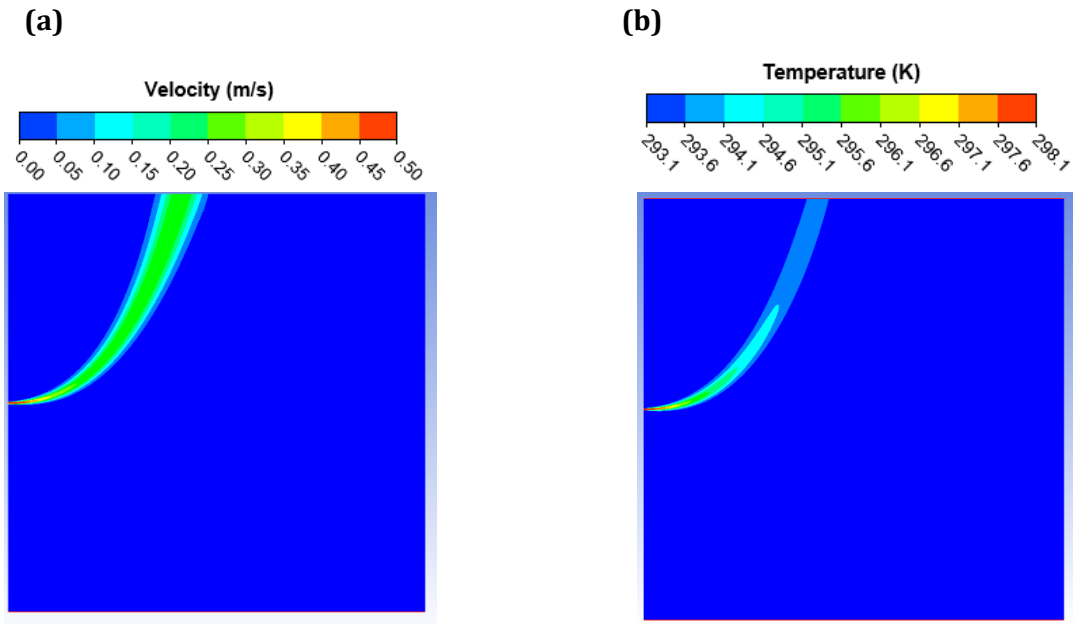

Figure 3-9. Contours of **a)** velocity magnitude and **b)** temperature in the buoyant jet case.

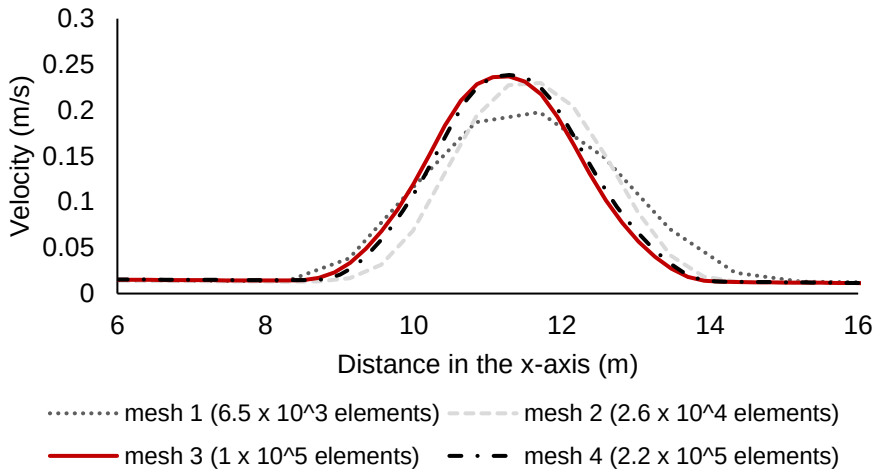

Figure 3-10. Velocity vs. distance in x-axis 5 m above discharge for a buoyant jet using structured meshes.

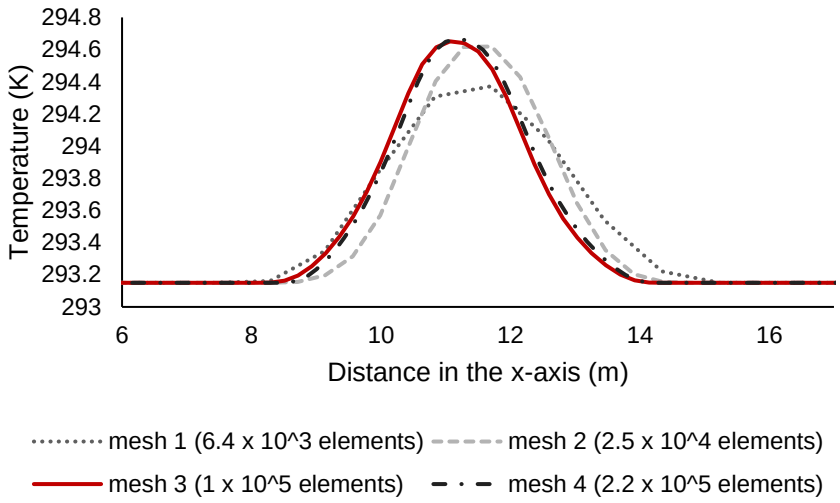

Figure 3-11. Temperature vs. distance in the x-axis 5 m above discharge for a buoyant jet using structured meshes.

Mesh independence was obtained after the second adaption, with the adapted mesh shown in Figure 3-12. As shown in Figure 3-13 and Figure 3-14, results for both velocity and temperature profiles are comparable to those of the structured mesh 3, although the adapted mesh size is more than ten times smaller. Compared to a pure jet, the buoyant jet requires a smaller mesh size, responding to the fact that high velocities are concentrated above discharge in a smaller area.

Table 3-7. Number of cells for each mesh adaption for buoyant jet case.

Mesh	No. of cells marked for refinement	No. of new cells (relative to mesh 1)	Total number of cells
1	---	---	6,435
1 adaption 1	594	1,728	8,163
1 adaption 2	2,223	7,050	13,485
1 adaption 3	8,160	25,911	32,346

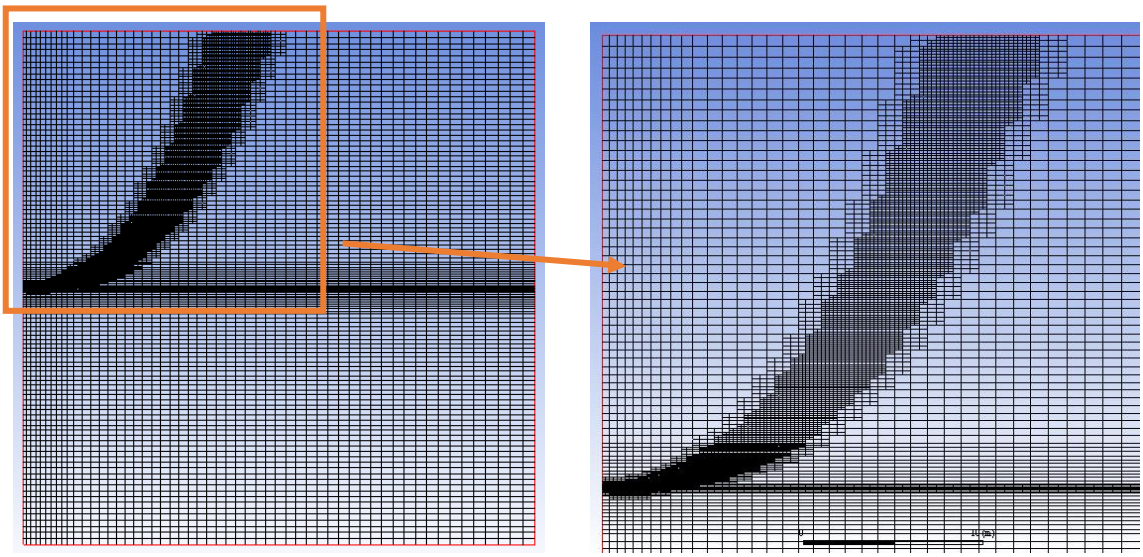

Figure 3-12. Mesh 1 after second adaption for buoyant jet modelling.

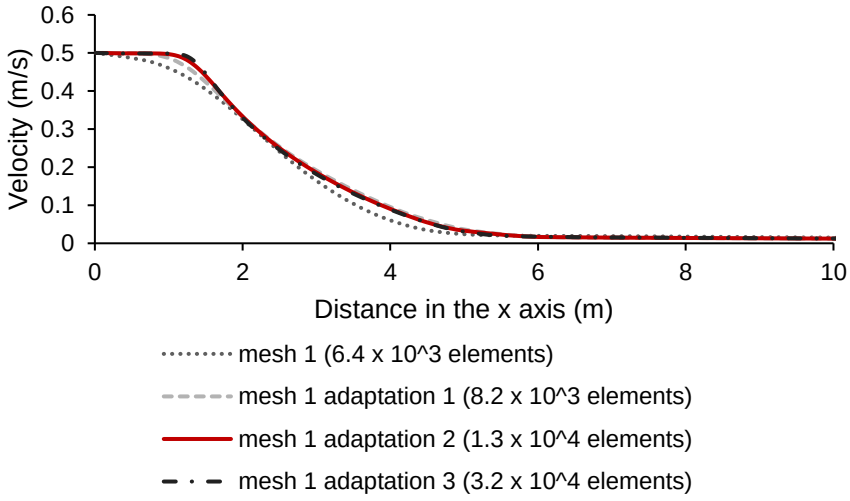

Figure 3-13. Velocity vs. downstream distance for a buoyant jet using different mesh adaptions.

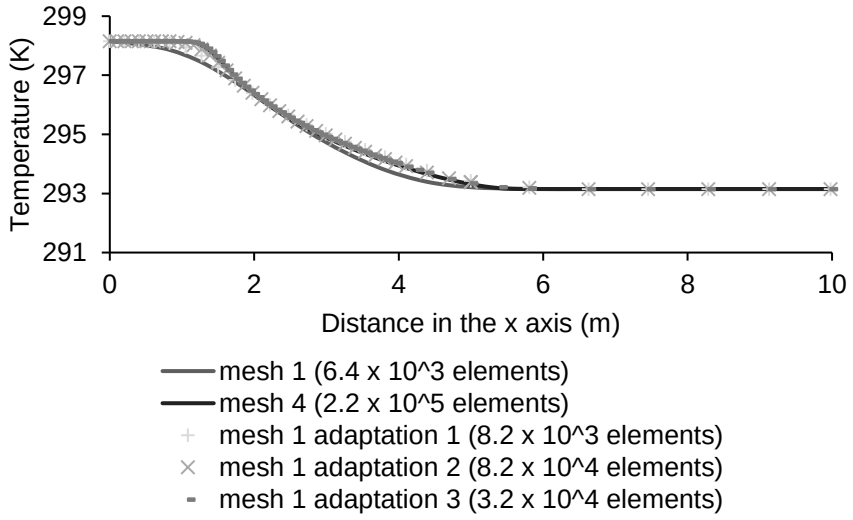

Figure 3-14. Temperature vs. distance in the x axis at the slot centreline for a buoyant jet.

3.3 SUMMARY AND PROPOSED METHODOLOGY FOR THREE-DIMENSIONAL MODELLING OF THE NEAR FIELD.

In this chapter, a summary of the governing equations solved for the simulation of jet and buoyant jet type flows that are conducted in this thesis is presented. This summary includes the description of the RANS equations and the different turbulence models used in this study, namely standard, realizable and RNG k-ε and k- ω SST. The equations governing the transport of scalars and the density of the water as a function of temperature and salinity are presented.

A mesh adaption approach is assessed through the simulation of two-dimensional pure jets and buoyant jets. This method consisted in the simulation of a specific scenario using a relatively coarse structured mesh initially. With the results obtained, further refinement was conducted in

the areas with higher velocity. This approach reduced the size of the required mesh by 10 times. It is then expected that at the three-dimensional level, this meshing approach could reduce the size of the required mesh by 100 times.

Resulting from the varied tests conducted on two-dimensional pure jet and buoyant jets, mesh adaption was identified as a time-efficient method for meshing this type of turbulent flows. However, in these cases, due to the absence of a co-flowing current, it was feasible to conduct such adaption based on the velocity magnitude in the domain, refining those areas with highest velocity. However, if a current is added to the flow, refinement in the zones with high velocity may include areas outside the edge of the buoyant jet, which do not necessarily need finer meshing. For this reason, for the validation cases conducted in this thesis, adaption was conducted based on salinity or scalar concentrations, refining those areas with higher salt concentrations.

4 NEAR FIELD MODELLING OF SINGLE PORT DISCHARGES.

4.1 INTRODUCTION.

Natural variations in ambient conditions make the collection and analysis of varied parameters in the near field of real scale marine outfalls a complex task. For this reason, the validation of a modelling approach is usually conducted with experimental data from studies at laboratory scale, since it allows better control over the ambient and discharge parameters to be analysed.

Early experimental research on the dynamics of buoyant jets was interested on the dynamics of positively buoyant jets. However, for practical reasons in cases modelling water discharges, the ejected fluid was usually denser than the receiving water body, in order to reduce the amount of salt and labour required (Fan & Brooks, 1967). This was also beneficial to monitor dilution. Most of these studies assumed an inverted vertical axis for analysing the results and assumed that that would be the behaviour of a positively buoyant jet with the same initial source of buoyancy. This approach is valid given that density differences are small (Kikkert, et al., 2007).

However, in recent years, due to the growth in the number of desalination plants discharging dense fluid into coastal waters, there has been an increment in the amount of research conducted to study the dynamics of vertical and inclined negatively buoyant jets, where the vertical component of the initial momentum is in the opposite direction of the buoyancy force. Despite the growth in experimental research around negatively buoyant jets, most existing entrainment and empirical models have been formulated based on positively buoyant jets and may overlook significant dynamics that are unique to negatively buoyant jets (Palomar, et al., 2012a; Palomar, et al., 2012b).

In this study, two main type of cases have been selected for validation: single port, consisting of a set of cases of horizontal and inclined negatively buoyant jets, and multiple port discharges. This chapter describes the validation cases conducted for single port discharges.

4.2 REVIEW OF EXPERIMENTAL STUDIES ON INCLINED DENSE JETS.

Early studies on negatively buoyant jets tended to focus on vertical discharges. Vertical discharges fall back directly onto themselves when discharged into stationary environments, resulting in lower dilutions when compared with inclined jets. In inclined jets, the horizontal component of momentum moves the effluent away from the point of discharge (Pincine and List, 1973; Roberts and Toms, 1987). To ensure maximum dilution, most dense wastewater discharges are conducted at inclined angles.

Varied experimental studies have analysed the effect of discharge angle on the trajectory of inclined negatively buoyant jets, particularly on the location of jet maximum rise height and return point. These studies observed that the maximum rise height and return point is a function of Froude number and obtained experimental coefficients of maximum rise height and return point for specific discharge angles, as defined in section 4.3.

The earliest investigation to assess the effect of inclination angle was by Zeitoun et. al. (1970), who concluded that an angle of 60° provided the longest trajectory and hence, higher dilution. For this reason, subsequent investigations performed by Pincine and List (1993), Roberts and Toms (1987) and Roberts et. al. (1997) focused on this discharge angle, measuring trajectory and dilution for cases with different densimetric Froude numbers.

Extensive experimental research has been conducted on inclined dense jets in uniform stagnant environment, focusing on the measurement of the coefficients of maximum rise height and return point for different discharge angles (Ferrari and Querzoli, 2010; Kikkert et. al., 2007; Papakonstantis et. al. 2011a, b; Crowe et. al., 2016). However, less attention has been given to the effect of co-flowing and cross-flowing currents on the trajectory and dilution of inclined dense jets.

Pincine and List (1973) presented the earliest study on the effect of currents flowing in the direction of a negatively buoyant jet with a source inclination angle of 60° and varied jet velocity to ambient velocity ratios, finding that dilution in the proximity of the discharge was relatively unaffected by the presence of a current. However, such dilution increased further downstream in comparison with equivalent dense jets in stagnant environment. This was later confirmed by Roberts and Toms (1987), who performed an investigation on negatively buoyant jets inclined at a source angle of 60°, with varying angles of ambient current to jet. They also found that inclined jets discharging in the opposite direction of the current provide lower dilution than their equivalent jet in stagnant environment.

The effect of density stratification on inclined dense jets have been scarcely studied. Bloomfield and Kerr (2002) performed an investigation on the sensitivity of inclined dense jets to changes in buoyancy frequency, initial momentum and Froude number. For this analysis, they conducted experiments on dense jets with discharge angles between 70° to 90°. However, this study did not evaluate the effect of stratification on final dilution but focused merely on the location of the maximum rise height of the plumes. Further investigation is required on the impact of density stratification on dilution along the inclined jet trajectory.

Table 4-1 presents a summary of the experimental studies that have been conducted on inclined dense jets, their measuring methods and range of source angles and Froude number evaluated. Results from these experimental cases are used in this chapter for comparison with modelling results.

Table 4-1. Summary of experimental studies on inclined dense jets.

	Experimental method	Source angles	Froude number	Ambient conditions	Parameters measured
Pincine and List (1973)	Direct conductivity measurements	60°	50–51.5	Uniform cross-flowing environment	Trajectory and dilution.
Roberts and Toms (1987)	Dye-attenuation technique	60°, 90°	12.2–26	Uniform environment Stagnant and cross-flowing environment	Location of centreline maximum rise height and dilution at maximum rise height and return point
Roberts et. al. (1997)	Laser induced fluorescence (LIF)	60°	20.5–35.7	Uniform stagnant environment	Location of upper boundary maximum rise height and return point, dilution at return point, ultimate dilution, end of mixing zone
Bloomfield and Kerr (2002)	Shadowgraph	30°–90°	Not stated	Uniform and stratified stagnant environment	Location of initial and final maximum rise height.
Ferrari and Querzoli (2004)	Laser induced fluorescence (LIF)	45°–90° (5° step)	8-30.8	Uniform stagnant environment	Trajectory, location of centreline maximum rise height and return point
Kikkert et. al. (2007)	Light attenuation (LA) and Laser induced fluorescence (LIF).	15°, 30°, 45°, 60°, 75°	27–89	Uniform stagnant environment	Location of centreline maximum rise height and return point, plume radius, velocity and dilution at maximum rise height and return point.
Shao and Law (2010)	Combined Particle Image Velocimetry (PIV) and Planar Laser Induced Fluorescence (PLIF)	30°, 45°	7.4-32.2	Uniform stagnant environment	Location of centreline maximum rise height and return point, velocity and concentration profiles
Papakonstantis et. al. (2011a, b)	Dye-attenuation technique	45°, 60°, 75°, 80°, 85°, 90°	7.5–59.2	Uniform stagnant environment	Location of upper boundary maximum rise height and return point, vertical concentration distributions, centreline dilution at maximum rise height and return point.
Lai & Lee (2012)	Planar laser-induced fluorescence (LIF) and Particle Image Velocimetry (PIV)	15°, 30°, 38°, 45°, 52°, 60°	10-40	Uniform stagnant environment	Location of centreline maximum rise height and return point, dilution at maximum rise height and return point
Oliver et. al. (2013)	Laser induced fluorescence (LIF)	15°, 30°, 45°, 60°, 70°,	14.9-106.4	Uniform stagnant environment	Location of centreline maximum rise height and return point, concentration profiles, velocity and dilution at maximum rise height and return point.
Crowe et. al. (2016)	Particle tracking velocimetry	15°, 30°, 45°, 60°, 65°, 70°, 75°	10.1–80.4	Uniform stagnant environment	Location of centreline maximum rise height and return point, plume radius, centreline velocity at maximum rise height and return point.

4.3 SUMMARY OF THE THEORY ON INCLINED NEGATIVELY BUOYANT JETS.

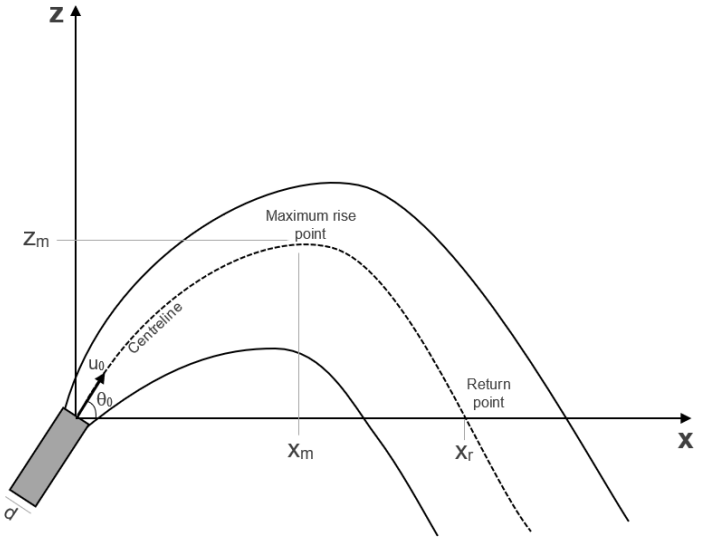

Figure 4-1. Schematic side view of a typical inclined dense jet.

As indicated in Figure 4-1, when water ejects from an inclined dense jet into a stagnant environment, the flow rises through the water column until it reaches a maximum rise height, after which it descends, reaching again the elevation of the source at a location termed the return point. The centreline of the flow is the location of the maximum velocity at a given cross-section. The centreline maximum rise height, located at an axial position, x_m, and a vertical position, z_m, and the centreline return point, x_r, have been found to be proportional to the Froude number and a function of the discharge angle (Crowe, et al., 2016; Kikkert, et al., 2007; Ferrari & Querzoli, 2010; Lai & Lee, 2012), as follows:

$$\frac{x_m}{F_0 d} = k_{xm}(\theta) \quad \textbf{(4.1)}$$

$$\frac{z_m}{F_0 d} = k_{zm}(\theta) \quad \textbf{(4.2)}$$

$$\frac{x_r}{F_0 d} = k_{xr}(\theta) \quad \textbf{(4.3)}$$

were k_{xm}, k_{zm} and k_{xr}, are the experimental coefficients for the position of the maximum height and return point.

Similarly, Crowe et. al. (2016) found that the centreline velocity at the maximum rise height, u_m, and at the return point, u_r, were also a function of Froude number for a given angle:

$$\frac{u_0}{F_0} = k_{um}(\theta) \quad \textbf{(4.4)}$$

$$u_m$$

$$\frac{u_0}{F_0 u_r} = k_{ur}(\theta) \quad \textbf{(4.5)}$$

where k_{um} and k_{ur} are experimental coefficients for the velocity at the maximum rise height and return point, respectively. These expressions are used in this study to compare available experimental data against modelling predictions.

4.4 DESCRIPTION OF VALIDATION CASES.

Modelling test cases defined for single port discharges were based on experimental setups from Crowe (2016), who performed experiments on angled dense jets. A summary of the cases is shown in Table 4-2.

The model domain used to simulate angled dense discharges was 2.3 m x 1.24 m x 1.78 m and the inlet jet had a diameter of 0.25 cm. Due to a salinity difference of 40 ppt, the incoming jets were 3% denser than the receiving ambient. Source angles ranged between 15° to 60°. Temperature was assumed constant at 22°C.

Table 4-2. Summary of discharge and ambient conditions of the dense jet test cases.

	Angle	**Inlet velocity**	**Diameter**	**Ambient density**	**Inlet density**	**Froude number**	**Inlet temperature**	**Reynolds number**
Symbol	θ	u_0	D	ρ_a	ρ_0	F	T_0	R
Units	°	m/s	mm	kg/m³	kg/m³	-	° C	-
	15	1.08– 6.82	2.5	997	1026.9	40 – 250	22	2,695 - 20,000
	30	1.08 – 6.72				40 – 250	22	2,695 - 20,000
	45	1.08 – 2.17				40 – 80	10, 22, 30	2,695 – 5,390
	60	1.08 – 2.17				40 – 80	22	2,695 – 5,390

4.5 MODELLING METHODOLOGY.

The CFD simulations on single port jets were based on the solution of the unsteady Reynolds-Averaged Navier-Stokes equations (uRANS). The sensitivity to the used turbulent closure models was evaluated. The turbulence models implemented are namely standard, realisable and RNG $k-\epsilon$ and $k-\omega$ SST. These CFD simulations were implemented in the finite volume-based commercial code ANSYS Fluent 18.2 (Ansys Inc., 2018). The governing equations solved are described in detail in section 3.2. Transient simulations were conducted in all cases implementing the SIMPLE scheme for the pressure-velocity coupling. Second-order spatial discretisation schemes were used for the continuity, momentum, turbulent kinetic energy, turbulent diffusivity and advection-diffusion equation.

For each case, the simulation period was in the range of 60-80 seconds, time in which a steady state had been reached in the area covering the trajectory of the plumes. Once this steady state flow field had been reached, a similar mesh adaption approach to that described in section 3.3 was conducted.

Fixed time stepping was used. The time step interval was adjusted for each case, ensuring that the Courant number was always less than 1.0 in the domain. Courant number is defined by the equation:

$$C = \frac{u\Delta t}{\Delta x} \leq 1 \tag{4.6}$$

4.5.1 Boundary conditions.

The top boundary was defined as a slip wall with zero gradient conditions, in order to simulate the free surface. The inlet was located at the centre of one of the lateral boundaries, with a uniform discharge velocity which depended on the case in study. Turbulence intensity, I, at the inlet was calculated based on the following equation

$$I = 0.16(Re)^{-1/8} \tag{4.7}$$

where Re is the Reynolds number of the flow. Equation 3.17 is the formula advised by the CFD software Ansys Fluent 18.2 for the estimation of the turbulence intensity at the core of a fully-develop duct flow, derived from an empirical correlation for pipe flows (Ansys Inc., 2018).

The bottom and three of the lateral boundaries were set as no-slip walls with zero gradient conditions. The boundary at the opposite face of the discharge was set as a pressure outlet. Although this is not the case in the experimental scenario since the flow is taking place in a tank, including a pressure outlet boundary in the domain ensures that the displaced volume can leave the domain. ***Table 4-3*** shows a summary of the boundary conditions for one the inclined dense jet cases. Other cases have similar boundary conditions and variations are only made to the velocity components for the inlet boundary.

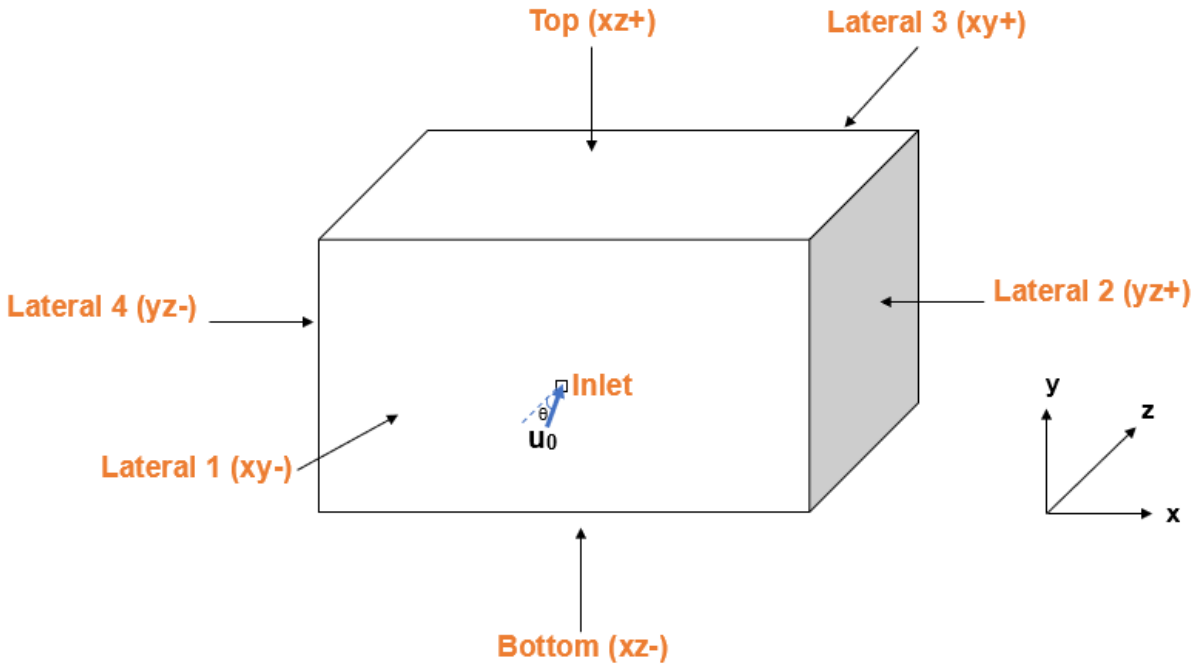

Figure 4-2. Schematic of the domain used for inclined dense cases with boundary names.

Table 4-3. Description of boundary conditions for one of the inclined dense jet cases.

Case	Boundary	Boundary type	Momentum				Thermal	Species	Turbulence	
			x-velocity (m/s)	y-velocity (m/s)	z-velocity (m/s)	Gauge pressure (Pa)	Temperature (°C)	Salinity concentration (ppt)	Turbulent intensity (%)	Hydraulic diameter (m)
1	Top (xz+)	Slip wall	N/A	N/A	N/A	N/A	Zero heatflux	Zero-gradient	N/A	N/A
	Bottom (xz-)	Non-slip wall	N/A	N/A	N/A	N/A	Zero heat flux	Zero-gradient	N/A	N/A
	Lateral 1 (xy-)	Non-slip wall	N/A	N/A	N/A	N/A	Zero heat flux	Zero-gradient	N/A	N/A
	Lateral 2 (yz+)	Non-slip wall	N/A	N/A	N/A	N/A	Zero heat flux	Zero-gradient	N/A	N/A
	Lateral 3 (xy+)	Pressure oulet	N/A	N/A	N/A	0	N/A	N/A	N/A	N/A
	Lateral 4 (yz-)	Non-slip wall	N/A	N/A	N/A	N/A	Zero heat flux	Zero-gradient	N/A	N/A
	Inlet	Velocity inlet	0	1.04	0.28	N/A	22	40	6	0.0025

4.5.2 Meshing approach.

For the validation cases presented in this chapter, a similar adaption approach to that described in section 3.3. was used. Adaption was conducted based on salinity concentrations, refining those areas with higher salt concentrations.

A mesh independence study was conducted, testing different initial mesh sizes between 0.7 to 3 x 10^6 elements, using a similar approach to that described in section 3.3. The most cost-efficient mesh that provided mesh independent results pair with the adaption method used was selected. The selected initial mesh had a size of 2.3 x 10^6 elements (see Figure 4-4). This initial mesh was uniform and structured, with rectangular hexahedral elements. The size of the elements grew gradually as we moved away from the point of discharge. The discharge pipe was modelled as an equivalent square, since the size of this port is sufficiently small for its shape to be irrelevant. This assumption was previously tested for a pure jet, modelled both as a circular pipe and an equivalent square pipe, finding no significant difference in the obtained results.

From the initial results obtained with the structured uniform mesh, mesh adaption was conducted in a series of stages. The first refinement was done to the cells in which salinity concentrations were higher than 2% of the initial salinity, corresponding to areas with salinity concentrations higher than 0.8 ppt. A second refinement was then conducted to those cells in which the concentration of salinity was higher than 3.2 ppt. The third layer of refinement was conducted on cells with salinity concentration higher than 9.6 ppt. The following layer of refinement, corresponded to the cells in which salinity was 14.4 ppt. Finally, in the areas closer to the initial zone of flow establishment (ZOFE), corresponding to locations in which salinity was higher than 19.2 ppt, a final adaption was conducted. No intermediate simulation was conducted between each refinement. This approach increased the size of the mesh between 2 to 3 times of its original number of cells. An example of a refined mesh for one of the inclined dense jets in study is shown in Figure 4-4.

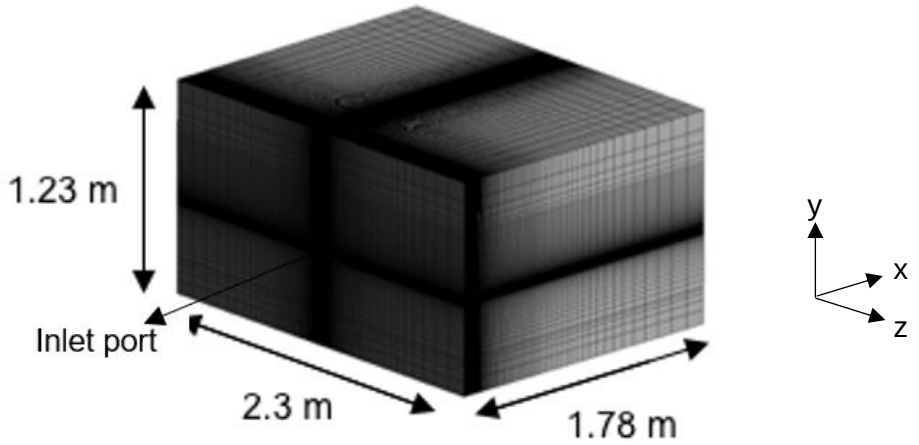

Figure 4-3. Initial structured mesh used for single port dense discharges.

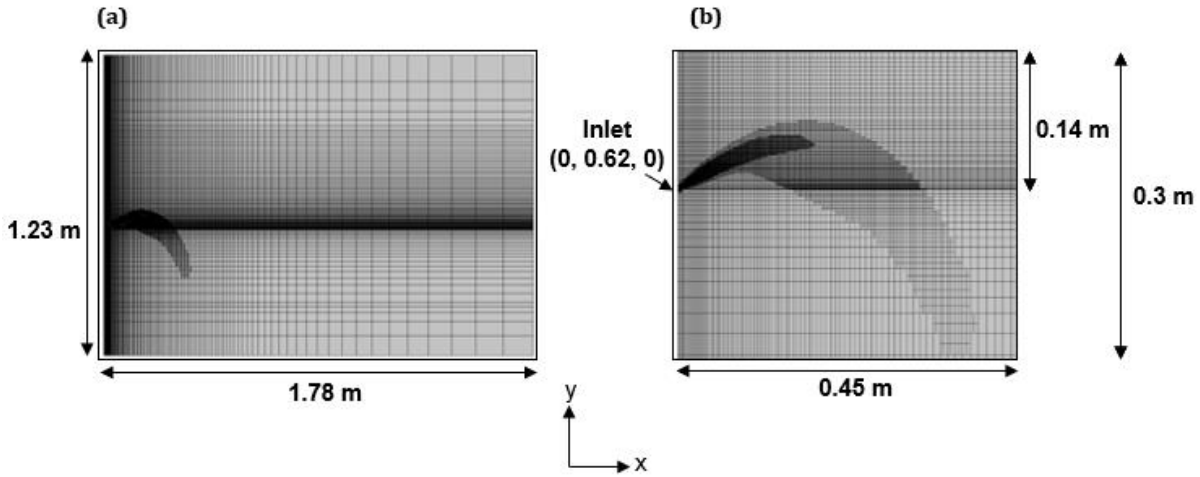

Figure 4-4. Adapted mesh for an inclined jet with source angle 30° and F_0= 40 at a central symmetry plane: **(a)** view of the central plane; **(b)** magnified view of the adapted mesh along the jet trajectory.

4.6 RESULTS AND DISCUSSION.

The prediction of geometric parameters, velocity and dilution from inclined dense discharges from desalination plants, liquefied natural gas plants, among other industries, is important for the design and monitoring of such discharges. In the following subsections, the accuracy of CFD models to predict the flow characteristics of dense jets inclined at different angles is discussed based on the solution of the validation cases described in section 3. Results are compared with available experimental data and entrainment models VISJET, CORJET and UM3.

4.6.1 Trajectory and general flow characteristics.

The contour and trajectory plots presented in this section (from Figure 4-5 to Figure 4-7, are not shown for the complete model domain but rather a magnified view of the upper half of the domain, where both the maximum rise height and return point are located. This means that such graphs depict the upper half of the plane above the inlet, which is located at coordinates (0, 0.62, 0), as shown in the magnified view of the central plane shown in Figure 4-4(b).

Mean velocity and salinity contours for inclined dense jets discharging at 15°, 30° and 45° are shown in Figure 4-6. The centreline of the discharge, defined as the location of local maximum velocity along the dense jet trajectory is shown in Figure 4-6. In this graph, typical features of inclined negatively buoyant jets are identified, including the asymmetry of the flow in respect to the centreline. This asymmetry responds to the detrainment of the flow in the inner side of the jet due to gravity, resulting in an unstable density gradient in this internal area. Entrainment models such as VISJET, CORJET and UM3 assume self-similar Gaussian distributions for velocity and scalar profiles; hence, they are not able to predict the detrainment that takes place in the inner side of the flow, an important characteristic of inclined dense discharges. This feature of the flow is further analysed in section 4.6.2.

In inclined dense jets, the flow is initially driven by the momentum of the discharge, following the trajectory imposed by the initial discharge angle. As it moves, the initial momentum decays until it becomes zero in a position called maximum rise height. Once it reaches the maximum rise

height, it starts to deflect towards the bottom of the tank due to the effect of buoyancy. Previous experimental studies have found that the trajectory of an inclined dense jet is proportional to Froude number for a given discharge angle (Crowe, et al., 2016; Papanikonstantis, et al., 2011a). This characteristic of the flow is illustrated in Figure 4-5, which compares the nondimensionalised trajectory of the flow at a discharge angle of 15° for different discharge velocities (i.e. Froude numbers).

In terms of trajectory, the results have some sensitivity to the turbulence model used, as can be seen in Figure 4-7a. The k-ε RNG and k-ω SST models provide the shortest trajectories for an angle of 45°. Closest estimations are provided by the realisable k-ε model. These coincides with previous studies that have observed that amongst the models in the k-ε family, the realisable k-ε is the only one capable of accurately predicting the spread of a round axisymmetric jet. The standard k-ε model has been found to overpredict this feature by 40% (Pope, 1978).

The trajectory predicted by the standard k-ε model is similar to that predicted by Zhang et. al. (2017). The small differences between the trajectories predicted may be a result from small differences in inlet boundary conditions. Furthermore, in Zhang et. al. (2017) the return point was located at the same height as the bottom boundary; hence, such boundary could be influencing the horizontal location of the return point and the overall trajectory of the jet, as has been identified by other studies (Shao & Law, 2010).

Results of the RNG k-ε and k- ω SST models were found to be very similar, coinciding with findings from Valero and Bung (2016), who compared the accuracy of these two models for the simulation of jets in cross-flow. Similarities between the RNG k-ε and k- ω SST model is likely to be a result of the latter behaving as a k-ε model in free-stream conditions.

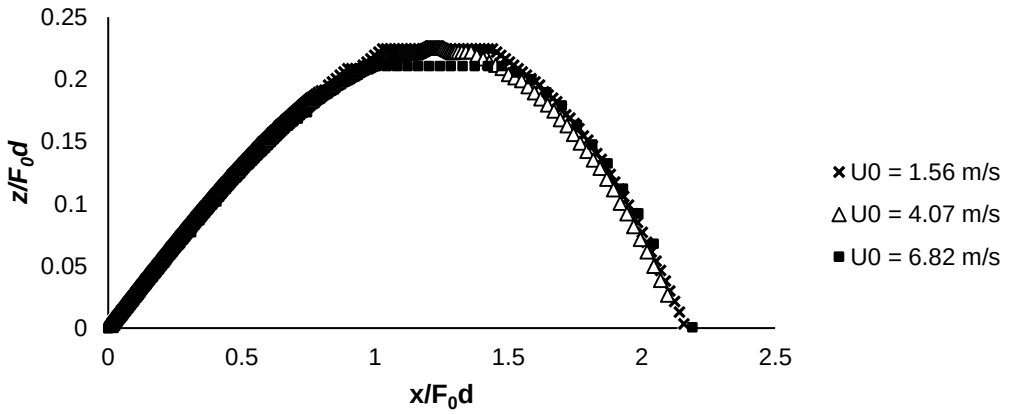

Figure 4-5. Nondimensionalised trajectory of jet centreline for all cases with discharge angle of 15°.

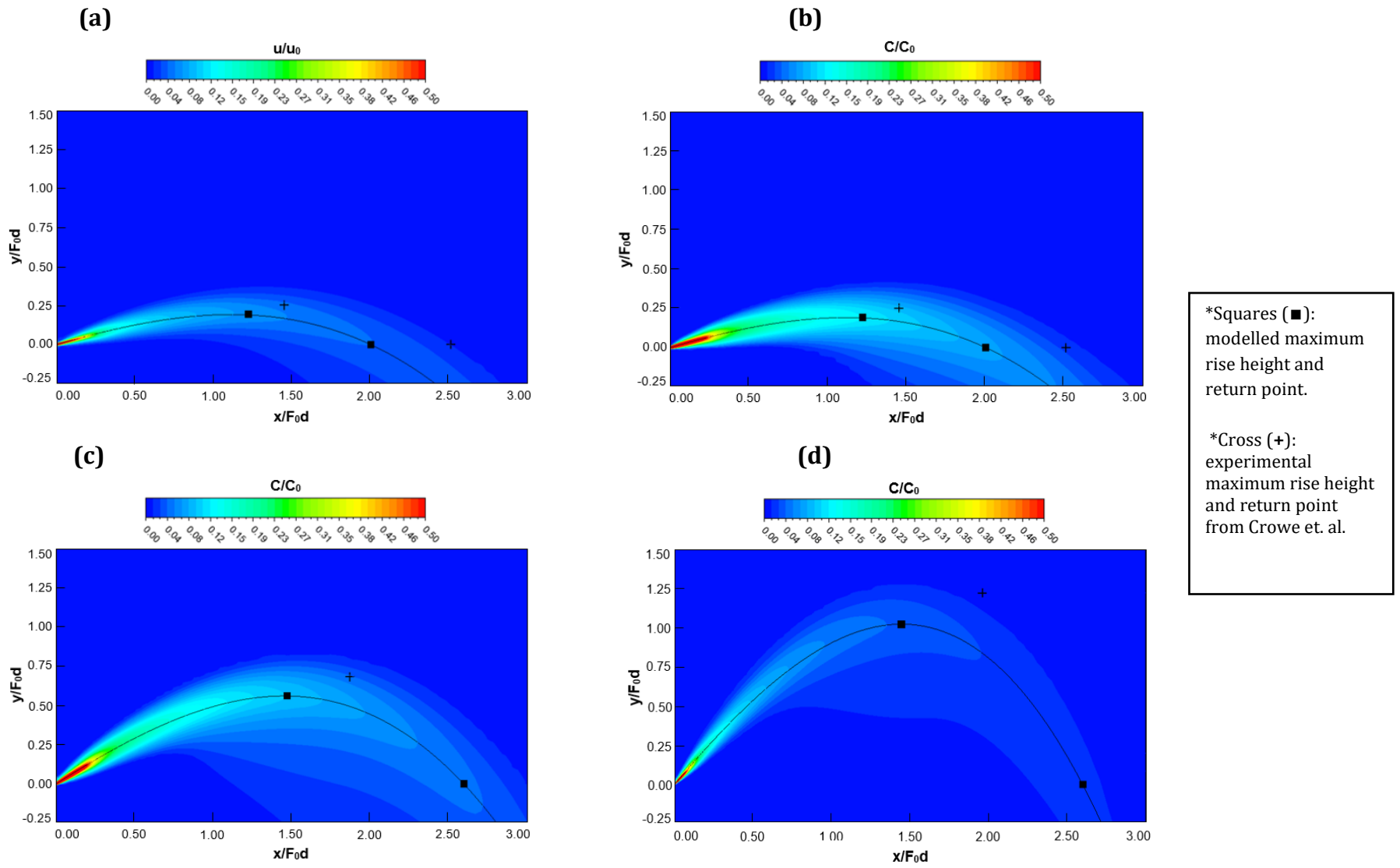

Figure 4-6. Contours of inclined dense jet with $F_0 = 40$: (**a)** velocity magnitude for case with discharge angle 15°; (**b)** salinity for case with discharge angle 15°; **(c)** salinity for case with discharge angle of 30°; and **(d)** salinity for case with discharge angle of 45°. These graphs do not show the complete model domain.

The modelled trajectory was also sensitive to turbulent Schmidt number (see Figure 4-7b). Amongst the values used, a turbulent Schmidt number of 1.4 seems to predict a trajectory closest to the experimental data. These results coincide with observations from Valero and Bung (2016), who found that a Schmidt number value of 1.4 provided the closest predictions for jet trajectory, when compared to results with other turbulent Schmidt numbers in the range from 0.7 to 1.3. However, comparisons from Valero and Bung (2016) were only limited to trajectory and spread; and velocity and scalar concentrations along the jet trajectory are not compared with experimental data. In this study, observations show that although a higher turbulent Schmidt number provides better results in terms of trajectory, increasing the turbulent Schmidt number leads to the under-prediction of dilution in the maximum rise height and return point. For this reason, a value in the range of 0.6 to 0.9 may be the most suitable for this type of flow. A value of 0.7 was selected as the preferred turbulent Schmidt number in this study, agreeing with recommendations by Yimer et. al. (2002), who conducted experiments in round turbulent jets.

In general terms, it is observed that RANS models are capable of predicting the behaviour of inclined dense jets. However, as other studies have observed, these models underpredict the horizontal trajectory of the dense jets (Choudhury, 1993; Shao & Law, 2010).

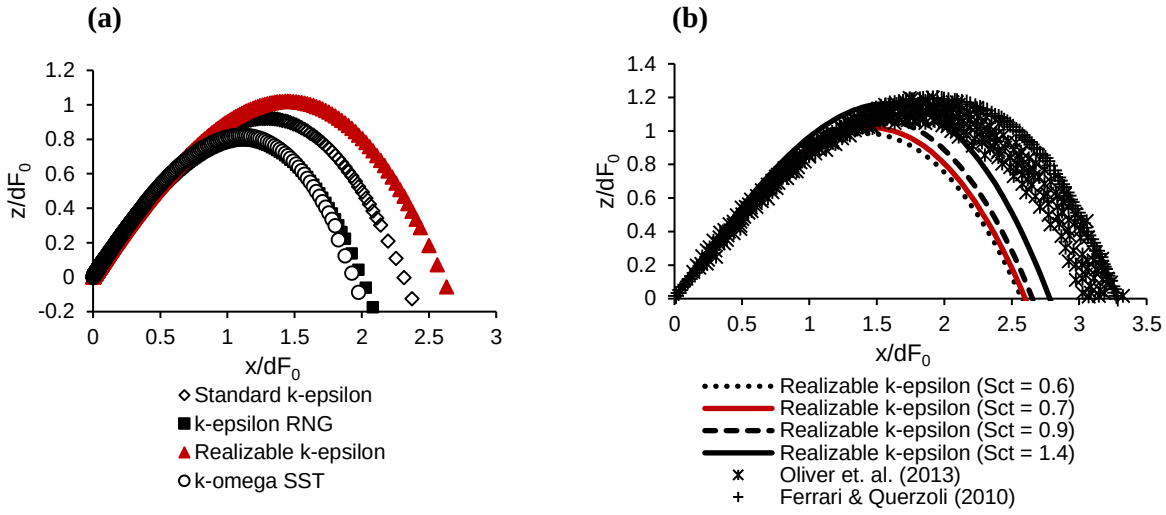

Figure 4-7. Comparison of plume trajectories for a discharge angle of 45°: **a)** different turbulence models; **b)** different turbulent Schmidt numbers for the realisable k-ε model compared to experimental data.

4.6.2 Cross-sectional profiles.

Mean salinity concentration profiles along the cross-section at maximum rise height for discharge angles of 15° and 30° are shown in Figure 4-8. The local concentration, C, is normalised by centreline concentration, C_c. The profiles display an asymmetric shape at the maximum rise height. This asymmetry is more prominent for higher discharge angles, as higher detrainment occurs in the inner side of the jet.

A Gaussian distribution was fitted to the mean concentration data as described in equation 4.8, where r is the radial distance along the cross-section and b_c is the jet width, corresponding to the location in which the local concentration C equals $e^{-1}C_c \approx 0.37C_c$.

$$\frac{C}{C_c} = \exp\left(-\frac{r^2}{{b_c}^2}\right) \qquad \textbf{(4.8)}$$

Due to the asymmetry of the jets, the jet width, b_c, is different depending on the side of the jet selected. In the present study, the value of the width selected is based on the concentration profile in the outer side of the jet.

The profiles obtained with the realisable k-ε model for discharge angles of 15°, 30° and 45° are compared with the profiles assumed by entrainment models CORJET, VISJET and UM3, which assume Gaussian and top hat distributions. The outer edge of the inclined dense jet fits the Gaussian distribution; however, in the inner side, the profile is much flatter. This deviation results from instabilities of the density gradients in the inner side of the flow, which leads to detrainment of flow from the jet. These internal instabilities are more prominent for higher discharge angles. The asymmetric nature of the concentration profiles around and beyond the maximum rise height has been observed by a number of studies (Kikkert, et al., 2007; Oliver, et al., 2008; Palomar, et al., 2012; Crowe, et al., 2016).

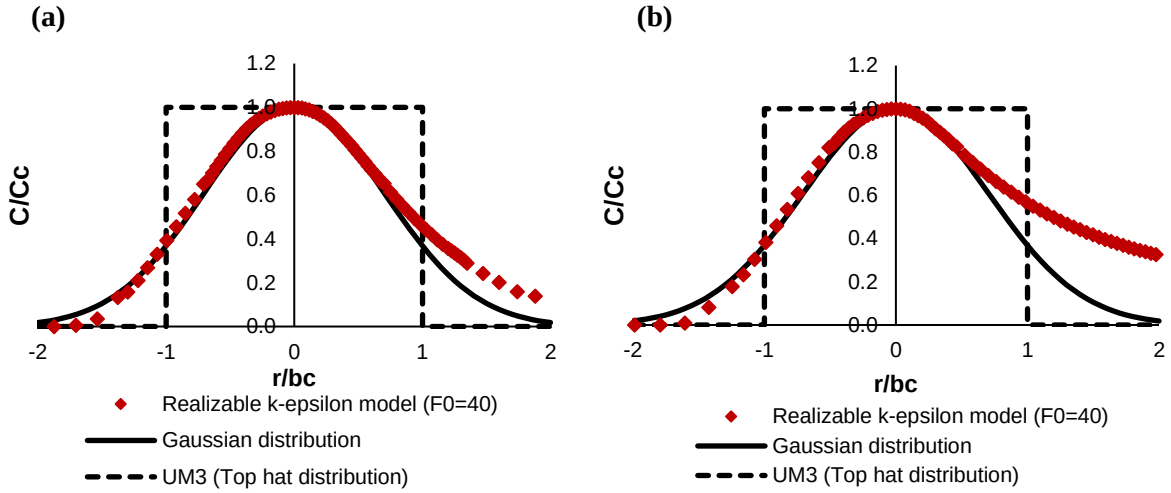

Figure 4-8. Cross-sectional nondimensionalised profiles of salinity for source angles of **(a)** 15° and **(b)** 30° with a F_0 = 40.

Results of the cross-sectional nondimensionalised profiles of concentration in the maximum rise height are compared to those obtained experimentally for a discharge angle of 45° (see Figure 4-9). The predicted profiles are a close estimation to the experimentally measured ones; however, higher detrainment is observed in the latter. Nonetheless, the realisable k-ε model provides the most accurate estimation when compared to entrainment models, which assume symmetric velocity and scalar concentration profiles and are hence not capable of depicting the detrainment that takes place in the inner side of the jets.

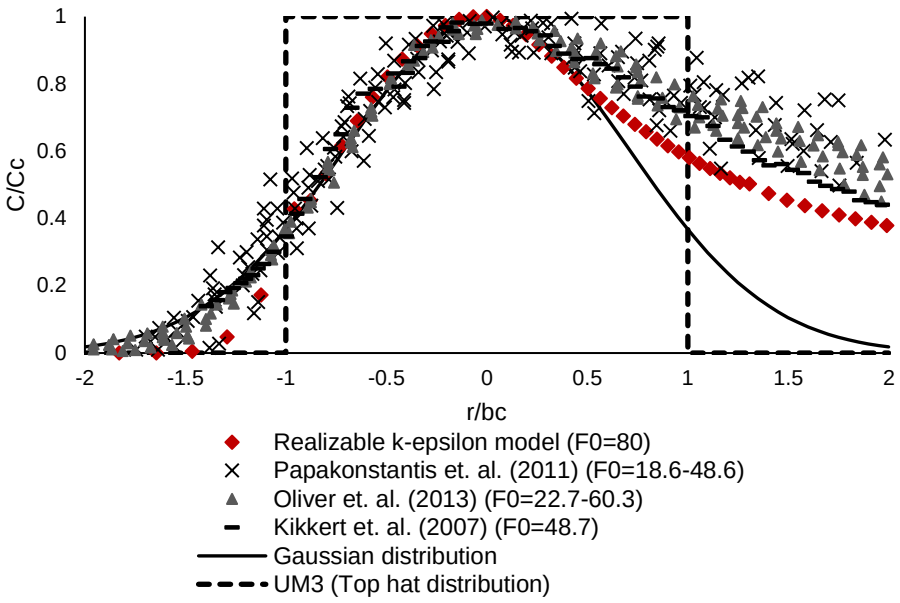

Figure 4-9. Cross-sectional nondimensionalised profiles of salinity for the source angle of 45° compared to experimental data.

An additional comparison with experimental data is presented in Figure 4-10, where the concentration distribution along the jet cross-section at the maximum rise height is compared with experimental data from Papakonstantis et. al. (2011b) and entrainment model UM3. The realizable k- ε model provides close estimations of the spread of salinity across this cross-section. UM3 predicts a plume radius that coincides with the area in which salinity concentrations are very close to zero in the outer edge of the plume; however, its assumption of a uniform distribution along the predicted diameter of the plume implies that the detrainment in the inner side of the plume is neglected.

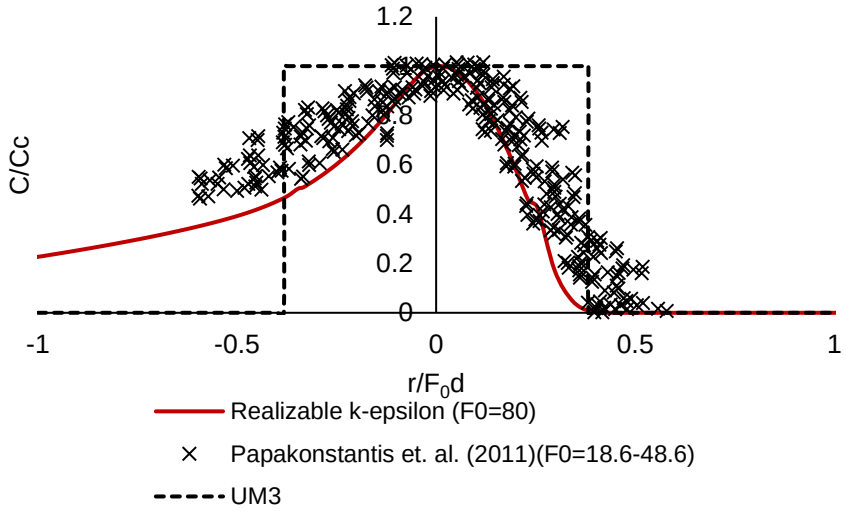

Figure 4-10. Vertical salinity concentration distribution at maximum rise height.

4.6.3 Geometrical parameters.

As previously mentioned, the vertical and horizontal position of maximum rise height and the horizontal position of the return point have been found to be proportional to Froude number for a given discharge angle (equations 4.1 to 4.3). Figure 4-11 summarises the experimental and modelling coefficients of geometrical parameters for angles of 15°, 30° and 45°. Amongst the different turbulence models used, the realisable k-ε model provides the most accurate results when compared to the experimental data.

Variations amongst experimental studies may respond to the experimental methods used. For instance, Kikkert et. al. (2007) found different experimental values when using Laser-induced fluorescence (LIF) and Light Attenuation (LA), finding that trajectory data was consistently higher in the results obtained from the LIF method. This responds to the fact that LIF methods are able to measure the flow behaviour within planar slices, whereas LA methods can only provide an integrated view of the flow along the perpendicular axis.

Figure 4-11a shows how various entrainment models and the realisable k-ε model compare to experimental coefficients of the vertical position of maximum rise height. In general terms, the realisable k-ε predicted coefficients of maximum rise height, $k_{zm,}$ are close to those obtained experimentally, following a similar trend.

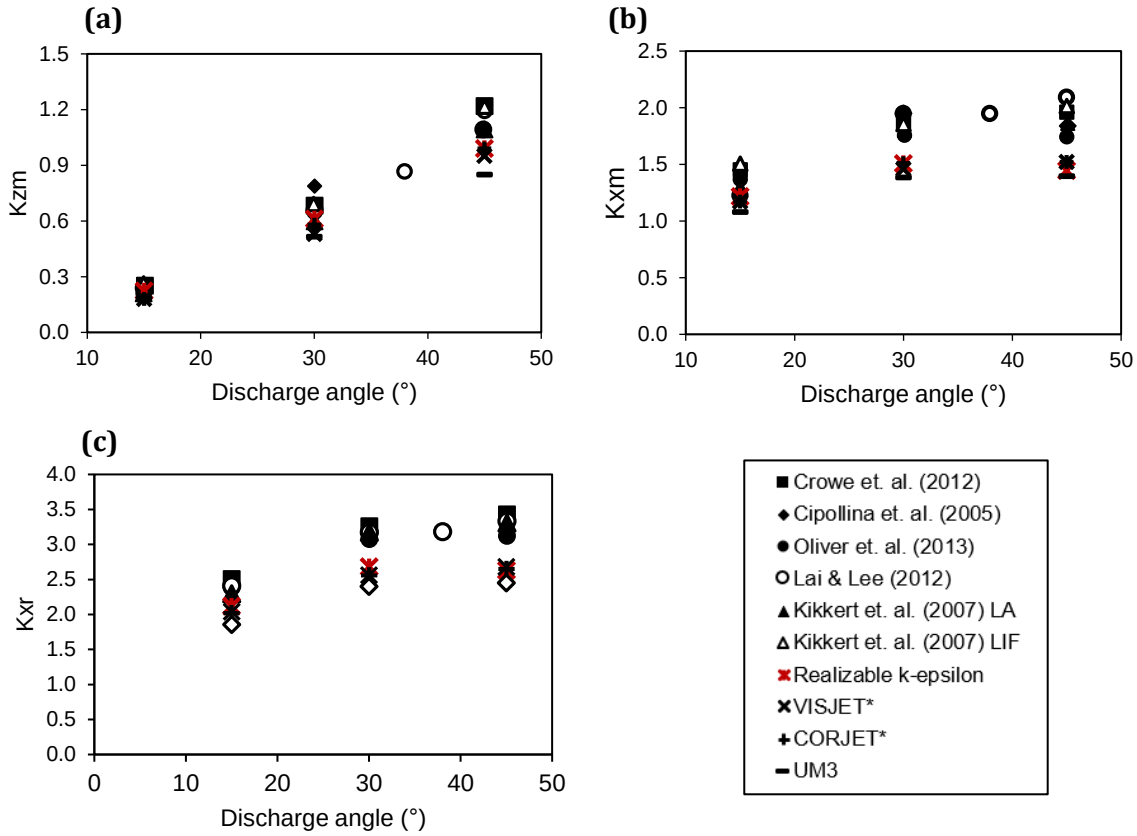

Figure 4-11. Coefficients of (a) vertical and (b) horizontal position of maximum rise height and (c) return point. *VISJET and CORJET data extracted from Crowe, et al. (2016) and Palomar, et al. (2012).

The coefficient $k_{xm,}$ which defines the horizontal position of the maximum rise height is underpredicted by all models for higher discharge angles. However, it is important to note that higher discrepancies are observed amongst experimental studies for this coefficient. This could respond to the shallow curvature near the centreline maximum rise height, which makes defining its horizontal position more difficult (Crowe, et al., 2016). In the realisable k-ε modelled cases, this shallow curvature is observed, depicting a plateau with a length of up to a fifth of the total horizontal trajectory, as can be seen in Figure 4-6. The selected centreline position corresponded to the central point along the plateau. Based on this assumption, the realisable k-ε model performs similarly to VISJET and CORJET and better than UM3.

The coefficient k_{xr} increases with discharge angle, reaching its maximum value at around 45°. Results obtained follow a similar trend to those obtained by experimental studies; however, all models seem to underpredict the location of return point (see Figure 4-11c). The realisable k-ε provides discrepancies when compared to experimental studies in the range of 8% to 25%, making k_x the geometrical coefficient most underestimated by this model. Higher discrepancies are observed for an angle of 45°.

The differences amongst experimental studies in the prediction of k_{xr} may be related to the position of the bottom boundary, since cases in which the lower boundary is closer to the discharge have more significant boundary interactions that can affect the position of the return point. This influence was observed by Shao & Law (Shao & Law, 2010), who found that to avoid the influences of boundary interaction at the return point, the ratio between the source height, $H_{s,}$ and $F_0 d$ must be higher than 0.74. In the scenarios modelled in the present study, this ratio ranges between 1 to 5; hence, bottom boundary influences are negligible.

Despite being able to simulate the dynamics of inclined dense jets, realisable k-ε results tend to underestimate the coefficients of maximum rise height and return point location. Hence, in terms of trajectory predictions, they may not indicate a significant improvement when compared to integral models VISJET and CORJET, especially for an initial angle of 45°, despite RANS models considering a more sophisticated implementation of the physics.

4.6.4 Dilution.

Centreline dilutions at maximum rise height, S_m, and return point, S_r, nondimensionalised by Froude number are plotted against discharge angle in Figure 4-12. Dilution has been found to be directly proportional to Froude number for a given discharge angle. It was observed that dilution increases with higher angles in the studied range ($0° < \theta < 45°$), coinciding with experimental observations (Launder & Spalding, 1974; Choudhury, 1993; Lai & Lee, 2012). Realisable k-ε model results compare well with experimental values, with higher accuracy than UM3 and CORJET models.

There is relative consistency in the experimental measurements of dilution at maximum rise height. The realisable k-ε model provides the estimations closest to experimental data, with differences in the range of 10% to 22%. On the other hand, the entrainment model UM3 overestimates the nondimensionalised dilution at the maximum rise height in the range of 70% to 80% when compared to experimental data. This implies that a design based on this modelling package would provide dilutions bellow the required level, which could lead to undesired pollution in receiving waters. Similarly, CORJET underestimates the nondimensionalised dilution

at the maximum rise height in the range from 10% to 40% for the angles studied. This underprediction implies that CORJET is a conservative model and hence, a design based on this model would not signify a risk for the environment. However, designs based on CORJET model will cost more than what is required if its dilution estimations were more accurate, particularly important when designing discharges at an industrial scale.

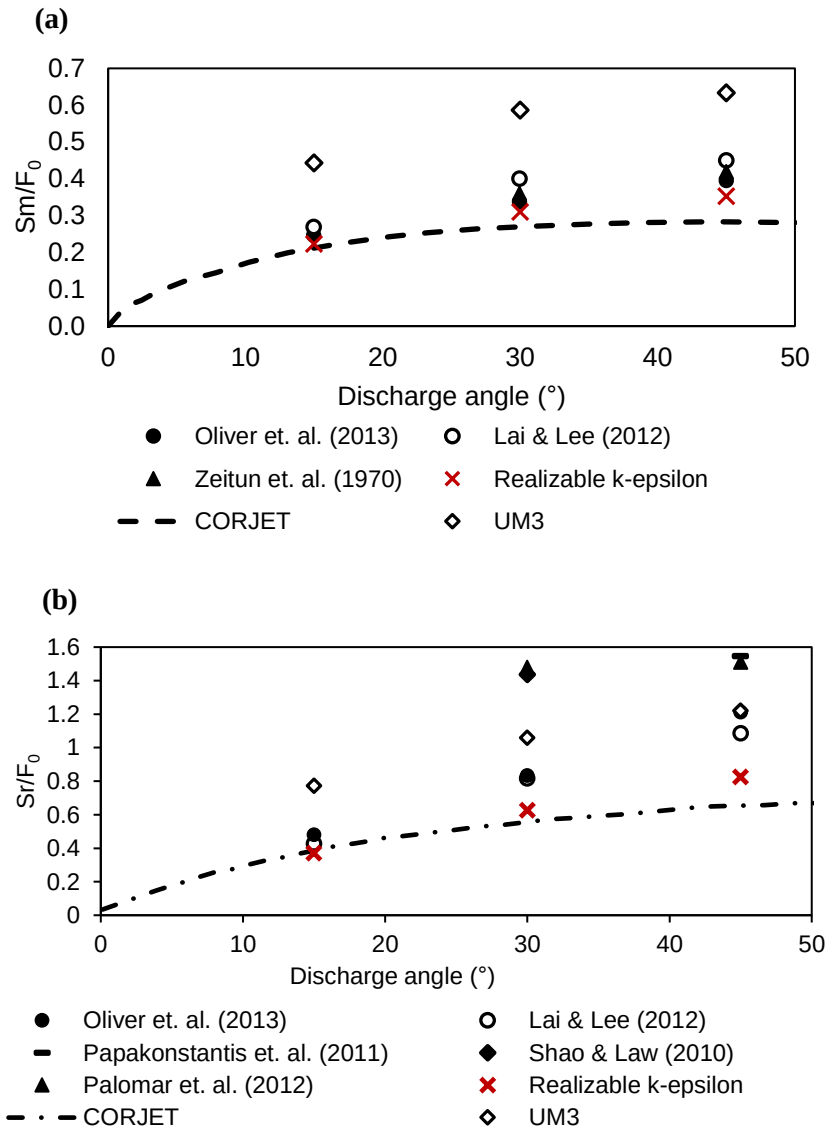

Figure 4-12. Nondimensionalised dilution vs. discharge angle: (a) at maximum rise height; (b) at return point.

Unlike dilution at the maximum rise height, the scatter of experimental predictions of dilution at the return point is large, despite the relative consistency in the experimental coefficients of return point location. This variation could result from differences in the location of the bottom boundary (Oliver, et al., 2013). Predictions from the realisable k-ε model are marginally closer to experimental data from Lai & Lee, (2012) and Oliver, et al. (2013) than CORJET. However, the realisable k-ε model underpredicts dilution in this position. This could be due to the observed underprediction of the position of return point. UM3 provides dilutions larger than Lai & Lee (2012) and Oliver, et al. (2013) but lower than Palomar, et al. (2012), Papakonstantis, et al. (2011) and Shao & Law (2010). Although its dilution estimations at the return point seem to be within

the range of the experimental data, they could rather be coincidental, considering that this model provides the least accuracy for predictions of trajectory, velocity and dilution at maximum rise height, when compared with experimental data. Furthermore, Palomar et. al. (2012) found different nondimensionalised dilutions predictions for UM3 at the return point, corresponding to values that are less than 50% the dilution for this model, which could imply that UM3 is very sensitive to input data.

4.6.5 Velocity.

Experimental studies conducted on inclined dense jets have focused on the generation of empirical coefficients for the position of maximum rise height and return point and dilution. In terms of velocity coefficients, Crowe et. al. (2016) conducted measurements that lead to conclude that the inverse of the centreline velocity magnitude (nondimensionalised by the initial discharge velocity) at maximum rise height and return point is linearly dependent on Froude number for all discharge angles.

Table 4-4 summarises the coefficients of centreline velocity at maximum height and return point obtained for different RANS and integral models. The realisable k-ε model with a Schmidt number of 0.7 is found to predict more accurately coefficients of centreline velocity at maximum rise height and return point, k_{um} and $k_{ur,}$ respectively. Its results differ from the experimental values in the range from 2.1% to 22.2%. This 22% discrepancy corresponds to the coefficient at return point for an angle of 45°, which coincides with the case in which the location of return point obtained experimentally and computationally differs the most. Entrainment models provide less accurate results, with discrepancies as high as 40%, 49% and 90% for VISJET, CORJET and UM3, respectively.

Table 4-4. Summary of experimental and modelled velocity coefficients for discharge angles of 15°, 30° and 45°.

Angle	Source	k_{um}	R^2	k_{ur}	R^2
15°	Crowe et. al. (2016)	0.251 ± 0.015	-	0.404 ± 0.015	-
	Realisable k-ε (Sct = 0.7)	0.216	0.998	0.360	0.999
	VISJET*	0.208	-	0.357	-
	CORJET*	0.192	-	0.333	-
	UM3	0.458	1.000	0.7047	1.000
30°	Crowe et. al. (2016)	0.356 ± 0.010	-	0.581 ± 0.020	-
	Realisable k-ε (Sct = 0.7)	0.318	0.999	0.543	0.987
	VISJET*	0.270	-	0.408	-
	CORJET*	0.303	-	0.384	-
	UM3	0.676	1.000	0.815	1.000
45°	Crowe et. al. (2016)	0.481 ± 0.014	-	0.693 ± 0.031	-
	Standard k-ε (Sct = 0.7)	0.524	-	0.573	-
	RNG k-ε (Sct = 0.7)	0.599	-	0.604	-
	k-ω SST (Sct = 0.7)	0.565	-	0.617	-
	Realisable k-ε (Sct = 0.6)	0.506	-	0.575	-
	Realisable k-ε (Sct = 0.7)	0.474	0.967	0.539	0.997

	Realisable k-ε (Sct = 0.9)	0.504	-	0.500	-
	Realisable k-ε (Sct = 1.4)	0.600	-	0.467	
	VISJET*	0.370	-	0.416	-
	CORJET*	0.384	-	0.357	-
	UM3	0.8814	0.999	0.814	1.000

*VISJET and CORJET data extracted from Crowe, et al. (2016) and Palomar, et al. (2012)

4.7 CONCLUSIONS.

The study conducted in this chapter has shown that RANS models can reliably be used for the simulation of inclined negatively buoyant jets. Different turbulence closure models were implemented, namely standard, RNG and realisable k-ε and k- ω SST. The main conclusions of this chapter are outlined below:

- The prediction of inclined dense jet trajectory and dilution is sensitive to turbulence models. Results obtained suggest that the realisable k-ε model is the most appropriate model for the simulation of inclined negatively buoyant jets.
- RANS models were found to be capable of predicting the typical characteristics of inclined negatively buoyant jets, including the detrainment that takes place in the inner side of the flow, a characteristic that is ignored by entrainment models that assume self-similar profiles along the jet cross-sections.
- The realisable k-ε model provides results with good agreement when compared to those obtained experimentally for the vertical location of maximum rise height of inclined negatively buoyant jets, with higher accuracy that entrainment models UM3, VISJET and CORJET for all discharge angles studied. However, the horizontal location of maximum rise height and return point is underpredicted by both the RANS and entrainment models.
- The advantage of the realisable k-ε model lies on its increased predictive capability for velocity and dilution at maximum rise height and return point, a feature that is important when it comes to designing real life marine outfalls.

5 COALESCING AXISYMMETRIC TURBULENT PLUMES.

5.1 INTRODUCTION.

In the previous chapter, the behaviour of buoyant jets exiting from single ports was studied, and comparisons between different modelling approaches were conducted. This analysis provides an important base for understanding the behaviour of buoyant jets and the parameters that play a role in determining their capacity for mixing. However, most marine outfalls end in a diffuser with multiple ports; therefore, understanding the basics of the interactions and coalescence of the plumes exiting from such ports and its effect on mixing is important for the design and modelling of marine outfalls. In this chapter, the coalescence of equal and unequal plumes is studied. Their behaviour is modelled using CFD techniques and compared with available experimental data and the predictions from entrainment models.

5.2 EXPERIMENTAL STUDIES ON COALESCING PLUMES.

Interacting laminar and turbulent plumes and buoyant jets occur extensively in nature and are relevant to many environmental and industrial applications. Heat sources in enclosed areas rise vertically and interact with each other as is also observed for plumes from smokestacks, volcanic eruptions and outfall discharges (Ramaprian & Chandrasekhara, 1989; Woods, 2010). Despite their numerous applications, there are relatively few studies on the coalescence of plumes.

Pera & Gebhart (1975) studied the laminar line and axisymmetric plumes. These plumes were thermally induced, and the interaction mechanisms between rising plumes as well as between a single plume and an adjacent surface were analysed. Plumes were observed to deflect towards each other or adjacent surfaces, in proportion to the spacing between them. This deflection is due to the restriction on the entrainment flow that is caused by the presence of another plume or a surface. For equal line plumes at larger spacing and shorter line sources, the plumes travel further before merging. In comparison, the effect of a wall on the inclination of the plume is equivalent to that of another plume of equal strength twice as far away. In the case of unequal line plumes, it was found that the stronger plume remains almost unaffected, whereas the weaker one is dominated by the presence of the other. On the other hand, axisymmetric plumes were found to have weaker interactions than plane plumes at the same spacing.

The interaction between unequal laminar plumes was further studied by Gebhart et al. (1976), who performed experiments on line plumes based on which an entrainment model was developed. This model predicts the location of the merging height and plume inclination; however, predictions do not show agreement with experimental values, particularly for cases with lower Grashof number. One of the reasons for the disagreement between experimental and predicted results could be that the model neglects the plume thickness when estimating the entrainment area.

Other studies that attempted to model the interaction between laminar plumes were conducted by Moses et al. (1991) and Moses, et al. (1993). The models assumed that the location at which two plumes merge corresponds to that in which the plume diameter equals the spacing between plumes. The location of the merging height was given as a function of source separation, viscosity,

buoyancy flux and Prandtl number. However, no comparison between observed and predicted values of the merging location was presented.

The coalescence of turbulent plumes is a process that occurs both naturally and in engineering applications. For this reason, various studies have focused on understanding the interaction between turbulent plumes, finding key similarities with the behaviour observed in laminar plumes. Ching et al. (1996) studied the interaction between turbulent line plumes in order to understand the behaviour of plumes generated by the refreezing of winter polar leads, which are the long narrow channels that are formed by openings in cracked ice sheets. The study compared two cases: 1) plumes exiting into a deep-water layer, called 'direct merging' experiments and 2) plumes exiting into the water with a strong density interface at a given distance below the surface, called 'indirect merging' experiments. The study found that in direct merging experiments, the plumes initially descend as if the other plume was not present but later start deflecting laterally towards each other. In indirect merging experiments, each plume descended as though there was no other plume or density interface. However, once the density interface was reached, the plumes bifurcated and spread horizontally in opposite directions until finally intersecting in their trajectory. Once the plumes intersected, they would rise to a maximum height; thereafter, the top of the plumes would deflect towards each other. The study also found that the location at which the plumes merged was dependent on fluid viscosity for Reynolds numbers under 8,000.

The subject of axisymmetric turbulent plumes was first addressed by Baines (1983). The study focused on experimental measurements on turbulent axisymmetric plumes; however, the dynamics of merging equal plumes is briefly addressed. The separate plumes started behaving as a single plume over a distance much shorter than the plume diameter. However, the merged plume cross-section changed to circular over a much longer distance.

Observations by Baines (1983) agree with those by Brahimi & Doan-Kim-Son (1985) according to which two clear zones are identified when axisymmetric turbulent plumes from two different sources interact: first, the interaction zone, at the end of which the plumes are no longer distinguishable and second, the self-preserving zone, in which the new formed single plume is axisymmetric and shows self-similar concentration profiles. The plume from the self-preserving zone is similar to that of a single source located at a "virtual origin".

Although these studies gave interesting insights on the behaviour of interacting axisymmetric turbulent plumes, their focus was mainly on the merged plume (or "self-preserving zone") and not in the process of coalescence itself (or "interaction zone"). Bjorn & Nielsen (1995) addressed this problem through proposing a model for the prediction of the coalescence of turbulent axisymmetric plumes. This model proposed that the velocity and temperature distribution in a plume can be superimposed. Comparisons with experimental data found that this hypothesis is incorrect since plumes were found to deflect towards each other due to the reduced entrainment area between them.

Kaye and Linden (2004) conducted a detailed study on the coalescence of axisymmetric turbulent plumes with equal and unequal sources of buoyancy. The study performed experiments for plumes separated by different spacings and with different sources of buoyancy. Based on experimental results, they proposed two models: an entrainment model for the interaction zone, considering the deflection towards each other displayed by the plumes; and a model to predict the "virtual origin" of the merged plume formed in the self-preserving zone. This study was extended by Cenedese & Linden (2014) with more recent experiments on the merging of axisymmetric turbulent plumes and the development of a model with "effective" entrainment constant, which allows the definition of a single expression for the different zones identified in the interaction between turbulent plumes.

The available literature on the coalescence of plumes provides a firm base for the validation of the CFD modelling approach proposed in this study. For such validation, a set of modelling cases were designed based on Kaye and Linden (2004). The results are compared with those obtained by the previous experiments described in this section.

Table 5-1. Summary of experimental cases on the coalescence of plumes.

	Flow regime	Type of plume source	Differences between buoyancy sources	Ambient conditions	Parameters measured
Pera & Gebhart (1975)	Laminar	Line and axisymmetric	Equal and unequal	Stagnant uniform	Inclination angles from vertical for plumes at different spacings and centreline temperature.
Gebhart et al. (1976)	Laminar	Line	Unequal	Stagnant uniform	Empirical ratios for flow, Grashof number and other fluid properties.
Moses et al. (1991)	Laminar	Line			Shadowgraphs of plumes merging at different times.
Moses et al. (1993)	Laminar	Line	Equal	Stagnant uniform	Shadowgraphs of plumes merging at different times.
Ching et al. (1996)	Turbulent	Line	Equal	Stagnant uniform	Plume cap location and width variation in time, merging height, time to merge depending on plume separation.
Baines (1983)	Turbulent	Axisymmetric	Equal	Stagnant uniform	Flow rate vs. downstream distance.
Brahimi and Doan-Kim-Son (1985)	Turbulent	Line	Equal	Stagnant uniform	Temperature, velocity and turbulent intensity profiles at different locations downstream.
Bjorn and Nielsen (1995)	Turbulent	Axisymmetric	Equal	Stagnant uniform	Velocity, velocity profiles and radius at different locations downstream.
Kaye and Linden (2004)	Turbulent	Axisymmetric	Equal and unequal	Stagnant uniform	Merging height and flow rate at different locations downstream.
Cenedese and Linden (2014)	Turbulent	Axisymmetric	Equal	Stagnant uniform	Merging height.
He et. al. (2018)	Turbulent	Axisymmetric	Equal	Linearly stratified	Maximum penetration depth, velocity profiles, turbulence parameters.

5.3 DESCRIPTION OF VALIDATION CASES.

Modelling cases for turbulent plumes were defined based on the experiments of Kaye and Linden (2004). They measured the merging height of coalescing axisymmetric equal and unequal turbulent plumes using dye attenuation and light-induced fluorescence methods.

The model domain was a tank 0.6 m square with a depth of 1.8 m. Two inlet nozzles were located on top of the tank (see Figure 5-1). Each inlet had a diameter of 5 mm, discharging at a flow rate of 2.5 cm^3/s. Density differences between the receiving ambient fluid and the discharged flow are due to different salinity concentrations. To provide the required density differences, salinity concentrations at the inlets were varied between 3 and 40 ppt. The spacing between the port centres was between 3 and 8 cm.

Two types of cases were modelled: those in which the buoyancy sources at the two inlets were equal and those in which one of the inlets had a higher buoyancy source than the other. A description of the cases modelled is shown in Table 5-2.

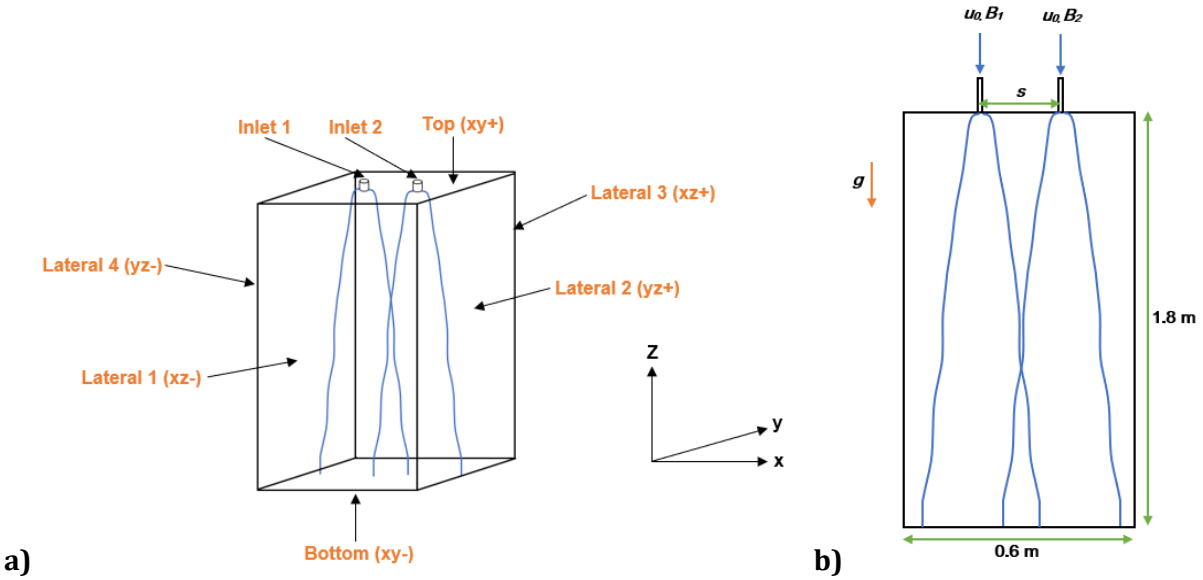

Figure 5-1. Schematic of modelling cases of coalescing axisymmetric turbulent plumes: a) three-dimensional view with boundary names; b) frontal plane view.

Table 5-2. Summary of modelling cases of coalescing axisymmetric turbulent plumes.

	Inlet velocity	Inlet density	Froude number	Source buoyancy per port	Buoyancy flux ratio	Spacing between ports	Reynolds number at inlets	Grashoff number at inlets
Symbol	u_0	ρ_0	F	B	$\Psi = B_1/B_2$	s	R	Gr
Units	m/s	kg/m^3	-	m/s^2	-	Cm	-	-
Equal plumes	0.127	1027	3.3 – 50.5	0.30	1	3 - 8	355	1.24 x 10^6
Unequal plumes	0.127	999.8 – 1027	3.3 – 12.8	0.03 - 0.30	0.1 - 0.9	5.5	355	9.3 x 10^4 – 1.24 x 10^6

Port diameter was fixed at 5 mm, ambient salinity of 0 ppt and ambient density was 996.8 kg/m^3.

5.4 MODELLING METHODOLOGY.

The CFD simulations on multiport buoyant jets were based on the solution of the unsteady Reynolds-Averaged Navier-Stokes equations (uRANS). Different turbulent closure models were tested, namely realisable and RNG $k-\epsilon$ and $k-\omega$ SST. These CFD simulations were implemented in the finite volume-based commercial code ANSYS Fluent 18.2 (Ansys Inc., 2018). Transient simulations were conducted in all cases implementing the SIMPLE scheme for the pressure-velocity coupling. Second-order spatial discretisation schemes were used for the continuity, momentum, turbulent kinetic energy, turbulent diffusivity and advection-diffusion equation. The governing equations solved are described in detail in section 3.2.

For each case, the simulation time from the beginning of the discharge was 60 seconds, ensuring that a steady state had been reached in the area covered 1.2 m downstream from the point of discharge. Once this steady state flow field had been reached, mesh adaption was conducted, and the simulation was continued until no further changes occurred due to mesh refinements. Fixed time stepping was used. The time step interval was adjusted for each case, ensuring that the Courant number was always less than 1.0 across the domain.

The discharging ports were located at the top of the tank and defined as inlet boundaries. At these boundaries, turbulence was defined using the hydraulic radius and turbulence intensity. Turbulence intensity was computed using equation 4.7. The top, bottom and lateral boundaries were defined as no-slip walls. A more detailed description of the boundary conditions assigned is shown in Table 5-3, for both equal and unequal plumes. For other cases, a similar approach was used, assigning the corresponding values of velocity and salinity concentration at the inlet boundaries.

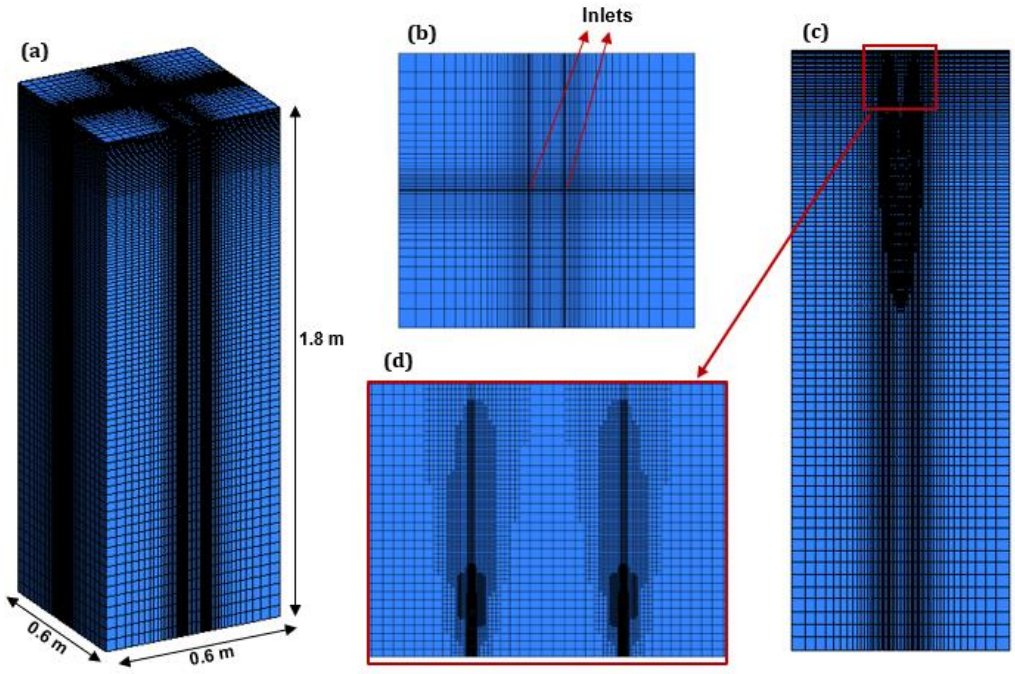

Figure 5-2. Modelling mesh for coalescing axisymmetric plumes exiting from ports spaced 8 cm apart: **(a)** three-dimensional view of the initial structured mesh; **(b)** top view of the initial structured mesh **(c)** adapted mesh for a case in a section along the centreline plane of the plumes; **(d)** closer view of the adapted mesh near the inlet.

Table 5-3. Description of boundary conditions for examples of equal and unequal axisymmetric turbulent plumes.

Case	Boundary	Boundary type	Momentum				Thermal	Species	Turbulence	
			x-velocity (m/s)	y-velocity (m/s)	z-velocity (m/s)	Gauge pressure (Pa)	Temperature (°C)	Salinity concentration (ppt)	Turbulent intensity (%)	Hydraulic diameter (m)
Equal plumes 1	Top (xy+)	Non-slip wall	N/A	N/A	N/A	N/A	Zero heatflux	Zero-gradient	N/A	N/A
	Bottom (xy-)	Pressure outlet	N/A	N/A	N/A	0	Zero heat flux	Zero-gradient	N/A	N/A
	Lateral 1 (yz-)	Non-slip wall	N/A	N/A	N/A	N/A	Zero heat flux	Zero-gradient	N/A	N/A
	Lateral 2 (yz+)	Non-slip wall	N/A	N/A	N/A	N/A	Zero heat flux	Zero-gradient	N/A	N/A
	Lateral 3 (xy+)	Non-slip wall	N/A	N/A	N/A	N/A	Zero heat flux	Zero-gradient	N/A	N/A
	Lateral 4 (yz-)	Non-slip wall	N/A	N/A	N/A	N/A	Zero heat flux	Zero-gradient	N/A	N/A
	Inlet 1	Velocity inlet	0	0	0.127	N/A	22	40	7.7	0.005
	Inlet 2	Velocity inlet	0	0	0.127	N/A	22	40	7.7	0.005
Unequal plume 1	Top (xy+)	Non-slip wall	N/A	N/A	N/A	N/A	Zero heatflux	Zero-gradient	N/A	N/A
	Bottom (xy-)	Pressure outlet	N/A	N/A	N/A	0	Zero heat flux	Zero-gradient	N/A	N/A
	Lateral 1 (yz-)	Non-slip wall	N/A	N/A	N/A	N/A	Zero heat flux	Zero-gradient	N/A	N/A

	Lateral 2 (yz+)	Non-slip wall	N/A	N/A	N/A	N/A	Zero heat flux	Zero-gradient	N/A	N/A
	Lateral 3 (xy+)	Non-slip wall	N/A	N/A	N/A	N/A	Zero heat flux	Zero-gradient	N/A	N/A
	Lateral 4 (yz-)	Non-slip wall	N/A	N/A	N/A	N/A	Zero heat flux	Zero-gradient	N/A	N/A
	Inlet 1	Velocity inlet	0	0	0.127	N/A	22	40	7.7	0.005
	Inlet 2	Velocity inlet	0	0	0.127	N/A	22	3	7.7	0.005

To implement a mesh adaption method like the one used for single port discharges in the previous chapter, a structured mesh was used to perform the initial simulation. An initial mesh ranging between 3.2 and 3.8 x 10^5 elements were used for the validation cases in coalescing axisymmetric turbulent plumes see Figure 5-2a-b. These initial meshes were uniform and structured, with rectangular hexahedral elements. The size of the elements increased gradually as the distance from the point of discharge increased. The discharge pipe was modelled as an equivalent square as was done for the inclined negatively buoyant jets in the previous chapter.

Once the initial simulation was performed, mesh adaption was conducted in a series of layers. The first refinement was done to the cells in which salinity concentrations were higher than 1% of the initial salinity, corresponding to areas with salinity concentrations higher than 0.4 ppt. A second, third and fourth layer of refinement was added to those cells in which the concentration of salinity was higher than 8%, 24% and 36% of the initial salinity, respectively. No intermediate simulation was conducted between each refinement. This approach increased the size of the mesh to about four times its original number of cells. A mesh independence study was conducted using the methodology described in section 3.2. Within this study, finer initial meshes as large as 1.2 x 10^6 elements were tested, finding that such changes did not change the obtained results significantly. Likewise, additional refinements to the mesh were performed, and no significant changes in the flow field were observed. Figure 5-2c-d shows the resolution of the adapted mesh in the area where the plumes are located for one of the cases simulated.

5.5 RESULTS AND ANALYSIS.

Understanding how plumes merge is essential for the design of multiple port discharges at real scale. The following subsections describe the processes that occur when equal and unequal turbulent axisymmetric plumes interact and the main parameters that govern their interaction. The location of the merging height is compared to experimental data and other entrainment models.

5.5.1 Equal plumes.

5.5.1.1 General flow characteristics.

Observations of the descent of two equal plumes in a homogenous environment were conducted by studying the concentration and velocity contours along the centreline plane, which is a vertical plane that divides the plumes into two equal parts. The location of the centreline plane can be observed in Figure 5-3. Figure 5-4 and Figure 5-5 show the time evolution of two equal plumes exiting from two parallel ports located 6.75 cm apart based on the contours of velocity and salinity concentration, normalised by their initial values. Please note that these figures do not show the complete domain in the vertical axis (z). The value of the ratio between downstream distance and port spacing at the bottom boundary is 26.6 for the case shown in Figure 5-4 and Figure 5-5.

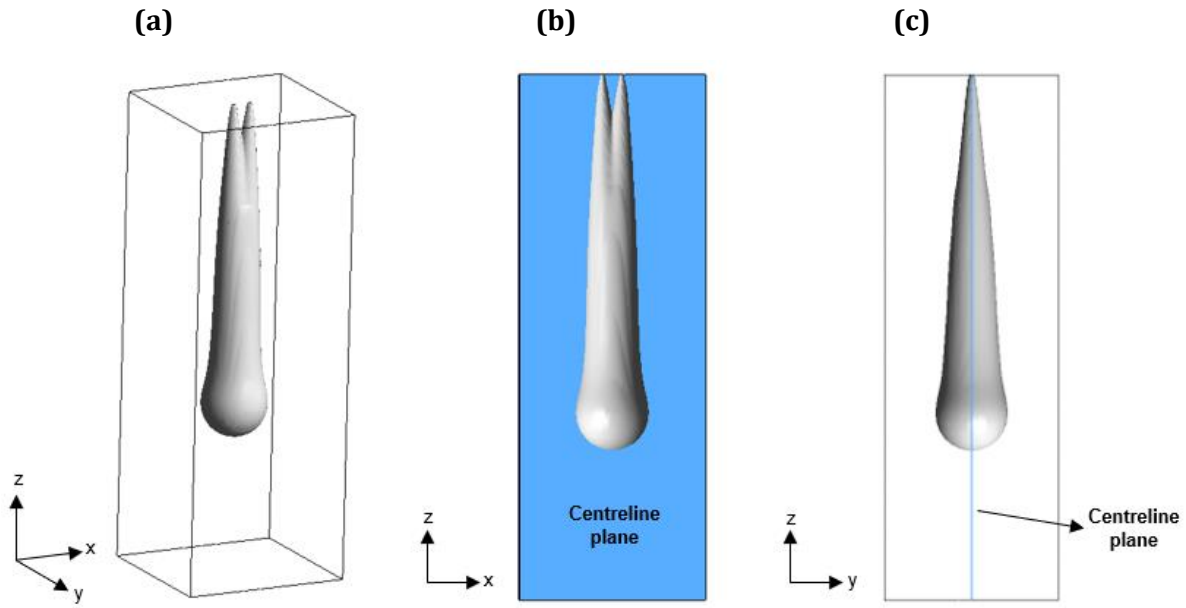

Figure 5-3. Isosurface at a normalised pollutant concentration of 0.0025 for two equal plumes spaced 6.75 cm apart after 60 s: **a)** three-dimensional view; **b)** frontal view; **c)** lateral view.

It is observed that the plumes show a mushroom-like pattern, with a stem and a cap leading the descent (see Figure 5-4-Figure 5-5). This pattern has been observed previously in both laminar and turbulent plumes (Moses et al., 1993; Ching et al., 1996). The caps tend to descend vertically, whereas the stems of the plumes are observed to deflect towards each other early on. As ambient fluid entrains the plumes, and the caps continue to approach each other, their velocity of descent increases, which leads to the reduction in the pressure between the two plumes. The reduced pressure between the plumes causes the stems to deflect more rapidly towards each other, further accelerating their descent. As the caps collide, as seen in Figure 5-4c and Figure 5-5c; they tilt to the sides as a new front develops. This was observed by Ching et al. (1996) in their study of the interaction between turbulent line plumes. The fully merged plume will have a similar shape to that of an individual plume.

From the previous observations of the changes in time, three main stages can be identified in the process of merging. In the initial stage, two independent plumes eject from two separate ports and descend, whilst they start to approach each other. In the second stage, the caps of said plumes touch and continue their descend, whilst the plume stems increasingly deflect towards each other. Finally, the two plumes fully merge downstream, behaving like one individual plume. Upstream, the flow will have reached a steady-state.

In the final stage of merging, the flow will behave differently depending on the region in study. Upstream, the plumes behave like independent plumes. This zone is followed by a transition region in which the plumes have touched but have not yet fully merged. Further downstream, a final region in which the plumes have merged and behave like a single individual plume is found. This behaviour has also been observed in previous research by Cenedese & Linden (2014).

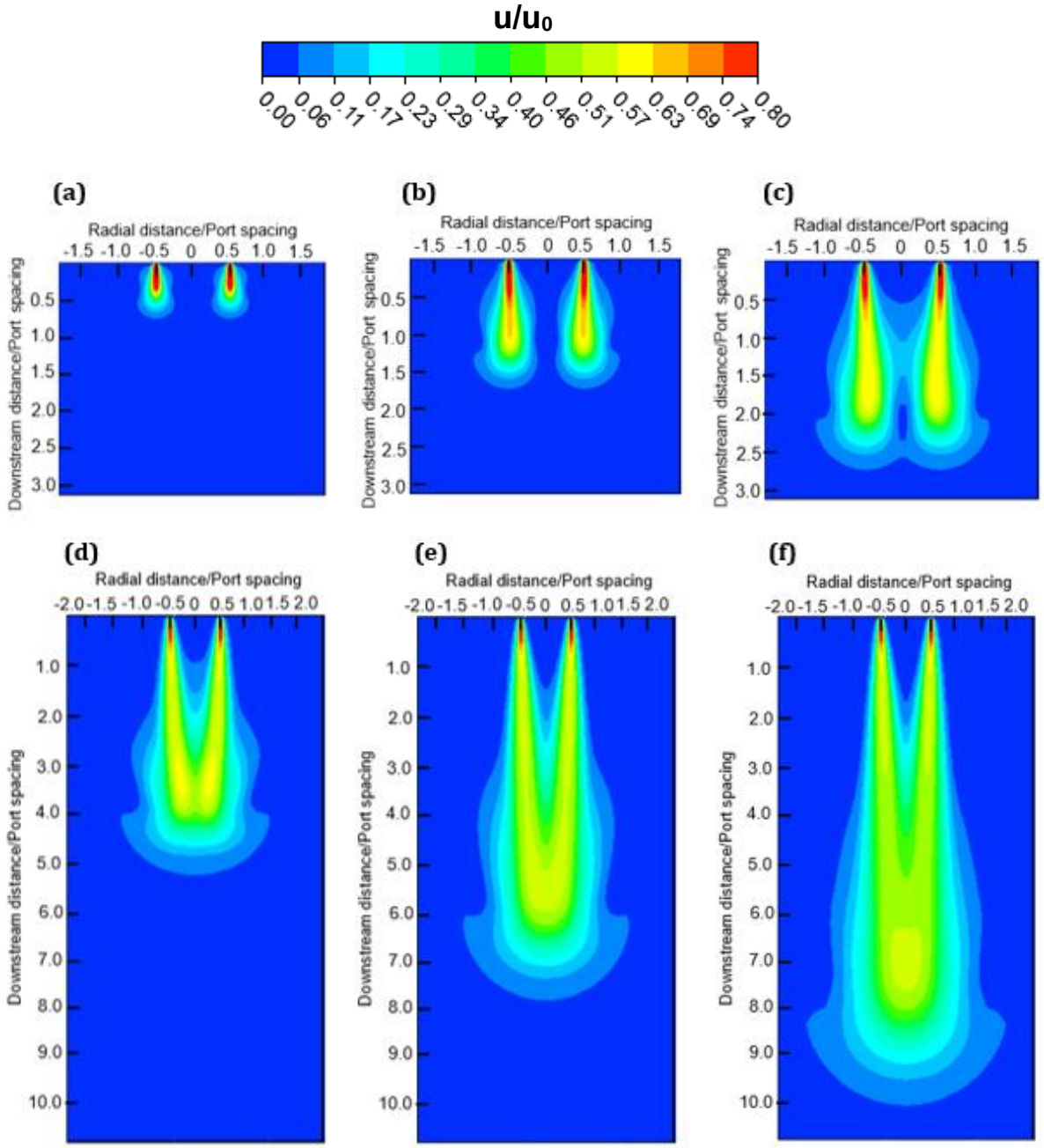

Figure 5-4. Time evolution of the normalised velocity magnitude of two equal descending plumes spaced 6.75 cm apart: **a)** t = 1 s; **b)** t = 3 s; **c)** t = 5 s; **d)** t = 10 s; **e)** t = 15 s and **f)** t = 20 s. These graphs do not show the complete domain along vertical axis.

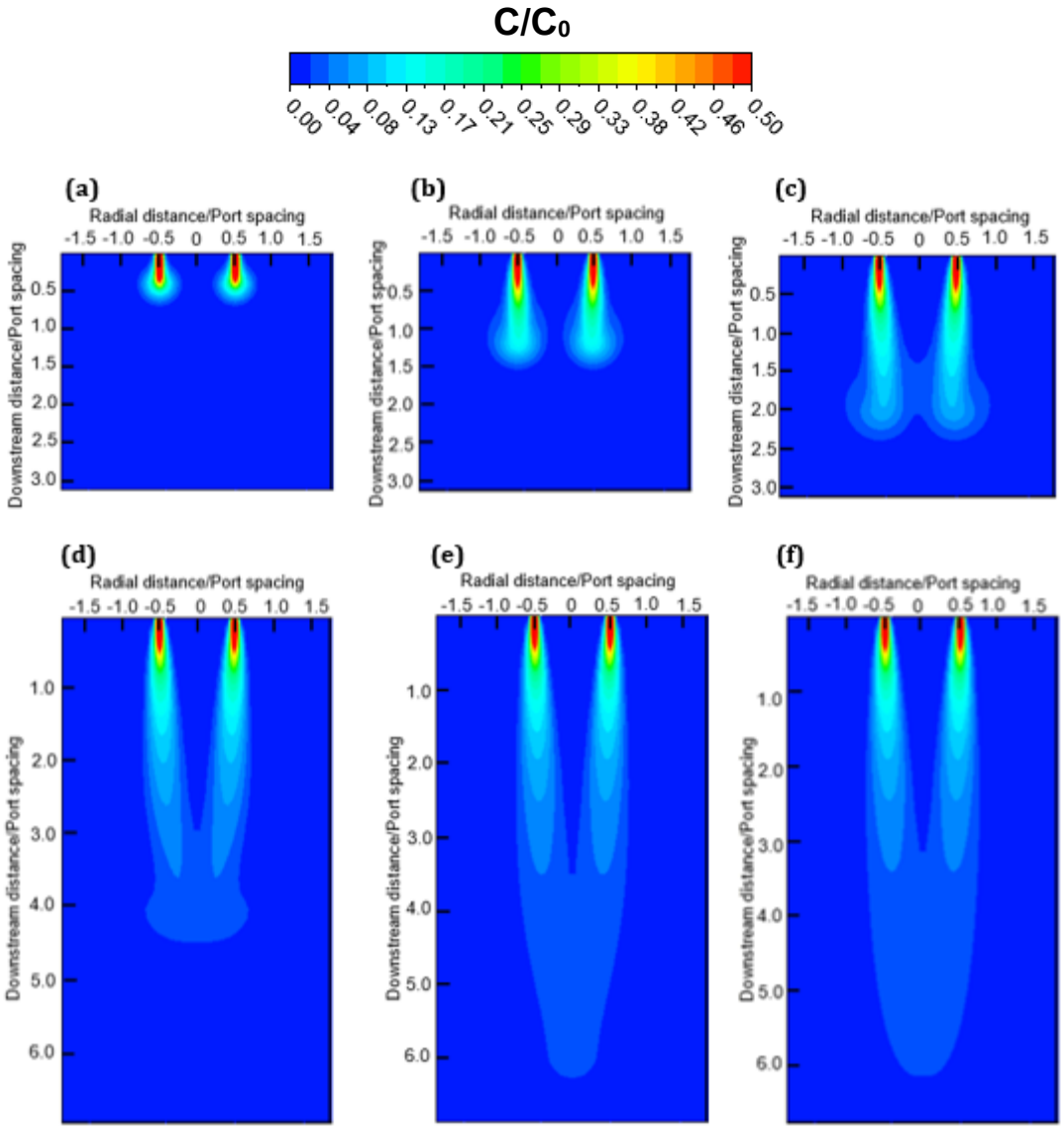

Figure 5-5. Time evolution of the normalised pollutant concentration of two descending plumes spaced 6.75 cm apart: **a)** t = 1 s; **b)** t = 3 s; **c)** t = 5 s; **d)** t = 10 s; **e)** t = 15 s and **f)** t = 20 s. These graphs do not show the complete domain along the vertical axis.

5.5.1.2 Merging height.

The location where the plumes are considered to have fully merged has been studied by Kaye and Linden (2004). For plumes with equal sources of buoyancy, this merging height was defined as the location in which we can no longer see two peaks in the buoyancy (or concentration) profiles (see Figure 5-6). This implies that the maximum buoyancy is in the centreline between both plumes. It is then assumed that from that point onwards, the flow behaves as a single plume.

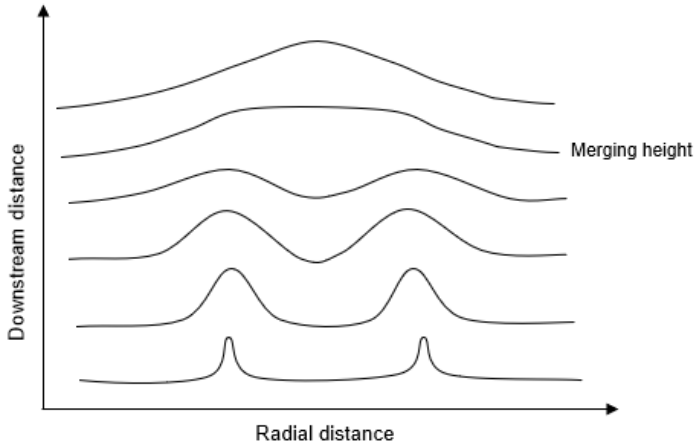

Figure 5-6. Schematic of merging height for equal plumes according to Kaye and Linden (2004).

To determine the merging heights of the cases studied, the concentration distribution of the plumes was plotted at different downstream locations (see Figure 5-7a). These locations were normalised by the corresponding port spacing, and the local concentration was normalised by the initial salinity concentration. Similar behaviour to that observed by Kaye and Linden (2004) in their experimental study was identified. Closer to the sources, the plumes show two parallel peaks. As they approach each other, the peaks seem to deflect, and the highest concentrations move further from the centreline of the sources and closer to the centre. Further downstream, the spacing between the concentration peaks is reduced until the trough between two plumes disappears, and the maximum concentration is located at the centreline of the two plumes. The same behaviour is observed for the plots of velocity distribution at different distances downstream, as seen in Figure 5-7b.

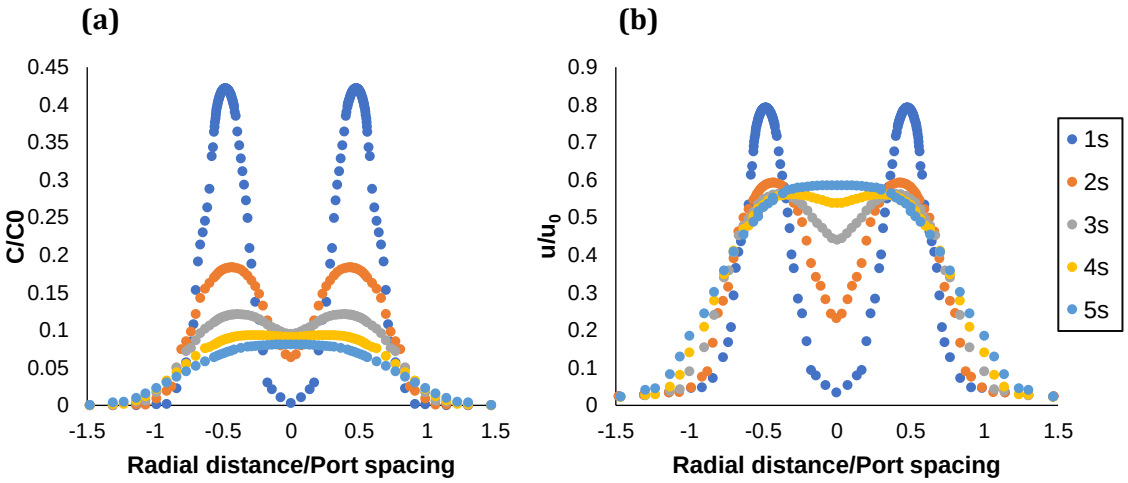

Figure 5-7. Distribution of **a)** scalar concentration (salinity) and **b)** velocity magnitude at different locations downstream for a case with initial port spacing of 6.75 cm.

Widely used entrainment models such as VISJET and UM3 apply different assumptions when modelling the merging between plumes. UM3 assumes a top-hat distribution of scalars along the cross-section of each plume. Therefore, the merging height is located where the plume diameter

equals the initial spacing between plumes. Merging is modelled by reducing the effective area of entrainment due to the interference between plumes (Baumgartner, et al., 1994). The deflection of the plumes towards each other is not considered. In Figure 5-8a, the scalar distribution at different locations downstream is illustrated. The downstream location is normalised by the port spacing. It can be observed that the plumes merge at a location downstream between 3-4 times the port spacing.

On the other hand, VISJET assumes a Gaussian distribution. The interaction between plumes is ignored; hence, the plumes are modelled as if they exited from single ports in an unbounded environment (Lee & Cheung, 1990). For the current study, it is assumed that the merging location for plumes modelled in VISJET corresponds to the location where the spacing between the plumes equals the plume diameter, even though we can observe a trough between the scalar profiles of the plumes at this location. Figure 5-8b shows the scalar profiles at different locations downstream. The plumes first touch at a location downstream between 3-4 times the port spacing.

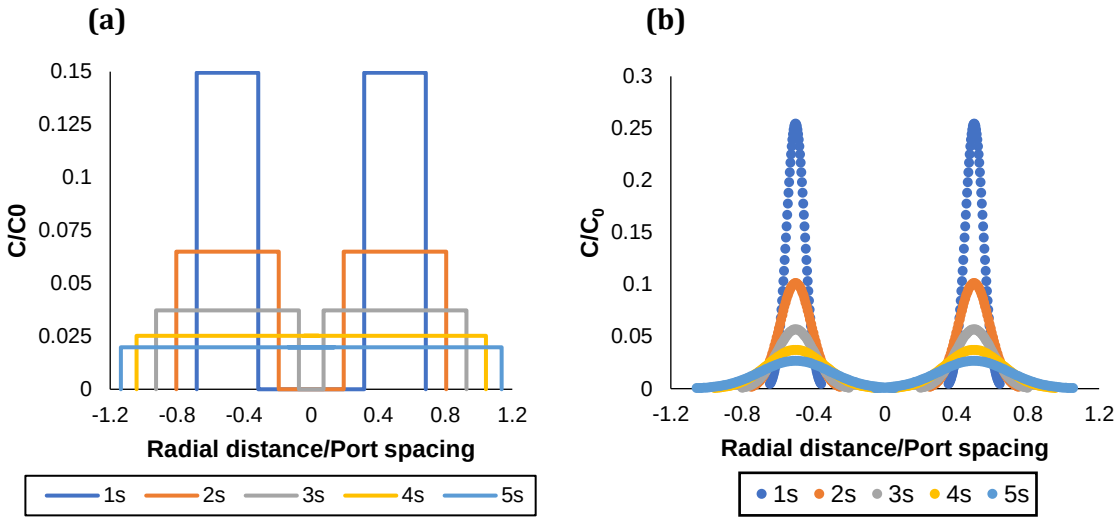

Figure 5-8. Distribution of scalar concentration (salinity) at different locations downstream for the case with the initial port spacing of 5.5 cm, according to entrainment models: **a)** UM3 and **b)** VISJET.

Figure 5-9a shows the contours of non dimensionalised salinity (local concentration, C, divided by initial concentration, C_0) for two equal plumes with a distance between ports of 5.5 cm after 60 seconds. Please note that in this graph, the vertical axis is reversed, and that only a fraction of this axis is shown. For the observed case, the bottom boundary corresponds to a ratio of 32.8 between downstream distance and port spacing. Red areas in the figure correspond to locations where the non dimensionalised salinity is in the range of 0.2 to 1. The downstream and radial distances are all shown non dimensionalised by port spacing.

The position of the merging height is plotted against port spacing in Figure 5-9b and compared to experimental data from Kaye and Linden (2004). In this graph, we can observe how the merging height location is directly proportional to the spacing between ports. No significant difference was found for the results of the realisable k-ε model when compared to the RNG k-ε model and the k- ω SST model. This can be due to insignificant wall effects in the flow in study.

The RANS models are observed to predict the physics of the flow accurately, although they slightly overpredict the location of the merging height for equal plumes.

As previously mentioned, the location of the merging height of equal plumes, z_m, is directly proportional to the port spacing, s. Therefore, it can be defined as:

$$z_m = \lambda_e \cdot s \qquad \textbf{(5.1)}$$

where λ_e is a constant value for all equal plumes.

For the cases modelled, the average value of λ_e was found to be 5.1, indicating that the plumes tend to be fully merged at a location of approximately 5.1 times the initial port spacing. From experimental observations by Kaye and Linden (2004), this value is 4.6. Discrepancies between experimental and modelled results could be due to slight underprediction in the deflection of the plumes towards each other. Despite this small difference, the tested RANS models show a good representation of the interaction between equal plumes.

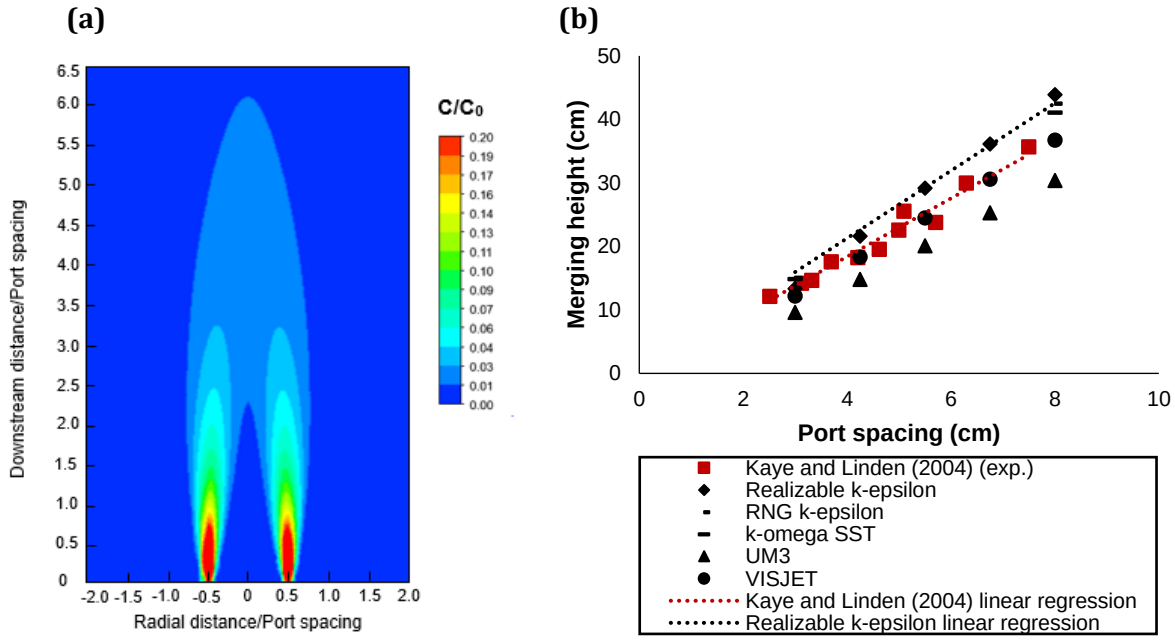

Figure 5-9. Merging height locations for equal plumes: **(a)** Contours of nondimensionalised salinity for two equal plumes with port spacing of 5.5 cm after 60 seconds using the realisable $k-\epsilon$ model; **(b)** Comparison of modelled and experimental merging height locations for equal plumes. In the contour graph, the vertical axis is reversed and only a portion of the domain along this axis is shown.

Entrainment model UM3 is observed to underpredict the location of the merging height, which is on average located at a location of 3.6 times the initial port spacing. A reason for such underprediction is the scalar distribution along the cross-section of the jet. Since the scalar profiles show a top-hat distribution, the trough between plumes disappears when they first touch (see Figure 5-8a). This differs with the behaviour observed experimentally, where the plumes first touch and continue their trajectory, becoming a single plume further downstream.

The merging locations observed for the entrainment model VISJET are closer to the experimental observations than those obtained by UM3 and RANS models. However, this location is based on

the assumption that the plumes fully merge once their diameter equals the spacing between them (i.e. when they first touch), despite the existence of a trough between plumes at this location. The scalar concentration is hence not its maximum at this location. This indicates that even though the merging height location predicted with the VISJET model is closer to the experimental data, other variables such as dilution and velocity at the merging height are not, an aspect that will be discussed further in the following subsection.

5.5.1.3 Dilution.

The most crucial parameter considered when designing and monitoring multiport discharges is dilution. Port spacing is a determining factor since the level of interaction between plumes influences the level of mixing observed. Figure 5-10 compares the normalised pollutant concentration along the centreline between plumes for all the port spacings studied. Highest pollutant concentration is observed for the case with the smallest port spacing, implying that the reduced entrainment area resulting from the proximity of the ports decreases mixing. The concentration peaks are found at a distance of approximately 20 times the diameter of the discharging ports, coinciding with the location of the larger differences between observed pollutant concentrations for the port spacing studied. At this location, the normalised concentration for a case with port spacing of 3 cm is 190% larger than that of the case with port spacing of 8 cm. However, further downstream, the differences in concentration between the cases with largest and lowest spacing reduce so that the concentration for a case of 3 cm spacing is approximately 130% larger than that of the case with port spacing with 8 cm.

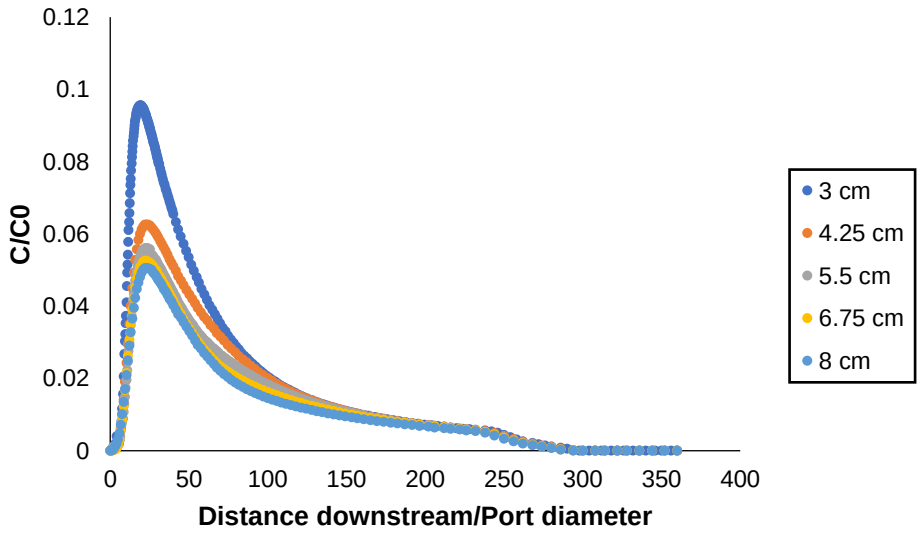

Figure 5-10. Comparison of normalised concentration along the centreline of two equal plumes for cases with different port spacings.

Further comparisons between different port spacings are shown in Figure 5-11, where dilution at the merging height location is plotted against port spacing. Dilution at the merging height increases with port spacing. A quadratic regression was fitted to the data, obtaining a minimum coefficient of determination (R^2) of 0.9999 for the range of port spacings studied. This indicates that dilution at the merging height increases quadratically with port spacing.

Despite the importance of the dilution parameter for the design and monitoring of multiple port discharges, there is no available experimental data on this aspect in coalescing axisymmetric turbulent plumes. However, dilution values obtained from the CFD simulations can be compared to other widely entrainment models such as UM3 and VISJET.

At the merging location, dilution values obtained by the realisable k-ε model and UM3 are very similar, with discrepancies between 9.2 and 11.7%. This is to be expected because even though the UM3 model does not consider the deflection in the plumes trajectory as they approach each other, it does account for the reduction of their effective entrainment area due to their proximity. However, that is not the case for the VISJET model.

As mentioned previously, the entrainment model VISJET does not model the interactions between adjacent plumes and the simulations are as though they were single port discharges. Two different approaches were used to determine the dilution at the merging height, according to VISJET. The first approach was to use the average dilution at that location. This value corresponds to the average dilution along the cross-section of a single plume. This approach provides a dilution that significantly differs from the results obtained by UM3 and the realisable k-ε model. Discrepancies between VISJET and UM3 range between 52 and 59%. On the other hand, VISJET dilution values were found to be 67 to 76% higher than the dilution values obtained with the realisable k-ε model.

A second approach to determine the dilution at the merging height with the VISJET model is to use the value of the dilution at the plume radius. This is due to the merging height being assumed to be located where the initial spacing between the plumes equals the local plume diameter. However, this value is significantly higher than the average value, since VISJET assumes that the concentration follows a Gaussian distribution (see Figure 5-8b). However, using this approach, VISJET dilution predictions at the merging height can be up to 54 times higher than values obtained with the realisable k-ε model and UM3. Therefore, a safer assumption would be to use the plume average dilution at the merging height location.

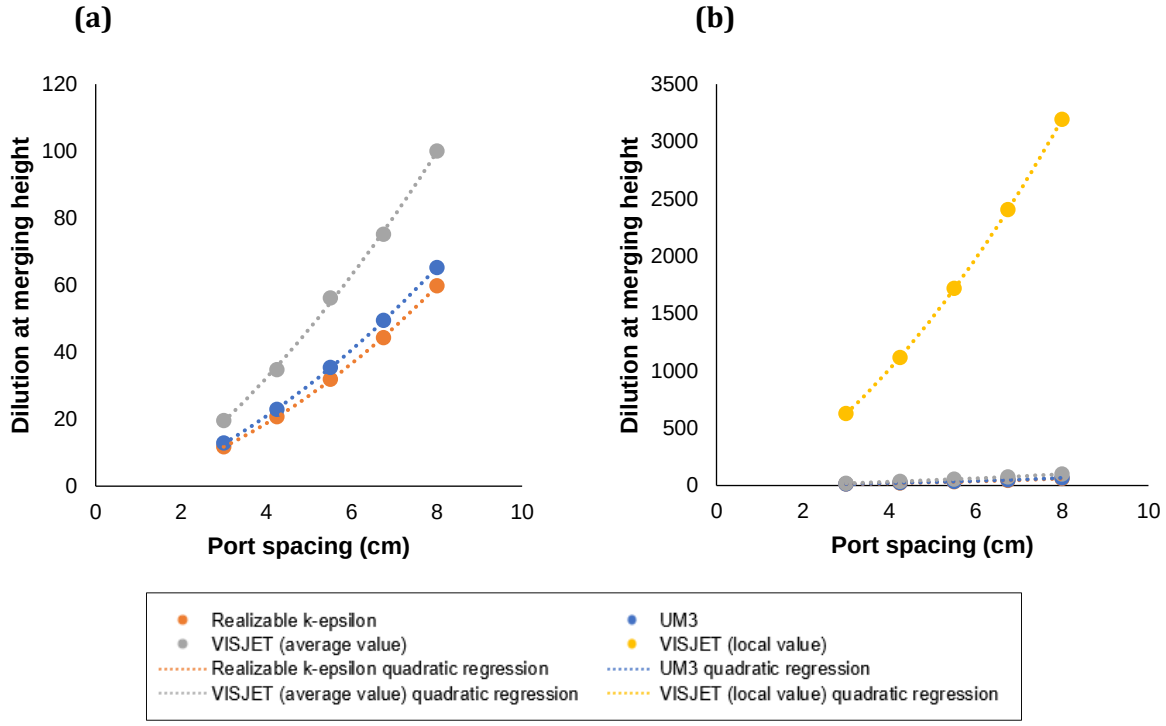

Figure 5-11. Comparison of predicted dilution at the merging height for different port spacings.

Additional comparisons of normalised concentrations as a function of downstream distance at the centreline between plumes indicate that even though dilution at the merging height might be similar for UM3 and the CFD methods, higher discrepancies are observed closer to the source (see Figure 5-12). Overall, both UM3 and VISJET seem to estimate superior mixing, which could be a result of their simplifications of the merging process.

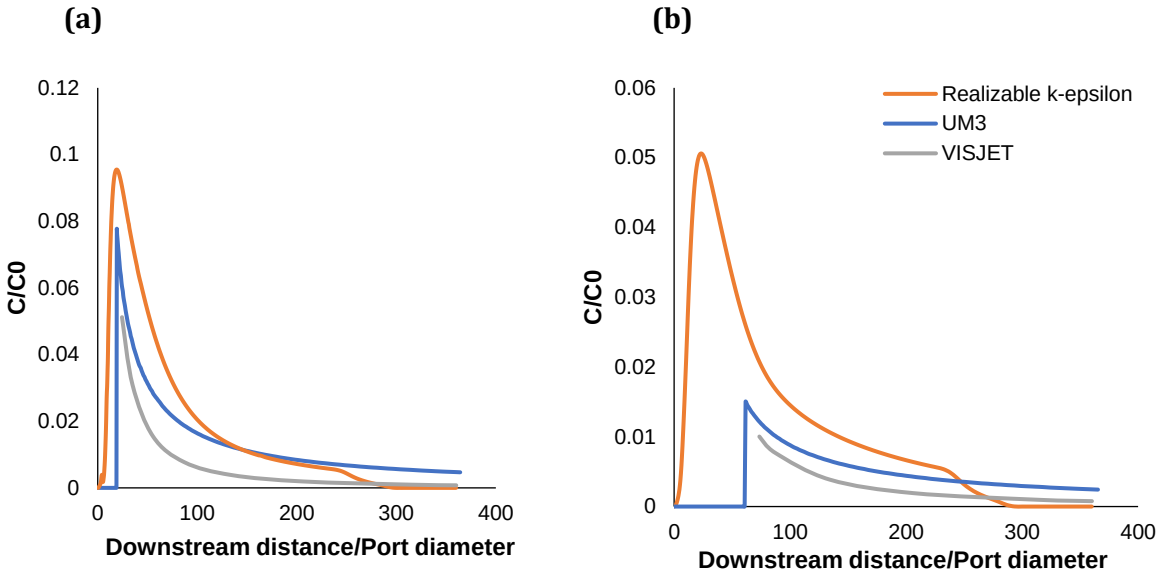

Figure 5-12. Comparison of predicted normalised concentration along the centreline of two equal plumes for cases with: **(a)** 3 cm and **(b)** 8 cm port spacing.

5.5.1.4 Turbulence parameters.

The spatial distribution of turbulence parameters, namely turbulence kinetic energy, turbulence dissipation and eddy viscosity are analysed in this subsection. From contour plots in the centreline plane of the flow after 60 seconds, the turbulence kinetic energy displays a mushroom-shaped spatial distribution, as shown in Figure 5-13a. The maximum turbulence kinetic energy was found to be located in the stem of the plumes, at a distance downstream of about 5 times the nozzle diameter. The turbulence kinetic energy continues to decrease further downstream and later increases at the cap (see Figure 5-13a). Maximum turbulence kinetic energy was observed to decrease with port spacing and is found to be in the range between 1.69×10^{-3} and 1.8×10^{-3} m^2/s^2 for the cases studied. A similar tendency was observed by He et al. (2018), who compared the effects of port spacing on two vent plumes discharging in a stratified ambience. A reason for such decrease as port spacing increases is the reduced interaction between plumes near the discharge nozzles.

Like turbulence kinetic energy, turbulence dissipation shows its highest value in the plume stem, as shown in Figure 5-13b. It is also observed to decrease with port spacing, coinciding with findings by He, et al. (2018). For the cases studied, it was found to be between 2.8×10^{-2} and 2.7×10^{-2} m^2/s^3.

Contrary to the distribution of turbulence kinetic energy and turbulence dissipation, the maximum eddy viscosity is found at the cap of the flow, as can be observed in Figure 5-13c, increasing with port spacing. It ranged between 0.82 and 0.845 Pa·s for the cases studied. Displaying its maximum value a the plume cap indicates the higher advection and mixing taking

place in this location at the time, mixing that in fact increases when the plumes are located more separate from each other.

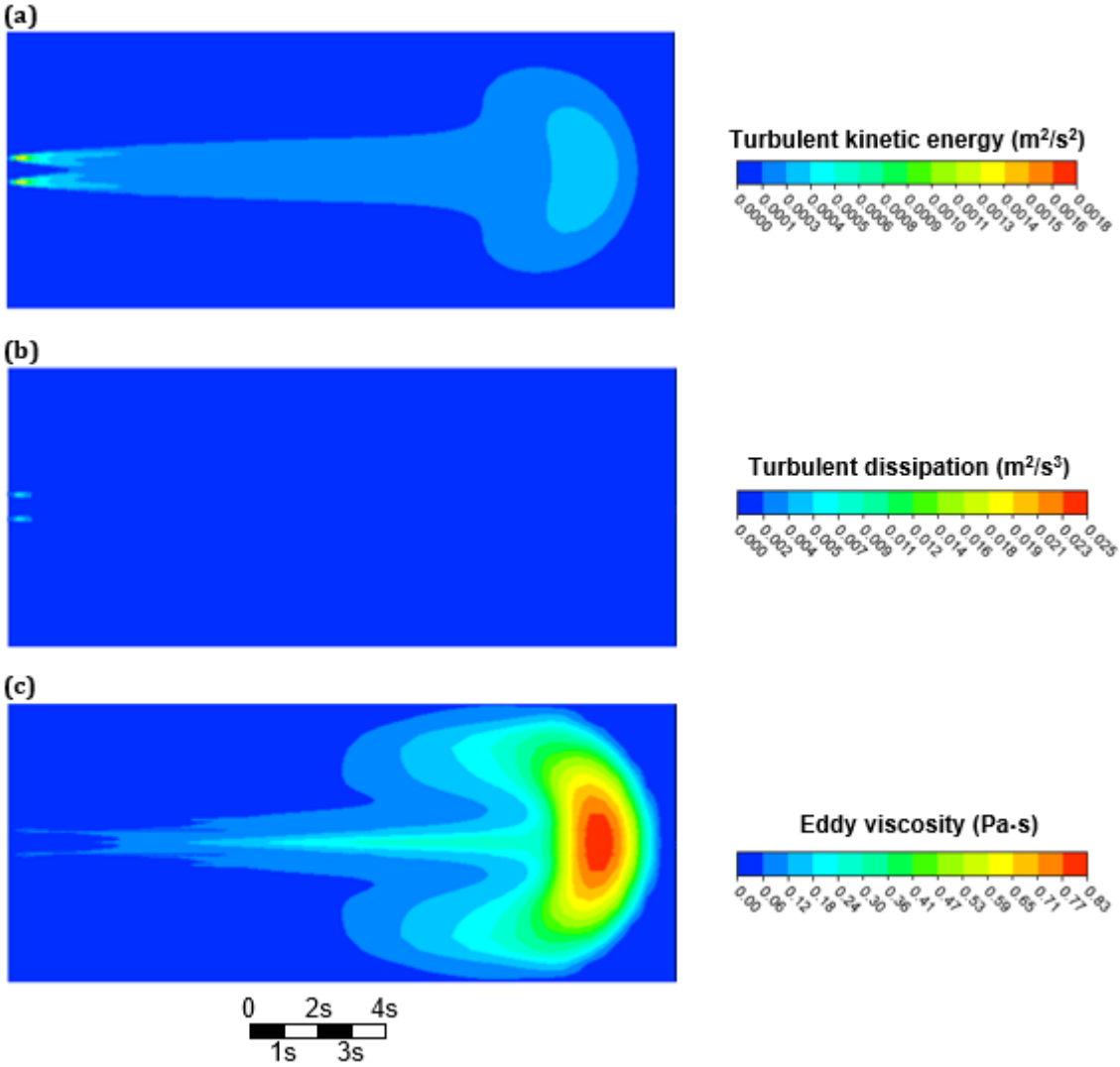

Figure 5-13. Contours of turbulence parameters at the centreline plane for a case of two equal plumes exiting from ports spaced 5.5 cm apart after 60 seconds: **a)** turbulence kinetic energy; **b)** turbulent dissipation; **c)** eddy viscosity. Please note that the graphs have been rotated for easier comparison and they do not show the complete vertical axis.

5.5.2 Unequal plumes.

5.5.2.1 General flow characteristics.

Experimental studies on the interaction between unequal plumes have found that their merging depends not only on the spacing between the ejecting ports but also on the ratio between their initial buoyancy sources (Gebhart et al., 1976; Kaye & Linden, 2004). In this study, a group of cases were modelled, varying the ratio of the buoyancy sources between 0.1 and 0.9. This implies that for the case with the biggest buoyancy difference, one of the plumes had an initial buoyancy source 10 times higher than the other.

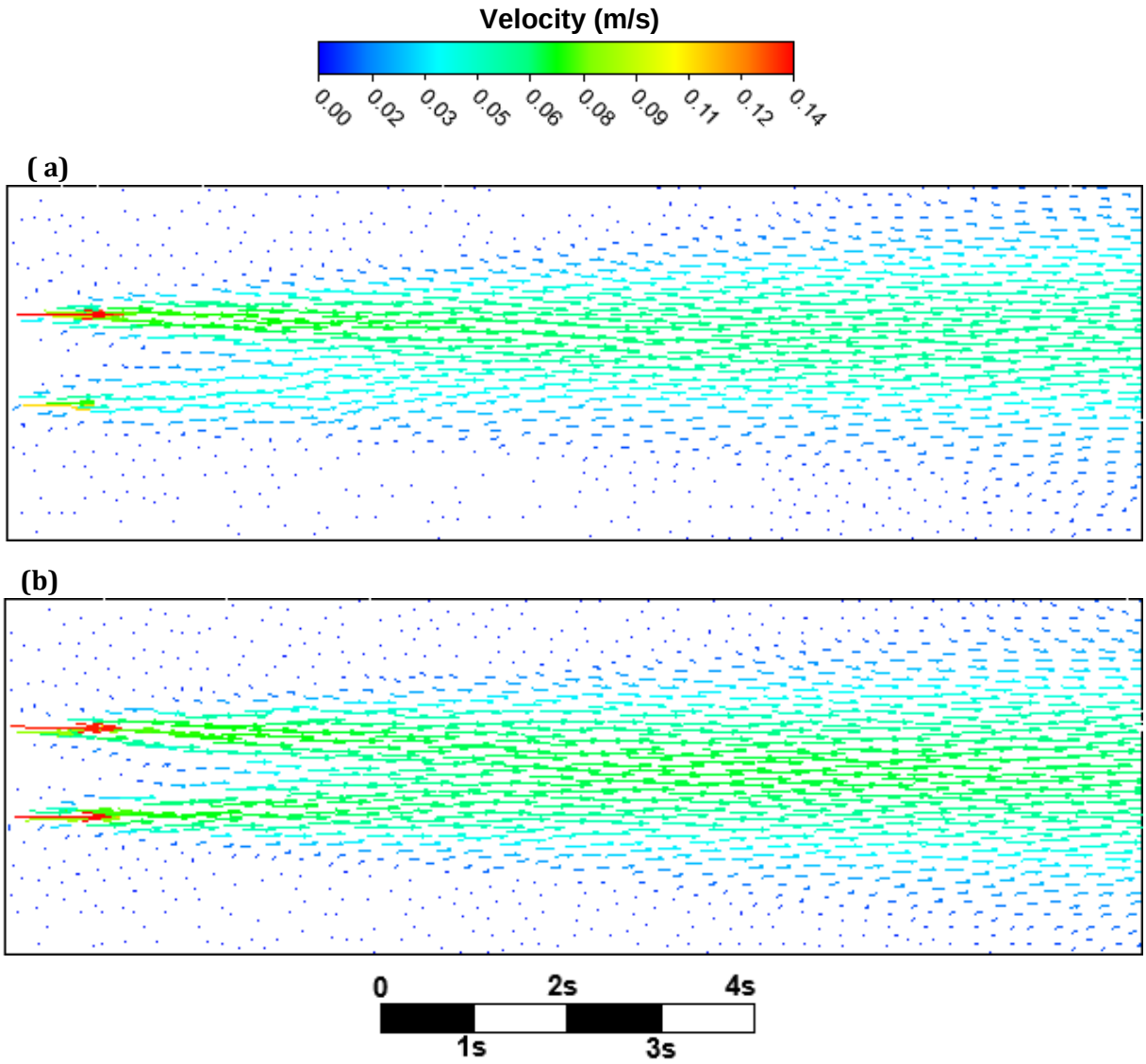

Figure 5-14. Vectors of velocity of two cases with same spacing (s = 5.5 cm) and different buoyancy ratio, after 60 seconds: **a)** buoyancy ratio of 0.2 and **b)** buoyancy ratio of 0.8. Please note that the graphs have been rotated for easier comparison and they do not show the complete vertical axis.

Observations from the vectors of velocity and the contours of normalised velocity and pollutant concentration at different times show that in unequal plumes, it is the plume with the lowest initial buoyancy source that deflects more strongly towards the other. In cases with very low buoyancy ratios, the plume with the highest initial buoyancy follows an almost vertical trajectory, as can be observed in Figure 5-15 and Figure 5-16. On the contrary, as the buoyancy ratio increases, the deflection on the plume with the highest buoyancy source also increases. This can be identified in the comparison of the two cases shown in Figure 5-14.

Like we observe in equal plumes, three main stages can be identified in the merging of unequal plumes. Initially, the plumes behave as if they were independent, as can be observed in Figure 5-15a and Figure 5-16a. As they approach each other, the plume with the lowest initial buoyancy starts deflecting towards the other, drawn by its entrainment field, as seen in Figure 5-15c and Figure 5-16c. As they start interacting, the cap of the plume with the highest buoyancy shifts towards the opposite side of the adjacent plume (see Figure 5-15d-e and Figure 5-16d-e). As they

continue to merge, the overall trajectory of the flow becomes vertical, and the deflection in the plume cap disappears, as in Figure 5-15f and Figure 5-16f.

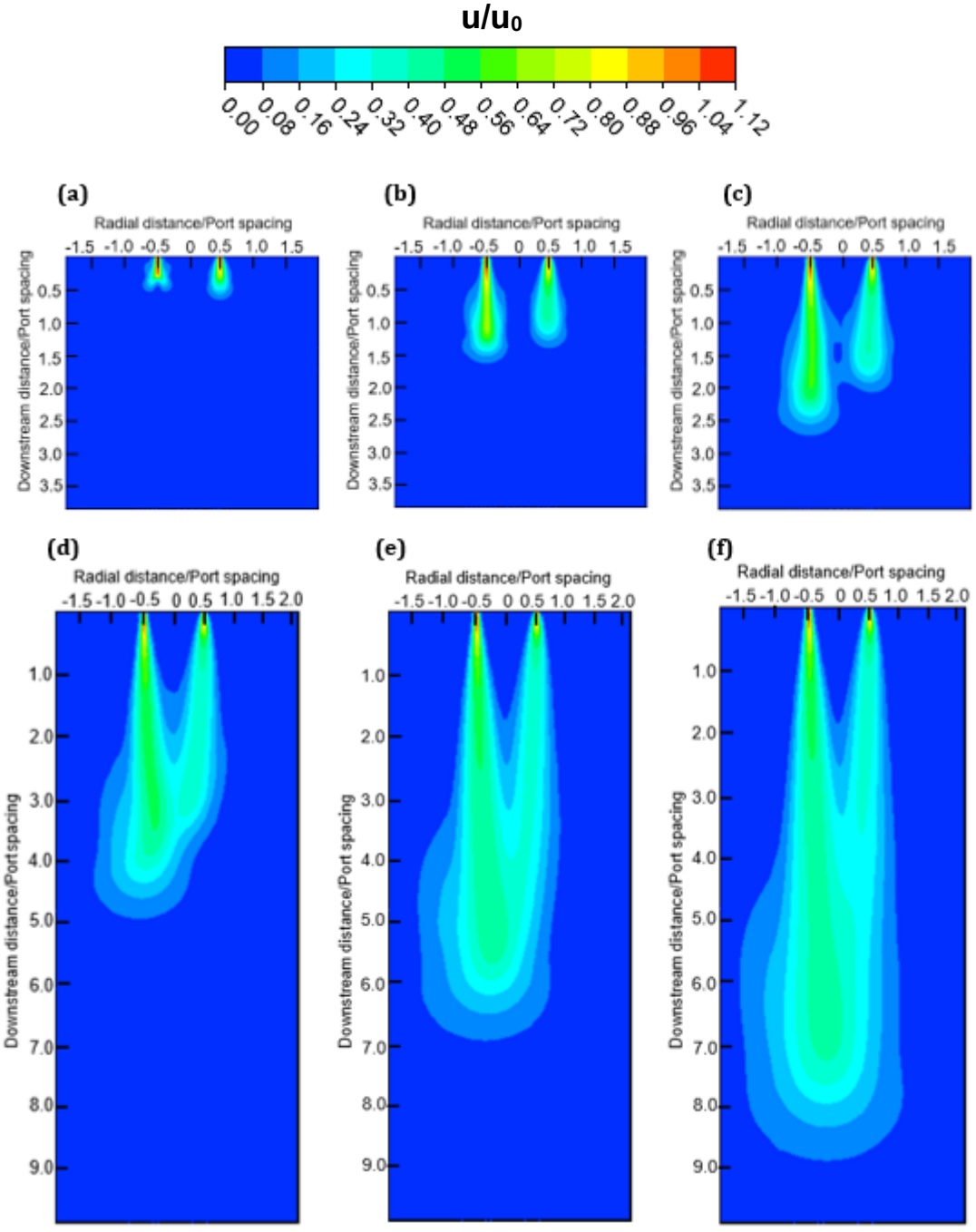

Figure 5-15. Time evolution of the non-dimensionalised velocity magnitude of two unequal descending plumes spaced 5.5 cm apart. The buoyancy ratio between the plumes is 0.2. **a)** t = 1 s; **b)** t = 3 s; **c)** t = 5 s; **d)** t = 10 s; **e)** t = 15 s and **f)** t = 20 s. These graphs do not show the complete domain along vertical axis.

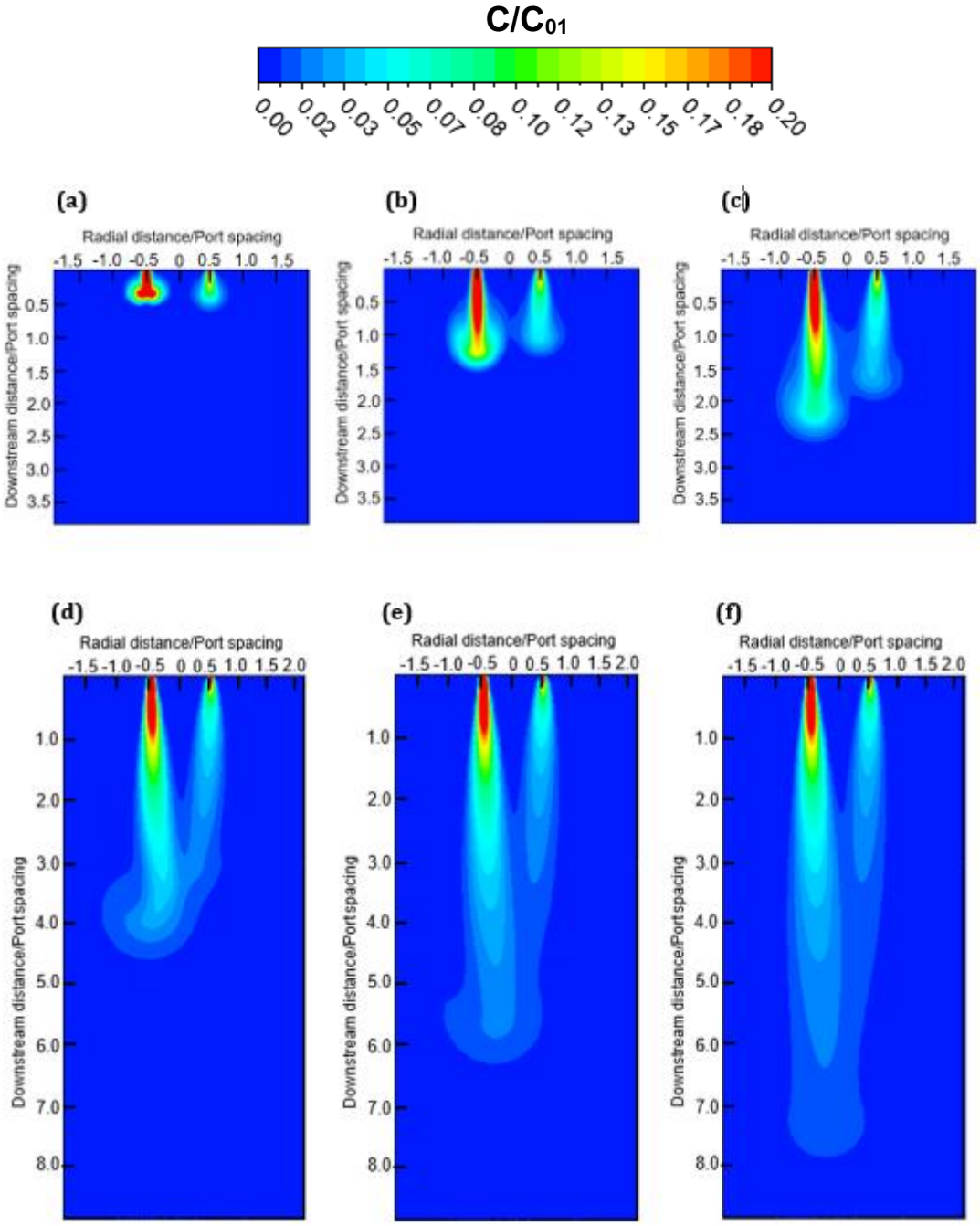

Figure 5-16. Time evolution of the non-dimensionalised pollutant concentration of two unequal descending plumes spaced 5.5 cm apart. Pollutant concentration is normalised by the highest initial pollutant concentration. The buoyancy ratio between the plumes is 0.2. **a)** t = 1 s; **b)** t = 3 s; **c)** t = 5 s; **d)** t = 10 s; **e)** t = 15 s and **f)** t = 20 s. These graphs do not show the complete domain along vertical axis.

5.5.2.2 Merging height.

Kaye and Linden (2004) defined the merging height of equal plumes as the location in which we can no longer see two peaks in the buoyancy profiles. However, in the case of plumes with unequal buoyancy fluxes, this definition no longer holds. In such case, Kaye and Linden (2004) propose the merging height to be defined as the location in which there is no longer a trough between two peaks in the buoyancy profiles (see Figure 5-17).

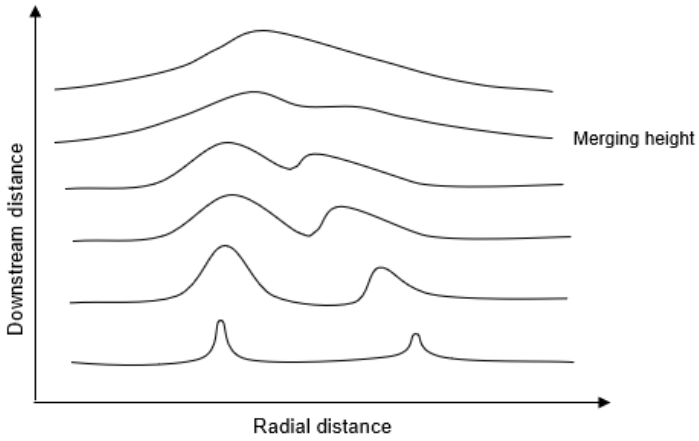

Figure 5-17. Schematic of merging height for unequal plumes according to Kaye and Linden (2004).

To determine the merging height for the cases in the study, the concentration distribution of the plumes was plotted at different locations downstream (see Figure 5-18a). The location downstream was normalised by the corresponding port spacing, and the local concentration was normalised by the highest initial salinity concentration, C_{01}. Similar behaviour to that observed by Kaye and Linden (2004) in their experimental study was identified. Closer to the sources, the plumes show two parallel peaks, one higher than the other. As they approach each other, the smallest peak deflects towards the highest. Further downstream, the smallest peak disappears, resulting in an asymmetric profile, with the highest concentration located on the side of the plume with the highest initial buoyancy. The same behaviour is observed for the plots of velocity distribution at different distances downstream, as seen in Figure 5-18b.

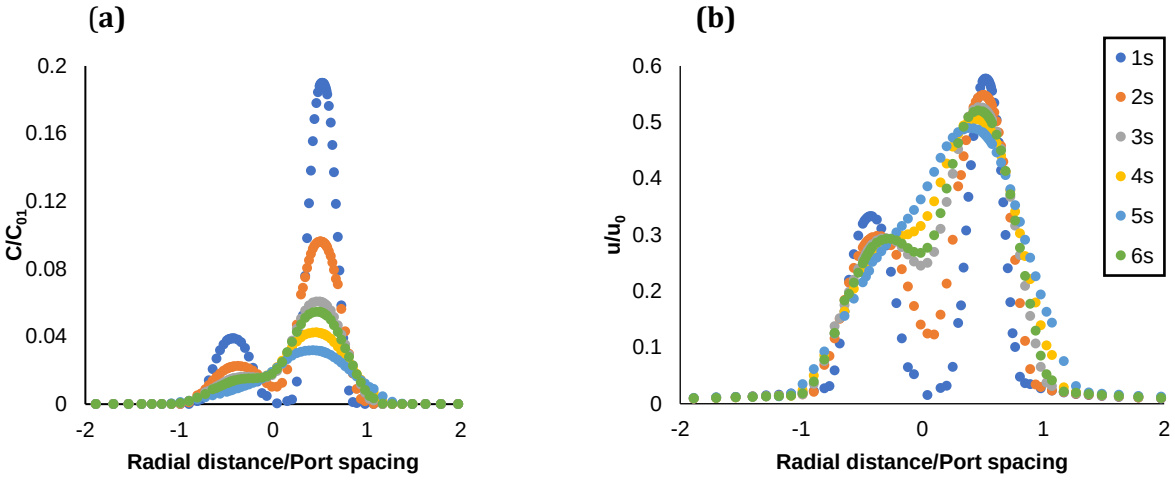

Figure 5-18. Distribution of **(a)** scalar concentration (salinity) and **(b)** velocity magnitude at different locations downstream for a case with initial port spacing of 5.5 cm and buoyancy ratio of 0.2.

Figure 5-19a shows the contours of non dimensionalised salinity for plumes with a buoyancy flux ratio of 0.2. This means that one of the plumes has 5 times the initial source of buoyancy of its adjacent one. Concentrations are normalised by C_{01}, corresponding to the initial salinity

concentration of the plume with the highest buoyancy flux. Red areas in the figure correspond to the location in which the non dimensionalised salinity is in the range of 0.2 to 1.

The realisable $k-\varepsilon$ model is able to predict the merging height location for unequal plumes, following a similar trend to that observed in the experiments (see Figure 5-19). However, over predictions are observed for higher buoyancy ratios. Nonetheless, this RANS model produces more accurate predictions of the merging height for lower buoyancy flux ratios when compared to the entrainment model developed by Kaye and Linden (2004), using the recommended entrainment coefficient of 0.09.

Most commercial software packages such as Visual Plumes (which includes UM3, NRFIELD, amongst other models) (Baumgartner, et al., 1994) and VISJET (Lee & Cheung, 1990), do not allow the modelling of unequal plumes. Hence, approximations should be made at the time of modelling, such as the use of equivalent equal plumes. However, this would not account for the deflection in the trajectory of the plumes that results from their different initial buoyancy sources.

The capacity of the realisable k-ε model to predict the dynamics of unequal plumes is hence particularly useful for the modelling of real-life marine outfalls, interactions between adjacent smokestacks and other engineering applications in which not all ports may be designed with the same geometry.

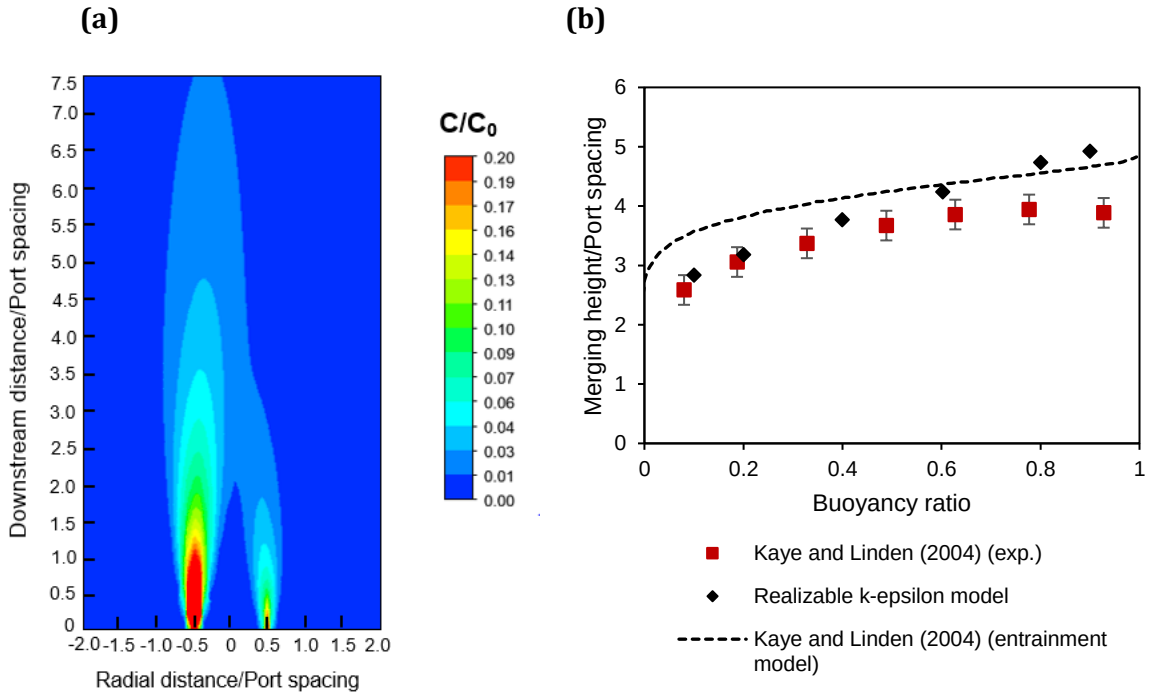

Figure 5-19. Merging height locations for equal plumes: **(a)** Contours of non dimensionalized salinity for two unequal plumes with port spacing of 5.5 cm and buoyancy flux ratio of 0.2; **(b)** Comparison of modelled and experimental merging height locations for unequal plumes. In the contour graph, the vertical axis is reversed and only a portion of the domain along this axis is shown.

5.6 CONCLUSIONS.

This chapter has studied the process of coalescence between plumes with both equal and unequal initial sources of buoyancy, by simulating scenarios at laboratory scale available in the literature. These simulations were conducted by implementing RANS turbulence models, namely realisable and RNG $k-\varepsilon$ model and $k-\omega$ SST. The main findings from this study are listed below:

- Comparisons with experimental data confirm that RANS models can accurately predict the physics of the interaction between equal plumes, including the deflection in the trajectory of the plumes due to the presence of the other. No considerable difference was found between the turbulence models studied, which include the realisable and RNG $k-\varepsilon$ model and $k-\omega$ SST. However, RANS models seem to slightly overestimate the location of the merging height for equal plumes.
- For equal plumes, dilution at the merging height increases quadratically with port spacing.
- When plumes with unequal sources of buoyancy interact, it is mainly the plume with the lower initial buoyancy that tends to deflect towards the other and more prominent deflection is observed as the buoyancy ratio between plumes decreases, coinciding with findings from experimental work conducted by Kaye and Linden (2004). Higher accuracy was observed for the CFD prediction of the merging height location for unequal plumes, especially those with lower buoyancy ratios.
- An advantage over traditional entrainment models such as UM3 and VISJET is identified by the use of RANS models. This is due to their capacity to simulate the deflection in the trajectory of the plumes as they approach each other. This aspect is of particular importance when dealing with real-scale marine outfalls, as will be addressed in the following chapter.

6 MULTIPLE PORT DISCHARGES FROM TEE-SHAPED RISERS AT REAL-LIFE SCALE. CASE STUDY: CARTAGENA DE INDIAS, COLOMBIA.

6.1 INTRODUCTION.

In previous chapters, the behaviour of both single and multiple port discharges at laboratory scale has been studied. CFD techniques have been used to predict the trajectory and dilution of buoyant jets in stagnant unstratified environments and the results obtained have been compared with available experimental data from the literature.

This chapter aims to understand the behaviour of multiple port discharges from Tee-shaped risers in both stagnant and flowing waters. For this purpose, the Cartagena marine outfall has been selected as a case study. A detailed description of this outfall is presented in the following subsection. Near field simulations of this outfall were conducted applying the methodology tested in previous chapters. Different scenarios with varying discharge and environmental conditions are modelled, in order to understand their effect on the trajectory and dilution of the effluent plumes, as well as the advantages and limitations of using CFD techniques for the simulation of real-life scale marine outfalls.

6.2 CARTAGENA MARINE OUTFALL SYSTEM.

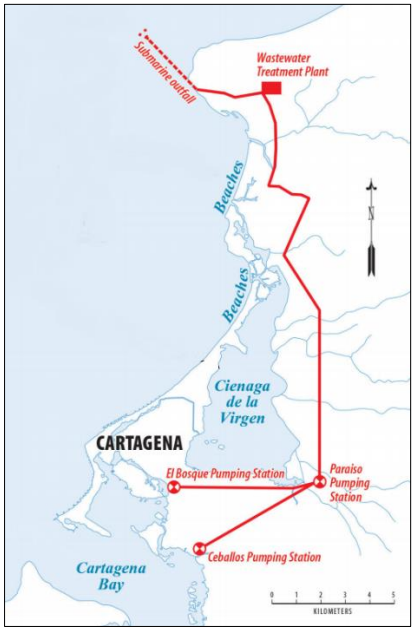

Figure 6-1. Location of the Cartagena's marine outfall system. Source: World Bank (2014).

Cartagena is a city located in the northern Coast of Colombia, at coordinates 10°25' North, 75°32' West. For more than three decades, untreated wastewater in Cartagena had been discharged into the Cartagena Bay (receiving 30%), a lagoon called Ciénaga de la Virgen (receiving 60%), and the in-city water courses that eventually reach the Bay and the Ciénaga (10%) (see Figure 6-1). Industrial wastewater from the industrial area of Mamonal was discharged directly into the

Cartagena Bay after minimal treatment. Such discharges caused an ecological decline to the rich ecosystems of these water bodies, including mangrove forests, fisheries, sea-grasses and coral reefs (World Bank, 2014). In order to prevent further damage to these ecosystems and ensure their restoration, by the early 2000s, Cartagena received a US$ 85 million loan from the World Bank to implement a wastewater master plan, with these main objectives:

- Convey the wastewater previously discharged into the Cartagena Bay and Ciénaga de la Virgen to the new central pump station.
- Pump all Cartagena's collected wastewater to a new treatment plant located 19 km to the north.
- Treat the wastewater at the new treatment plant and discharge into the Caribbean Sea through a submarine outfall.

The original design of this submarine outfall was planned in the year 2000, based on extensive monitoring of the oceanographic conditions in the selected area of discharge and the projected wastewater flow. This original design included:

- A submarine outfall located at Punta Canoa, 2.85 km long, 2 m diameter, discharging at a depth of 20 m, with a total discharge capacity of 4 m^3/s in 2025.
- A diffuser 500 m long with 27 T-shaped risers spaced every 20 m, each riser containing 2 ports for a total of 54 ports with a diameter of 20 cm. The diffuser was to be aligned 115° to true North.

In the year 2013, a consultant was hired to conduct simulations to revise the design of the outfall using the semiempirical model, NRFIELD. The purpose of this revision was to ensure that dilution rates were in the order of 100:1 85% of the time. The revised design proposed an outfall of 92 Tee-shaped risers spaced every 4 m and a 100 mm diameter. The length of the diffuser was designed to be 364 m.

Despite the extensive simulations that had been undertaken throughout more than 10 years, the constructed outfall does not match any of the designs which had been previously tested with the NRFIELD modelling approach. Instead, an outfall with a total of 102 Tee-shaped risers with 204 outlet ports with a diameter of 100 mm was constructed. Two additional outlet ports are in the closed end of the pipe, with a diameter of 200 m. The spacing between ports is unclear. For the simulations performed in this chapter, a diffuser length of 500 m was assumed, meaning a port spacing of 5 m. The two ports located at the end of the pipe were not considered for these simulations.

Added to the changes described above, the alignment of the Tee-shaped risers was also altered. As opposed to the conventional alignment in which each riser is located parallel to the other, in the Cartagena outfall, all risers were aligned with the diffuser and with each other, as shown in Figure 6-2. A schematic comparison of the original design from 2000 versus the constructed outfall is shown in Figure 6-3.

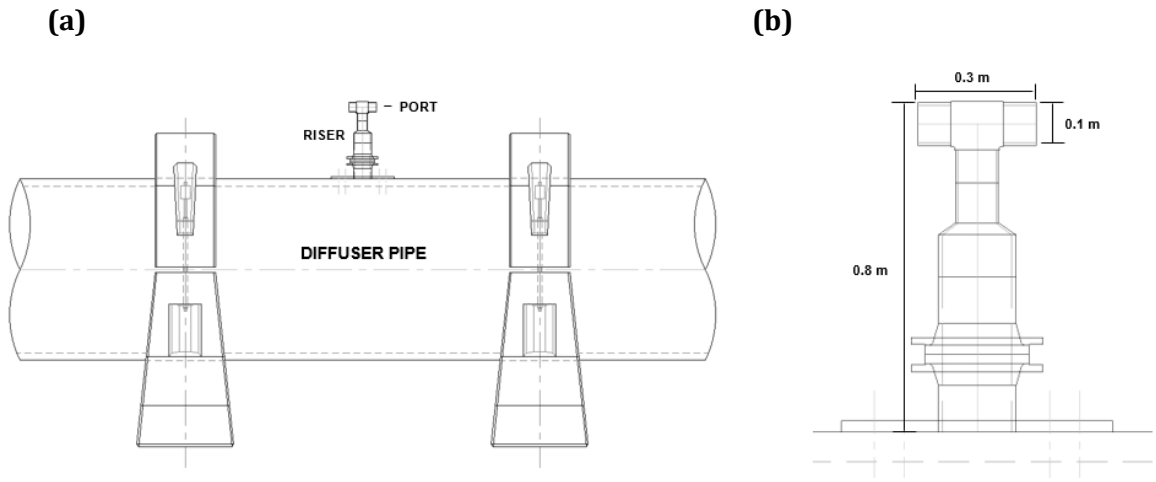

Figure 6-2. a) Lateral view of Cartagena marine outfall diffuser with riser; **b)** riser dimensions. Source: Aguas de Cartagena.

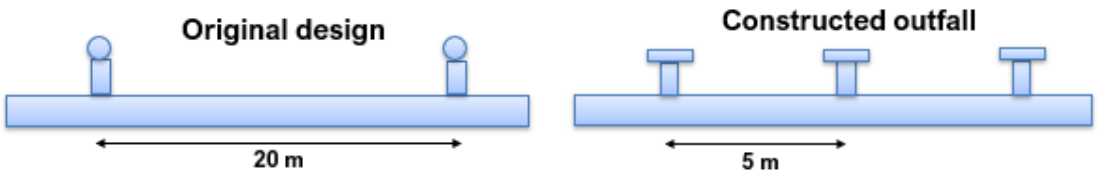

Figure 6-3. Schematic of **a)** original design from 2000 (port alignment A); **b)** outfall as constructed (port alignment B).

Since the commissioning of the Cartagena marine outfall, regular monitoring of the flow and quality of the effluent from the wastewater treatment plant has been conducted. Flow measurements are conducted on a daily basis at the wastewater treatment plant, whereas water quality parameters such as BOD, total and faecal coliforms, enterococci, sediments, amongst other parameters are measured on a monthly basis.

Data of average flow per month is shown in Figure 6-4. Discharge flow tends to be higher in September and November, coinciding with the rainy season. Maximum average flow values observed are in the order of 3.4 m^3/s, whereas the lowest observed values are around 1.8 m^3/s. Based on this monthly data, it can be said that the average annual flow increased 20% from 2013 to 2016.

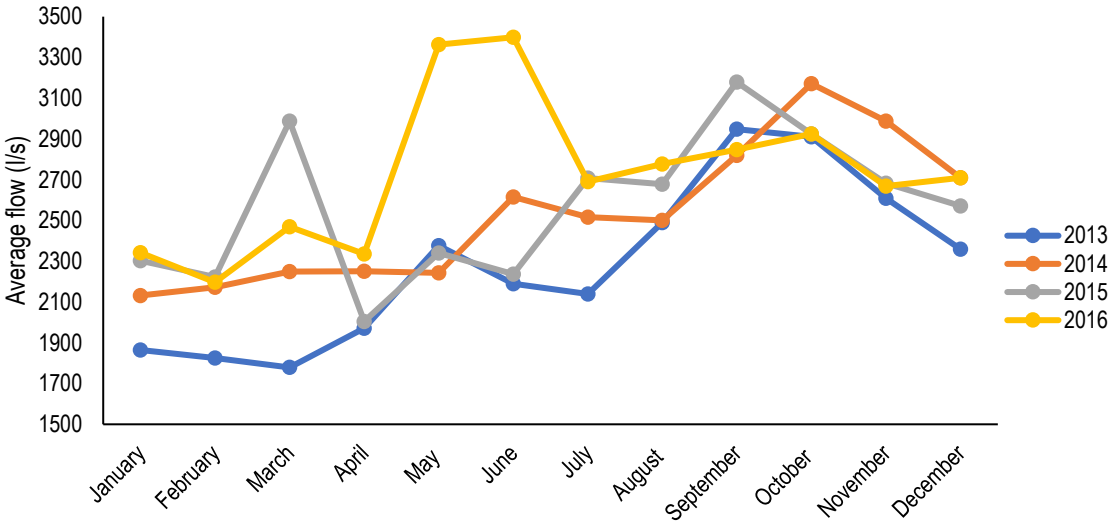

Figure 6-4. Average monthly flow measured at the outlet in the Cartagena wastewater treatment plant from 2013 to 2016. Source: Aguas de Cartagena (2017).

In the following subsections, a summary of available monitoring data from current velocity and direction and density stratification in the area of the Cartagena marine outfall is presented.

6.2.1 Current velocity and direction.

Since the selection of the site for wastewater discharge, various monitoring programmes have been conducted, measuring velocity magnitude and preferred direction of the currents in the area. The first monitoring programme was conducted from January 1998 to February 1999, using an Acoustic Doppler Current Profiler (ADCP), located at a water depth of 17.7 m, at about 2.5 km from the coast.

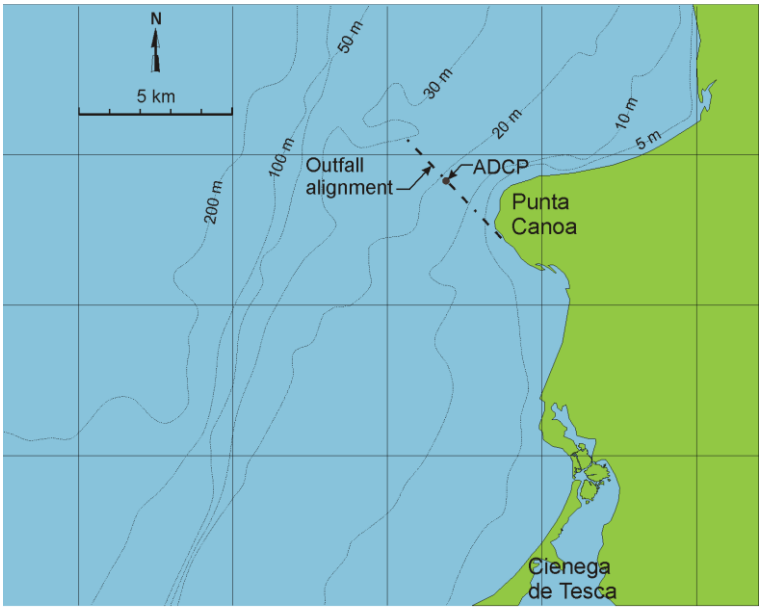

Figure 6-5. Location of ADCP for the January 1998 monitoring programme. Source: Roberts (2003)

During this period, it was observed that the preferred direction of the currents was along an axis approximately 25° to true North. The deeper currents are very uniform in direction whereas the upper currents tend to be shifted somewhat counterclockwise. Seasonal variations were observed, with the current moving towards South East from February to early May. From early May, the currents switched towards North East, with oscillations to South East. The direction of the currents is uniform along the water depth.

Based on the preferred current direction observed in this initial monitoring programme, the designer team proposed that the outfall should be aligned 115° to true North, so that the current was always perpendicular to the ports alignment, as it has been proved to result in maximum dilution (Roberts et. al. 1989). However, the actual direction in which the outfall was aligned was 137° to true North.

Further monitoring was conducted from June 2014 to May 2015. A Rotor Current Meter (RCM) was moored at coordinates 10° 34' 23.8" N, 75° 31' 48.3" W, at a water depth of 16 m (Novoa, 2015). The RCM measured current velocity and direction every 15 minutes, although only average monthly values are available today.

Measurements with the RCM found that average monthly current values at this depth range between 0.1 to 0.25 m/s, being September and October the months with lower current velocities. The prevalent current direction was NE.

The most recent monitoring of current velocity and direction took place in the year 2018. It was conducted by the University of Cartagena, using two current profilers Aquadopp by Nortek moored at a water depth of 9 and 20 m, respectively.

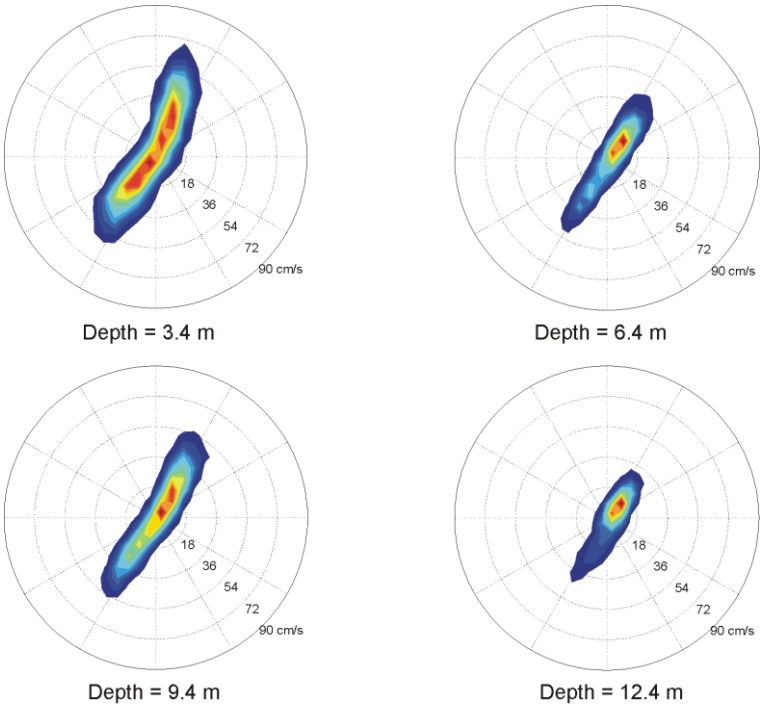

Figure 6-6. Histogram of current velocity and direction from January 1998 to February 1999.

Current velocity and direction measurements for the period between August 25th 2018 and October 10th 2019 have been extracted from the current profiler located at a depth of 9 m. Measurements show that the current has a preferred direction towards N-NE at water depths between 7.8 m to 9 m. Closer to the surface, the prevalent current direction is N-NW. Oscillations towards SW, with an angle between 190° to 200° to true North, are observed, although this occurs less than 2% of the time in the period studied.

Average current velocities from the period between August and October 2018 are 0.15, 0.18, 0.22 and 0.25 m/s at water depths 7.8, 6.8, 5.8 and 4.8 m, respectively. It is observed that water velocities are higher as we get closer to the surface.

6.2.2 Density stratification.

From January to June 1998, density stratification was measured by means of a profiling instrument deployed at various locations off the Cartagena coast. A total of 188 profiles were obtained, showing a relatively weak density stratification, varying from 0 to up to 0.9 kg/m^3 at water depths of up to 60 m. The density difference is mainly due to temperature variations, which can be up to 1°C (See Figure 6-7).

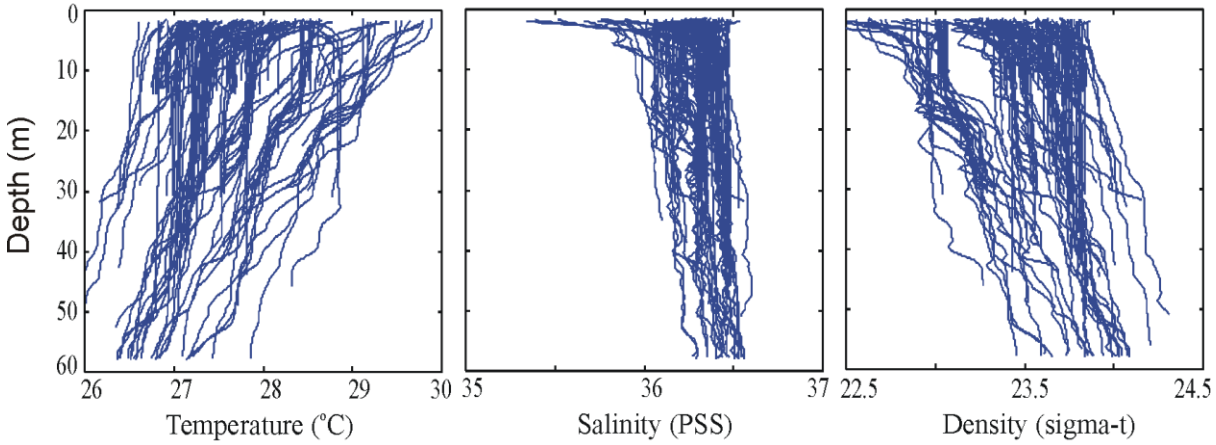

Figure 6-7. Temperature, salinity and density stratification measured from January to June 1998. Each line represents a measured profile, summing up to a total of 188 lines.

More recent measurements conducted in the area of study by the University of Cartagena between April 2018 and December 2018 corroborate these findings. Seawater temperature and salinity were measured at the surface and bottom at varied locations, finding temperature differences no larger than 0.5°C between surface and bottom and salinity differences no larger than 1.5 ppt.

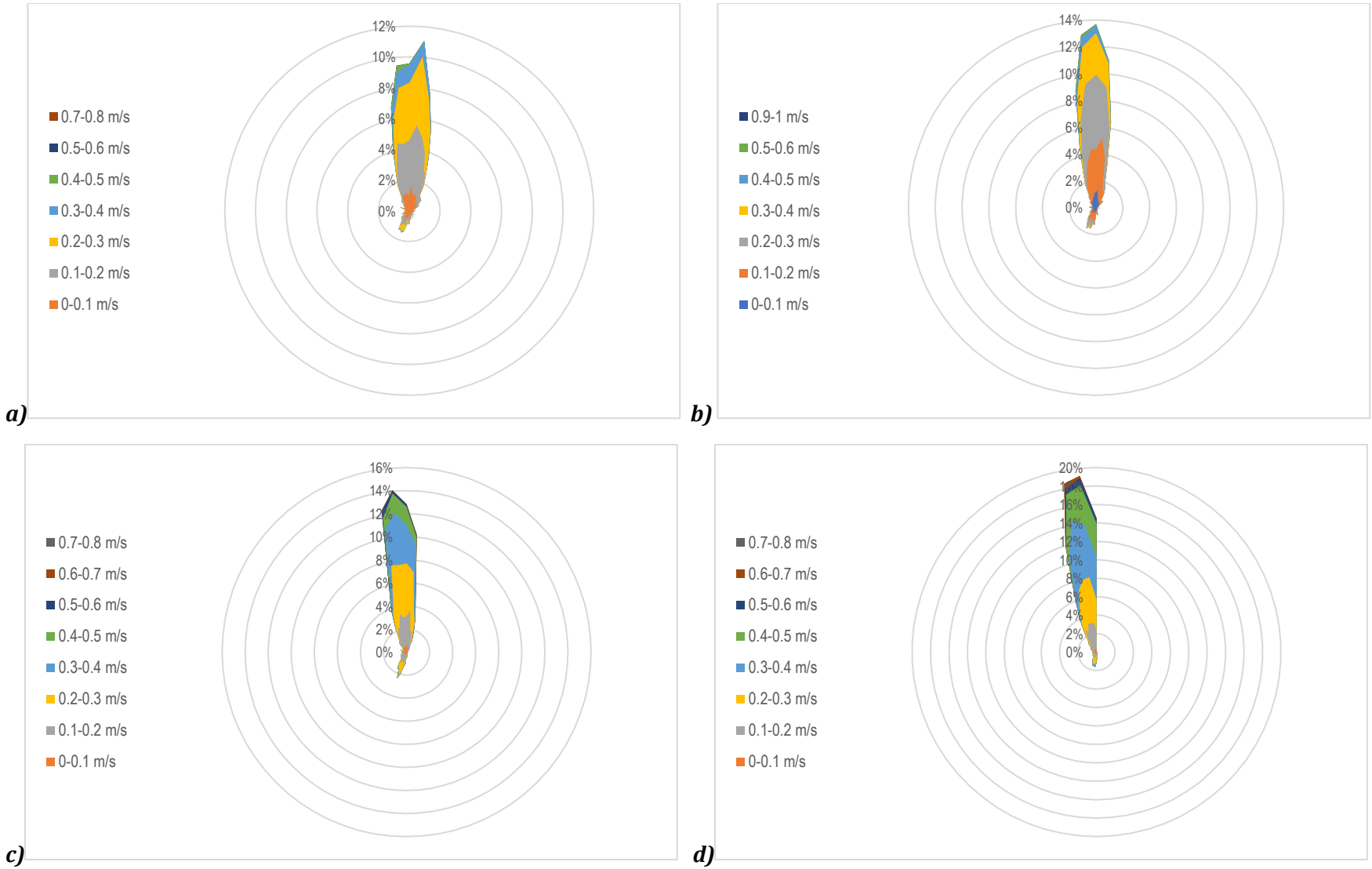

Figure 6-8. Histogram of current velocity and direction at water depth: **a)** 7.8 m**; b)** 6.8 m**; c)** 5.8 m; **d)** 4.8 m. Data obtained from August to October 2018. Source: University of Cartagena, 2018.

6.3 DESCRIPTION OF MODELLING CASES.

The time-varying environmental and discharge conditions in a real-life marine outfall result in an infinite number of potential scenarios. For this reason, it is important to prioritise those scenarios that could be considered more critical for the dilution of the effluent in the receiving water, which is the ultimate goal of this type of disposal system.

This chapter focuses on answering two main questions:

1) What are the effects of different discharge and environmental conditions on the merging and mixing of buoyant jets from Tee-shaped risers; and
2) what is the recommended framework for the CFD modelling of marine outfalls at a real-life scale?

By answering the first question, it is also possible to understand the effects that the different changes that were done to the original design of the Cartagena marine outfall could have had on the mixing capacity of the outfall. To answer these questions, a total of 14 different modelling scenarios were selected, varying current velocity and direction, density stratification, discharge flow rate, port alignment, size and spacing.

Furthermore, by assessing this variety of scenarios, it is also possible to construct a comprehensive framework for decision-making. This framework would enable the designer to decide the most suitable CFD modelling approach to simulate real-life marine outfalls under different conditions, minimising its computational cost.

The following subsections include a detailed description of the different parameters that were varied for the simulations conducted in this chapter and the reasoning behind it.

6.3.1 Discharge flow.

According to the monitoring data available, the average flow per month ranged between 1.8 to 3.5 m^3/s. The total flow to be discharged was divided by the number of ports. According to the area of each port, the velocity ejecting from it was then calculated.

Considering that available data is of average values and that the flow may present peaks and low values during a given day, the values selected to assess the sensitivity to discharge flow were in the range of 1.6 m^3/s to 12.8 m^3/s. Although the values towards the higher end are very unlikely to happen in the case of the Cartagena marine outfall, they were tested in order to predict the maximum capacity of the outfall under critical conditions. The baseline flow rate value was assumed as 3.2 m^3/s.

6.3.2 Current velocity and direction.

According to monitoring data, current velocity magnitude varies with time and along the water depth. However, for the purpose of this study, a non-time varying and uniform current value is assumed. The values assumed for study are 0.1, 0.2 and 0.3, since the current is typically within this range. The baseline current magnitude was assumed as 0.1 m/s, since lower currents represent a more critical condition for mixing.

The current direction was mostly assumed perpendicular to the diffuser, as it is the direction in which the diffuser was meant to operate. However, based on recent current measurements from August to October 2018, the current preferred direction in this period was towards N-NW.

Assuming that the current has a direction of 0° to true North, the angle between the diffuser and the current is 43° (see Figure 6-9). The effect of this inclination angle was also evaluated.

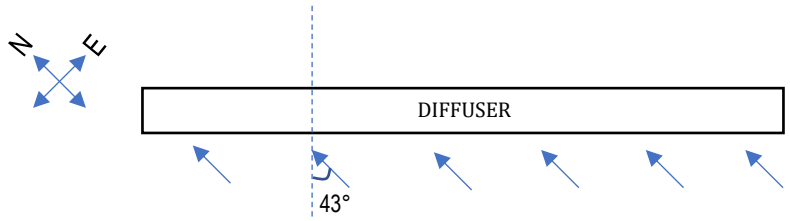

Figure 6-9. Schematic of angle of current in respect to the diffuser when the current travels towards North. Risers are oriented parallel to the diffuser as in port alignment type B.

6.3.3 Port spacing and alignment.

The port spacing defined in the Cartagena outfall is 5 m. On the other hand, the original design of the Cartagena outfall proposed spacing between ports of 20 m. To assess the effect of this change on the trajectory of the plumes and their dilution, port spacing values of both 5 and 20 m were simulated in this study.

Two different port alignments were studied: risers parallel to the diffuser (port alignment B) and risers perpendicular to the diffuser (port alignment A), as shown in Figure 6-3. Most cases are simulated with the risers parallel to the diffuser, as it is the arrangement in the Cartagena outfall; however, for studying the effects of alignment on the behaviour of the flow, the perpendicular riser alignment is also studied.

6.3.4 Port size.

The constructed Cartagena outfall consists of 204 ports with a diameter of 0.1 m. However, the original design proposed a larger diameter of 0.2 m. Most of the simulations in this chapter were conducted using a port diameter of 0.2 m. Nonetheless, additional simulations were conducted for a port size of 0.1 m, to compare the effects of different port sizes on the overall behaviour of the flow.

6.3.5 Density stratification.

In the area of discharge, water density is relatively uniform and the minimal differences in it respond to temperature differences as opposed to salinity differences. In order to assess the effect of this parameter on the trap height of the plumes, a temperature difference of 1°C was assumed for some cases with different current and discharge velocity.

6.4 Modelling methodology.

The following subsections summarise the methodology used for the simulation of multiple port diffusers with Tee-shaped risers. The CFD simulations on multiport buoyant jets were based on the solution of the unsteady Reynolds-Averaged Navier-Stokes equations (uRANS). Different turbulent closure models were tested, namely realisable and RNG $k-\epsilon$ and $k-\omega$SST. These CFD simulations were implemented in the finite volume-based commercial code ANSYS Fluent 18.2 (Ansys Inc., 2018). Transient simulations were conducted in all cases implementing the SIMPLE scheme for the pressure-velocity coupling. Second-order spatial discretisation schemes were

used for the continuity, momentum, turbulent kinetic energy, turbulent diffusivity and advection-diffusion equation. The governing equations solved are described in detail in section 3.2.

6.4.1 Model domain.

The Cartagena marine outfall has a 500 m diffuser with a total of 102 Tee-shaped risers. However, the simulation of the whole extension of the diffuser using CFD techniques would have a very high computational cost. In order to simplify the simulation, only five T-shaped risers were modelled, assuming that each is representative of 3 types of risers that can be found in a diffuser (see Figure 6-10). This classification was made based on how merging between adjacent ports occurs. Type A risers are located on the edge of the diffuser, which means they are only 2 of the 102 risers installed in the Cartagena marine outfall. Type A risers may be affected by lateral effects due to the current. If the spacing between risers is small enough that the current cannot flow between risers, such current will become faster on the edge of the diffuser.

A type B riser is located between an edge riser and a type C riser. Like edge risers, only 2 risers in the Cartagena marine outfall are type B. Type C are central risers, and current lateral effects can be considered irrelevant. The merging point location and subsequent dilution for each plume will hence depend on the type of riser from which they come. We assume that 98 of the 102 Cartagena risers are type C.

Results from the discharge of the 10 ports simulated (see Figure 6-10) can then be scaled to the real number of ports present in Cartagena. This can be done by identifying the equivalent area and concentration profiles that each type of riser represents. This area can then be multiplied by the corresponding number of risers.

It could be argued that since most of the ports in the Cartagena outfall are type C, edge effects can be neglected, and a simulation of three risers (or one riser, with two symmetry planes to the sides) could be enough; however, in the case of a current that is inclined in respect to the riser alignment, symmetry is no longer conserved and the location of the riser plays an even more important role on the behaviour of its corresponding plumes.

For the simulations presented in this chapter, the size of the domain to study varied depending on the corresponding port spacing and water depth for each scenario. For most cases, a water depth of 22 m was used and risers were located every 5 m, as in the Cartagena marine outfall. This meant that the domain in study had typical dimensions of 100 x 80 x 22 m. To reduce computational time, only half of the domain was modelled using a symmetry plane that divided the type C riser in two equal parts. Exceptions applied for the cases in which the presence of an inclined current meant that the flow was no longer symmetric. For some cases where the current velocity was higher, resulting in a larger near field, the domain was extended in the downstream direction.

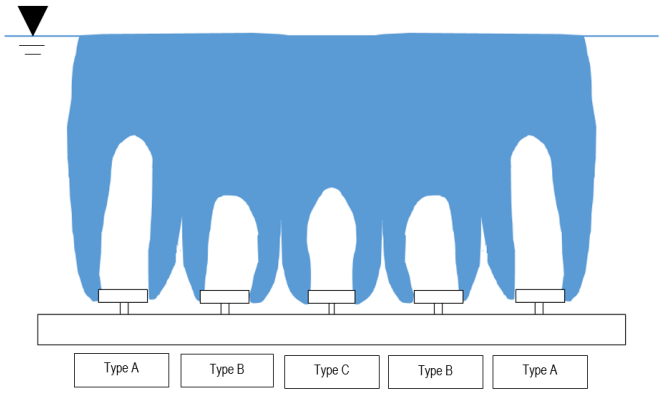

Figure 6-10. Schematic of multiple port discharge in a stationary unstratified environment and riser classification according to its position in the diffuser.

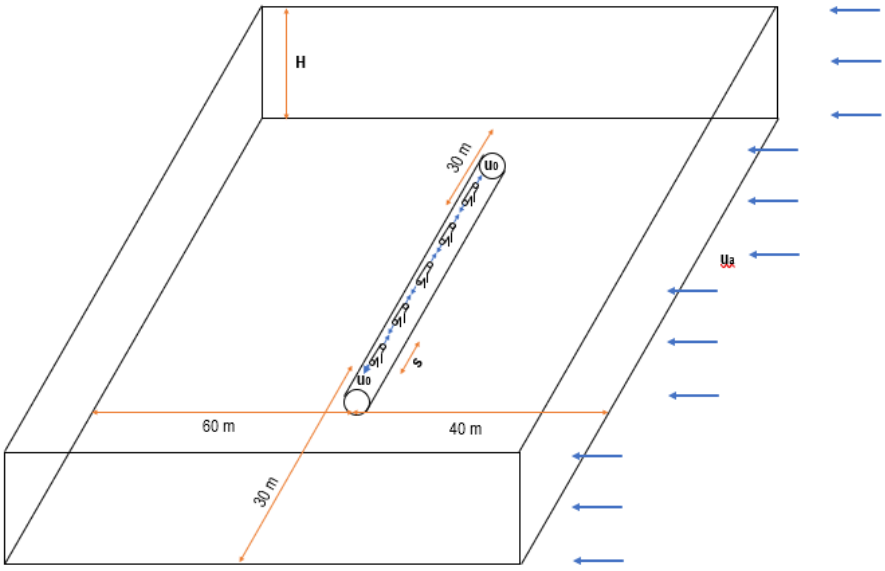

Figure 6-11. Schematic of the typical domain used for the Cartagena marine outfall simulations.

6.4.2 Meshing approach.

In order to ensure the mesh independence of the results, a similar approach to that described in section 3.3 was used and the performance of initial meshes ranging between 0.5 to 4.4 x 10^6 elements was evaluated. The most cost-efficient meshes that provided mesh independence paired with the solution-based adaption were selected. Depending on the spacing between ports and whether a symmetry plane was used, the size of the selected meshes ranged between $7x10^5$ to $1.5x10^6$ elements. The most common mesh, which had a port spacing of 5 m and used a symmetry plane, had a size of $7x10^5$ elements and is shown in Figure 6-12. Each case was run until the plume reached the surface and achieved a steady-state, which took between from 300 to 500 seconds for the cases studied. Once the plume reaches the surface and has reached steady-state, the mesh is adapted in two stages. The first adaption was conducted in those areas in which the normalised pollutant concentration was higher than 0.001. A second adaption was conducted in those areas where the normalised pollutant concentration was higher than 0.02. An example of an adapted mesh for a case with no current and initial port velocity of 0.5 m/s (total flow of 3.2 m^3/s) is shown in Figure 6-13.

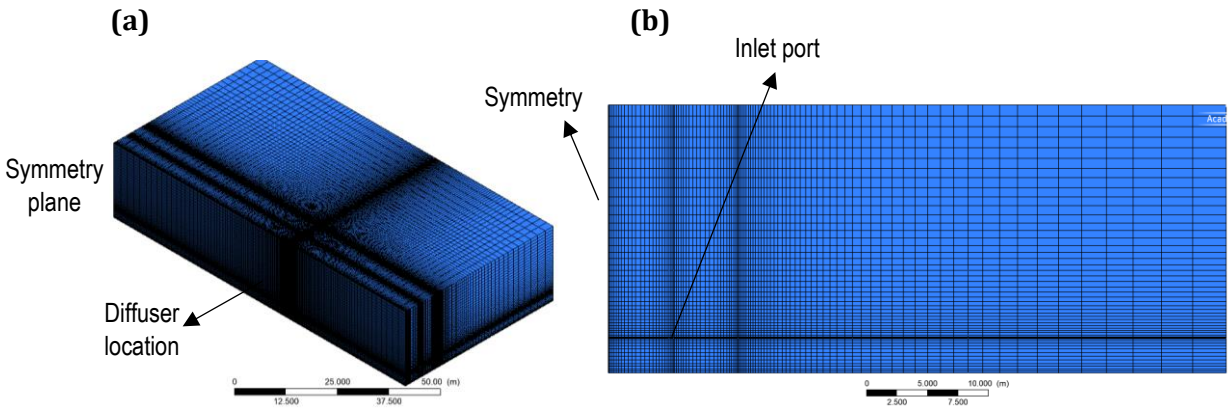

Figure 6-12. Typical initial mesh used for the Cartagena marine outfall simulations: **a)** three-dimensional view of the mesh; **b)** cross-sectional view of the mesh at the central plane of the diffuser.

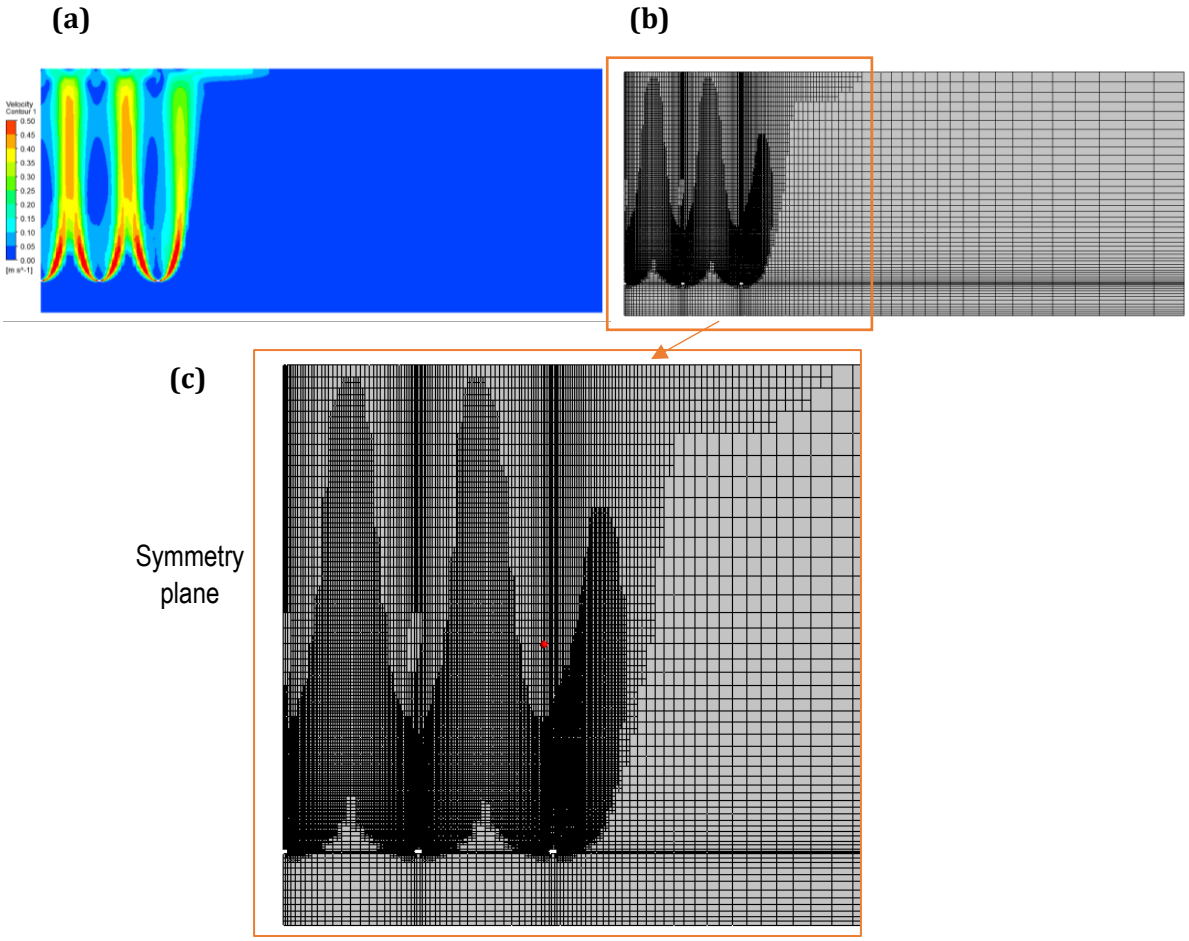

Figure 6-13. a) Contours of velocity at the central plane of the diffuser for a stationary unstratified flow with discharge velocity of 0.5 m/s; **b)** Cross-sectional view of the adapted mesh at the central plane of the diffuser; **c)** Magnified view of the adapted mesh at the location of the discharged plumes.

6.4.3 Boundary conditions.

In all simulations conducted in this chapter, the top boundary was defined as a slip wall with zero gradient conditions, in order to represent the free surface. The wastewater discharge ports were

located in the central area of the domain, as shown in Figure 6-14. From each port, wastewater was discharged at a uniform velocity, which depended on the case in study. Turbulence intensity, I, at the discharging ports and current inlets were calculated based on the following equation

$$I = 0.16(Re)^{-1/8} \quad \textbf{(6.1)}$$

where Re is Reynolds number.

The bottom was defined as a no-slip wall. One of the sides is a slip wall whilst the other is defined as a symmetry plane.

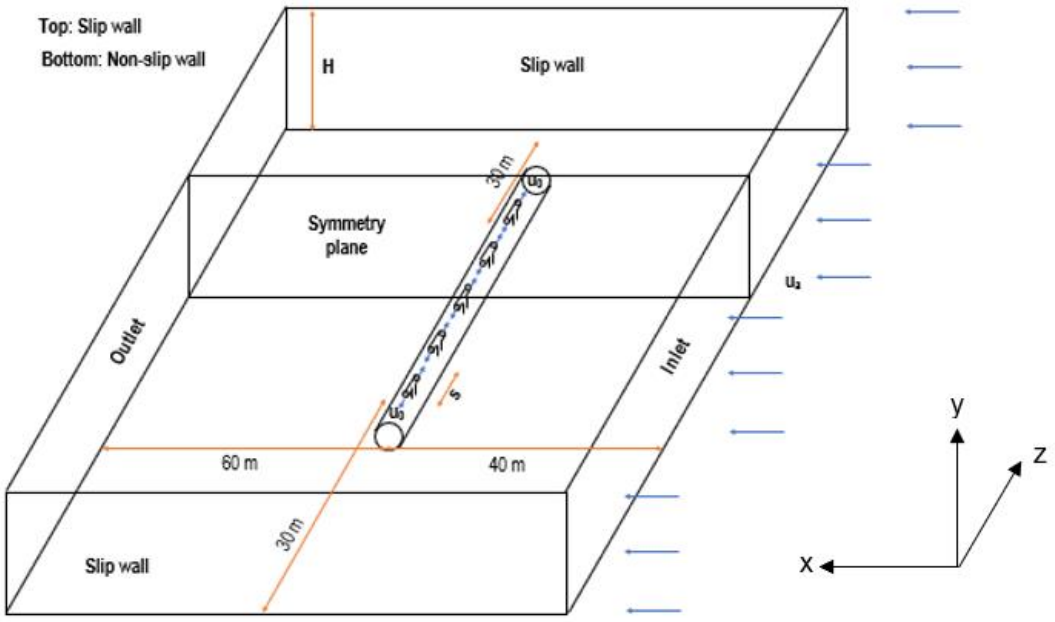

Figure 6-14. Schematic of the typical boundary conditions for the Cartagena marine outfall simulations.

In the cases in which symmetry was not conserved due to the presence of an inclined current, the front and right side of the domain were assigned as inlets, and the left and back side of the domain as outlets.

The current was initially modelled using a coarser mesh until the flow was fully developed, and the resulting profile was then input at the inlet boundary. In the presence of density stratification, a user-defined function was used that established temperature along the water depth as a function of vertical position. The equation solved by this user-defined function was:

$$T_y = 0.04545 \cdot y + 301.5 \quad \textbf{(6.2.)}$$

Where T_y is the temperature in Kelvin (K) at a given vertical location, *y*.

A description of the boundary conditions used for some of the cases studied in this chapter is given in Table 6-1. For other cases, a similar approach is used, varying the corresponding velocity magnitudes and turbulence parameters at the inlets.

Table 6-1. Description of boundary conditions for some of the Cartagena marine outfall cases.

Case	Boundary	Boundary type	Momentum				Thermal	Species	Turbulence	
			x-velocity (m/s)	y-velocity (m/s)	z-velocity (m/s)	Gauge pressure (Pa)	Temperature (°C)	Salinity concentration (ppt)	Turbulent intensity (%)	Hydraulic diameter (m)
S2	Top (xz+)	Slip wall	N/A	N/A	N/A	N/A	Zero heatflux	Zero-gradient	N/A	N/A
	Bottom (xz-)	Non-slip wall	N/A	N/A	N/A	0	Zero heat flux	Zero-gradient	N/A	N/A
	Lateral 1(xy-)	Slip wall	N/A	N/A	N/A	N/A	Zero heat flux	Zero-gradient	N/A	N/A
	Lateral 2 (yz-)	Pressure outlet	N/A	N/A	N/A	N/A	Zero heat flux	Zero-gradient	N/A	N/A
	Lateral 3 (xy+)	Slip wall	N/A	N/A	N/A	N/A	Zero heat flux	Zero-gradient	N/A	N/A
	Lateral 4 (yz+)	Pressure outlet	N/A	N/A	N/A	N/A	Zero heat flux	Zero-gradient	N/A	N/A
	Inlets 1-5	Velocity inlet	0	0	±0.5	N/A	31	40	3.7	0.2
F2	Top (xz+)	Slip wall	N/A	N/A	N/A	N/A	Zero heat flux	Zero-gradient	N/A	N/A
	Bottom (xz-)	Non-slip wall	N/A	N/A	N/A	0	Zero heat flux	Zero-gradient	N/A	N/A
	Lateral 1(xy-)	Slip wall	N/A	N/A	N/A	N/A	Zero heat flux	Zero-gradient	N/A	N/A
	Lateral 2 (yz-)	Velocity inlet	0.1 (average)	0	0	N/A	28	0	2.4	36.2

			Imported parabolic profile							
	Lateral 3 (xy+)	Slip wall	N/A	N/A	N/A	N/A	Zero heat flux	Zero-gradient	N/A	N/A
	Lateral 4 (yz+)	Pressure outlet	N/A	N/A	N/A	N/A	Zero heat flux	Zero-gradient	N/A	N/A
	Inlets 1-5	Velocity inlet	0	0	±0.5	N/A	31	40	3.7	0.2
F12	Top (xz+)	Slip wall	N/A	N/A	N/A	N/A	Zero heat flux	Zero-gradient	N/A	N/A
	Bottom (xz-)	Non-slip wall	N/A	N/A	N/A	0	Zero heat flux	Zero-gradient	N/A	N/A
	Lateral 1(xy-)	Velocity inlet	0.07 (average) Imported parabolic profile	0	0	N/A	28	0	2.4	36.2
	Lateral 2 (yz-)	Velocity inlet	0.73 (average) Imported parabolic profile	0	0	N/A	28	0	2.5	38.1
	Lateral 3 (xy+)	Pressure outlet	N/A	N/A	N/A	N/A	Zero heat flux	Zero-gradient	N/A	N/A
	Lateral 4 (yz+)	Pressure outlet	N/A	N/A	N/A	N/A	Zero heat flux	Zero-gradient	N/A	N/A
	Inlets 1-5	Velocity inlet	0	0	±0.5	N/A	31	40	3.7	0.2
S1	Top (xz+)	Slip wall	N/A	N/A	N/A	N/A	Zero heat flux	Zero-gradient	N/A	N/A

	Bottom (xz-)	Non-slip wall	N/A	N/A	N/A	0	Zero heat flux	Zero-gradient	N/A	N/A
	Lateral 1(xy-)	Slip wall	N/A	N/A	N/A	N/A	Zero heat flux	Zero-gradient	N/A	N/A
	Lateral 2 (yz-)	Velocity inlet	0.1 (average) Imported parabolic profile	0	0	N/A	Imported linear profile. Equation (6.2.)	0	2.4	36.2
	Lateral 3 (xy+)	Slip wall	N/A	N/A	N/A	N/A	Zero heat flux	Zero-gradient	N/A	N/A
	Lateral 4 (yz+)	Pressure outlet	N/A	N/A	N/A	N/A	Zero heat flux	Zero-gradient	N/A	N/A
	Inlets 1-5	Velocity inlet	0	0	±0.5	N/A	31	40	3.7	0.2

6.5 RESULTS AND DISCUSSION.

6.5.1 Near field modelling of an outfall discharge in an unstratified stagnant environment.

The dynamics of merging plumes from multiple port diffusers are complex and depend on a great variety of parameters. In a stagnant environment, the flow is driven mainly by the initial momentum of the discharge and buoyancy source, as described in section 2.1.1. As had been observed in previous simulations on axisymmetric plumes in Chapter IV, the merging location for adjacent plumes depends on the spacing between them and differences in their sources of energy (buoyancy or momentum).

Two cases in stagnant unstratified environment were used for comparison. Ambient characteristics were maintained; however, the alignment of the ports was varied. The purpose of this comparison was to understand the behaviour of multiple-port discharges from Tee-shaped risers in a stagnant environment and to analyse the effects of having different port alignments on such behaviour. A complete description of the cases used for comparison is given in Table 6-2.

Table 6-2. Description of cases in stagnant unstratified environment.

	Parameter	Symbol	Case	
			S1	**S2**
Discharge conditions	Velocity (m/s)	u_0	0.5	
	Flow rate per port (m^3/s)	Q/n	0.016	
	Temperature (°C)	T_0	31	
	Port diameter (m)	d	0.2	
	Port spacing (m)	s	5	
	Type of port alignment	-	A	B
Ambient characteristics	Current velocity (m/s)	u_a	0	
	Ambient temperature (°C)	T_a	28	
	Salinity (ppt)	S	36.5	
	Water depth (m)	H	20	22
Nondimensional parameters	l_m	-	0.22	

In diffusers with a conventional Tee-shaped riser alignment (type A from Figure 6-3), plumes ejecting from opposing ports would rise and, depending on the spacing between risers, they would merge or not with their adjacent plumes before reaching the surface. After reaching the surface, the formed wastefield spreads laterally. The plume ejecting from the central riser (plume C), shows a vertical trajectory; however, plumes A and B deflect towards the central plume (see Figure 6-16). This shows that in cases where more than two equal plumes are adjacent to each other, the plumes would deflect towards the centre, drawn by each other's entrainment field, as was observed in the studies of coalescing axisymmetric plumes (Chapter V).

(a)

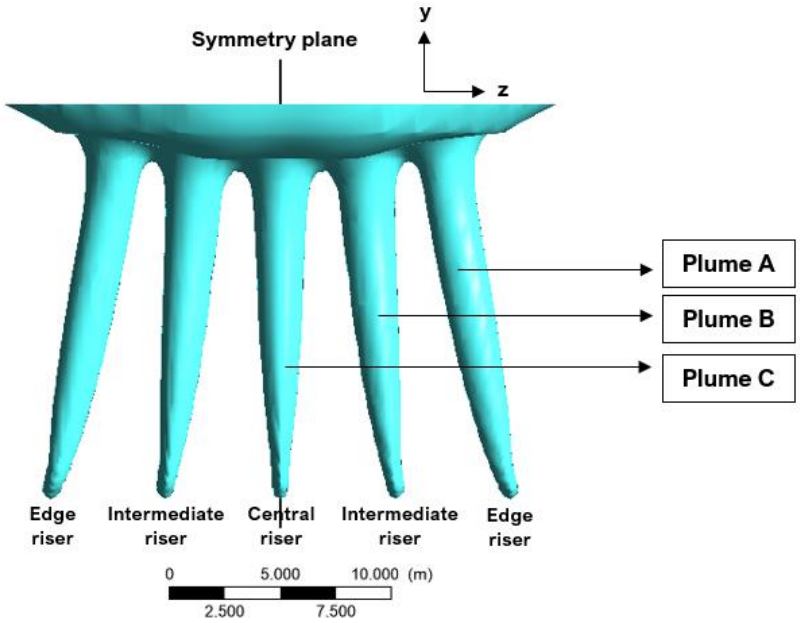

(b)

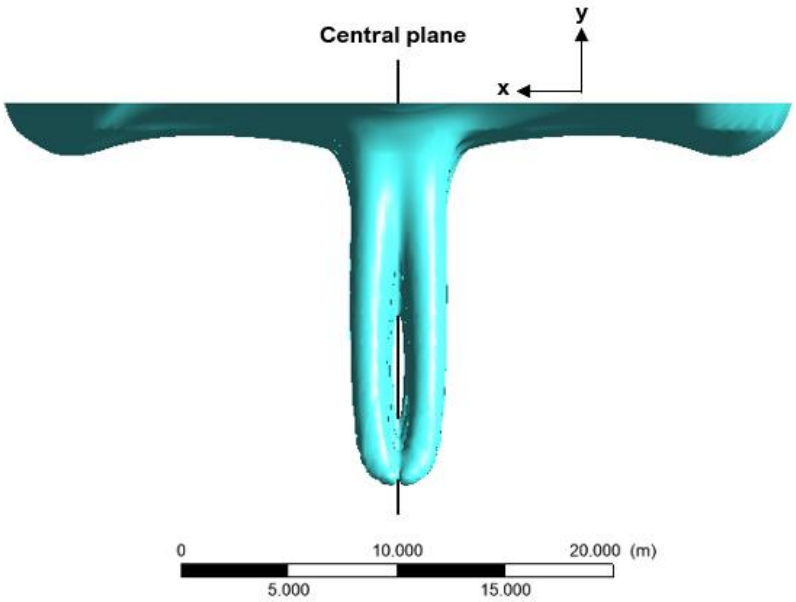

Figure 6-15. Isosurface at locations where dilution is 1:125 for case S1: **a)** front view; **b)** lateral view.

(a)

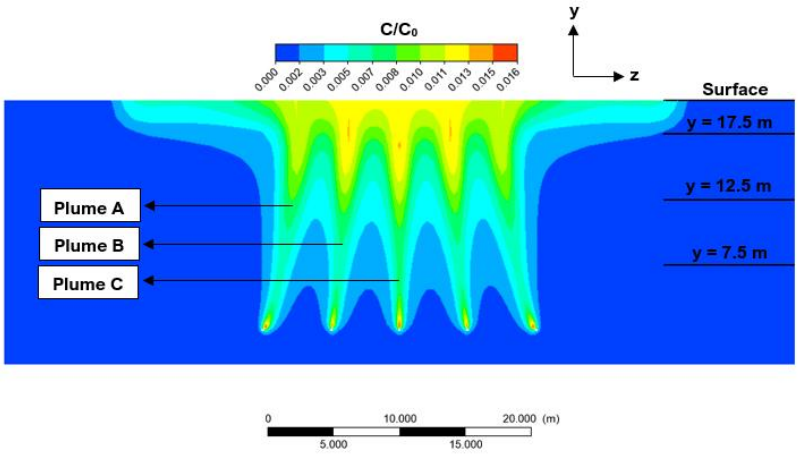

(b)

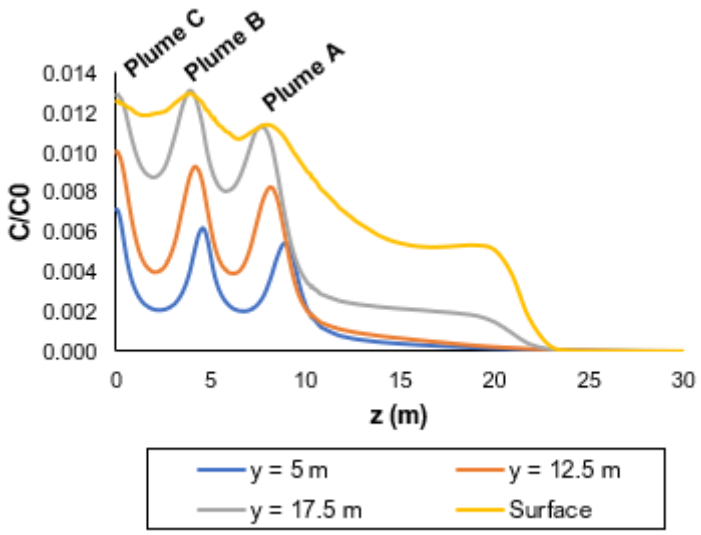

Figure 6-16. **a)** Contours of normalized pollutant concentration at central plane; **b)** Normalized pollutant concentration along different water depths for case S1.

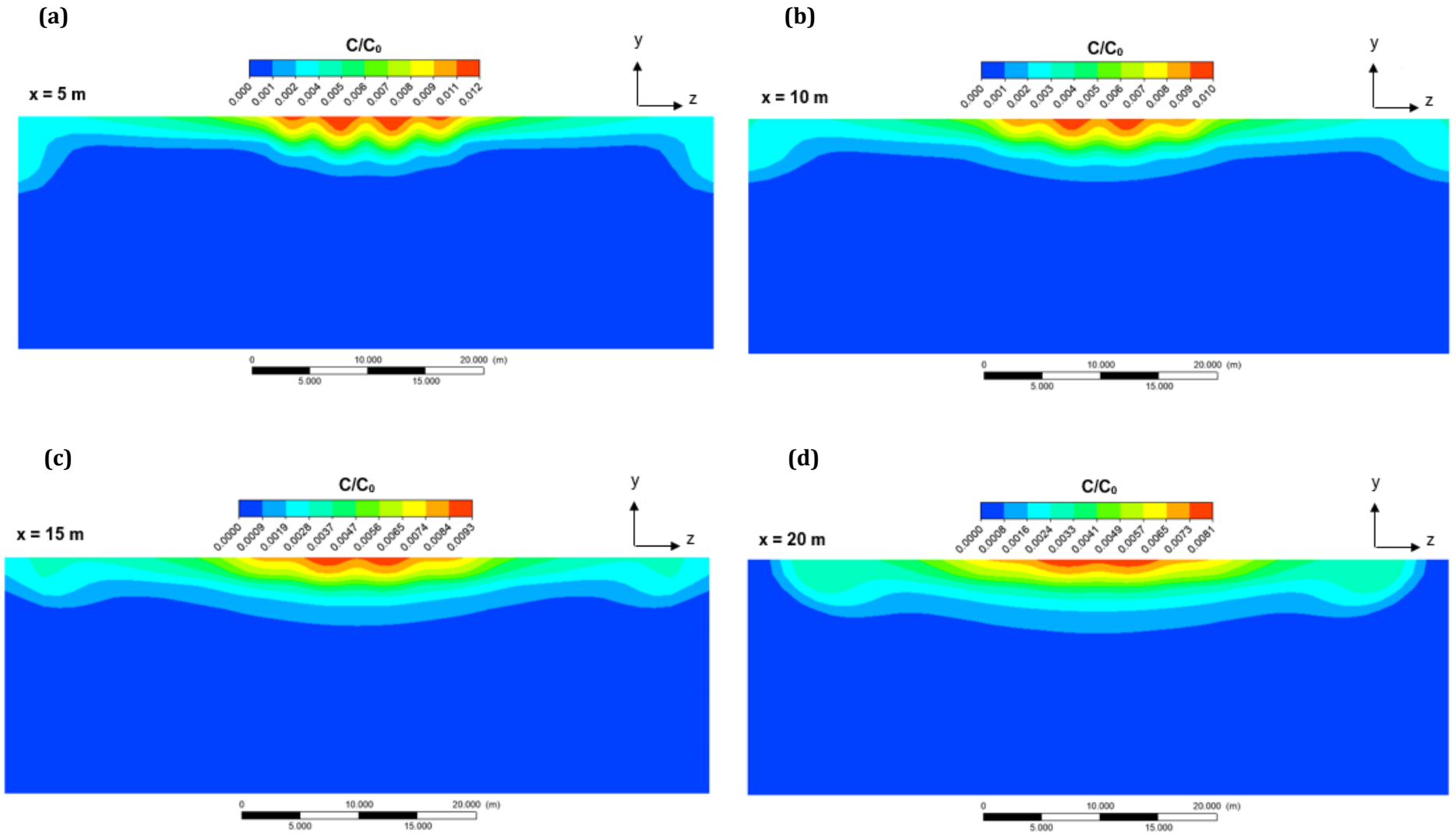

Figure 6-17. Contours of normalised pollutant concentration at **a)** x = 5 m; **b)** x = 10 m; **c)** x = 15 m; **d)** x = 20 m. Case S1. Please note that these graphs do not show the complete domain along the z axis.

Differences in pollutant concentration are observed for plumes A, B and C at different water depths in a type A riser alignment. This is due to their deflection towards the centre, which leads the central plumes to show higher pollutant concentration than those located at the edges. In the case studied, plumes ejecting from adjacent risers do not fully merge before reaching the surface (Figure 6-16a) and their full merging process occurs further downstream. As the plumes continue to merge in the region of lateral spreading, the pollutant concentration continues to decrease, as can be seen in the contours of normalised pollutant concentration at different locations shown in Figure 6-17. The spreading not only occurs in the x-direction, but also to the sides of the diffuser in the z-direction.

For diffusers with type B alignment, different dynamics are observed since their positioning supposes that must plumes would exit the ports, collide with the plume exiting the adjacent port and subsequently rise to the surface. The plumes at the edges do not merge immediately with the others, behaving as individual plumes until they merge with the adjacent ones as they approach the surface. Once the plumes reach the surface, they spread laterally, forming a wastefield, predominantly in the x-direction. The lateral spreading in the z-direction observed for a diffuser with port alignment type A does not take place as significantly in a diffuser with port alignment type B.

Three types of plumes are identified for type B alignment (see Figure 6-18): plume A, a plume located at the edge of the diffuser; plume B, the merged plume from an edge and intermediate riser; and plume C, the merged plume from an intermediate and central riser. Pollutant concentrations for plumes B and C are found to be equal along their trajectory (see Figure 6-19). On the other hand, plume A shows lower pollutant concentration since it only merges with the other plumes closer to the surface. In a diffuser with a higher number of risers, it can be assumed that most of the plumes would behave as plumes B and C, and only those located at the edges would behave differently.

Contrary to what occurs in a diffuser with port alignment type A, in a diffuser with type B alignment, the pollutant concentration in the central plane decreases as it approaches the surface, since most of the merging occurs near the discharge as opposed to at the surface. These differences can be identified by comparing Figure 6-16 and Figure 6-19.

In the region of lateral spreading, pollutant concentrations continue to decrease, as seen in contours of pollutant concentration at different locations downstream in Figure 6-20. Vortices originate where the plume impacts the surface, providing additional mixing as ambient fluid continues to entrain the wastefield (see Figure 6-21). The vortices slow along the trajectory, ultimately subsiding, as is shown in Figure 6-21d. This has been observed by previous studies on multiple port diffusers with alignment type A in unstratified environments (Daviero, 1998; Tian, et al., 2004a).

Observations of the turbulent kinetic energy at different locations downstream from the discharge are shown in Figure 6-22 for case S2. Higher turbulent kinetic energy is initially observed in the proximity of the discharge. It then decreases as the plumes rises to the surface, where it increases again due to the vortices created as they impact the surface. This agrees with observations from coalescing axisymmetric plumes described in Chapter V and findings from numerical simulations of a diffuser with port alignment type A by Xue, et al. (2014). As the formed wastefield travels downstream, turbulent kinetic energy continues to decrease. Similar behaviour was observed for diffusers with port alignment type A.

(a)

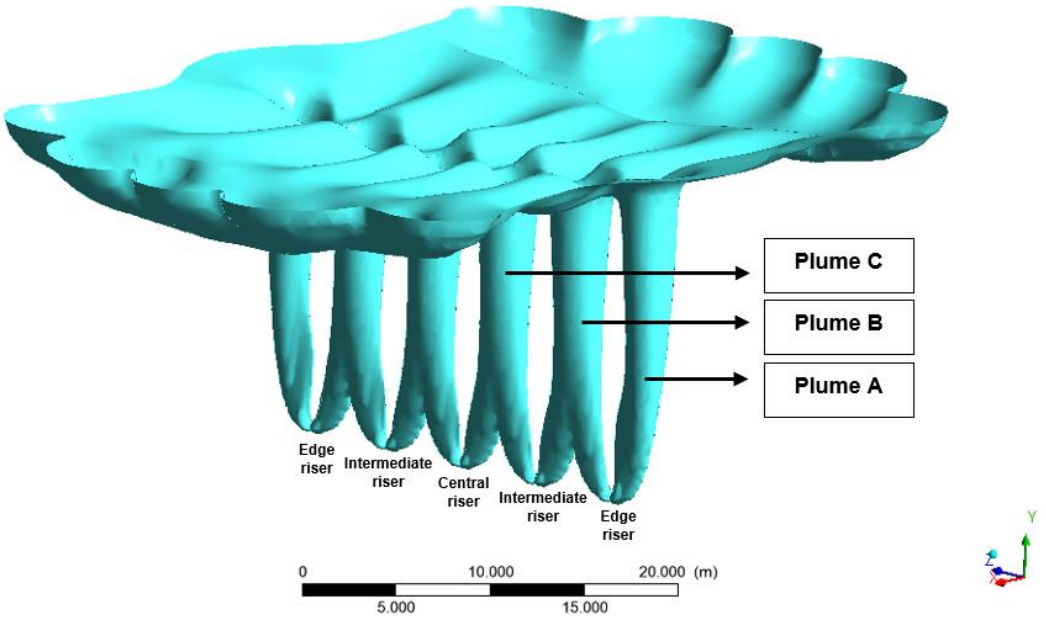

(b)

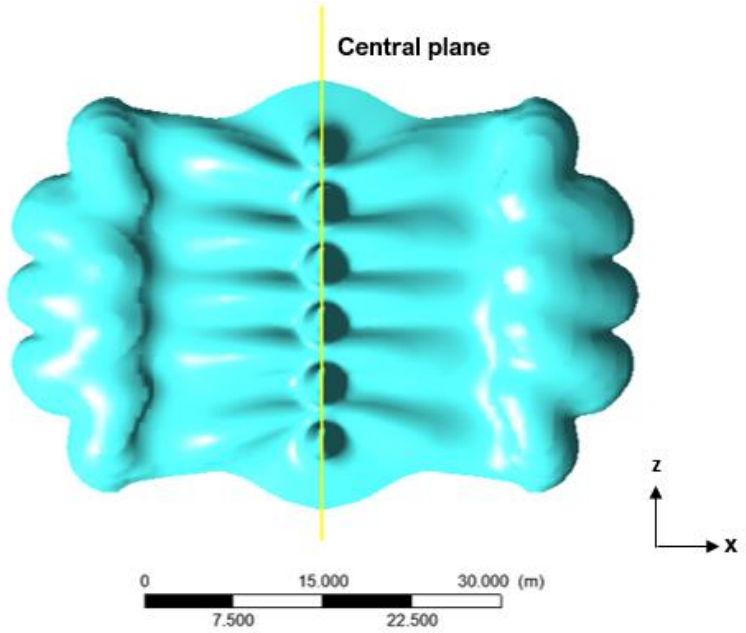

Figure 6-18. Isosurface at locations where dilution is 1:200 for a case S2: **a)** inclined view; **b)** top view.

(a)

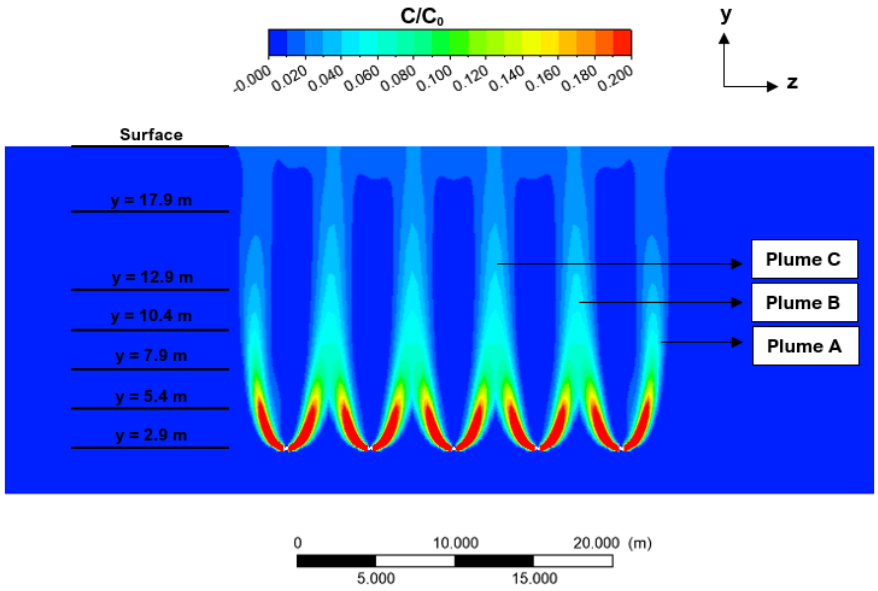

(b)

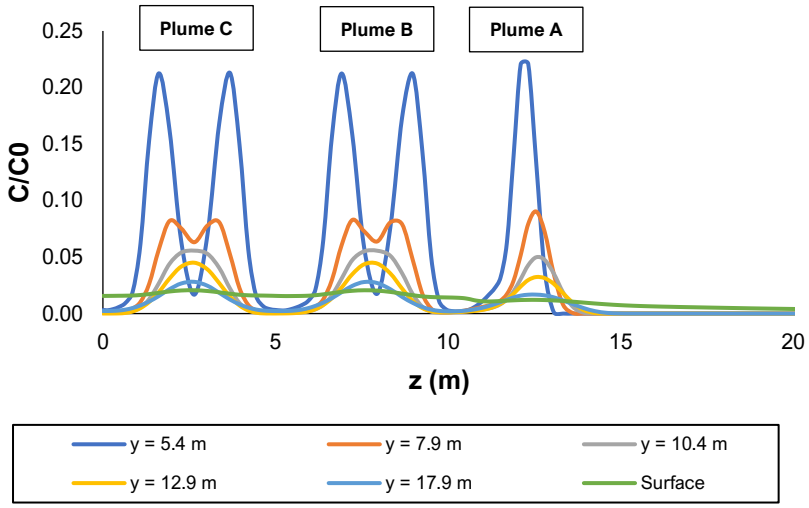

Figure 6-19. a) Contours of normalized pollutant concentration at central plane; **b)** Normalized pollutant concentration along different water depths. Case S2.

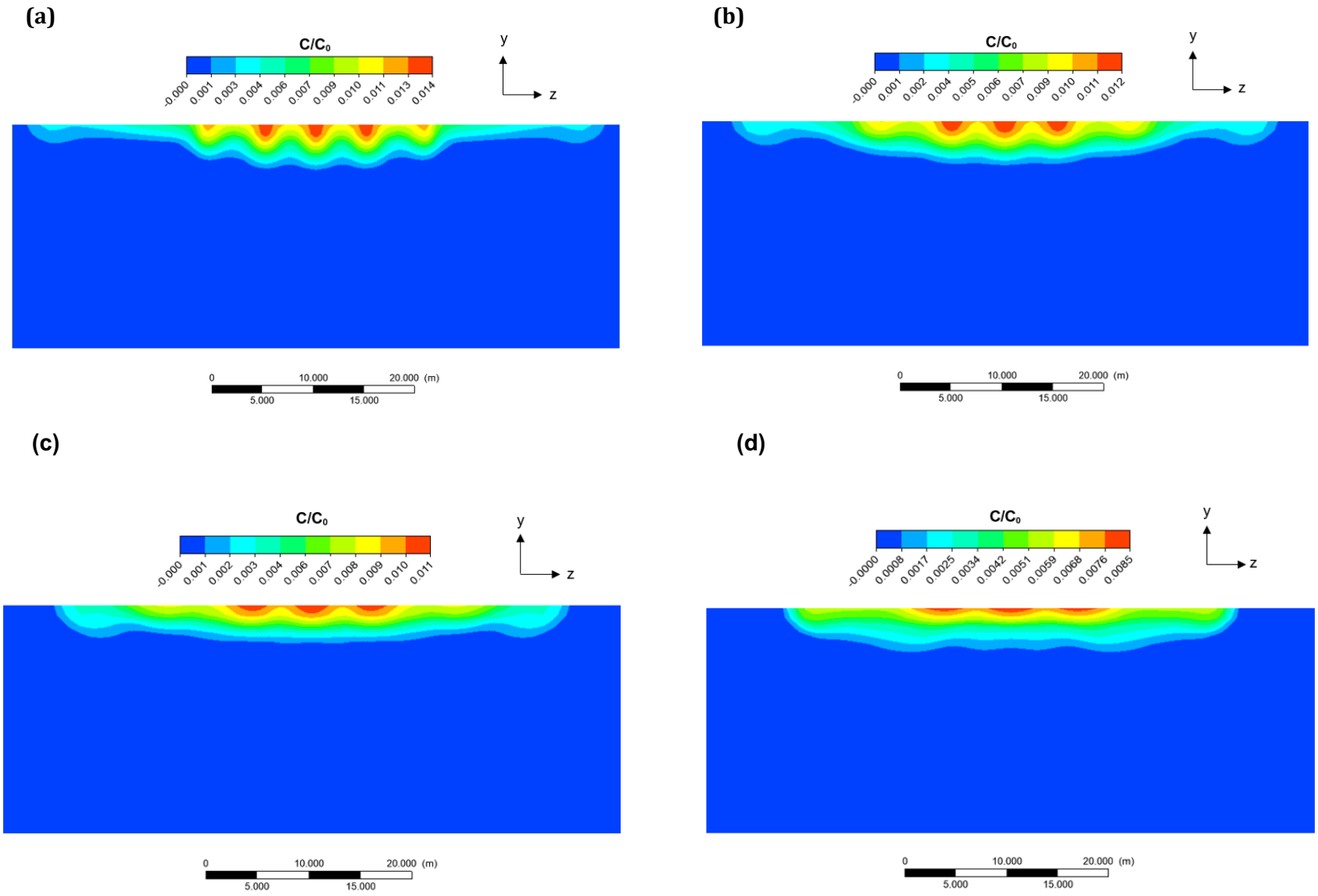

Figure 6-20. Contours of normalized pollutant concentration at **a)** x = 5 m; **b)** x = 10 m; **c)** x = 15 m; **d)** x = 20 m. Case S2.

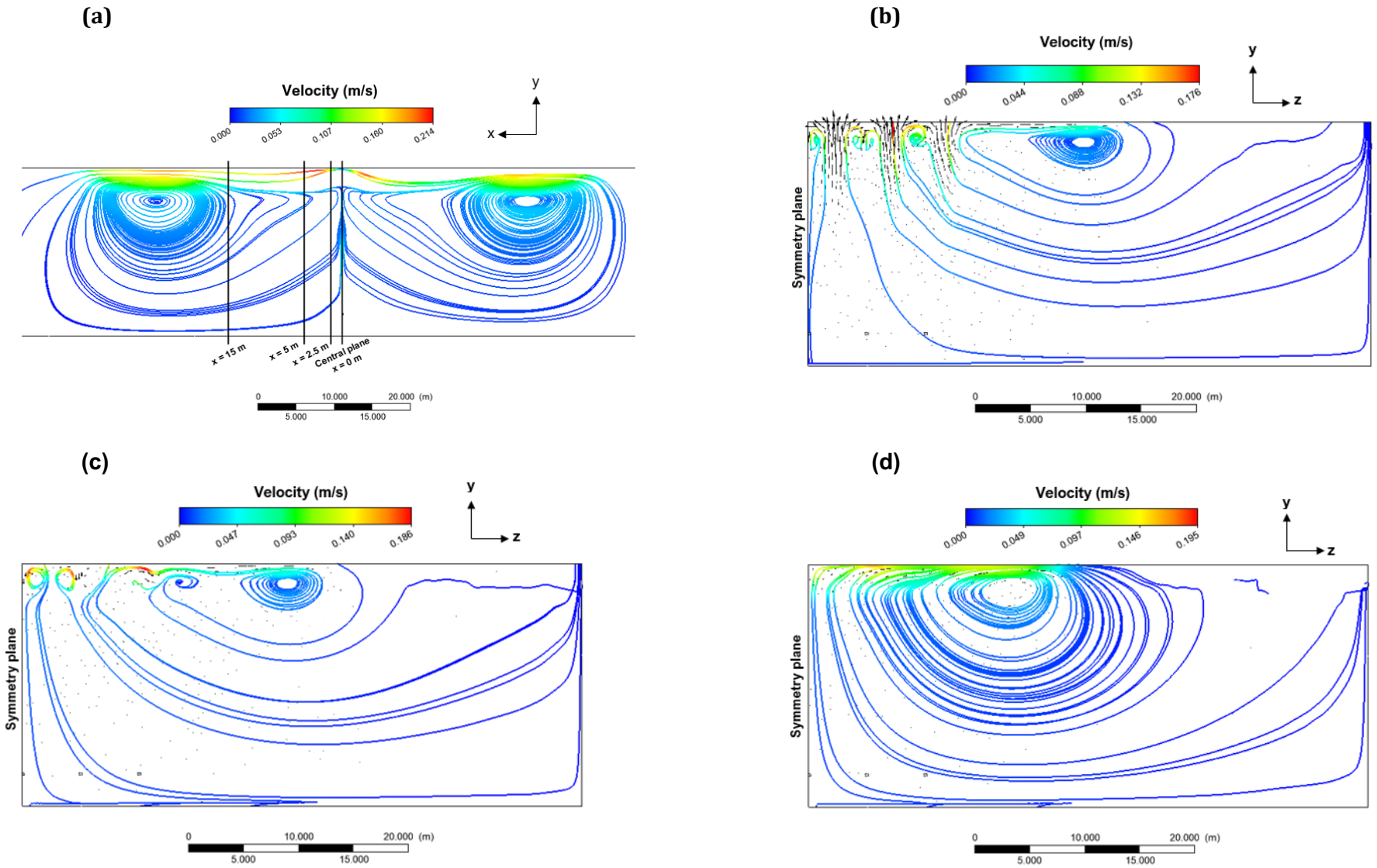

Figure 6-21. a) Lateral view of the velocity field in the symmetry plane; **b)** Cross-sectional view of the velocity field at x = 2.5 m; **c)** Cross-sectional view of the velocity field at x = 5 m; **d)** Cross-sectional view of the velocity field at x = 15 m. Case S2. These graphs show both stream line and velocity vectors.

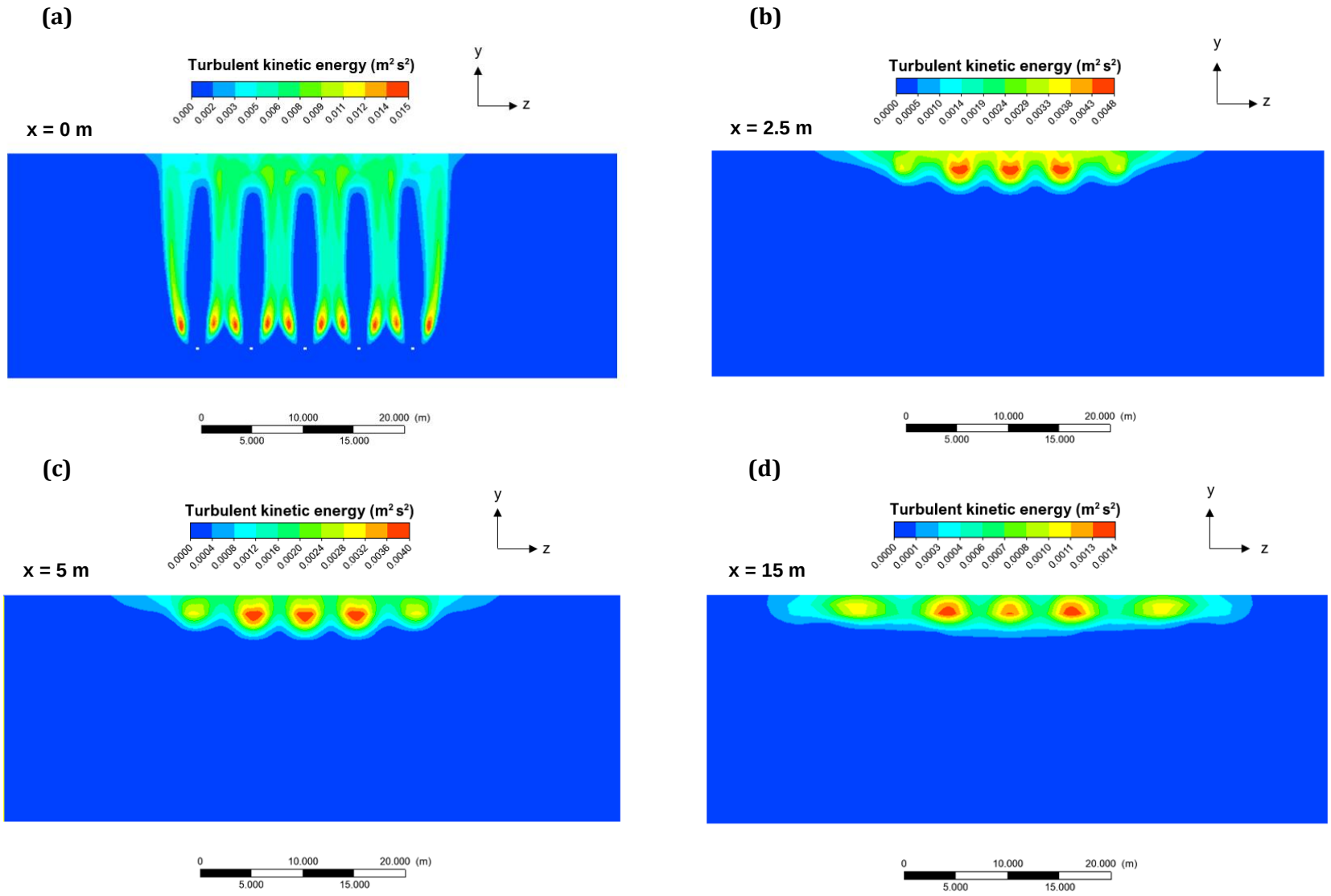

Figure 6-22. Contours of turbulent kinetic energy at: **a)** the central plane; **b)** x = 2.5 m; **c)** x = 5 m; **d)** x = 15 m. Case S2.

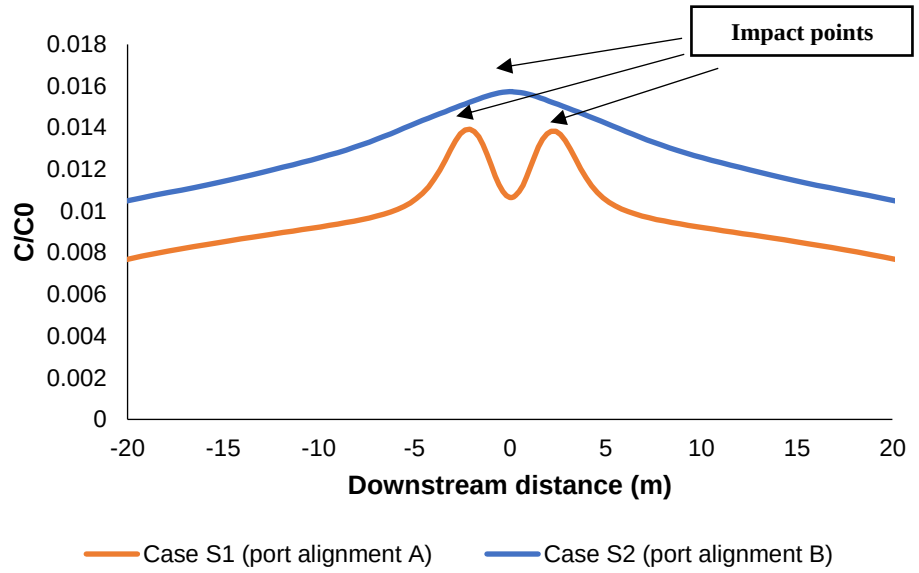

Figure 6-23. Normalised concentration at the surface along the symmetry plane for plumes with different port alignment in stationary environment.

Comparisons of the contours of pollutant concentrations at different locations downstream for cases S1 and S2 (Figure 6-17 and Figure 6-20), indicate that higher dilution is achieved with the conventional alignment (type A) in stagnant waters. For further analysis, the surface concentration of the effluent has been plotted for cases S1 and S2, at different locations along the x-axis. The symmetry plane was selected as the location for comparison, since it is in this plane where the maximum concentrations are found.

For a port alignment type A, two peaks are found a few metres away from the diffuser (x = 0 m) (see Figure 6-23). Each peak represents the impact points, locations where the plumes from each side of the diffuser reach the surface. Beyond these two peaks, the pollutant concentration continues to decrease. At the impact location, a dilution of 73:1 is observed. Further downstream, 20 m away from the discharge, a dilution level of 127:1 has already been achieved. This agrees with experimental findings by Tian, et al. (2004a), who observed additional mixing beyond the impact point. This mixing can be the result of continuous entrainment of the ambient water and turbulence advected from the rising plumes to the region of lateral spreading. Under the discharge and ambient conditions of case S1, empirical formulations by Tian, et al. (2004a) predict that horizontal mixing ends at a distance of 15.5 m away from the discharge, location that they define as the end of the near field. According to this empirical formulations, the dilution at the end of the near field for case S1 is 157:1. However, CFD predictions found that pollutant concentrations do continue to decrease beyond 15.5 downstream, although at a relatively low rate. The dilution predicted by Tian, et al. (2004a) is around 30% higher than that found by CFD simulations. Differences could be due to scale effects as empirical formulations are based on laboratory experiments.

On the other hand, for case S2, a single peak is observed at the surface along the x-axis. At this peak, which corresponds to the impact point, dilution is approximately 63:1, 13% lower than that observed at the impact points of case S1. Further downstream, discrepancies between the pollutant concentration observed for case S1 and S2 are 26%, higher than those observed at the impact points. This indicates that using a type B diffuser alignment reduces the outfall's capacity for mixing, as it effectively reduces the spacing between plumes at the discharge height. This reduction results in faster merging and consequently, diminishes the entrainment of ambient fluid into the plumes. However, this conclusion is valid for a situation where there is no current

and a different dynamic is observed in a flowing environment. The effect of port alignment in the presence of a current is analysed in the following section.

6.5.2 Near field modelling of an outfall discharge in an unstratified flowing environment.

In flowing ambient water, the plumes are not only subject to the effect of their initial momentum and buoyancy but also to that of the current speed and angle relative to the diffuser. Research has been previously conducted on line plumes exiting from diffusers with port alignment type A into unstratified water (Roberts, 1979). They have found that the dynamic effect of the current can be expressed by the Roberts Froude number, which is a ratio between current velocity and buoyancy. Three different flow regimes have been identified (see Figure 6-24). For lower Roberts Froude numbers (F< 0.2), the flow rises to the surface and spreads upstream as a wedge, and downstream, a horizontal spreading field is formed, commonly known as wastefield. As we increase the relative strength of the current over the initial buoyancy, the plume gets attached to the lower boundary and mixes vertically, a regime often called forced entrainment. For very high Roberts Froude numbers (F>>1), the upstream wedge disappears. In this study, numerical observations for varied cases with port alignment type B show agreement with this classification, implying that the shift in the riser alignment has no effect on the type of flow regime observed for specific Froude numbers.

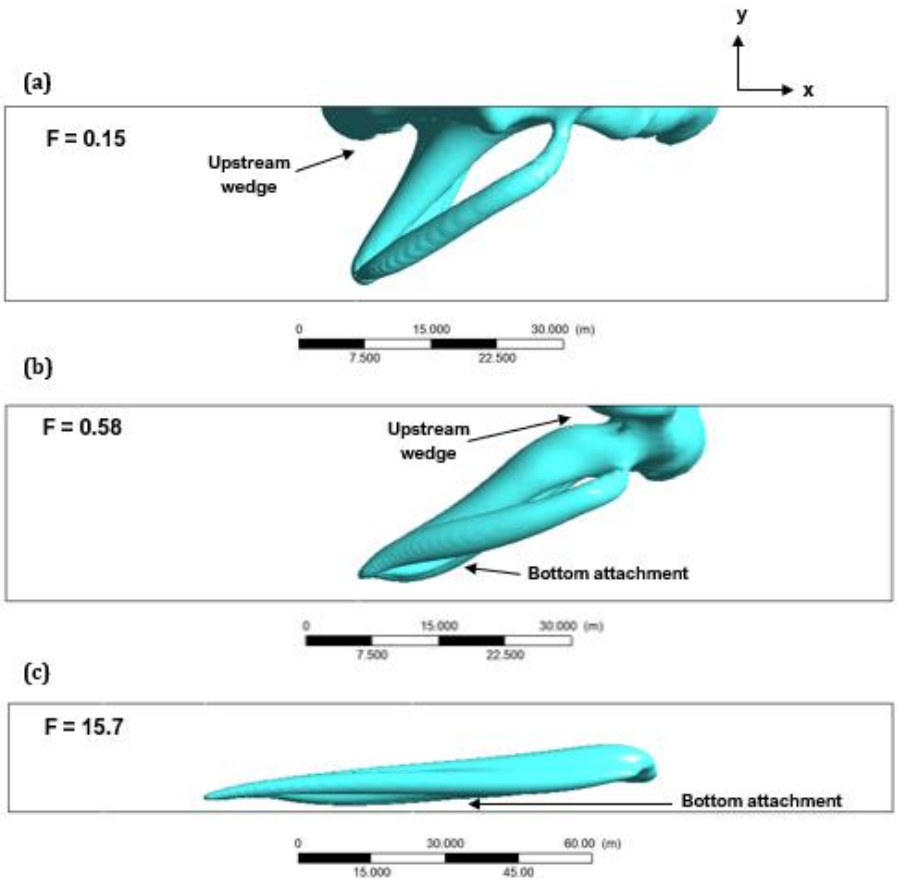

Figure 6-24 . Isosurface: **a)** at locations where dilution is 1:100 for a case with F = 0.15; **b)** at locations where dilution is 1:400 for a case with F = 0.58; and **c)** at locations where dilution is 1:1000 for a case with F = 15.7.

6.5.2.1 Roberts Froude number dependence.

Extensive literature on discharges from T-shaped risers in a flowing environment has focused on the effect of this nondimensional parameter on the near field dilution, length and thickness of the wastefield (Roberts, 1979; Tian, et al., 2004b; Xue, et al., 2014). The use of this parameter eliminates the need to focus on specific variables such as discharge flow and ambient current velocity individually, allowing more general comparisons between cases.

In this study, Roberts Froude numbers varied in the range between 0.15 and 15.7. Higher Roberts Froude numbers correspond to the cases in which the current velocity prevails over the initial buoyancy of the discharge.

Table 6-3. Description of cases used to assess Roberts Froude number effect on the flow.

	Parameter	Symbol	Case						
			F1	**F2**	**F3**	**F4**	**F5**	**F6**	**F7**
Discharge conditions	Velocity (m/s)	u_0	0.25	0.5	0.75	1	2	0.5	0.5
	Flow rate per port (m^3/s)	Q/n	0.008	0.016	0.024	0.031	0.063	0.016	0.016
	Temperature (°C)	T_0	31						
	Port diameter (m)	d	0.1						
	Port spacing (m)	s	5						
	Type of port alignment	-	B						
Ambient characteristics	Current velocity (m/s)	u_a	0.1	0.1	0.1	0.1	0.1	0.2	0.3
	Current direction (°)	-	90						
	Ambient temperature (°C)	T_a	28						
	Salinity (ppt)	S	36.5						
	Water depth (m)	H	22						
Nondimensional parameters	Froude number	F	1.16	0.58	0.38	0.29	0.15	4.65	15.7
	l_m	-	0.09	0.22	0.38	0.56	1.41	0.22	0.22

Tian et. al. (2004) proposed formulations to predict the near field dilution, length and thickness for T-shaped risers with port alignment A, based on experimental observations using 3DLIF and probe conductivity tests. For closely spaced ports (s/H < 0.5), as is the cases of the diffuser studied in this section, the plumes were found to behave like line plumes, and the empirical equations proposed by them for the prediction of the dilution, S_n, and length of the near field, x_n, are:

$$\frac{S_n q}{uH} = 0.77 \pm 15\% \quad \textbf{(6.3)}$$

$$\frac{x_n}{H} = 2.5F^{1/3} \pm 20\% \quad \textbf{(6.4)}$$

To compare the results obtained for the T-shaped risers with port alignment B, the surface concentrations along the symmetry plane were plotted (centreline of plume C). The length of the near field was defined as the location in which the plumes reach the surface, known as the impact point. The focus is mainly on the central plume, since it represents the behaviour of most of the plumes in a diffuser, apart from those located at the edges.

Figure 6-25 shows the variation of surface pollutant concentration in the downstream distance for those cases in which the plumes were found to reach the surface. In cases where the ambient current velocity was 0.2 m/s and 0.3 m/s (cases F6 and F7), the plume was found to get trapped under the surface due to their high Roberts Froude number (see

Figure **6-24**c). It is observed that the concentration is at its peak at the impact point. Additional mixing occurs at the water surface, in the region of lateral spreading. For cases with lower Froude number (F3, F4 and F5), an initial steep decrease is observed downstream from the impact point. After this initial steep decrease, dilution continues taking place, but at a slower pace. For these cases, another concentration peak was observed upstream from the impact point, although smaller than the one observed at the impact point. This peak is indicated in Figure 6-25 as upstream spreading. This corresponds to those plumes with an upstream wedge, in which the plume is able to spread both downstream and upstream from the discharge due to the slower current.

Cases with higher Froude numbers are observed to reach the surface further from the discharge location, extending the length of the near field. Furthermore, the peak that is observed at the impact point flattens. This is due to a decrease in the mixing rate of the effluent after the plumes reach the impact point. This agrees with findings by Tian, et al. (2004b), who observed that the increase in dilution beyond the impact point is significantly lower as the Roberts Froude number increases. They suggest that this reduction in mixing is due to the absence of vortices beyond the impact point for cases with F ≥ 0.26. A comparison of the observed turbulence kinetic energy at a distance of 5 m downstream from the impact point is shown in Figure 6-27, comparing two cases with different Froude numbers. Turbulence kinetic energy is approximately 50% lower for the case in which F = 0.28, and the recirculation at the surface is not as strong as those observed for F = 0.15.

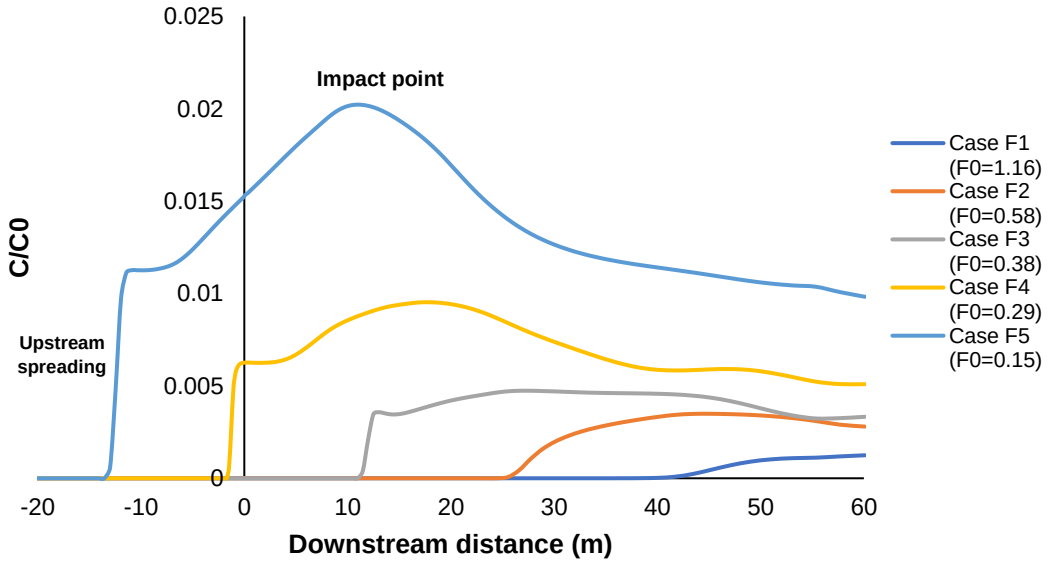

Figure 6-25. Downstream normalised pollutant concentration at the surface for cases with different Roberts Froude number.

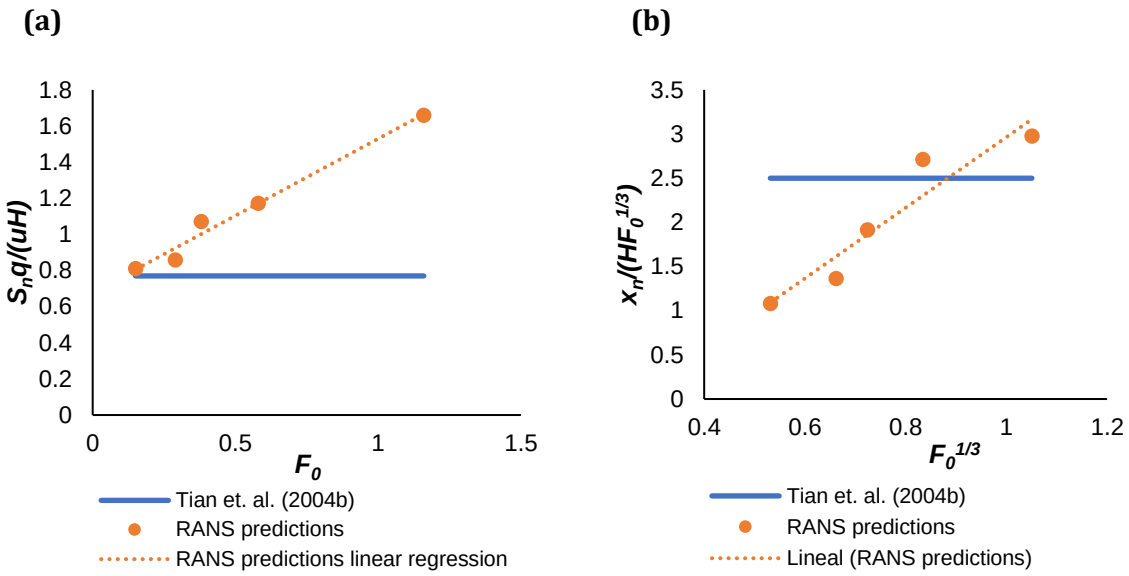

Figure 6-26. Near field dilution and length as a function of Froude number. RANS predictions are compared with empirical formulations from Tian et. al. (2004b).

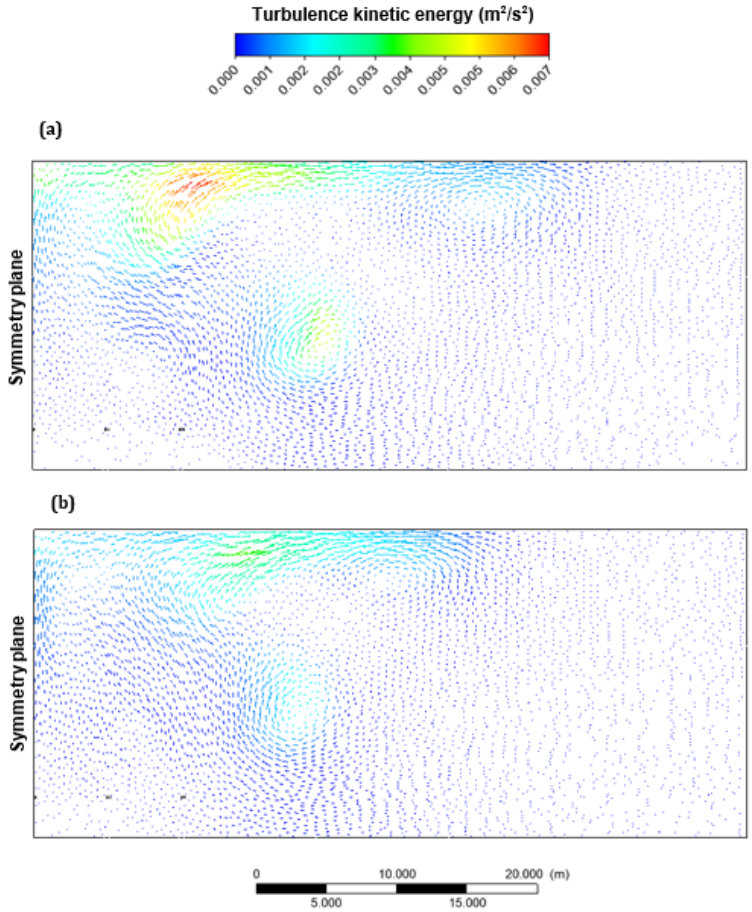

Figure 6-27. Turbulence kinetic energy vectors 5 m downstream from the impact point for: **a)** case F5 (F = 0.15) and **b)** case F4 (F = 0.28)

The predicted dilution and length of the near field is found to follow a different trend to that observed by Tian et. al. (2004b) for diffusers with port alignment type A (see Figure 6-26a). The ratio of $\frac{S_n q}{uH}$ is found to increase proportionally with Froude number, contrary to the findings of Tian et al. (2004b), who found this value to be constant and independent of this parameter. Similar discrepancies were found for the length of the near field. A reason for this disagreement could be the different port alignment used. This argument is further explored in the following subsection.

Overall, dilution rates for the range of Froude numbers studied were found to be over the typical desired value for marine outfalls, which is minimum 100:1 (Roberts, 2003; Bleninger, 2006). The only case that was found to have dilution under this value was case F5 (F_0= 0.15). However, this case corresponds to a discharge flow rate of 12.82 m^3/s, which is 4 times the average flow rate in the Cartagena marine outfall. The outfall could potentially serve a flow rate of up to 6.4 m^3/s under a perpendicular current as low as 0.1 m/s. For higher current velocities (cases F6 and F7), the length of the near field was found to be beyond 100 m downstream from the discharge, which was the maximum distance downstream modelled in this study. However, the dilution rate at this location is approximately 1014:1 at this location for a case with current velocity of 0.3 m/s (case F7), and it can only be expected to increase further downstream.

6.5.2.2 Effect of port alignment and spacing.

In order to assess the differences between diffusers with different port alignments, four cases with equal discharge and ambient conditions were compared (see Table 6-4). Plumes exiting from diffusers with port alignment type A were observed to rise faster to the surface, since the plume in counterflow merges quickly with the plume in cross-flow (see Figure 6-28a and Figure 6-30a). On the other hand, in diffusers with port alignment type B, the plumes take longer to reach the surface since the current has higher interaction with all the plumes, decelerating the merging process and extending the length of the near field. In the cases with small port spacing (F4 and F8), the plumes from a port alignment type B reach the surface approximately 10 m downstream from the location at which the plumes from a port alignment type A reach the surface (see Figure 6.29).

Table 6-4. Description of cases used for the comparison of different port alignments.

	Parameter	***Symbol***	***Case***			
			F4	**F8**	**F9**	**F10**
Discharge conditions	Velocity (m/s)	u_0	1			
	Flow rate per port (m^3/s)	Q/n	0.016			
	Temperature (°C)	T_0	31			
	Port diameter (m)	d	0.2			
	Port spacing (m)	s	5	5	20	20
	Type of port alignment	-	A	B	A	B
Ambient characteristics	Current velocity (m/s)	u_a	0.1			
	Current direction (°)	-	90			
	Ambient temperature (°C)	T_a	28			
	Salinity (ppt)	S	36.5			
	Water depth (m)	H	20	22	20	22
Nondimensional parameters	Froude number	F	0.58			
	l_m	-	0.22			

The differences in dilution between the two different types of diffusers are small, however, port alignment B shows a somehow larger dilution, especially at the impact point (see Figure 6-29). This is due to the extended length of the near field that this type of alignment provides, allowing

a larger distance for mixing to occur. Furthermore, in a conventional port alignment, the plume in counter-flow serves a barrier from the current to the plume in co-flow. With port alignment type B, all the plumes are equally exposed to the current, increasing mixing. This indicates that even though a diffuser for port alignment type B poses a disadvantage in the absence of a current, that is not the case for diffusers discharging in a flowing environment.

This difference in the effect of the current on the mixing for the different port alignment explains the trend observed in subsection 6.5.2.1. In a diffuser with port alignment type B, the plumes interact more with the current and both near field length and dilution are observed to be proportional to the Roberts Froude number, which is an indicator of the relative strength of the current over the initial buoyancy of the discharge.

(a)

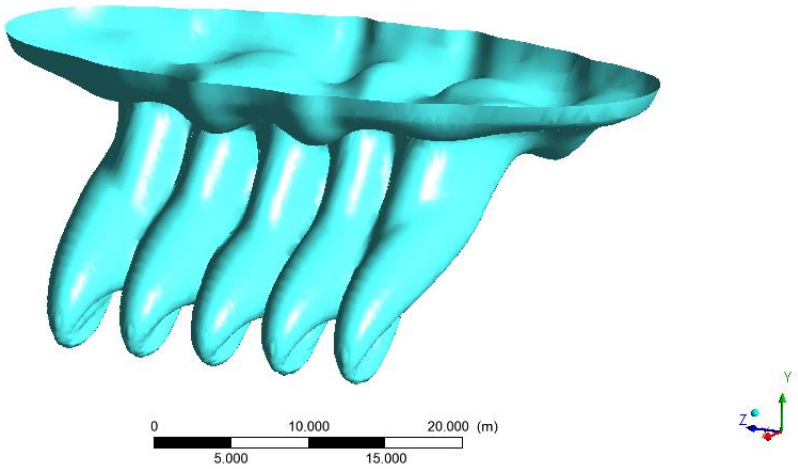

(b)

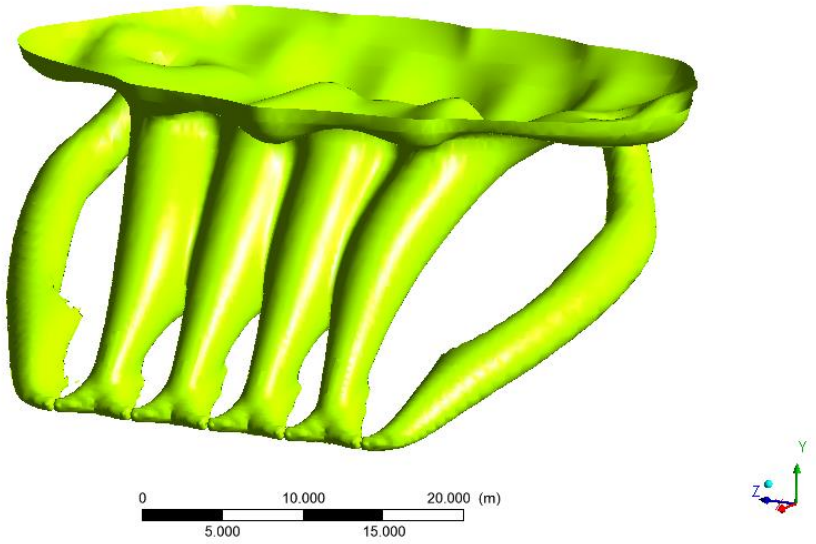

Figure 6-28. Isosurface of dilution at 1:200 for: **a)** case F8 (port alignment type A) and **b)** case F2 (port alignment type B).

Comparisons done so far are focused on diffusers where the ratio of port spacing to water depth (s/H) is below 0.5, which would result in plumes conventionally classified as line plumes. In order to study the effects of port alignment on plumes exiting from a diffuser with larger port spacing (s/H ≈ 1), cases F9 and F10 are compared. Conventional diffusers with this ratio of spacing to water depth are considered to be in a transition zone and their behaviour falls somewhat between that of both line and point plumes (Tian, et al., 2004b).

For larger port spacings, the plumes from adjacent risers were found to only merge at the surface, as observed in Figure 6-30. In the case with port alignment type B, the plumes at the edges do not show a significant difference in their trajectory and dilution when compared to the central plumes. This could indicate that edge effects may only be significant in closely spaced risers.

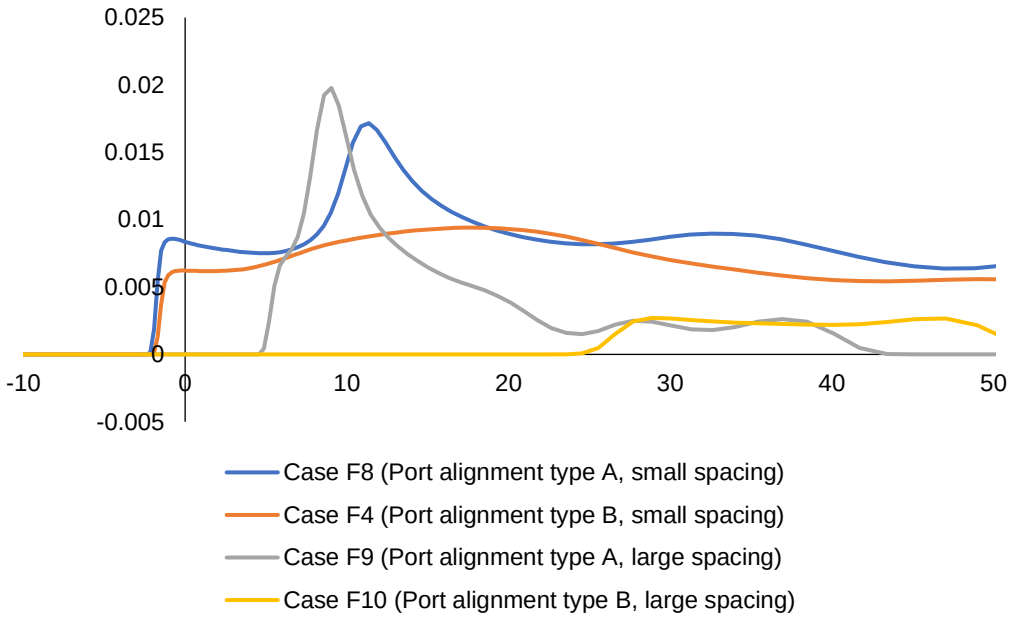

Figure 6-29. Downstream normalised pollutant concentration at the surface for cases with different port alignments.

Comparisons between plumes with large port spacing indicate similarities with the results obtained for smaller port spacings. Port alignment type B continues to provide a longer near field, which differs by about 40 m, which is double the spacing between ports, consistent with the observations for cases F4 and F8 (see Figure 6-29 and Figure ***6-30***). However, for cases with port alignment type A, dilution decreases much more significantly downstream from the impact point when compared with scenarios with port alignment type B. This shows that plumes from conventional diffusers may lead to higher concentrations near the discharge but further downstream, both types of port alignments provide similar results. However, it is important to highlight that these comparisons are conducted for a fixed Froude number of 0.29 and a different behaviour may be observed for other flow regimes.

Another aspect in which plumes from diffuser type A and B differ significantly is in the thickness of the wastefield. For instance, comparing contours of pollutant concentration for cases F4 and F8, as shown in Figure 6-31 Figure 6-32, whilst the effluent from type A diffuser shows a a wastefield with a thickness that corresponds to 32% of the water depth in the conditions studied, for a diffuser type B the wastefield thickness is only 25% of the water depth. The thicker

wastefield of the port alignment type A may be due to the fact that the plume in counterflow lays on top of the plume in coflow, which increases the thickness of the wastefield layer.

Regarding the effects of port spacing, comparisons for both types of alignment indicate an advantage for cases with larger spacing (i.e. longer diffuser), which increases dilution about 2-3 times for the port spacings studied. Port spacing shows a more significant effect on the location of the impact point for cases with port alignment type B.

(a)

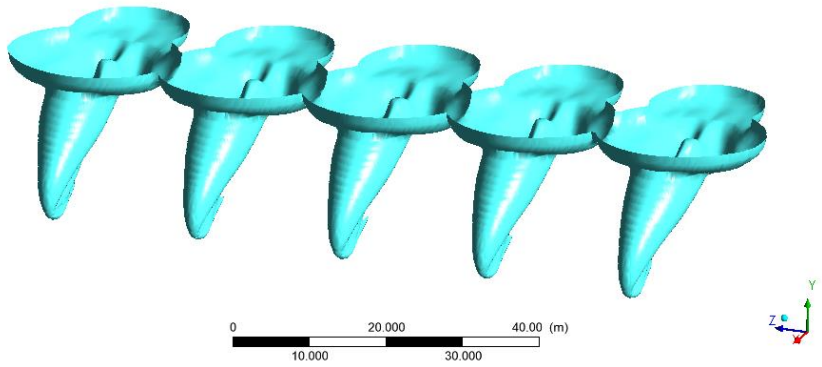

(b)

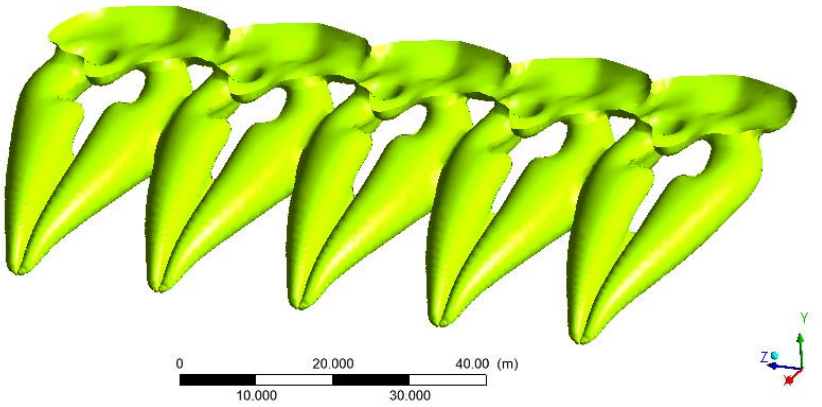

Figure 6-30. Isosurface at locations where dilution is 1:1000 for: **a)** case F9 (alignment type A); **b)** case F10 (alignment type B).

Despite the observed advantages of a larger port spacing, these benefits are reduced in cases where the length of the diffuser is fixed, indicating a reduced number of discharging ports. If the diffuser length was fixed, a port spaced every 5 m would discharge approximately ¼ of what a port spaced every 20 m would. In this case, such comparison can be made for cases F1 and F8 with port alignment type B. The dilution obtained with the smaller spacing is approximately 1.8 times higher for a fixed diffuser length. The length of the near field is not significantly changed by the larger port spacing.

These observations can lead us to safely conclude that port alignment has indeed a relevant effect on the trajectory and mixing of the plumes, and that the behaviour of a diffuser with the port alignment of the Cartagena marine outfall is not accurately predicted using formulations based on conventional port alignments.

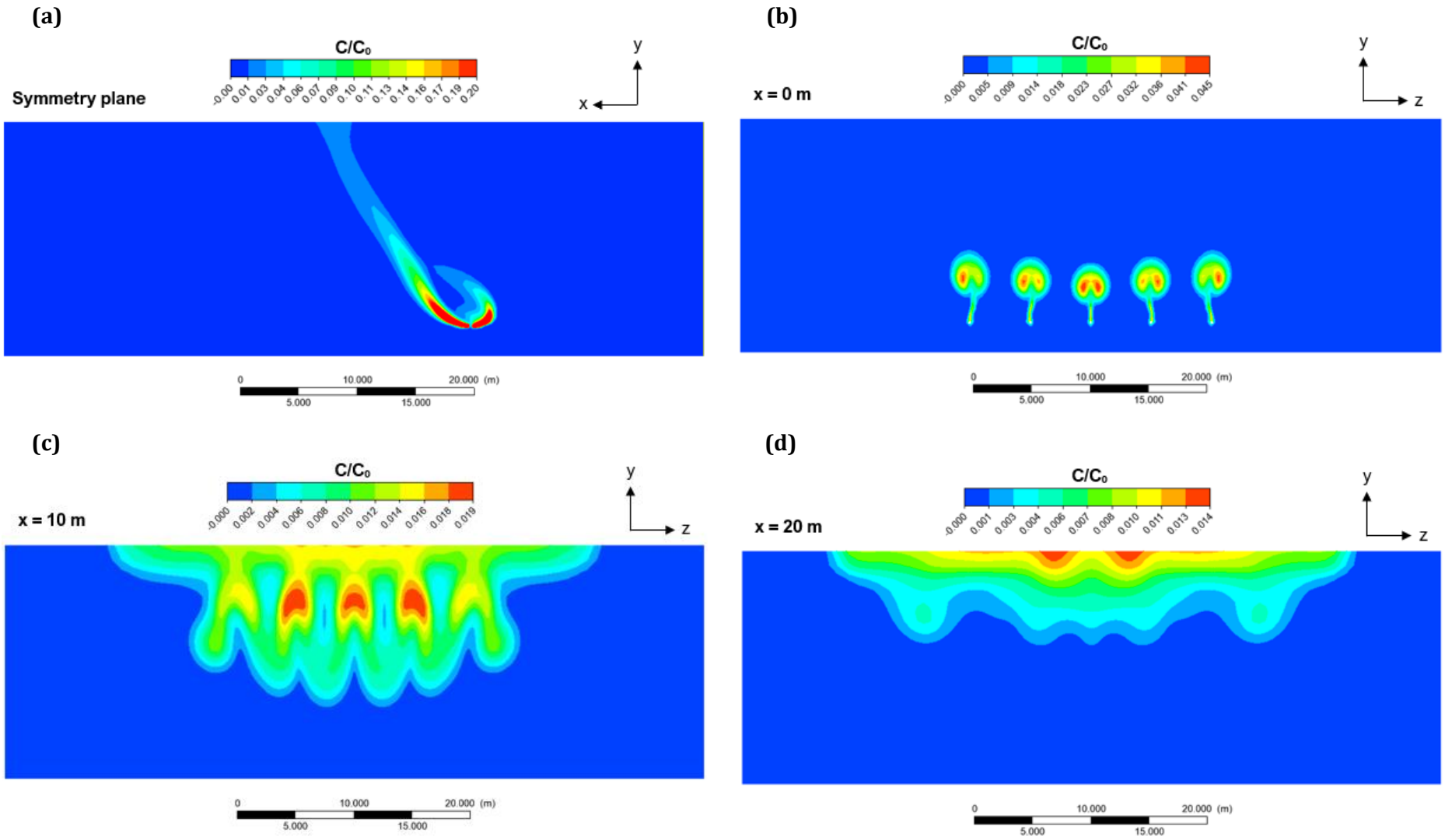

Figure 6-31. Contours of normalized pollutant concentration at **a)** symmetry plane; **b)** x = 0 m; **c)** x = 10 m; **d)** x = 20 m. Case F8 (port alignment type A).

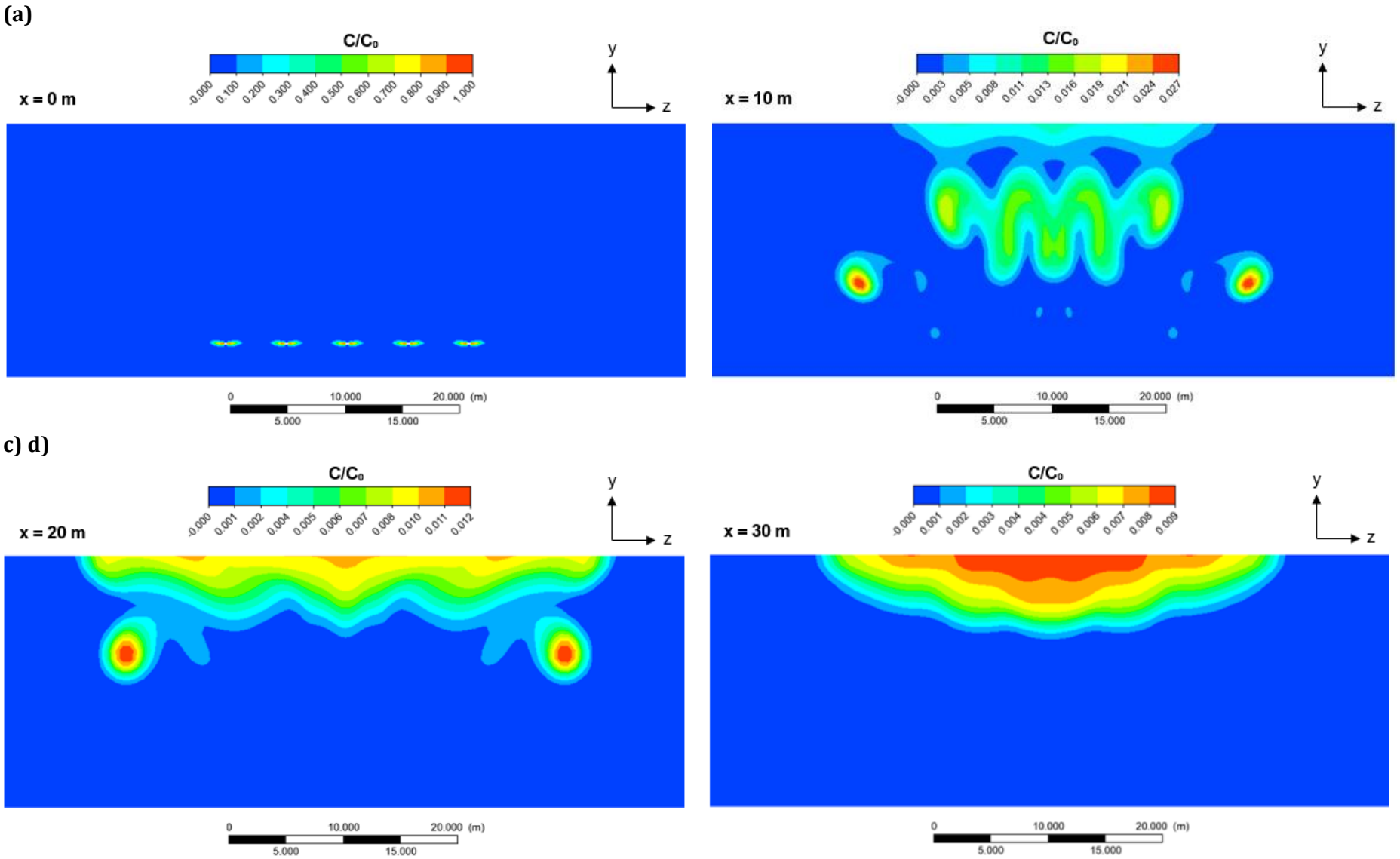

Figure 6-32. Contours of normalized pollutant concentration at **a)** x = 0 m; **b)** x = 10 m; **c)** x = 20 m; **d)** x = 30 m. Case F4 (port alignment type B).

6.5.2.3 Effects of port size.

In order to study the effects of port size on the flow behaviour, two cases with the same ambient conditions and flow rate but different port sizes were studied. This with the purpose of understanding the effects on the change in the design constructed in the Cartagena outfall, as described in section 6.2. The reduced diameter results in the smaller ports discharging at a higher exit velocity. The cases used for comparison are described in Table 6-5.

Table 6-5. Description of cases used for the comparison of different port sizes.

	Parameter	***Symbol***	***Case***	
			F2	**F11**
Discharge conditions	Velocity (m/s)	u_0	0.5	2
	Flow rate per port (m^3/s)	Q/n	0.016	0.016
	Total flow rate (m^3/s))	T_0	3.2	3.2
	Temperature (°C)	D	31	31
	Port diameter (m)	S	0.2	0.1
	Port spacing (m)	-	5	5
	Type of port alignment	u_a	B	B
Ambient characteristics	Current velocity (m/s)	-	0.1	0.1
	Current direction (°)	T_a	90	90
	Ambient temperature (°C)	S	28	28
	Salinity (ppt)	H	36.5	36.5
	Water depth (m)	F	22	22
Nondimensional parameters	Froude number	-	0.58	0.58
	l_m		0.22	0.89

Observations indicate the shape of the plumes changes for different port diameters, as seen in Figure 6-33a. In the case of the smaller port size, the plumes reach the surface nearer to the discharge area, at a location 10 m closer when compared to the impact point for the larger port diameter (see Figure 6-33b). This is due to the increased initial momentum flux.

This additional momentum observed in the plumes from smaller port diameters also increases edge effects, as the plumes at the edges travel further in the z-direction (see Figure 6-35a). In case F2, with larger port diameter, the plumes at the edges are closer to the central plumes, as seen in Figure 6-34. On the other hand, in the case with smaller port diameter, the central plumes (type B and C from classification in section 6.5.1) quickly merge, separated from the plumes located at the edges, which only merge with the others at the surface, as seen in Figure 6-35. This increased momentum is what leads the central plumes to reach the surface closer to the discharge when compared to the impact point observed for a larger port diameter.

Likewise, dilution is affected by the size of the port. Plumes from larger ports achieve a dilution 1.5 times that observed for a smaller port at the impact point. However, the discrepancies between achieved dilution become smaller further downstream, although they continue to be significant. For instance, at 60 m downstream, the dilution achieved in the scenario with larger ports is 1.3 times that achieved by the diffuser with smaller ports (see Figure 6-33b).

These findings disagree with previous studies that estimate that for the typical outfall, nozzle size is not a relevant scale (Brooks, 1980; Roberts, et al., 1989a). The change in nozzle size in the cases compared, increased four times the l_m length scale, which determines the strength of the initial momentum over the initial buoyancy. According to Brooks (1980), marine outfalls where $l_m/H < 0.25$ operate such that the flows are mainly driven by their buoyancy and the effect of the source momentum is negligible. Cases F2 and F11 have a ratio l_m/H of 0.01 and 0.04, respectively.

However, even though the flow is mostly dominated by the initial buoyancy and the ambient current, results from CFD simulations from this study indicate that the initial momentum flux influences the dilution and length of the near field in the cases studied.

The disagreement with previous studies on the effect of the initial source of momentum may result from the different port alignment used. In a diffuser with port alignment type B, adjacent plumes start interacting as soon as they exit the ports, and plumes with higher exit velocities would in fact merge faster. This faster merging is what reduces the length of the near field and the outfall's capacity for dilution. For a case with port alignment type A as that used in the study of Roberts, et al. (1989a), increasing the initial velocity may not accelerate the merging of the plumes as the risers are located parallel to each other.

(a)

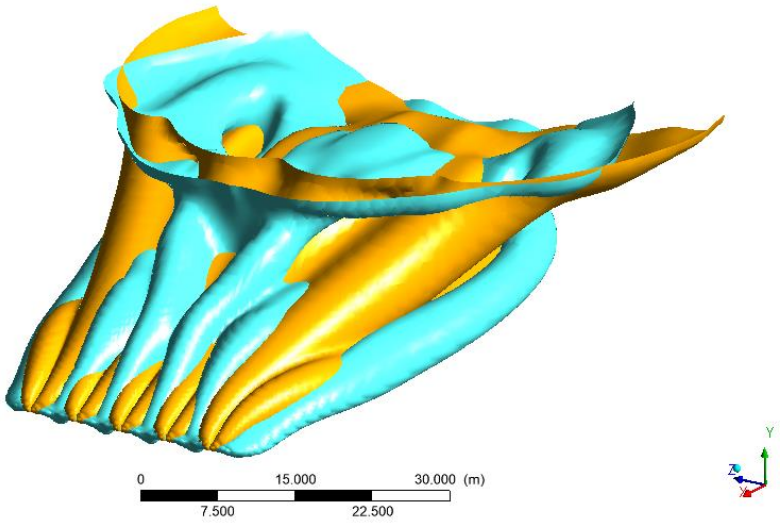

(b)

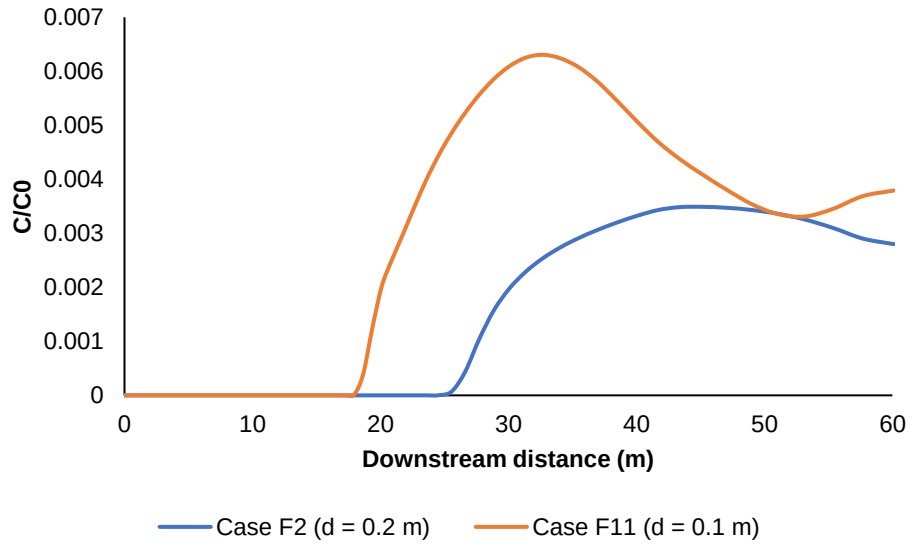

Figure 6-33. a) . Isosurface at locations where dilution is 1:1000 for case F2 (orange) and F11 (blue); **b)** Downstream normalised pollutant concentration for cases F2 and F11.

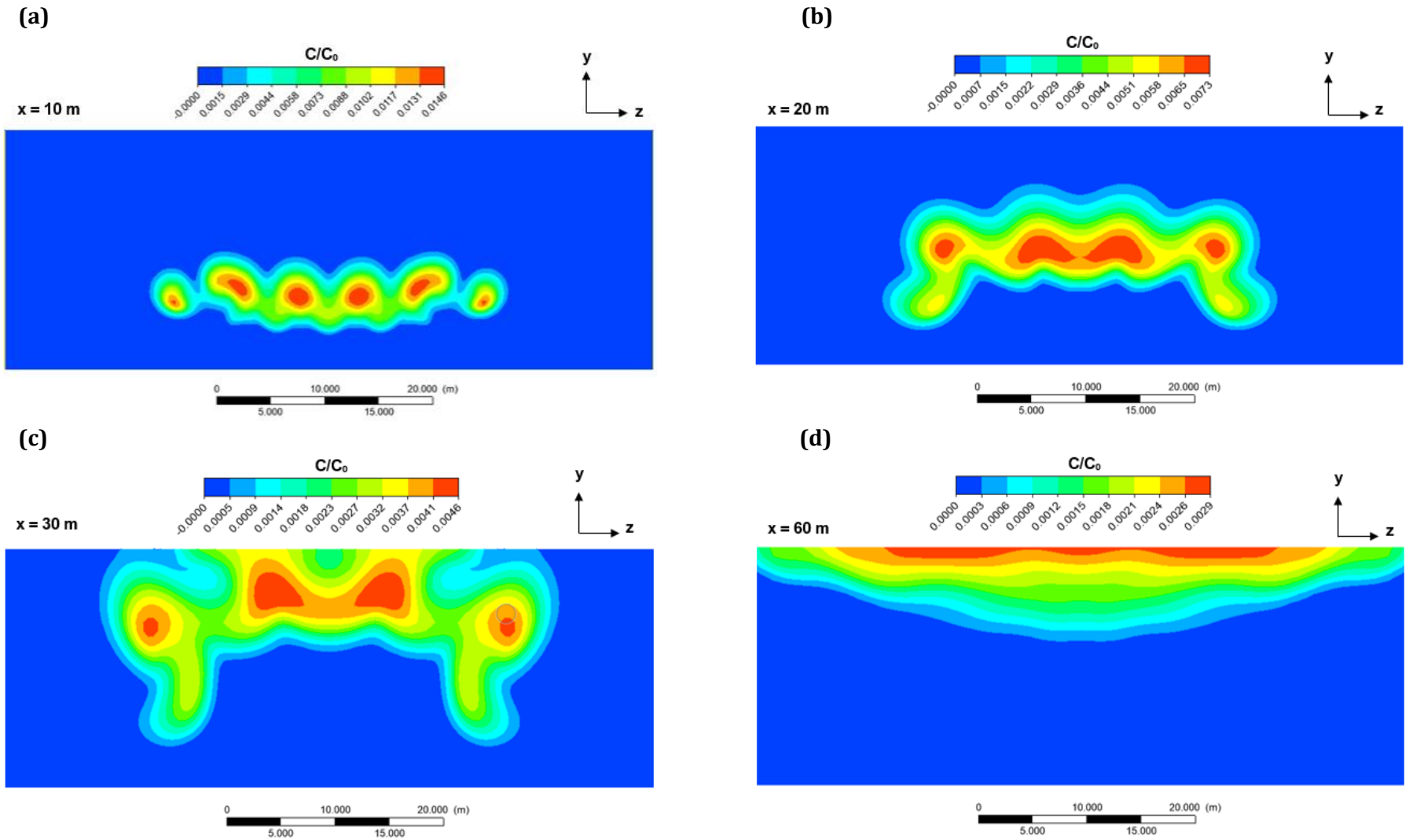

Figure 6-34. Contours of normalized pollutant concentration at **a)** x = 10 m; **b)** x = 20 m; **c)** x = 30 m; **d)** x = 60 m. Case F2 (port diameter of 0.2 m).

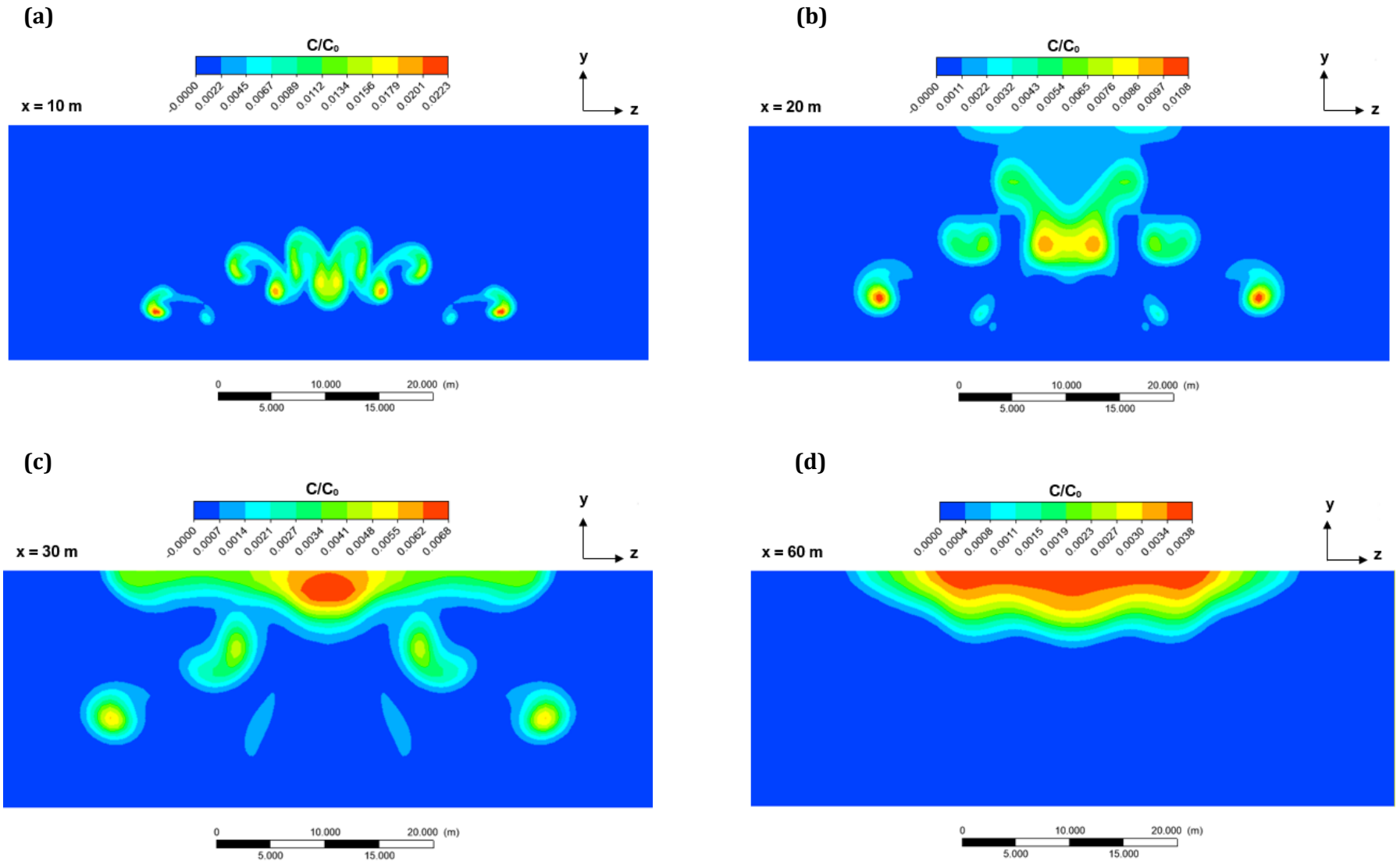

Figure 6-35. Contours of normalized pollutant concentration at **a)** x = 10 m; **b)** x = 20 m; **c)** x = 30 m; **d)** x = 60 m. Case F11 (port diameter of 0.1 m).

6.5.2.4 Effect of current direction.

All the cases described so far in this chapter assume a current perpendicular to the diffuser. However, as was described in section 6.3.2., that is not always the case in the Cartagena marine outfall. In order to evaluate the effect of current direction on the behaviour of the discharging plumes in the Cartagena marine outfall, two cases with equal discharge conditions are compared. Current velocity magnitude is maintained but for one of the cases, a current direction of 43° as shown in Figure 6-9 is used.

Table 6-6. Description of cases used for the comparison of different current direction.

	Parameter	***Symbol***	***Case***	
			F2	**F12**
Discharge conditions	Velocity (m/s)	u_0	0.5	
	Flow rate (m^3/s)	Q/n	0.0157	
	Temperature (°C)	T_0	31	
	Port diameter (m)	D	0.2	
	Port spacing (m)	S	5	5
	Type of port alignment	-	B	B
Ambient characteristics	Current velocity (m/s)	u_a	0.1	0.1
	Current direction (°)	-	90	43
	Ambient temperature (°C)	T_a	28	28
	Salinity (ppt)	S	36.5	36.5
	Water depth (m)	H	22	22
Nondimensional parameters	Froude number	F	0.58	-
	l_m	-	0.22	0.22

A comparison of the trajectory and shape of the plumes for cases F2 and F12 is shown in Figure 6-36. In the presence of an inclined current, the length of the near field is reduced and the plumes reach the surface approximately 15 m downstream from the discharge area, indicating a near field almost 3 times smaller than that obtained for a scenario with a perpendicular current.

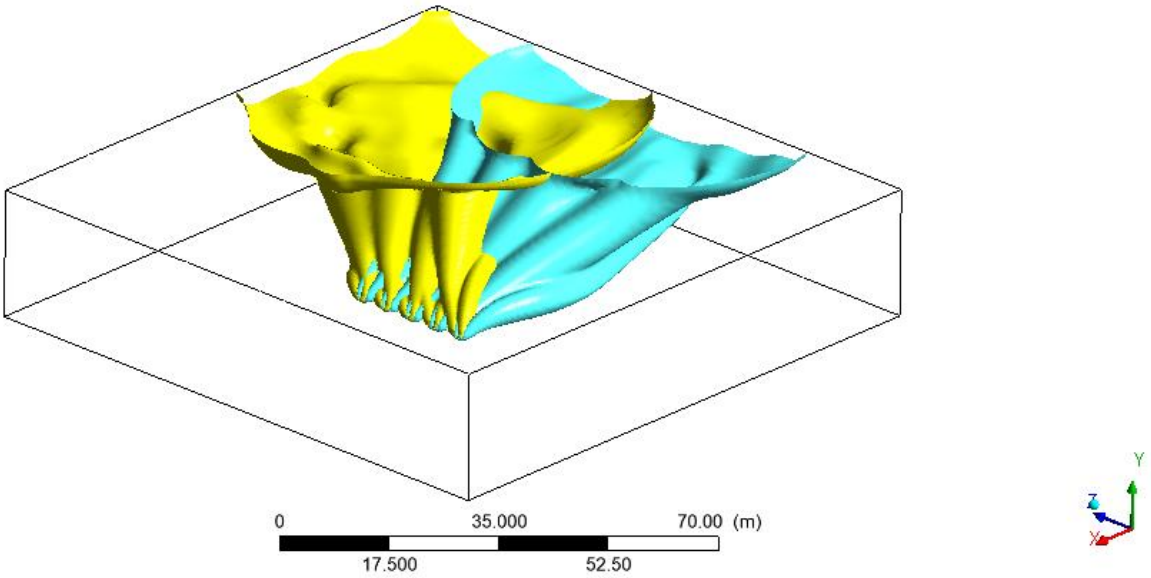

Figure 6-36. Isosurface at locations where dilution is 1:1000 for case F2 (blue) and F12 (yellow).

Additional to the observed effects on the length of the near field, an inclined current influences how the pollutant concentration is distributed along the z-axis, which is parallel to the diffuser. In cases with a perpendicular current, symmetry is observed, and the plumes located at the edges show lower pollutant concentration that those located in the central part of the diffuser. This can be observed in the contours of pollutant concentration at different locations downstream for case F2 (see Figure 6-34). However, in the presence of an inclined current, a different pollutant distribution is observed. The plumes located upstream from the inclined current (the right side of the isosurface in Figure 6-37) show higher pollutant concentration, as they serve as a barrier for the plumes further downstream.

The presence of an inclined current reduces the diffuser capacity for dilution, as can be observed when comparing Figure 6-34Figure 6-38. In an inclined current, some plumes serve as a barrier from the current for other; therefore, not all the plumes are equally exposed to it, reducing its capacity for mixing. Furthermore, as the plumes are pushed together, their capacity to entrain the ambient fluid is reduced. Consequently, the scenario with an inclined current of 43° as that used in case F12 achieves only 67% of the dilution that is observed for a perpendicular current as in case F2. This agrees with findings from previous studies by Roberts, et. al. (1989a), who stated that diffusers provide the maximum dilution when they are aligned perpendicular to the current.

In summary, the presence of an inclined current reduces the diffuser's capacity for mixing and results in a non-symmetrical distribution of the effluent in the z-axis. Similar effects are expected to occur in cases with port alignment type A.

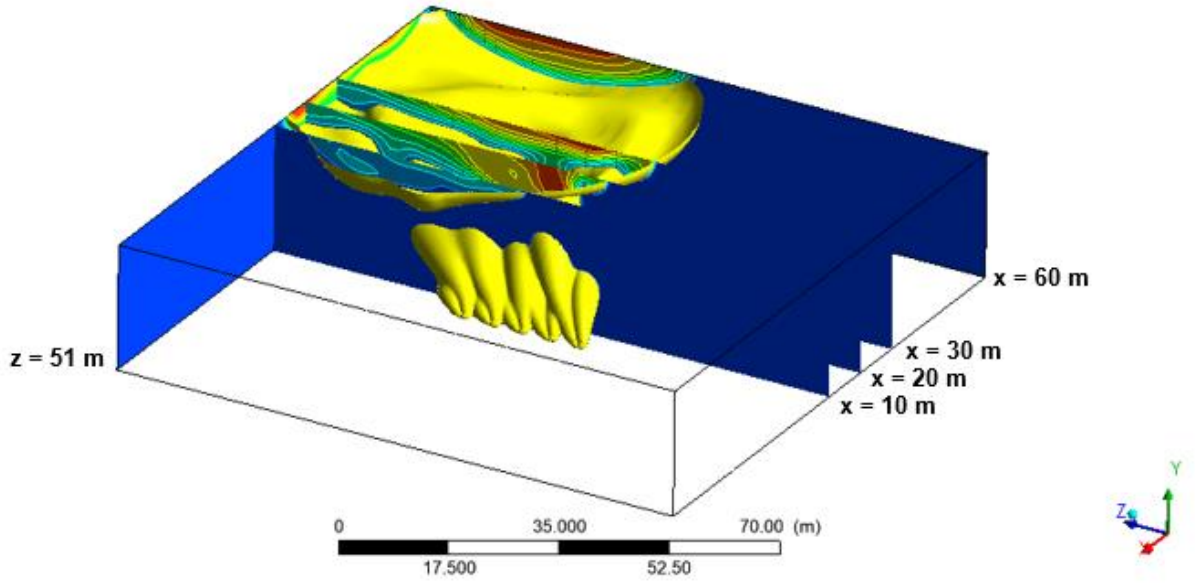

Figure 6-37. Isosurface at locations where dilution is 1:1000 for case F12 showing cross-sectional contours at different location downstream in the x and z axis. The legends of the contours at each cross-section are shown in Figure 6-38.

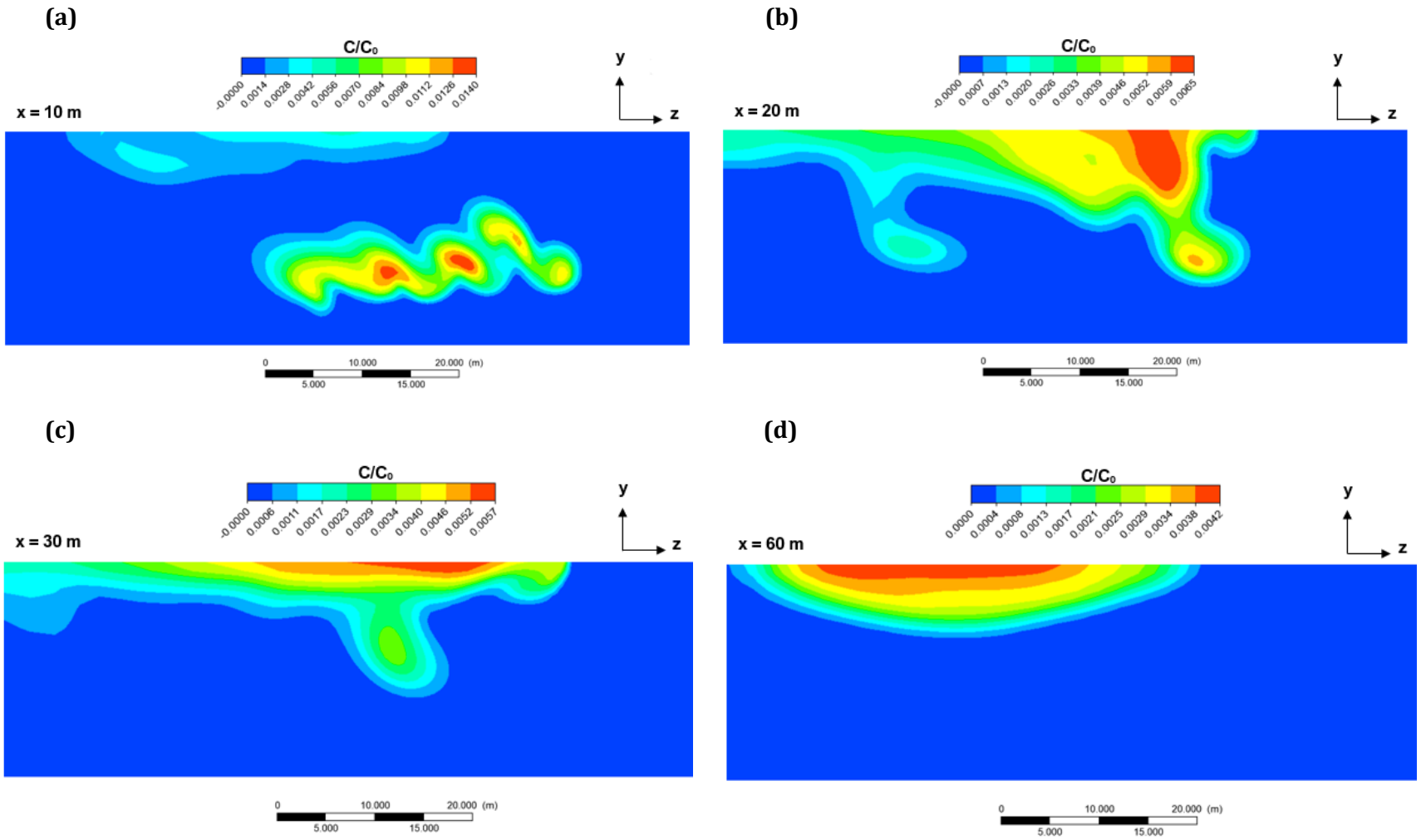

Figure 6-38. Contours of normalized pollutant concentration at **a)** x = 10 m; **b)** x = 20 m; **c)** x = 30 m; **d)** x = 60 m. Case F12 (port diameter of 0.1 m).

6.5.3 Near field modelling of an outfall discharge in a stratified flowing environment.

The scenarios previously described in this chapter are under the assumption that no density stratification is present in the near field of the Cartagena marine outfall. However, some stratification, although weak, is observed in this region, resulting primarily from temperature differences between the surface and bottom of the domain, as described in section 6.2.2.

Table 6-7. Description of cases used for the comparison of different current direction.

	Parameter	***Symbol***	***Case***	
			F2	**ST1**
Discharge conditions	Velocity (m/s)		0.5	
	Flow rate (m^3/s)	u_0	0.0157	
	Temperature (°C)	Q/n	31	
	Port diameter (m)	T_0	0.2	
	Port spacing (m)	d	5	
	Type of port alignment	s	B	
Ambient characteristics	Current velocity (m/s)	-	0.1	
	Current direction (°)	u_a	90	
	Ambient temperature at the surface(°C)	T_{as}	28	
	Ambient temperature at the bottom (°C)	T_{ab}	27	
	Salinity (ppt)	S	36.5	
	Water depth (m)	H	22	
Nondimensional parameters	Froude number	F	0.58	
	l_b	-	10.5	
	l_m	-	0.22	
	Buoyancy frequency	N	0.011	

The overall shape of the plumes is not significantly altered by the presence of the stratification implemented in case ST1 (see Figure 6-39). This can be further confirmed by comparing results from the contours of pollutant concentration shown in Figure 6-34 and Figure 6-40. However, the length of the near field is extended as the plume travels further before reaching the surface, as can be seen in Figure 6-39. Dilution is not significantly altered by the presence of this low-density stratification and it is only reduced by about 7%. An even weaker effect is to be expected for larger Froude numbers. This indicates that for cases with weak stratification like that found in the proximity of the Cartagena marine outfall diffuser, the effect of density stratification can be neglected without significantly affecting the accuracy of the results obtained.

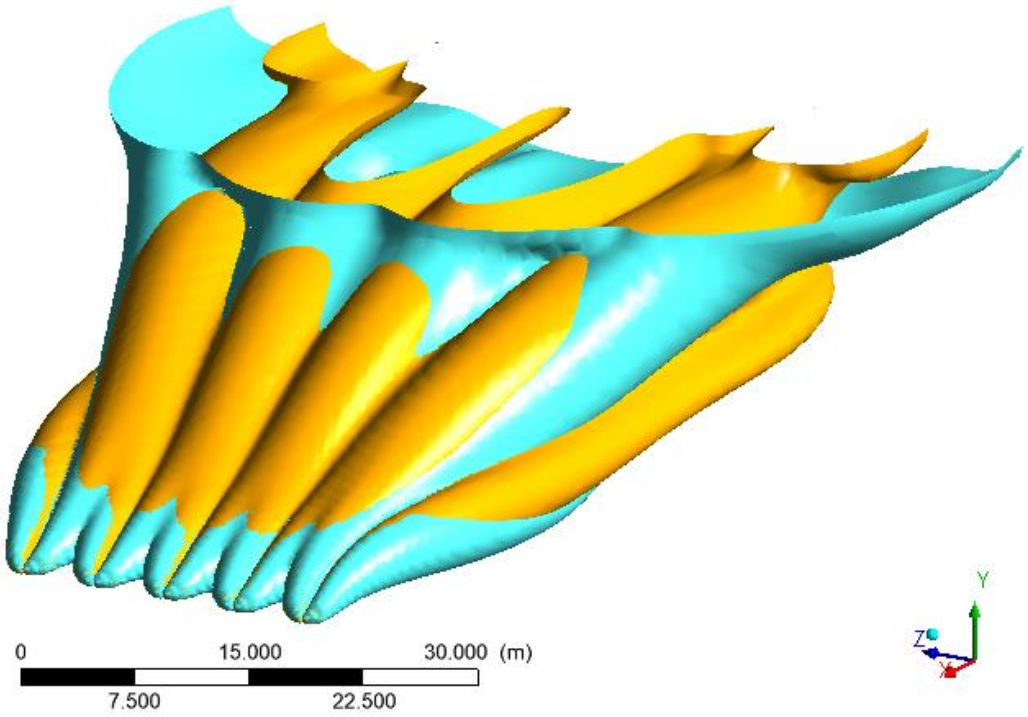

Figure 6-39. Isosurface at locations where dilution is 1:1000 for case F2 (blue) and ST1 (orange).

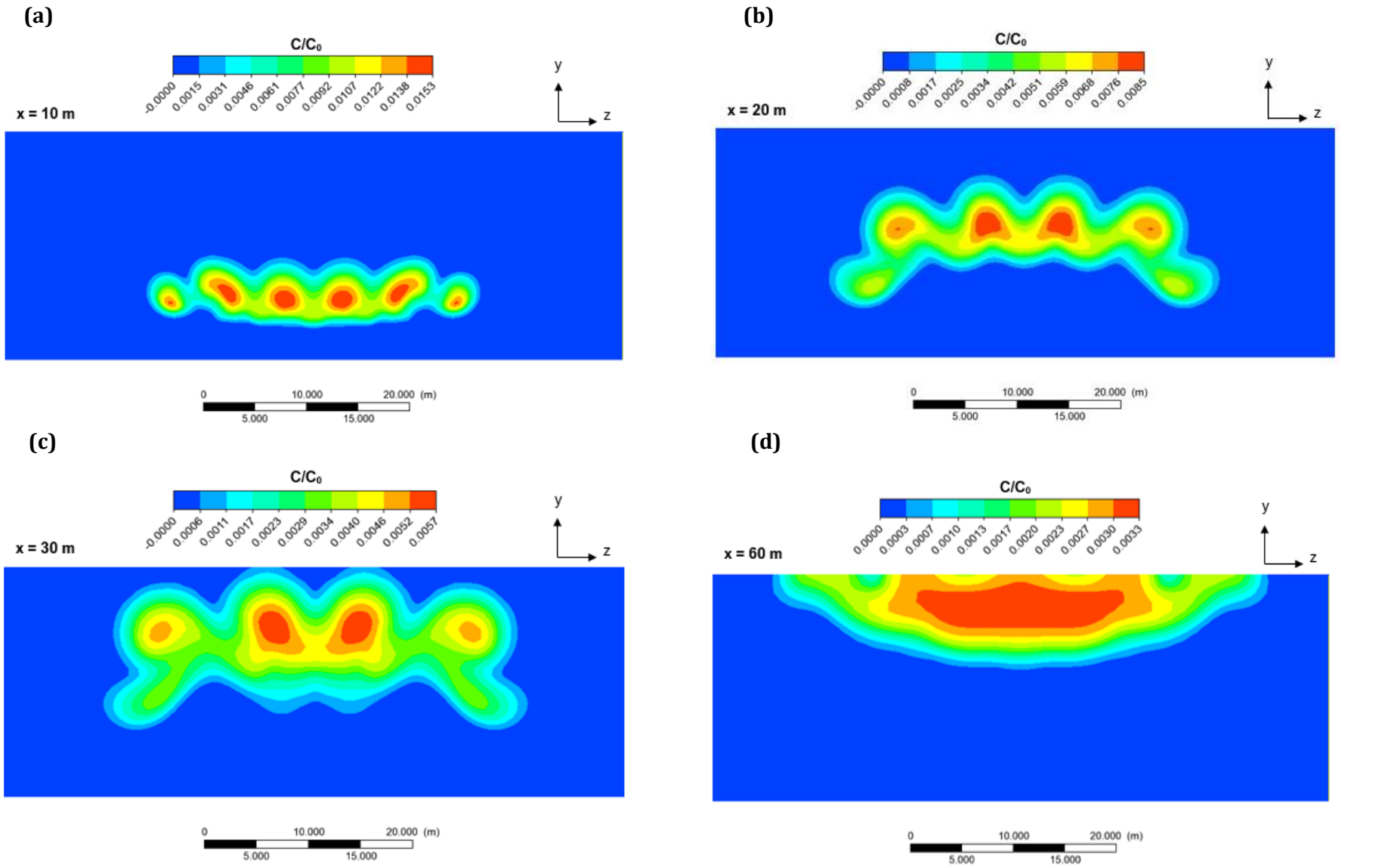

Figure 6-40. Contours of normalized pollutant concentration at **a)** x = 10 m; **b)** x = 20 m; **c)** x = 30 m; **d)** x = 60 m. Case F2 (port diameter of 0.2 m).

6.5.4 Summary of the effects of the changes in the constructed Cartagena marine outfall design.

As was mentioned previously in section 6.2, the original design of the Cartagena marine outfall was altered at the time of construction. The changes done to its original design include:

- Change in the alignment of the risers, from port alignment type A to type B.
- Increased number of risers, from 54 to 102. Since the length of the diffuser was maintained, this implied a reduction in the port spacing, from 20 m to 5 m.
- Reduced port diameter, from 0.2 m to 0.1 m.

The effects of these changes in the performance of the constructed diffuser were assessed individually in the previous subsections. A summary of its implications is described below:

- The change in the diffuser alignment signifies reduced dilution in scenarios of stagnant environment. A similar behaviour is observed for Froude numbers below 0.25 (see Figure 6-26a). However, for scenarios with Froude number over 0.25 the dilution achieved by port alignment type B is higher than that of a conventional port alignment, due to the more uniform exposure of all the discharged plumes to the current, thereby improving its mixing capabilities. The detrimental very low Froude numbers would only take place when very high flow rates are discharged (around 12.8 m^3/s), and/or current velocities close to zero. The maximum average discharge flow rate observed in the Cartagena marine outfall between 2013 and 2016 was 3.4 m^3/s. Therefore, scenarios where the port alignment implemented in the Cartagena marine outfall reduces the dilution achieved by the diffuser are rare. Nonetheless, it is important to consider that the effect of unsteady ambient and discharge conditions and potential pollutant build-up in the proximity of the discharge has not been studied and a different diffuser alignment may have a negative impact on this aspect.
- Increasing the number of risers and thereby reducing the spacing between ports resulted in a significant improvement in the near field dilution of the Cartagena marine outfall for the scenarios studied. This agrees with findings from laboratory-based studies on Tee-shaped risers with port alignment type A (Tian, et al., 2004b). For a case with perpendicular current of 0.1 m/s and discharging flow rate of 1.6 m^3/s, the simulation conducted in this chapter found that the increase in the number of ports increased dilution 1.8 times.
- The reduction in port diameter from 0.2 m to 0.1 m had a detrimental effect on the capacity for dilution of the resulting diffuser for the cases studied. The dilution obtained from a diffuser with smaller ports was between 30 to 50% lower for the scenarios studied.

In summary, the changes conducted to port alignment and number of discharging ports were favourable for the performance of the Cartagena marine outfall. Although the reduction in port diameter negatively affected the outfall's capacity for dilution, its negative effect is significantly lower than the advantages obtained from the change in port alignment and more importantly, the increase in the number of discharging ports. Additional research is required to study the effects of these changes on potential concentration build-up in the area of the discharge.

6.6 PROPOSED METHODOLOGY FOR THE NEAR FIELD SIMULATION OF REAL-LIFE MARINE OUTFALL DISCHARGES.

The lessons learned from the CFD simulation of the Cartagena marine outfall for varying discharge and ambient conditions were the base for the development of a framework for the implementation of RANS modelling techniques for the simulation of the near field of real-life marine outfall discharges. This proposed methodology has been organised by stages, as described below.

Step 1: Identify the most critical scenarios for dilution based on the observed discharge and ambient conditions for the marine outfall to simulate. The three-dimensional CFD modelling, despite the enhanced meshing techniques proposed in this research, continues to be computationally expensive, and the simulation of the scenarios presented in this study could take between 5 to 15 days using High Performance Computing resources. Therefore, the use of CFD techniques could be used for critical scenarios or other situations in which conventional semiempirical and/or entrainment models may result in significantly lower accuracy. Some of these situations include:

- Where significant boundary interactions take place, including outfall discharging in relatively shallow waters.
- Scenarios in which the diffusers have more complex or unconventional alignments, such as the constructed alignment of the Cartagena marine outfall.
- Diffusers in which adjacent ports have different sizes or water discharges from different sources that interact with each other. This implies that the simulation of unequal plumes is required.
- Cases in which significant edge effects are observed, including short diffusers with closely spaced ports.
- Scenarios in which the ambient current is not perpendicular to the diffuser but rather inclined.

Step 2: Select the most efficient domain and mesh for the simulation of the scenarios selected. In the selection of the domain, it is important to consider if simplifications can be undertaken to reduce its size, including the use of symmetry planes. For cases where edge effects may be significant, particularly for small port spacings ($s/H<1$), the simulation of 5 risers as implemented for the Cartagena marine outfall can be conducted. For more widely spaced ports, this edge effects are reduced, and the simulation 2 or 3 risers may suffice.

In terms of meshing, one main question should be asked at the beginning of this process: how much precision is required for this project? The research presented in this study focused on obtaining mesh independent results at all relevant areas of the plumes studied. This mesh independence was achieved by using a relatively coarse initial mesh and conducting additional refinements based on an initial solution. However, this level of precision may be required for the design and monitoring of marine outfalls, and simplifications can be made. The modeller should then perform a mesh independence study and decide the level of accuracy may suffice to predict the overall behaviour of the flow and the dilution obtained in the near field. The mesh adaption method used in this work could help greatly on reducing the computational cost of the mesh without sacrificing the required accuracy.

Step 3: Decide the turbulence model and other turbulence parameters to be used. Based on the results of this study, the realizable k-ε is a reliable model for the simulation of buoyant jet

discharges from single and multiple port discharges. Turbulent Schmidt number is recommended within 0.6 and 0.9, as discussed in Chapter IV.

This framework is proposed under the assumption that time-dependent variations in the discharge and ambient conditions are not simulated at the near field level, since the time scale in which near field processes occurs is a matter of minutes (between 6 and 7 minutes for the cases studied in this chapter), and no significant changes in the discharge and ambient conditions may occur in this small time frame.

6.7 CONCLUSIONS.

The near field of a real-life scale marine outfall located in the city of Cartagena, Colombia was successfully simulated using the RANS realisable k-ε model. The computational cost of modelling a real-life scale outfall was reduced by simulating only 5 risers of the 102 Tee-shaped risers present in the Cartagena marine outfall and the use of a mesh adaption approach. The domain used enabled the study of plume behaviour based on their location in the diffuser, and the prediction of their trajectory and capacity for dilution. The main conclusions drawn from this study are listed below:

- The location of a plume in the diffuser affects their merging process and capacity for mixing. Plumes located at the edges moves further before merging with the adjacent plumes when compared to the plumes exiting from central risers. For this reason, plumes located at the edges show lower pollutant concentrations. Further downstream, as they approach the central plumes, they suddenly deflect towards the central area, drawn by the stronger entrainment field of the already merged central plumes. This agrees with laboratory and numerical findings of the studies on unequal plumes described in the previous chapter.
- In a stagnant unstratified environment, the use of a diffuser with port alignment type B rather than a conventional port alignment, reduces the diffuser capacity for mixing. Port alignment type A shows a dilution 13% higher at the impact point and 26% higher further downstream when compared to port alignment type B.
- In a flowing environment with Froude numbers higher than 0.15, port alignment type B shows greater capacity for dilution than a conventional port alignment. This is due to all the plumes being equally exposed to the current, as opposed to having some plumes in counter-flow and some in co-flow, as is the case for diffusers with port alignment type A. In this conventional port alignment, the plume in counter-flow serves as a barrier from the current for the plume in co-flow, reducing its potential for mixing.
- Port size has a more significant effect on the performance of a diffuser with port alignment type B when compared to a conventional port alignment. Smaller ports reduce the diffusers capacity for dilution when discharging equal flow rates.
- Most of the changes done to the original design of the Cartagena marine outfall were favourable for its performance. Although using a smaller port diameter reduced the outfall's capacity for mixing, this negative effect is much less significant than the advantages obtained from the change in port alignment and more importantly, the increase in the number of discharging ports.

7 COUPLING NEAR FIELD AND FAR FIELD MODELS.

7.1 Introduction.

The previous chapters have focused on the local effects of single and multiple port discharges in the near field, examining the effects of diffuser geometry and ambient conditions on the dilution achieved at the outfall scale. However, further from the source, the transport of the effluent is mainly driven by the ambient conditions, which are intrinsically complex in coastal waters, where a variety of unsteady processes take place.

This chapter aims to understand the effect that the method for coupling the near field of wastewater discharges has on the far field flow. To test the effect of the coupling method, discharge and ambient conditions on the transport at the far field scale, the Cartagena marine outfall is used as a case study. The far field of this outfall has been previously studied by Bleninger (2006) and Roberts & Villegas (2006), who coupled near field results predicted by CORMIX and NRFIELD models, respectively, with the Delft3D coastal circulation model.

Near field results of dilution and plume shape obtained in the previous chapter using CFD techniques are used as discharge conditions for the simulation of the far field in this chapter. Delft3D-FLOW, a hydrodynamic and transport model part of the open-source software Delft3D (DELTARES, 2011), is used for the far field simulation. Finally, an overall framework for the simulation of marine outfall discharges at different scales is proposed.

It is important to highlight that the aim of this chapter is to understand the effect of the coupling method and ambient conditions in a *real-life* far field area. The results obtained will be indicative and cannot be considered representative of the real performance of the Cartagena marine outfall, since many significant processes such as wind, density stratification and tidal variations are not considered in the simulations presented here, as is described in the following subsection.

7.2 Methodology for near and far field coupling of the Cartagena marine outfall.

In this subsection, a detailed description of the methodology used for the simulation of the far field of the Cartagena marine outfall is presented. This includes a description of the governing equations, numerical methods, boundary conditions and an in-depth analysis of two specific coupling methods that are later analysed.

7.2.1 Governing equations.

The far field simulation of the Cartagena marine outfall is based on the numerical solution of the Unsteady Reynolds-Averaged Navier-Stokes equations for an incompressible fluid, as described in section 3.2.1. The shallow water and Boussinesq assumptions are used.

In the horizontal direction, orthogonal curvilinear co-ordinates were used. In the vertical direction, a σ-coordinate system is used. This system consists of a series of layers that follow the bottom topography and the free surface.

Under the shallow water assumption, the vertical momentum equation is reduced to the hydrostatic pressure equation, and the vertical accelerations due to buoyancy effects and topography variations are not accounted for. The hydrostatic pressure equation for a σ-grid is given by:

$$\frac{\partial P}{\partial \sigma} = -g\rho h \quad \textbf{(7.1)}$$

The transport of pollutants and tracers in the domain is modelled by solving the advection-diffusion equation (as described in Chapter III). The density of the water is modelled as a function of temperature and salinity using the UNESCO formulation (equation 3.19 from Chapter III).

The turbulence closure is achieved using the standard k-ε model, defined in equations 3.9-3.10. The bed shear-stress is determined using the Manning equation. For the cases modelled here, a constant Manning coefficient of 0.0025 $m^{-1/3}/s$ is assumed.

7.2.2 Computational domain and spatial discretization.

As previously mentioned, the Cartagena marine outfall has been selected for the evaluation of the coupling approach between near and far field. The computational domain chosen for the far field simulations covers an area of 27 km by 35 km around the outfall location. This computational domain and the corresponding grid have been previously used by Bleninger (2006) and Roberts & Villegas (2006). It is assumed that this area is small enough to consider that spatial climatic variations have negligible effects on the hydrodynamics of the flow.

A structured curvilinear grid (in plan) was used, so that lines are curved following the shape of the land boundaries. The area with the highest grid resolution is located near the area of discharge, with a minimum grid size of 50 m. Closer to the open boundaries, the size of the grid is approximately 2300 m (see Figure 7-1).

For the vertical discretization, the σ-coordinate system was used, which divides the water depth in layers, following the topography. To accurately solve near-bed and near-surface processes, higher resolution was assigned to these areas. A total of 13 layers were assigned and the layer thickness of each layer from top to bottom was: 2%, 3%, 4.5%, 6.75%, 10%, 15%, 17.5%, 15%, 10%, 6.75%, 4.5%, 3% and 2 % of the water depth (see Figure 7-2).

Figure 7-1 shows the horizontal grid applied to the Cartagena far field computational domain. The highest resolution near the discharge area can be observed. In the graphic Columns 1 to 6 correspond to the cells along the diffuser length.

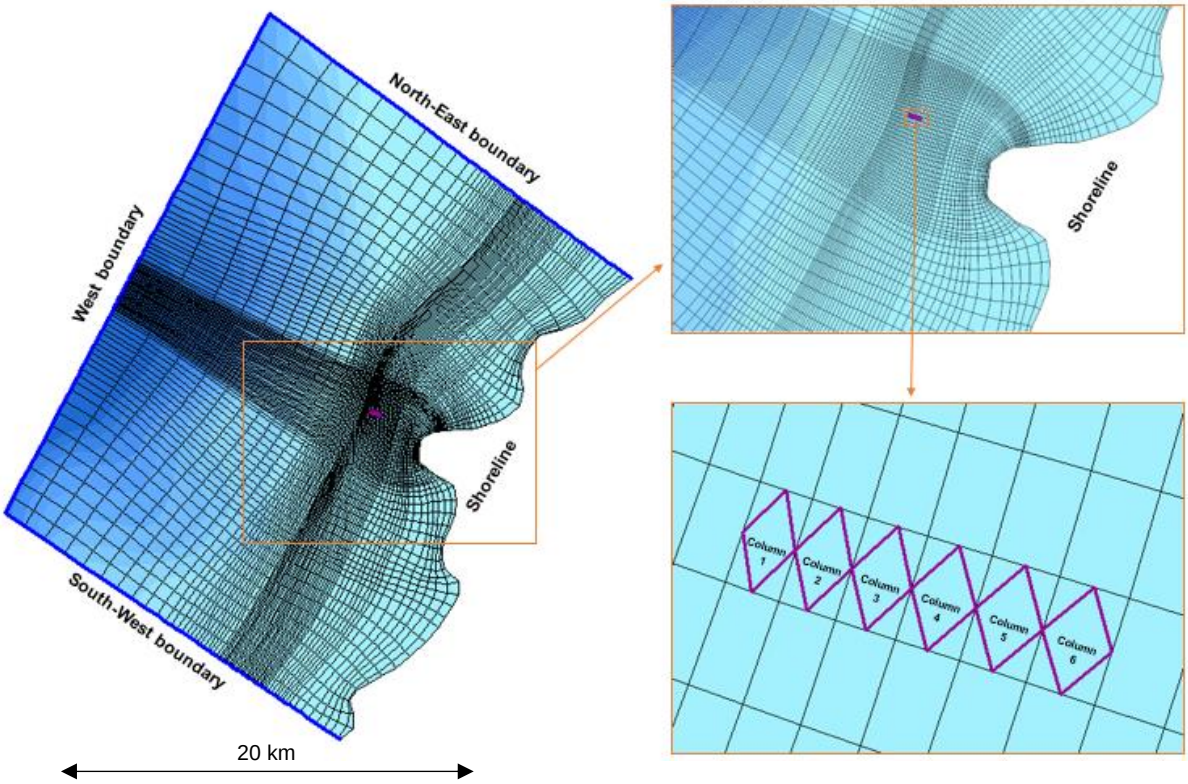

Figure 7-1. Computational domain for far field simulations of the Cartagena outfall. Column 1 to 6 correspond to the cells along the diffuser length.

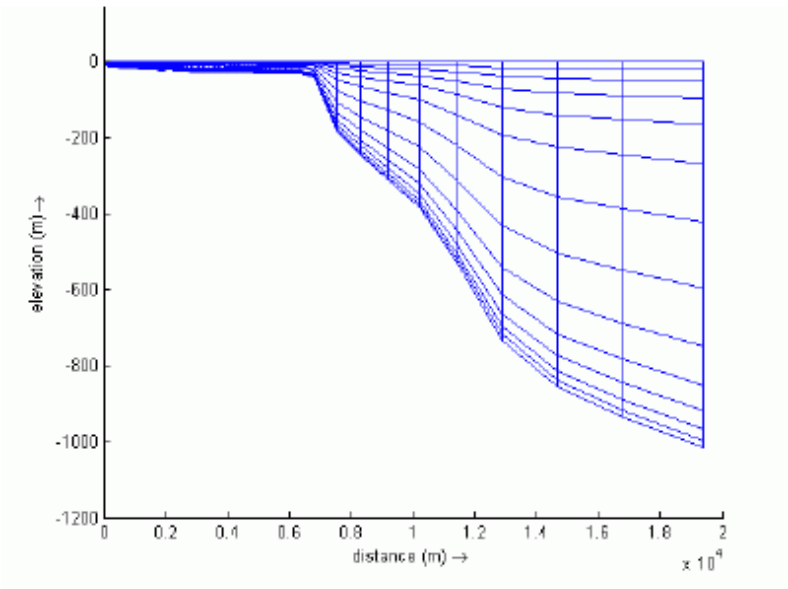

Figure 7-2. Vertical cross-section through model domain. The outfall is located approximately 2.8 km from the shore, which corresponding to the shallow area in this graph.

7.2.3 Temporal discretization.

Simulations were undertaken for a one-month period, which hypothetically corresponds to February 1998. Since stratification was not simulated, the required time step to obtain convergence was 5 minutes, as was previously tested by Roberts & Villegas (2006) and Bleninger (2006) for the selected grid.

7.2.4 Open boundary conditions.

The open boundaries represent the influence of the area beyond the model domain. A constant water level or current was assigned to each boundary. Tidal variations, salinity and temperature stratification were considered to have a small effect and thus not necessary, this had the effect of simplifying the far field model.

- **North-East Boundary:** Steady currents were assigned, perpendicular to the boundary and ranging between 0.1 m/s and 0.3 m/s towards the South-West, since measured currents are within this range most of the time.
- **West Boundary:** A constant water level of 0 m from the reference level was assigned. No tidal variations were applied.
- **South-West boundary:** Steady currents were assigned, perpendicular to the boundary and ranging between 0.1 m/s and 0.3 m/s towards the South-West.

7.2.5 Initial conditions.

The initial conditions are zero water elevations and velocities at all grid points. The results of this initial simulation are used as initial conditions for the next run. After approximately a week of simulation, the effects of the initial conditions were considered to no longer be present.

7.2.6 Discharge conditions.

In order to couple the near and far field, the outfall effluent must be connected to the far field as a discharge.

From near field simulations, it was observed that the furthest that the plume travels before reaching its maximum rise height (which defines the end of the near field) for current magnitudes within the range studied (0.1 to 0.3 m/s) is approximately 100 m downstream from the diffuser location. This distance is negligible considering the expanse of the domain; therefore, little effects should be expected if the discharge is located along the diffuser length. Bleninger (2006) followed the same premise when coupling the near and far field of the Cartagena outfall.

The vertical distribution of the discharge is a more complex task. Bleninger (2006) simplified this by dividing the effluent flow by the number of cells selected for coupling. By assuming that the flow exiting each cell is equal, a higher exit velocity would be observed at the surface, which decreases moving down the water column.

This method of coupling ignores the concentration profiles obtained in the near field modelling, focusing solely on the location of the plume and not on the distribution of the effluent in that location. Employing this method would signify that the precision of the near field model has little effect on the far field model. To take into account the distribution of the effluent at the location of coupling obtained in the near CFD model, a different approach was formulated and tested against the Bleninger (2006) method.

Figure 7-3 shows the shape of a plume resulting from the discharge of 3.2 m^3/s of wastewater in an environment with perpendicular current of 0.3 m/s (case 2 of Table 7-2). The plume shows the appearance of being trapped below the surface due to the high current velocity. The following steps detail the coupling process applied to this specific case.

Step 1: *Selection of the coupling location.*

As was previously discussed, the distance that the plume travels before reaching the end of the near field for the cases studied are insignificant in comparison to the size of the domain. For this reason, the selected location for coupling in the horizontal plane corresponds to the length of the diffuser, along Columns 1 to 6 (see Figure 7-1).

In the vertical plane, the specific layers in which coupling is conducted are identified from the distribution of the pollutant at a vertical cross-section intersecting the end of the near field.

For case 2, the contours of normalised pollutant concentration are shown in Figure 7-3. It is observed that the pollutant is concentrated in the top 9 σ-layers of the Delft3D domain. Figure 7-4 shows a clearer depiction of this. In this figure, the coupling area is specified between the two central T-shaped risers. Since only 5 of the 102 T-shaped risers in the Cartagena outfall diffuser were modelled using the CFD approach, it is not possible to automatically transfer all the velocity and concentration profiles obtained in the near field model to the far field one. By selecting the central area as the area to transfer, possible edge effects that have little effect on most of the T-shaped risers located in the Cartagena outfall are eliminated.

Resulting from this analysis, it is then concluded that for case 2, the discharge should be assigned to the top 9 σ-layers of Columns 1 to 6 (see Figure 7-5).

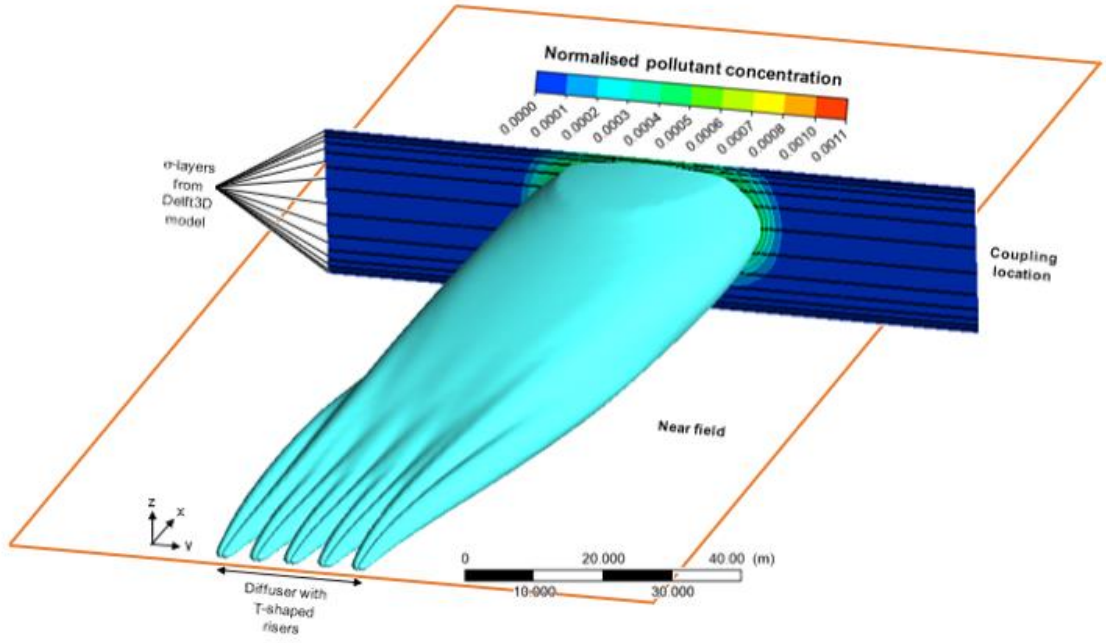

Figure 7-3. Near field results for an outfall discharging a flow of 3.2. m^3/s in an ambient with perpendicular current velocity of 0.3 m/s. The isosurface of the plume at a normalised pollutant concentration 0.001 is shown as well as the contours of normalised pollutant concentration at the coupling location. The orange lines give an approximate idea of the size of a cell in the far field model near the area of discharge.

Step 2: *Identifying the effluent distribution in the selected coupling location.*

The discharge conditions are assigned to the model by inputting a discharge flow to each cell in which coupling is conducted. A constant pollutant concentration of 100 kg/m^3 is found in the discharge, so that the variations of the incoming pollutant mass depends only on the flow variations per cell and cell size.

In order to transfer the shape of the concentration profiles into the far field model (see Figure 7-4b), an equivalent velocity profile is computed. Note that an equivalent velocity profile rather than a flow profile is computed first, to consider the different cell sizes and ensure that the exit velocity is constant for each water layer.

In order to produce the equivalent velocity profile, the concentration profile is simplified, assigning constant values to each layer. The pollutant concentration assigned to each layer, $C_{layer\ i}$, is the maximum value observed in that specific layer. The local pollutant concentration per layer, $C_{layer\ i}$, is then normalised by the maximum concentration value observed in all the layers, C_{max}. In the example case, the maximum concentration value observed is 0.0011, as can be observed in Table 7-1.

Once the local velocity per layer has been defined as a percentage of the maximum value observed, the maximum velocity in the domain is then computed. This maximum velocity is defined by the calculation:

$$Total\ discharge\ flow = \sum\left((Normalised\ velocity)_{layer\ i} \cdot (Area)_{layer\ i}\right) \cdot \boldsymbol{Max.velocity} \quad \textbf{(7.2)}$$

Once the maximum velocity in the domain is computed, the velocity per layer can then calculated -multiplying this value by the corresponding normalised velocity of each layer (see Table 7-1). The total flow assigned to each cell is finally computed by multiplying the cell area by the corresponding velocity. The total flow obtained by adding the flow in each cell corresponds to the effluent flow of the outfall, ensuring the conservation of mass.

The velocity and flow distribution obtained for the example case is shown in Figure 7-6. A similar approach is replicated for all cases where coupling between near field CFD simulations and the far field is conducted.

(a)

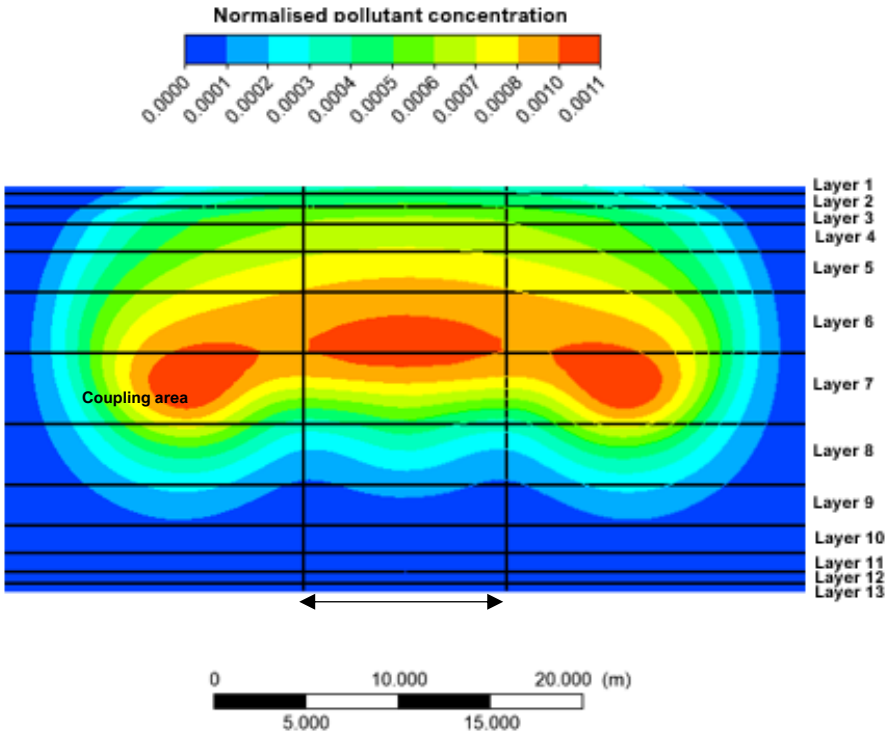

(b)

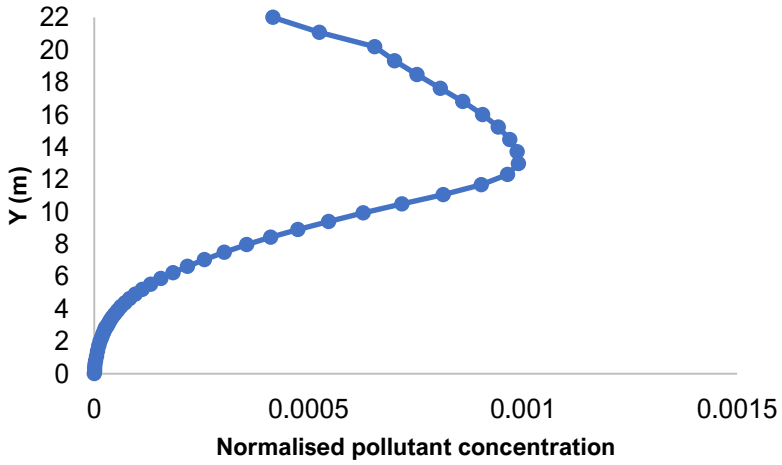

Figure 7-4. Near field results for a case of an outfall discharging a flow of 3.2. m^3/s in an ambient with perpendicular current velocity of 0.3 m/s. **a)** Contours of normalised pollutant concentration at the coupling location; **b)** Normalised pollutant concentration profile along the water depth at the coupling location.

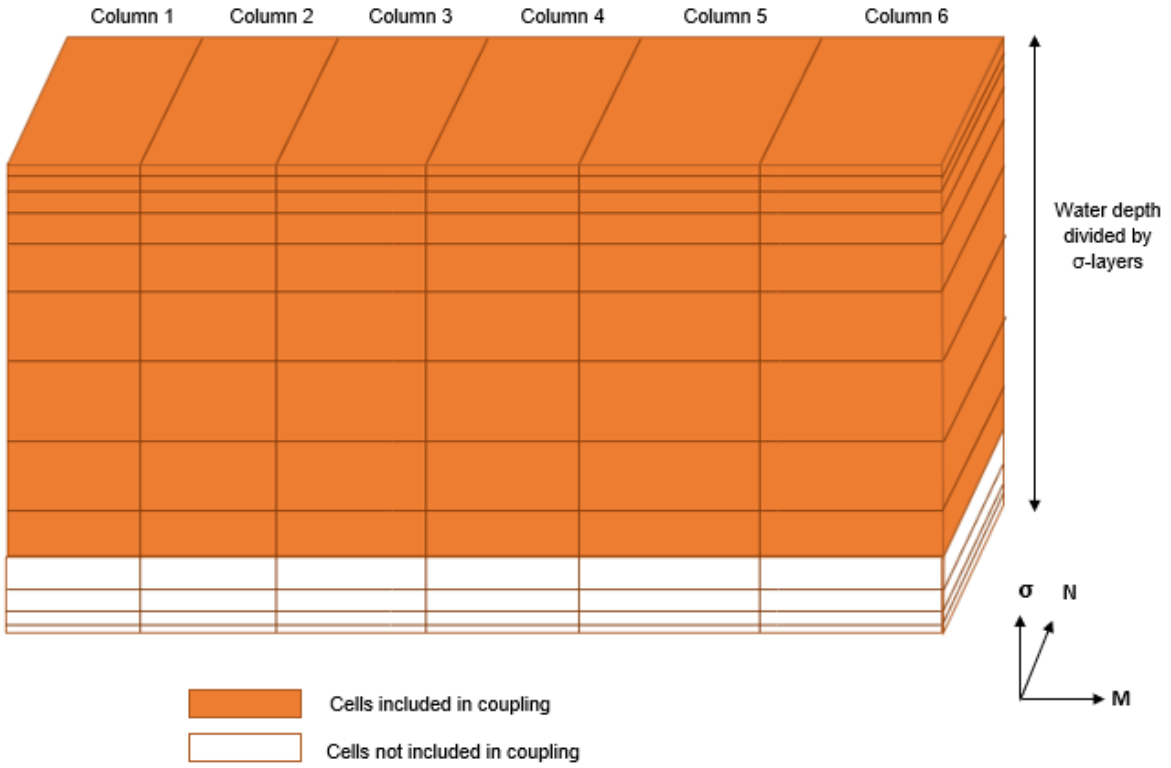

Figure 7-5. Schematic of the cells included in coupling the case 2, discharging a flow of 3.2. m^3/s in an ambient with perpendicular current velocity of 0.3 m/s. For the location of Columns 1 to 6 in the far field domain, see Figure 7-1.

Table 7-1. Computation of velocity profile to be assigned to the far field model for the case with outfall discharge of 3.2 m^3/s and current velocity of 0.3 m/s.

	$C_{layer\ i}$	$\frac{C_{layer\ i}}{C_{max}}$	**Normalised velocity**	**Velocity per layer (m/s)**
Layer 1	0.0005	45.45%	45.45%	0.00021
Layer 2	0.0006	54.55%	54.55%	0.00025
Layer 3	0.0007	63.64%	63.64%	0.00029
Layer 4	0.0008	72.73%	72.73%	0.00033
Layer 5	0.001	90.91%	90.91%	0.00041
Layer 6	0.0011	100.00%	100.00%	0.00046
Layer 7	0.0011	100.00%	100.00%	0.00046
Layer 8	0.0005	45.45%	45.45%	0.00021
Layer 9	0.0002	18.18%	18.18%	0.00008
Maximum velocity observed (m/s)				0.00046

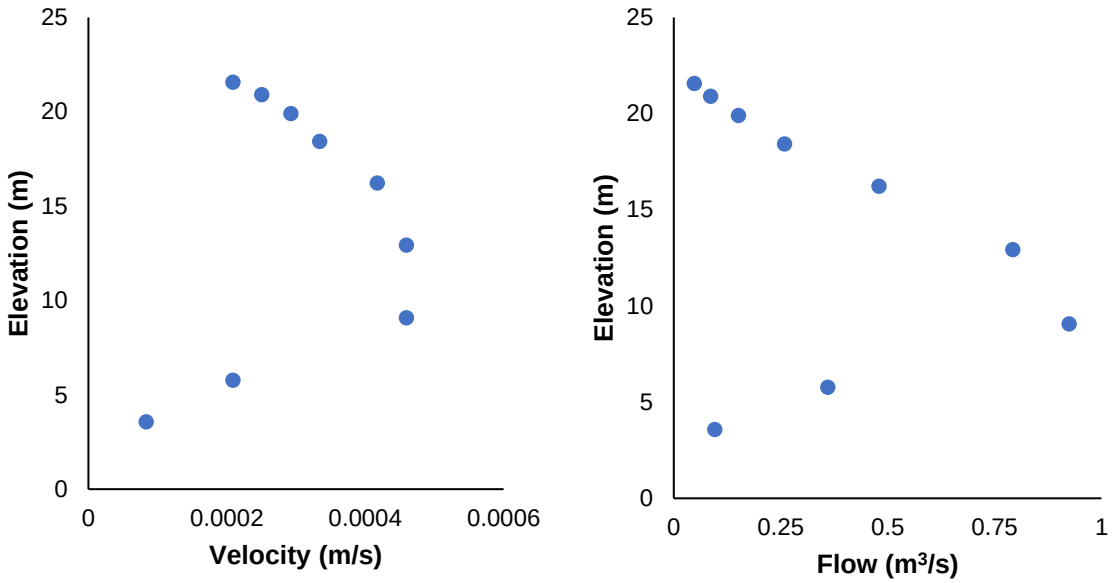

Figure 7-6. a) Velocity and **b)** flow distribution along the water depth obtained for case 2, with outfall discharge of 3.2 m^3/s and current velocity of 0.3 m/s.

7.2.7 Summary of modelling cases.

A set of cases is defined to assess three main aspects: 1) effect of the coupling method used; 2) effect of the initial ambient conditions; 3) effect of the initial discharge flow rate. A summary of the cases modelled for coupling the near and far field of the Cartagena marine outfall are described in Table 7-2.

Table 7-2. Summary of modelling cases.

Case	North-East boundary	South-West boundary	West boundary	Wind	Discharge	Purpose
Case 1	Constant current of 0.3 m/s perpendicular to the boundary towards South-West.	Constant current of 0.3 m/s perpendicular to the boundary.	Constant water level of 0 m. No tidal effects.	The effect of wind is ignored.	Constant discharge of 3.2 m/s. Flow is distributed equally over top cells identified in case 2.	To compare the effect of using the coupling approach of Bleninger (2006).
Case 2	Constant current of 0.3 m/s perpendicular to the boundary.	Constant current of 0.3 m/s perpendicular to the boundary.	Constant water level of 0 m. No tidal effects.	The effect of wind is ignored.	Constant discharge of 3.2 m/s. Flow is distributed according to CFD results.	To compare the effect of using profiles obtained from CFD simulation for different current velocities and
Case 3	Constant current of 0.1 m/s perpendicular	Constant current of 0.3 m/s perpendicular	Constant water level of 0 m. No tidal effects	The effect of wind is ignored.	Constant discharge of 3.2 m/s. Flow is distributed	

	to the boundary.	to the boundary.			according to CFD results.	discharge flows.
Case 4	Constant current of 0.1 m/s perpendicular to the boundary.	Constant current of 0.3 m/s perpendicular to the boundary.	Constant water level of 0 m. No tidal effects	The effect of wind is ignored.	Constant discharge of 6.4 m/s. Flow is distributed according to CFD results.	

7.3 RESULTS AND DISCUSSION.

In the following subsections, the results from simulations of two cases with different coupling approaches, ambient and discharge conditions is presented. This is followed by a detailed analysis and comparison of their relative performance. Such analysis serves as a base for the construction of a detailed coupling approach that is proposed for the simulation of real-life marine outfalls under time-varying conditions.

7.3.1. Comparison between coupling methods.

The following two coupling methods are compared in this section:

- *Coupling method 1:* equal flow exiting from each discharge cell (case 1).
- *Coupling method 2*: flow distribution based on the predicted shape of the effluent plume from the CFD model (case 2).

From the plume shape obtained for the CFD near field simulation, it was found that the effluent is located in the top nine layers of columns 1 to 6 for the discharge and ambient conditions defining case 1 and 2.

As described above in the methodology section, both cases are forced by a current velocity of 0.3 m/s towards South-West at both the North-East and South-West open boundaries. The effluent discharge is constant over time, with a total value of 3.2 m^3/s. This case was chosen since under these discharge conditions, a current velocity of 0.3 m/s results in a plume that is trapped under the surface; therefore, the vertical distribution of the effluent is significantly different for both coupling methods. For cases with lower current velocity, the plume reaches the surface and the highest effluent concentration is found at the top, which is like the plume shape that is obtained using coupling method 1.

The results obtained fluctuate during the first week, after which convergence is achieved where the simulations reach a state that can be considered steady with very minimal changes observed in the velocity field and the spatial distribution of the effluent. All results shown in the following subsections correspond to this end of the modelling period.

7.3.1.1. Depth averaged velocity.

Depth averaged velocity vectors for cases 1 and 2 are shown in Figure 7-7. No variations are observed on the velocity distribution across the domain. This result is to be expected, since the only difference between both cases is the approach to coupling the discharge in the domain. The discharge flow is too small to have a significant effect on the velocity field. This is the case of the

majority of wastewater marine outfalls that typically operate in such a way to that a minimum dilution of 100 is achieved (Bleninger, 2006).

For the cases presented, the velocity is approximately 0.11 m/s in the area of discharge, moving uniformly towards South-West, perpendicular to the diffuser. Higher velocities are observed near the open boundaries.

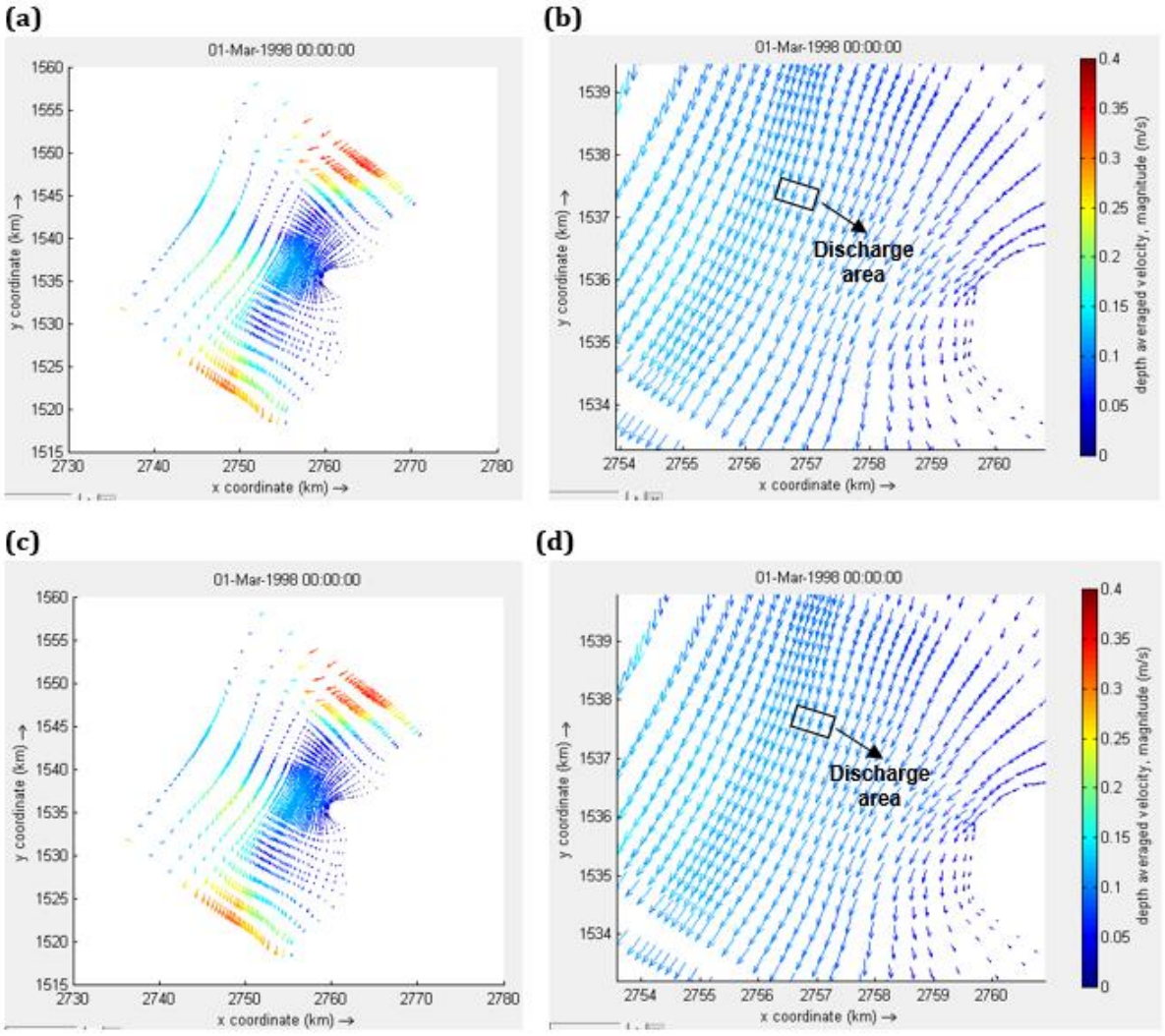

Figure 7-7. Depth averaged velocity vectors in: a) model domain of case 1; b) discharge area of case 1; c) model domain of case 2; c) discharge area of case 2.

7.3.1.2. Spatial distribution of the outfall effluent.

The goal of far field modelling is understanding the transport and mixing of the outfall effluent. For this reason, it is important to compare the spatial distribution of the effluent due to the different coupling methods used.

Overall, both cases show a similar trajectory of the outfall plume, demonstrating that it is primarily moved by the current and the momentum from the discharge has little effects on the overall trajectory of the effluent. Starting from the region of the discharge, the outfall effluent is initially transported by the current towards the South-West. It spreads laterally and as it

approaches the South-West boundary, its trajectory shifts towards the South until it reaches the shoreline.

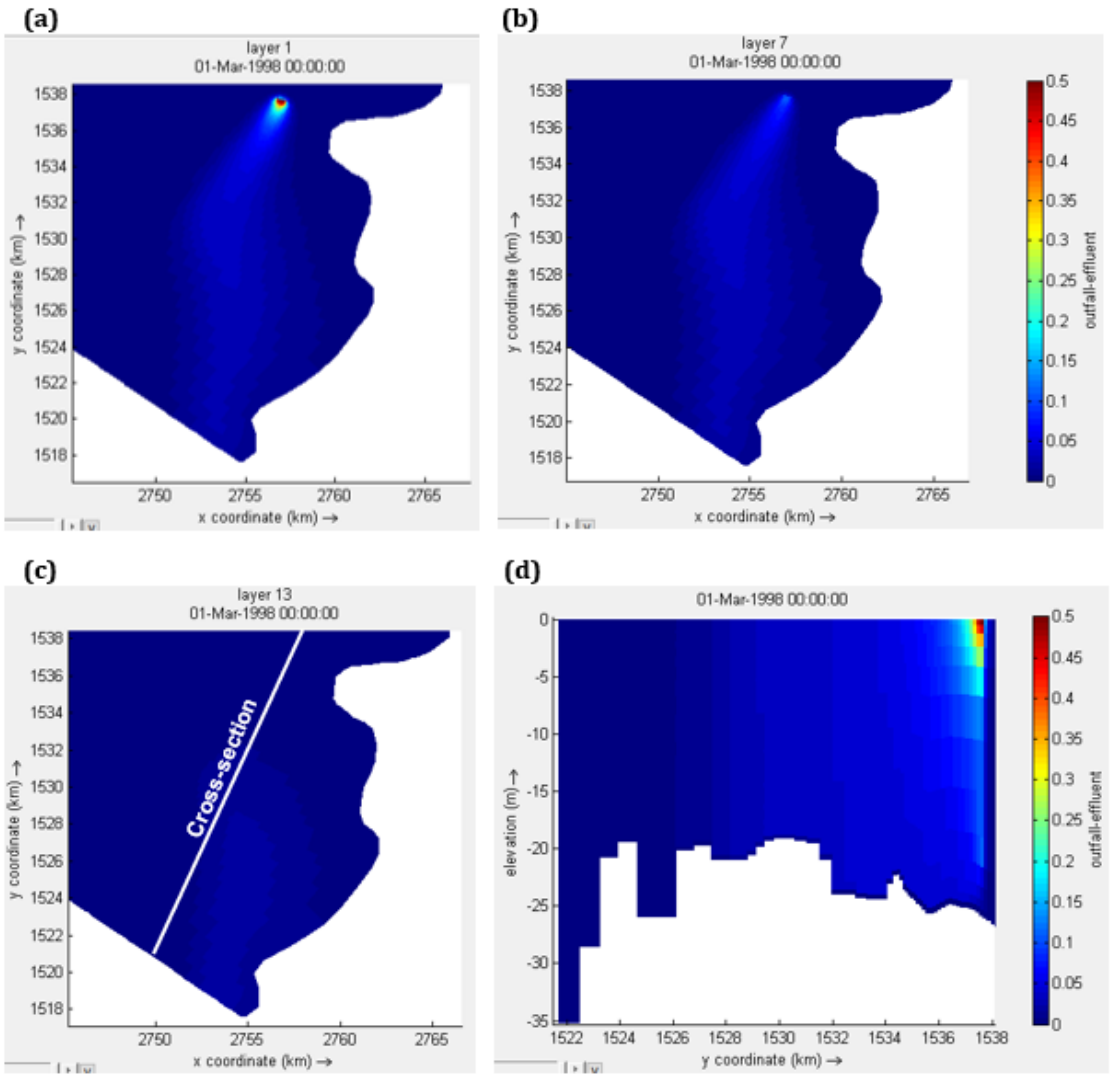

Figure 7-8. Contours of effluent concentration (kg/m^3) at different locations for case 1: a) water surface; b) top 58.75% of the water depth, c) bottom; d) along the cross-section shown in (c).

Despite the similarities in the overall trajectory of the outfall plume in the far field for the different coupling methods studied, the local concentrations of the pollutant vary. Figure 7-8. and Figure 7-9. show the contours of effluent concentration over a cross-section that cuts the diffuser in half (starting from coordinates X: 2757 km, Y: 1538 km) and continues downstream, parallel to the North-East boundary. In these figures, differences in the vertical distribution of the outfall effluent near the source are evident. For case 1, higher pollutant concentrations are found closer to the surface, reducing towards the bottom. On the other hand, case 2 shows higher concentrations mid-depth. However, the peak concentrations in case 2 are lower than those found in case 1.

The uniform flow distribution assumption used in case 1 implies that closer to the top where cells are smaller, higher pollutant concentration will be found. Despite the different values obtained near the discharge, further downstream, the effluent becomes more uniformly distributed

vertically and no significant difference is observed for the coupling methods studied. This is further confirmed in the comparison between vertical distributions of the outfall effluent downstream, approaching the South-West boundary, with coordinates X: 2754 km, Y: 1519 km (see Figure 7-10a). The difference between the obtained values is approximately 0.9%, as can be observed in Figure 7-10b.

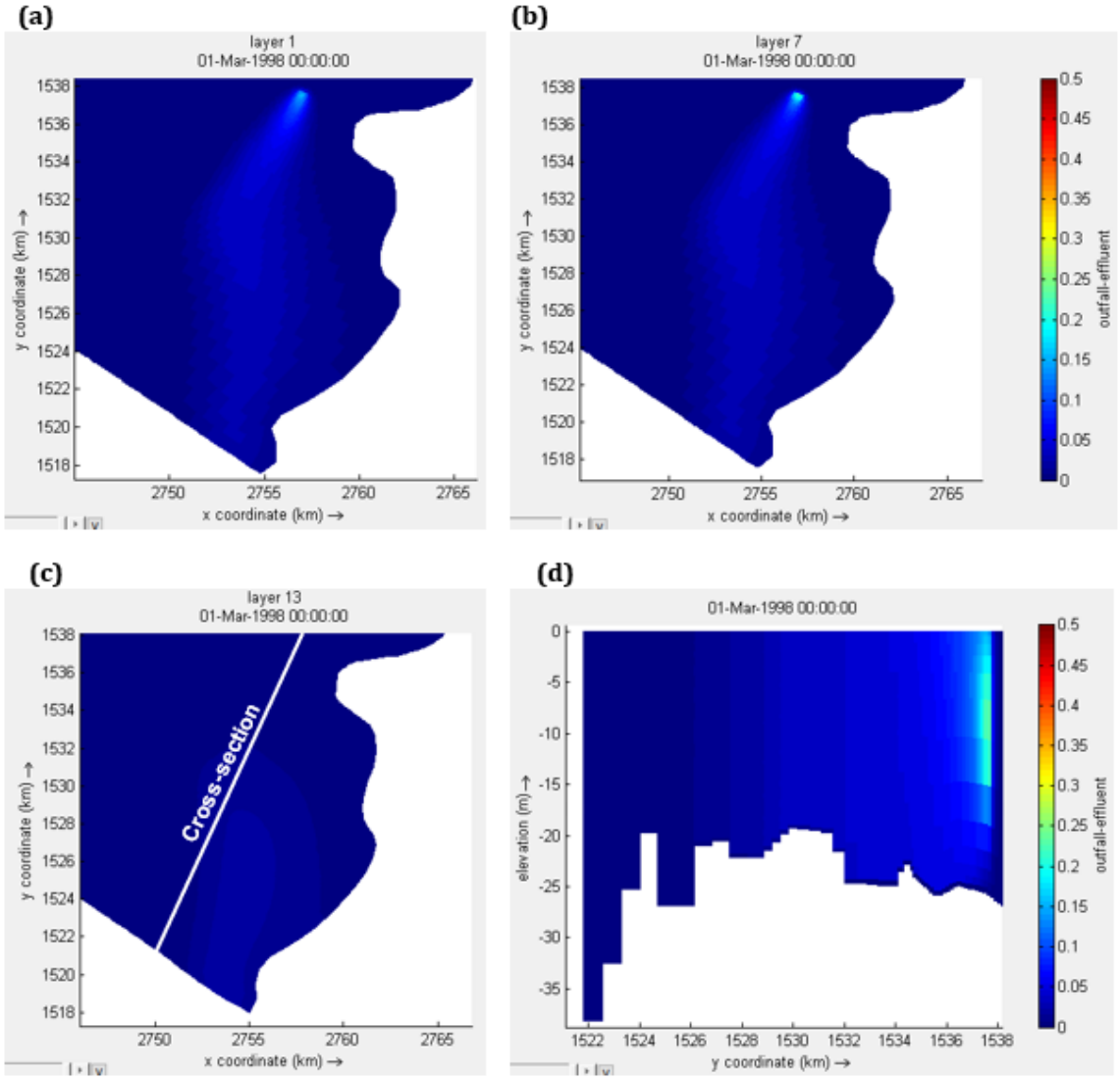

Figure 7-9. Contours of effluent concentration (kg/m^3) at different locations for case 2: a) water surface; b) top 58.75% of the water depth, c) bottom; d) along the cross-section shown in (c).

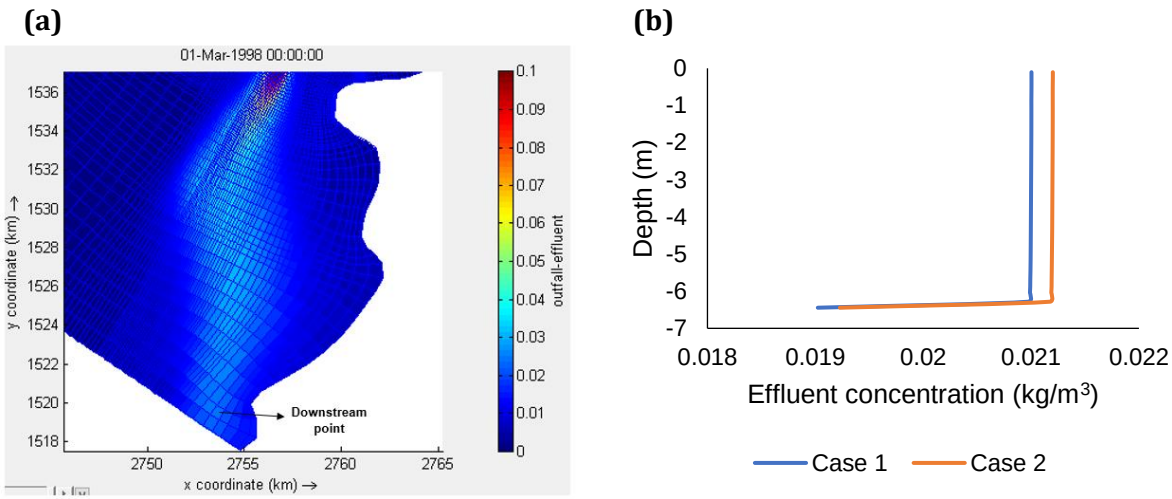

Figure 7-10. (a) Location of downstream point near the South-West boundary in a effluent contour plot of case 1; (b) Comparison of the vertical effluent distribution at the downstream point shown in (a).

Despite the similarities in the overall trajectory and pollutant concentration downstream, it is important to note that in the presence of wind, the vertical distribution of the pollutant would have a greater effect on its transport and mixing, since the wind would lead to different velocity magnitude and/or direction nearer the surface. Similar effects could be expected from tidal forcing and density stratification. Therefore, it seems reasonable to assume that once this variable is taken into account, the differences found for the different coupling methods would have greater significance.

The similarities in the downstream effluent concentration and its ultimate uniform distribution result from the vertical spreading of the effluent. In the absence of tidal forcing, wind and density-driven currents, the effluent is expected to diffuse along the water column and ultimately reach a uniform distribution.

Overall, it can be concluded that in the absence of tidal forcing, wind and density-driven currents, both coupling approaches tested only represent significant differences near the discharge and, for the case studied, up to 5 km downstream. Therefore, a more accurate distribution of the pollutant in the near field, as that obtained from CFD methods, may only have a substantial effect in cases where the velocity magnitude and/or direction varies significantly along the water depth.

7.3.2. Effects of current velocity magnitude.

In order to understand the effects of the current velocity magnitude, two main cases are compared, assigning currents of 0.3 m/s (case 2) and 0.1 m/s (case 3) perpendicular to the North-East and South-West boundaries and in the South-West direction. The discharge flow is constant for both cases and equal to 3.2 m^3/s, but its distribution along the water depth is different and based on the shape of the plume obtained from the near field results.

In the case with a current velocity of 0.3 m/s, the CFD obtained plume is distributed over the top 9 layers, with the highest pollutant concentrations found in the mid-depth of this layers (as shown in subsection 7.2.7). On the other hand, for case 3, the effluent is distributed over the top 6 layers, and the maximum pollutant concentration is found at the surface.

7.3.2.1. Depth-averaged velocity.

As is to be expected, the overall direction of the flow in the domain is not significantly altered by the changes in the assigned current velocities at the boundaries. However, near the discharge, the current direction shifts about 45° towards the East in case 3. This could be due to the lower current velocity magnitude that makes the flow direction more susceptible to changes in the terrain.

Near the discharge area, the observed current velocity is approximately 0.08 m/s for case 3, compared to the 0.11 m/s value found for case 2. This indicates that even though the current velocity magnitude assigned at the open boundaries in case 2 is 3 times that assigned in case 3, the difference in the local velocity near the discharge is not as large.

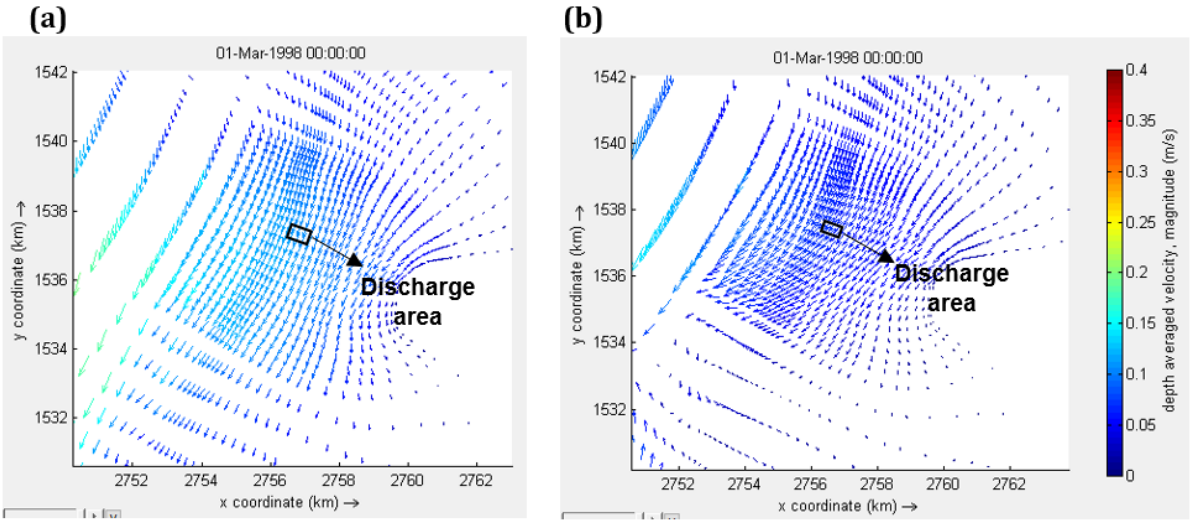

Figure 7-11. Depth-averaged velocity near the discharge area for: a) case 2 and b) case 3.

7.3.2.2. Spatial distribution of the outfall effluent.

Two main aspects play a role in the observed spatial distribution of the outfall effluent for the cases compared here: firstly, the magnitude and direction of the current in the domain and secondly, the vertical distribution of the outfall effluent at the discharge.

The shifts observed in the depth-averaged velocity direction for case 3 results in the plume having a different trajectory to that observed for case 2, reaching the shoreline closer to the discharge area (see Figure 7-12). This is due to the 45° shift in the current direction that was described in the previous subsection, which results in the plume deviating its trajectory, initially further from the shore and later shifting again towards the shoreline.

This observation is further confirmed in the comparison between effluent concentration at the shoreline shown in Figure 7-13. The highest effluent concentrations are found nearer to the discharge area for case 3. Nonetheless, the effluent concentration is more uniformly distributed horizontally along the downstream side of the shoreline for this case. On the other hand, higher values are only found in the far South edge for case 2. Higher dilution is clearly observed for the case with the highest current velocity, as is to be expected, which is easily identified by comparing Figure 7-9 and Figure 7-12.

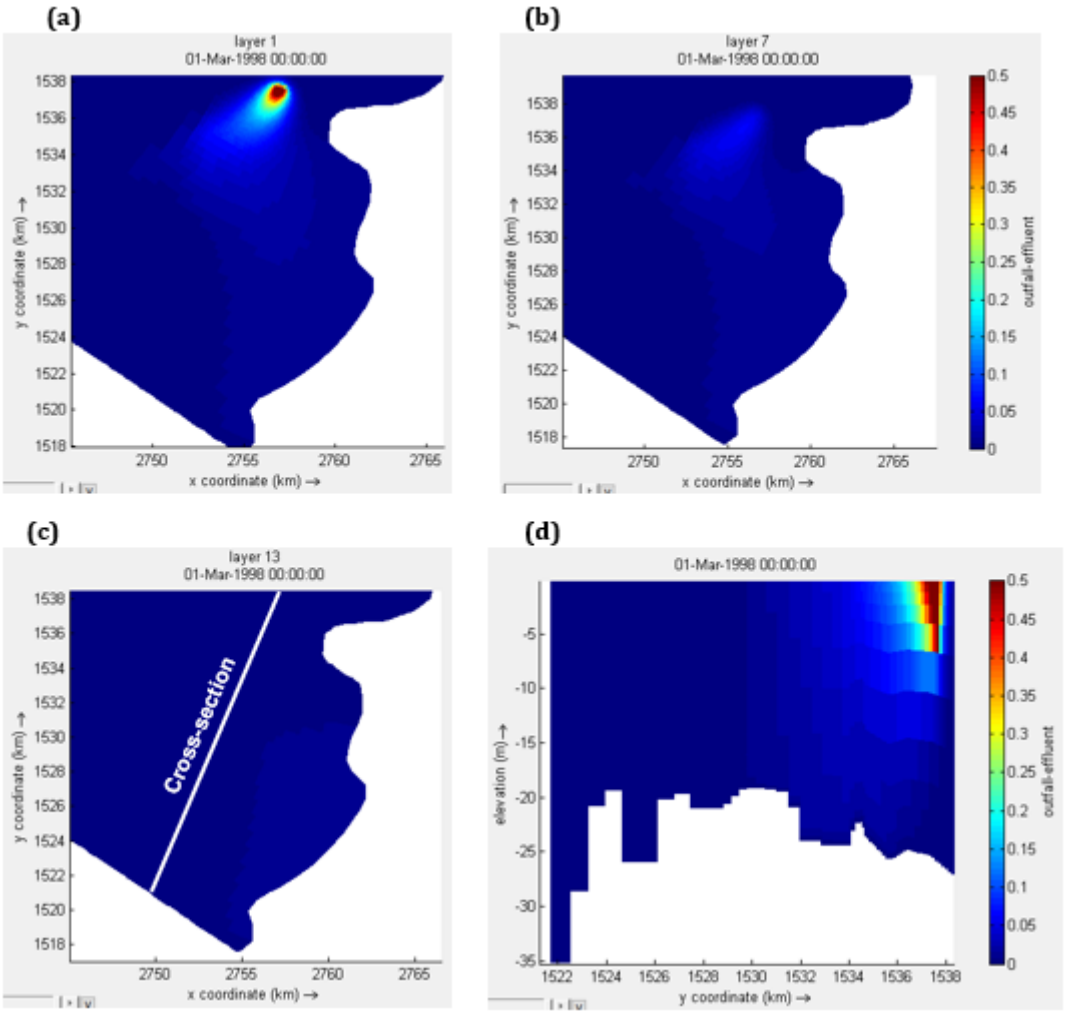

Figure 7-12. Contours of effluent concentration (kg/m^3) at different locations for case 3: a) water surface; b) top 58.75% of the water depth, c) bottom; d) along the cross-section shown in (c).

The second aspect that could affect the observed differences in the spatial distribution of the effluent is the initial discharge distribution along the water depth, which was assigned based on the near field modelling results. For case 2, the higher initial current resulted in the plume being distributed over a wider area (top 9 layers), getting trapped under the surface so that the maximum pollutant concentration is found below the surface (see Figure 7-9d). On the other hand, for case 3, the lower current velocity allowed the plume to quickly rise to the surface, reducing its mixing capacity in the near field. This resulted in a plume where the maximum pollutant concentration is found at the surface (see Figure 7-12d).

Similar to what is observed in the previous subsection where two coupling approaches are compared, the initial distribution of the discharge has larger effects at the local level. However, with the lower ambient current magnitude and shift in direction observed for case 3, the vertical distribution of the effluent takes longer to become uniform when compared to case 2, due to the reduced mixing. Hence, an for observation case 3 is higher concentrations are found near the surface, even as far as along the shoreline, as shown in Figure 7-13b.

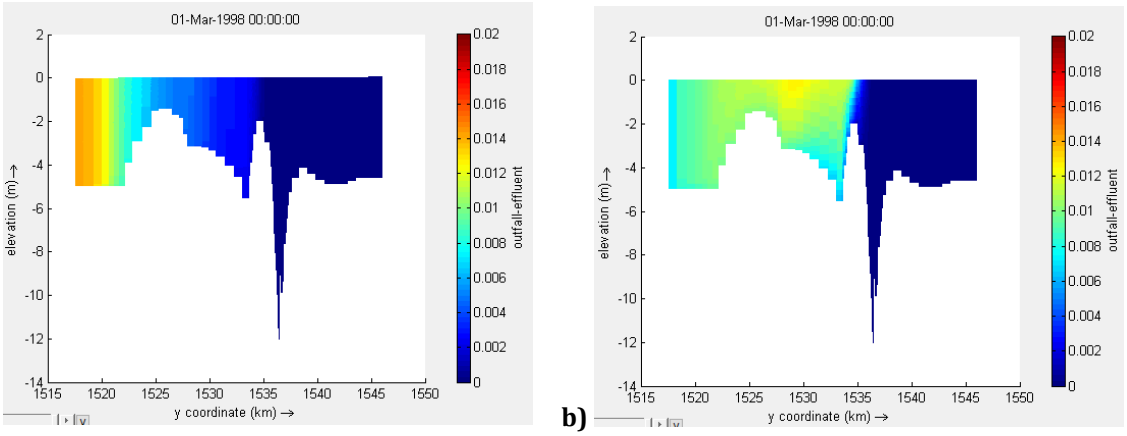

a) **b)**

Figure 7-13. Comparison of effluent concentration (kg/m3) along the shoreline for **a)** case 2 and **b)** case 3.

7.3.3. Effects of effluent discharge flow.

In the previous subsections, the effects of the discharge distribution and the varying ambient conditions have been tested, maintaining a constant discharge flow rate of 3.2 m^3/s. In this subsection, the effect of the discharge flow rate is tested by doubling its value. The initial current velocity magnitude at the boundaries is set at 0.1 m/s. Cases 3 and 4 from Table 7-2 are compared. These particular scenarios were chosen since a lower current velocity represents a more critical condition for mixing.

As previously described, the near field simulations for case 3 found that under this discharge and ambient conditions, the plume rises to the surface and the highest effluent concentration is found at the top. The effluent is distributed over the top 6 layers. A similar plume shape was observed for case 4.

7.3.3.1. Depth-averaged velocity.

As observed in the comparison between cases 1 and 2, no significant difference was found in the overall direction and trajectory of the flow in the domain for cases 3 and 4, despite the increased flow rate of case 4. This indicates that even though a higher effluent flow is being discharged in case 4, it is still not significantly large enough to alter the flow field both near the discharge and further downstream. The observed velocity field for both cases is accurately represented as shown in Figure 7-11b.

7.3.3.2. Spatial distribution of the outfall effluent.

The variation in the discharge flow rate did not alter the overall distribution of the effluent in the domain, indicating that the major factor driving how the effluent is transported are the ambient hydrodynamics. This coincides with the theoretical definition of the far field as the region where the ambient conditions dominate the behaviour of the plume (Morelissen, et al., 2013; Roberts, 2013; Roberts, et al., 2010).

The results obtained show that doubling the initial flow rate simply increased the concentration of the pollutant in the field, without altering the overall horizontal and vertical distribution of the effluent in the domain, as can be seen by comparing Figure 7-12 and Figure 7-14, and the concentration along the shoreline in Figure 7-15.

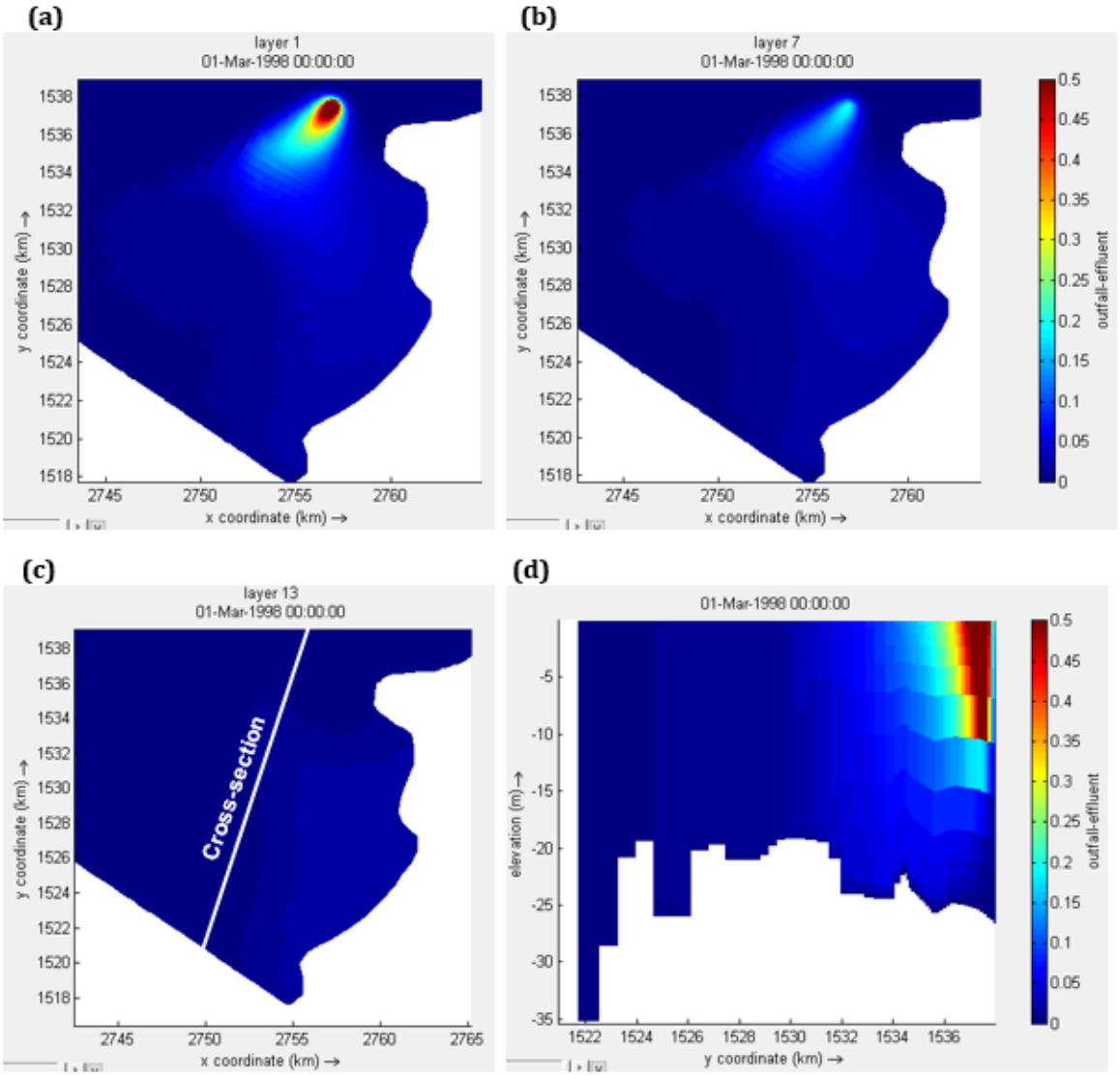

Figure 7-14. Contours of effluent concentration (kg/m^3) at different locations for case 4: **a)** water surface; **b)** top 58.75% of the water depth, **c)** bottom; **d)** along the cross-section shown in (c).

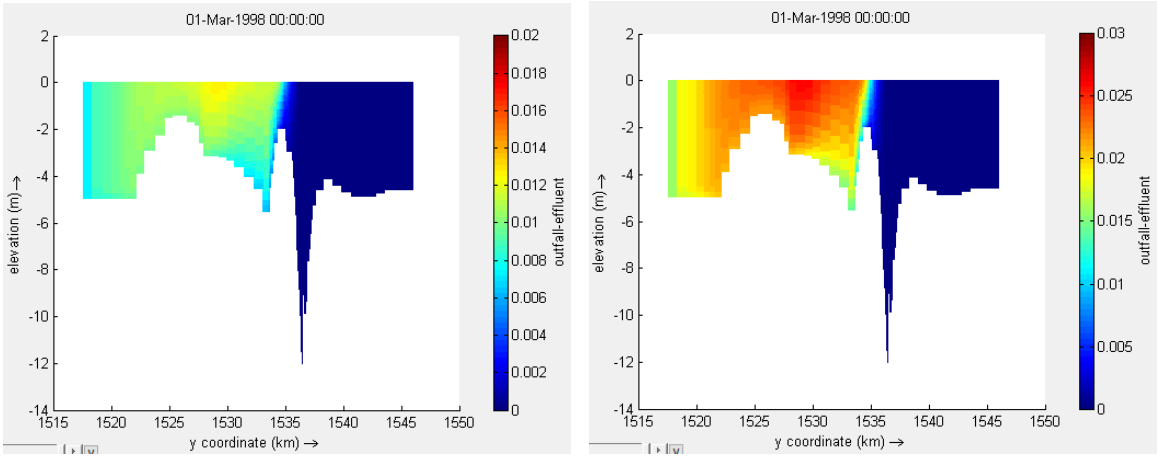

Figure 7-15. Comparison of effluent concentration (kg/m^3) along the shoreline for **a)** case 3 and **b)** case 4.

7.4. PROPOSED COUPLING METHODOLOGY FOR REAL-LIFE MARINE OUTFALLS.

In order to simplify analysis to enable interpretation of specific behaviour, the cases studied in this chapter assumed steady discharge and ambient conditions, neglecting complex unsteady processes that take place in the far field. In a real-life scenario, the discharge flow rate would change throughout a day due to varying water usage. Other variables such as current velocity magnitude and direction, water elevation, wind and density stratification would also show unsteady patterns that have been ignored in this study to isolate particular variables and analyse their effect.

For the simulation of a real-life marine outfall with the purpose of design or monitoring, these unsteady processes should be considered. Although this level of complex modelling is outside the scope of this study, a proposed methodology for it is described below, which could be serve as a guide for future work.

Step 1: Model the near field of the marine outfall of study, using measured and/or predicted data on the local ambient characteristics in the area of discharge and the time-varying discharge flow rates. The methodology described in Chapter VI could be used for the simulation of this area of the domain.

The possible combinations of flow rate and ambient conditions will be large. To reduce the number of near field simulations required, the cases can be grouped in different ranges, considering that within the ranges selected, no significant changes in the predicted plume shape should be observed. Within each range, the worst discharge and ambient conditions for dilution are used to represent the group.

For each one of the near field simulations conducted, the location of the plume in the far field should be identified and the corresponding distribution of the effluent in the cells selected for coupling can be decided using the methodology described in subsection 7.2.7.

Step 2: Based on measured and predicted data of the environmental and discharge conditions in the study area, simulate the time period of interest, using a far field ocean circulation model such as Delft3D-FLOW. Important environmental variables to consider for the simulation are measured and/or predicted current velocity and water elevations at the open boundaries over an extended time period. Wind speed and direction and density stratification profiles due to temperature or salinity variations in the area should also be considered. The discharge conditions should be coupled into the far field model by selecting the predicted plume that corresponds to the specific range (from step 1) in which each scenario falls.

These conditions are input into the far field circulation model to predict the hydrodynamic conditions in the area of study.

Step 3: Couple the resulting hydrodynamic model to a water quality model to predict the level of microbiological, organic and/or inorganic pollution in the far field that could result from outfall discharges. The far field circulation software Delft3D includes two water quality modules, namely D-Water Quality and D-Waq PART, which can be easily coupled with the Delft3D-FLOW model results.

7.5. Conclusions.

In this chapter, the effect of the coupling method, the discharge and ambient conditions on the far field model of the Cartagena outfall were investigated. Time-dependent and other complex processes such as tidal forcing, density stratification and wind effects were ignored to allow for a detailed study of the simplified problem so that the effects of individual aspects could be well understood as an important first step.

The main conclusions of this chapter are outlined as follows:

- The study has shown that it is possible to couple the near field detailed CFD model results to the far field circulation model Delft3D. This was achieved by generating an equivalent discharge flow vertical profile to input into the far field model, based on the concentration profile obtained from the CFD simulation of the near field.
- In the absence of tidal forcing, density stratification and wind effects, the added accuracy achieved in the prediction of the plume shape using CFD methods may not have a significant impact on the far field transport of the effluent. This is due to the flow being mainly driven by the ocean currents and overall hydrodynamic conditions of the receiving waters at the far field scale. The distribution of the effluent in the horizontal plane is not significantly altered based on the coupling method used. On the other hand, the vertical distribution of the effluent only differs significantly in the area near the discharge and further downstream, a similar and uniform vertical distribution is observed for both coupling methods studied here.
- The horizontal distribution of the effluent in the domain depends only on the magnitude and direction of the ocean currents. In the range studied, the discharge flow rate has no effect on the shape of the effluent plume in the far field and only local concentrations change based on the flow rate being discharged.
- Further research using the coupling methodology evaluated in this chapter would allow the time-dependent aspects and concentration build-up to be considered. It is expected that the discharge vertical distribution would have more significance in scenarios were the current velocity magnitude and direction varies along the water depth. This would be the case in real-life scenarios in which tidal forcing, density stratification and wind effects are accounted for.

8 CONCLUSIONS AND FURTHER WORK.

8.1 SUMMARY.

Marine outfalls are a wastewater disposal system commonly used in coastal areas. They consist of a pipe or tunnel or the combination of both, and ends with a series of diffusers. The purpose of the diffuser is to inject and encourage mixing of the wastewater effluent in the receiving environment.

Modelling is an important tool for the design and monitoring of marine outfalls. Due to the different processes occurring at various time and spatial scales this modelling has conventionally been divided in two regions: near and far field. In the near field, the flow is mainly driven by the initial momentum and buoyancy of the discharge. Contrary to this, in the far field, the flow is governed by the wider ocean hydrodynamics. Since ocean hydrodynamics are out of the designer's control, research on modelling the performance of marine outfalls is primarily focused on the near field.

Traditionally, the near field of marine outfalls has been modelled using entrainment and semiempirical models. However, these models have the disadvantage of overlooking or simplifying important aspects of near field mixing including boundary interactions and merging between adjacent plumes. CFD modelling techniques have great potential for the simulation of the near field of marine outfall. However, the application of CFD modelling to marine outfalls is challenging, due their complex geometry and the different length scale between diameter of the discharging ports and the characteristic length of the receiving waters.

The aim of this study was to assess how coupling CFD near field models with far field circulation models can be implemented to improve predictive capability of dilution and pollutant fate and transport in the near and far field of marine outfalls with multiport diffusers. In order to achieve this aim, four main objectives were established. The conclusions of this project as they relate to its objectives are discussed in detail in the following subsection.

8.2 CONCLUSIONS.

8.2.1 Objective 1: To develop a RANS modelling methodology to simulate near field mixing and dilution of marine outfalls.

In order to develop an adequate RANS modelling methodology, simple two-dimensional jet and buoyant jet problems were simulated. These two-dimensional cases were modelled using the standard k-ε model. At this stage of the study, the focus was on identifying the most appropriate meshing methodology to be used. Other aspects of the model development such as turbulence model and turbulent Schmidt number sensitivity were not considered in the stage, but were analysed later during the model validation, as will be described in the following subsection.

The complex geometry of marine outfalls and the different length scales between the discharging ports and the receiving environment made the use of structured grids computationally expensive, with excessively large meshes required for the simulation of the near field. To tackle this issue, a mesh adaption methodology was evaluated.

This mesh adaption methodology consisted in refinement of the mesh based on a preliminary solution. This preliminary solution was obtained from an initial simulation using a uniform structured mesh. Based on this initial solution, the mesh was refined in the areas where higher velocity magnitude was located. By using this method, the size of the required mesh to achieve mesh independence was reduced by about 10 times when compared to using uniform structured meshes. These results were achieved for a two-dimensional domain, which indicates that when used in three-dimensional simulations, this adaption methodology could reduce the size of the mesh up to 100 times when compared to using uniform structured grids.

Although for the two-dimensional cases studied at this stage the use of mesh refinement could easily be done based on velocity magnitude, in cases where a coflowing current is present, this becomes a more complicated task. In these cases, mesh refinement can be done using scalars such as salinity, temperature or pollutant concentration, obtaining similar results.

Overall, a mesh adaption approach was found to be an efficient method to reduce the computational cost of using RANS models for the prediction of marine outfall discharges. The conclusions from the validation of this methodology at laboratory scale and its implementation at real-life scale are discussed in the following subsections.

8.2.2 Objective 2: To validate the developed RANS methodology using experimental data at laboratory scale available in the literature.

The validation of the modelling methodology developed here was conducted for two main types of flows: firstly, single port dense discharges and secondly, turbulent axisymmetric plumes with both equal and unequal initial sources of buoyancy.

Understanding the behaviour of dense discharges have become of great importance due to the increased use of desalination plants. In this study, the simulation of single port dense discharges was conducted using a similar domain, discharge and ambient conditions used by Crowe (2016) in their laboratory experiments. The angle of discharge was varied between 15° and 45°. Different RANS turbulence models and turbulent Schmidt numbers were implemented to assess the sensitivity of the solution to the turbulence parameters used. A similar meshing approach to that developed for two-dimensional jets and buoyant jets was used, refining the areas with highest salinity concentration. Three main parameters were compared with available experimental data: buoyant jet trajectory, velocity and dilution. The main conclusions obtained from the simulation of single port dense discharges are:

- RANS models can predict the dynamics of single port dense discharges, including the detrainment that takes place in the inner side of inclined dense jets, especially at higher inclination angles. This is an advantage compared to traditional entrainment models that assume self-similar velocity and scalar distributions along the cross-sections of the plumes, ignoring the detrainment that occurs in the inner side of the jets. This advantage is reflected on the RANS model capacity to produce better velocity and dilution estimations when compared to other entrainment models.
- Amongst the turbulence models used, namely standard, realizable and RNG k-ε and k-σ SST, the realizable k- ε model provides the closest estimations of the trajectory of inclined dense jets at different discharge angles. However, this model tends to underpredict the location of maximum rise height and return point, since the predicted jet trajectory is shorter than that obtained empirically. Predictions of buoyant jet trajectory from the realizable k- ε model are comparable to those of entrainment models VISJET and CORJET.

The entrainment model UM3 provides the shortest trajectories amongst the models studied.

- The modelled trajectory was also sensitive to turbulent Schmidt number. This parameter was varied between 0.6 and 1.4. Amongst the values evaluated, a turbulent Schmidt number of 1.4 seems to predict a trajectory closest to the experimental data. However, although a higher turbulent Schmidt number provides better results in terms of trajectory, increasing the turbulent Schmidt number leads to the under-prediction of dilution in the maximum rise height and return point. For this reason, a value in the range of 0.6 to 0.9 is concluded to be the most suitable for this type of flow.
- The realizable k-ε models provide estimations of dilution at the maximum rise height of higher accuracy than entrainment models CORJET and UM3, which provide discrepancies between modelled and experimental values of up to 80%. At the return point, the scatter of experimental data is large; however, both the realizable k-ε and entrainment models underpredict dilution at this location. Despite this, lower discrepancies were observed for the realizable implementation.
- Velocity estimates obtained with the realizable k-ε model are significantly more consistent with experimental data than those obtained by entrainment models. Discrepancies between modelled and observed values range between 2.1% to 22.2% whereas VISJET, the model that provides the closest estimation amongst entrainment models, have discrepancies ranging from 12% to 40%.

Additional to the validation of single port discharges, the interaction between buoyant jets is of great importance for understanding the behaviour of marine outfall diffusers, which typically consist on multiple discharging ports aligned next to each other. To study this aspect, the experimental domain, discharge and ambient conditions of two dense plumes discharging into a stagnant environment from Kaye and Linden (2004) were simulated using RANS turbulent models. The spacing between ports and the initial sources of buoyancy of the plumes were varied to examine their effect on the overall mixing and dilution of the plumes. The main conclusions drawn from these simulations are described below:

- RANS models can accurately predict the physics of the interaction between equal plumes. This includes the deflection in the plumes trajectory that occurs as they approach each other, drawn by their entrainment fields. This poses an advantage over traditional entrainment models, that assume that plumes exiting from adjacent ports follow parallel trajectories.
- Turbulence models used include the realisable and RNG $k-\varepsilon$ model and $k-\omega$ SST models. Results show little sensitivity to turbulence model, potentially due to the insignificant wall effects observed in this type of flow.
- RANS models seem to slightly overestimate the location of the merging height for equal plumes. On the contrary, entrainment model UM3 underpredicts this parameter. Entrainment model VISJET seems to show closer agreement to the experimental data; however, its results are not valid beyond the merging location, since the interaction between the plumes is not modelled, assuming that they are single and independent plumes.
- For equal plumes, dilution at the merging height increases quadratically with port spacing. The realizable k-ε model produces results comparable to those obtained by the entrainment model UM3. VISJET results show a dilution significantly higher than that obtained by other models.
- When plumes with unequal sources of buoyancy interact, the plume with the lower initial buoyancy tends to deflect towards the other. The deflection of the weakest plume is more

prominent in scenarios with lower buoyancy ratio. Higher accuracy was observed for the CFD prediction of the merging height location for unequal plumes when compared to entrainment model developed by Kaye and Linden (2004), especially those with lower buoyancy ratios.

In conclusion, the objective of validating the developed RANS model was achieved. The realizable k- ε model was identified as the most suitable for the simulation of single and multiple buoyant jets. The methodology proposed and validated here was tested in a real-life scale outfall, and the main conclusions drawn from this study are presented in the following subsection.

8.2.3 Objective 3: To simulate mixing and dilution in the near field of a real-life scale marine outfall, using the Cartagena marine outfall as a case study.

The proposed CFD methodology was tested and validated for the simulation two and three dimensional single and multiple port discharges. Using this validated methodology, the near field of a real-life scale marine outfall located in the city of Cartagena, Colombia was simulated. The constructed Cartagena marine outfall consists of a diffuser of 500 m length, with 102 Tee-shaped risers with port diameter of 0.1 m. Discharge and ambient conditions were varied, not only to assess the performance of this outfall but also to understand the effects of changes that were done to the outfall design at the time of construction. The discharge parameters evaluated include discharge flow rate, port size and spacing and port alignment. In terms of the environmental factors, the effect of varied current velocity magnitude and direction and density stratification were also evaluated. The conclusions obtained from this study are listed below:

- The Cartagena marine outfall was successfully modelled using a simplified domain, which included only 5 of the 102 risers found in the Cartagena marine outfall. This domain enabled the study of the different behaviour of the plumes based on their location in the diffuser. Lower pollutant concentrations were observed for the plumes located at the edges. As they start approaching the central plumes, they suddenly deflect towards the central area, drawn by their stronger entrainment field, coinciding with the findings of the studies on unequal plumes at laboratory scale.
- In the scenario where the diffuser is discharging into a stagnant unstratified environment, port alignment has a significant effect on the dilution achieved in the near field. Two port alignments were compared: the conventional one, in which the Tee-shaped risers are located parallel to each other and perpendicular to each other, which correspond to the intended design of the Cartagena marine outfall; and the constructed alignment, where the risers are located in line with each other and parallel to the diffuser. The conventional port alignment shows a dilution 13% higher at the impact point and 26% higher further downstream when compared to Cartagena constructed alignment. This indicates that using the constructed diffuser alignment reduces the outfall's capacity for mixing, as it effectively reduces the spacing between plumes at the discharge height. Different results were obtained for diffusers discharging into a flowing unstratified environment.
- In a flowing unstratified environment, three different flow regimes are identified, coinciding with research findings by Roberts, et. al. (1989a). These flow regimes depend on the Roberts Froude number, a parameter that determines the relative strength of the current over the initial buoyancy of the plumes. For lower Froude numbers, the plumes rise to the surface and once they have reached this maximum height, horizontal spreading occurs, both upstream (as a wedge) and downstream from the discharge location. However, as the Froude number increases, this upstream wedge disappears, and bottom

attachment occurs near the discharge. For very high Froude numbers ($F \gg 1$), the plumes show bottom attachment and may become trapped below the surface.

- In scenarios of a diffuser discharging in a flowing unstratified environment, the constructed port alignment shows a somehow larger dilution, especially at the impact point. This is due to the absence of a plume in counter-flow, which in a conventional port alignment serves as a barrier from the current to the plume in co-flow. With the constructed port alignment, all the plumes are equally exposed to the current, extending the length of the near field and increasing mixing. This indicates that the type of diffuser constructed in Cartagena only poses a disadvantage for scenarios with very low Froude numbers, like in the absence of a current.
- In a diffuser with the constructed port alignment, the size of the ports and therefore its initial momentum has a more significant effect on the obtained dilution and length of the near field. This is due to the quick interaction that occurs when the ports are facing each other, which differs what is observed in a conventional port alignment where the plumes start to interact further downstream from the discharge.
- Overall, port alignment has great effect on the length and dilution obtained in the near field; therefore, modelling the Cartagena marine outfall using traditional methods that assume that risers are aligned parallel to each may not provide accurate results.
- Regarding the effects of port spacing, comparisons for both types of alignment indicate an advantage for cases with larger spacing (i.e. longer diffuser), which increases dilution about 2-3 times for the port spacings studied, which are 5 and 20 m. Port spacing shows a more significant effect on the location of the impact point for cases with the constructed port alignment when compared to the conventional one.
- The presence of an inclined current reduces the diffusers capacity for dilution, agreeing with previous studies by Roberts, et. al. (1989a), that shows that diffusers provide the maximum dilution when they are aligned perpendicular to the current. Furthermore, the presence of an inclined current increases the effects of plume location and those plumes located upstream from the inclined current will show higher pollutant concentration, as they serve as a barrier for the plumes further downstream.
- The stratification observed in the near field of the Cartagena marine outfall is due to temperature difference of about 1°C between the surface and bottom. This stratification has very little effects on the overall trajectory of the plumes, which continue to reach the surface even under these circumstances. Dilution is only minimally reduced by about 5% in the presence of stratification for the cases compared.

8.2.4 Objective 4: To assess different approaches for coupling the near field RANS model of Cartagena with a far field circulation model.

In the previous stages, the study focused on the simulation of the near field using CFD techniques. The final stage of this project had the objective of understanding the effects of coupling method, discharge and ambient conditions on the far field model, using the Cartagena marine outfall as a case study scenario. The main conclusions obtained from this study are listed here:

- The CFD model results were successfully coupled to the far field circulation model Delft3D by inputting a near field discharge flow vertical profile into the far field model. This profile was generated based on the concentration profile obtained from the RANS simulation of the near field, for specific discharge and ambient conditions. Time-dependent and other complex processes such as tidal forcing, density stratification and wind effects were ignored to isolate the individual parameters of interest for their analysis.

- In the far field, the flow is mainly driven by the ocean currents and overall hydrodynamic conditions of the receiving waters. The used coupling method only had a significant impact on the vertical distribution of the effluent in the proximity of the discharge. The distribution of the effluent in the horizontal plane is mainly driven by the ocean current magnitude and direction. This indicates that the greater precision obtained in the near field CFD simulations had little effect on the far field results obtained. However, it is expected that it would have a more significant effect in cases where in scenarios were the current velocity magnitude and direction varies significantly along the water depth, which would be the case when tidal forcing, density stratification and wind effects are taken into account. Further research is necessary to test this hypothesis.

8.2.5 Aim.

The overall of this thesis was achieved and a framework for the application of CFD near field models and its subsequent coupling with far field circulation models was proposed. RANS turbulence models produce reliable predictions of single and multiple port buoyant jet discharges from marine outfalls. The computation cost of this modelling method was reduced by implementing solution-based mesh adaption.

8.3 RECOMMENDATIONS FOR FURTHER WORK.

This study has successfully undertaken a detailed investigation to analysis and appraise the modelling of two and three-dimensional buoyant jet discharges at both laboratory and real-life scale based on the available time and resources. As a result, some interesting aspects of marine outfall dilution and mixing could be further investigated in future studies. Some suggestions of future research are presented below.

- Time-dependent processes and variations in the discharge and ambient conditions would be the next step in understanding the behaviour of models. These time-dependent processes include tidal variation, changes in discharge flow rate during a given day, wind effects, density stratification and concentration build-up. Further work is required to understand how this time-dependent process could affect dilution and transport in the near and far field of marine outfalls.
- Additional work is also recommended regarding the simulation of single port dense discharges, with further analysis on the sensitivity to initial turbulence parameters, in order to understand the reasons behind the underprediction of the buoyant jet trajectory observed for the RANS turbulence models and entrainment models.
- Once time-dependent processes are considered, near field RANS model results could be compared to field measurements conducted in the Cartagena marine outfall area, in order to further validate the capability of this models at real-life scale.
- Further studies on different of port alignments at laboratory scale may enhance our understanding of the effects of this parameter on the overall trajectory and dilution of the near field.

9 REFERENCES.

Akar, P. & Jirka, G., 1991. *CORMIX2: An expert system for hydrodynamic mixing zone analysis of conventional and toxic multiport diffuser discharges,* Athens, Georgia: United States Environmental Protection Agency.

Ansys Inc., 2018. *Ansys Fluent User's Guide Release 18.2,* s.l.: s.n.

Baines, D., 1983. A technique for the direct measurement of volume flux of a plume. *Journal of Fluid Mechanics,* Volumen 132, pp. 247-256.

Baumgartner, D., Frick, W. & Roberts, P., 1994. *Dilution models for effluent discharges,* Newport, Oregon: Environmental Protection Agency.

Baumgartner, D., Frick, W. & Roberts, P., 1994. *Dilution models for effluent discharges,* Newport, Oregon: Environmental Protection Agency.

Bedri, Z., Bruen, M. & Dowley, A., 2011. A three-dimensional hydro-environmental model of Dublin Bay. *Environmental Modelling & Assessment,* Volumen 16, pp. 369-384.

Bjorn, E. & Nielsen, P., 1995. Merging thermal plumes in the indoor environment. *Indoor Environmental Technology,* R9541(54), pp. 1-6.

Bleninger, T., 2006. *Coupled 3D hydrodynamic models for submarine outfalls: Environmental hydraulic design and control for multipor diffusers.* Karlsruhe: Doctoral thesis: University of Karlsruhe.

Bloomfield, L. & Kerr, R., 2002. Inclined turbulent fountain. *Journal of Fluid Mechanics,* Volumen 451, pp. 283-294.

Blumberg, A., Ji, Z. & Ziegler, C., 1996. Modeling outfall plume behaviour using far field circulation model. *Journal of Hydraulic Engineering,* 122(1), pp. 610-616.

Brahimi, M. & Doan-Kim-Son, 1985. Interaction between two turbulent plumes in close proximity. *Mechanics Research Communicatins,* Volumen 12, pp. 249-255.

Brooks, N., 1980. *Synthesis of stratified slow phenomena for design of outfalls.* Trondheim, Norway, Proc. 2nd. Int. Symp. on Stratified Flows.

Carvalho, J., Roberts, P. & Roldao, J., 2002. Field observations of Ipanema Beach Outfall. *Journal of Hydraulic Engineering,* 128(2), pp. 151-160.

Carvalho, J. y otros, 2013. Modeling the Praia dos Ingleses submarine outfall, Florianópolis, Santa Catarina, Brazil. *Water science & Technology,* 67(8), pp. 1832-1840.

Cenedese, C. & Linden, P., 2014. Entrainment in two coalescing axisymmetric turbulent plumes. *Journal of Fluid Mechanics,* 752(R2), pp. 1-12.

Chin, D. & Roberts, P., 1985. Model of dispersion in coastal waters. *Journal of Hydraulic Engineering,* 111(1), pp. 12-28.

Ching, C., Fernando, H. & Mofor, L., 1996. Interaction between multiple line plumes: A model study with applications to leads. *American Metheorological Society,* Volumen 26, pp. 525-540.

Choudhury, D., 1993. *Introduction to the renormalization group method and turbulence modeling,* s.l.: Fluent Inc. Technical Memorandum TM-107.

Cipollina, A., Brucato, A., Grisafi, F. & Nicosia, S., 2005. Bench-scale investigation of inclined dense jets. *Journal of Hydraulic Engineering,* 131(11), pp. 1017-1022.

Crowe, A., Davidson, M. & Nokes, R., 2016. Velocity measurements in inclined negatively buoyant jets. *Environmental Fluid Mechanics,* Volume 16, pp. 503-520.

Daviero, G., 1998. *Hydrodynamics of ocean outfall discharges in unstratified and stratified flows.* Georgia, Atlanta: PhD Thesis, School of Civil Engineering, Georgia Institute of Technology.

Daviero, G. & Roberts, P., 2006. Marine wastewater discharges from multiport diffusers III: Stratified stationary water.. *Journal of Hydraulic Engineering,* 132(4), pp. 404-410.

DELTARES, 2011. *Delft3D-FLOW: User Manual.* Version 3.15 ed. Delft, Netherlands: DELTARES.

Doneker, R. & Jirka, H., 2007. *CORMIX User Manual: A hydrodynamic mixing zone model and decision support system for pollutant discharges into surface water,* Washington, D.C.: United States Environmental Protection Agency.

Etemad-Shahidi, A. & Azimi, A., 2007. Simulation of thermal discharges using two mixing zone models. *Journal of Coastal Research,* Volumen 50, pp. 663-667.

Fan, L. & Brooks, N., 1967. *Turbulent buoyant jets into stratisfied or flowing ambient fluids.* Pasadena, California: California Institute of Technology.

Ferrari, S. & Querzoli, G., 2010. Mixing and re-entrainment in a negatively buoyant jet. *Journal of Hydraulic Engineering,* Volumen 48, pp. 632-640.

Fischer, H. et al., 1979. *Mixing in inland and coastal waters,* New York: Academic.

Frick, W. y otros, 2003. *Dilution models for effluent discharges,* Athens, Georgia: United States Environmental Protection Agency.

Gebhart, B., Shaukatullah, H. & Pera, L., 1976. The interaction of unequal laminar plane plumes. *International Journal of Hear Mass Transfer,* Volume 19, pp. 751-756.

He, Z. y otros, 2018. Dynamic interaction and mixing of two turbulent forced plumes in linearly stratified ambience. *Journal of Hydraulic Engineering,* Volumen 12, p. 144.

Jirka, G., 2004. Integral model for turbulent buoyant jets in unbounded stratified flows. Part I: Single round jet.. *Environmental fluid mechanics,* Volumen 4, pp. 1-56.

Kaye, N. & Linden, P., 2004. Coalescing axisymmetric turbulent plumes. *Journal of Fluid Mechanics* , Volumen 502, pp. 41-63.

Kikkert, G., Davidson, M. & Nokes, R., 2007. Inclined negatively buoyant discharges. *Journal of Hydraulic Engineering,* Volumen 133, pp. 545-554.

Lai & Lee, 2012. Mixing of inclined dense jets in stationary ambient. *Environmental Fluid Mechanics,* Volumen 16, pp. 503-520.

Launder, B. & Spalding, D., 1974. The numerical computation of turbulent flows. *Computer Methods in Applied Mechanics and Engineering,* 3(2), pp. 269-289.

Lee, J. & Cheung, V., 1990. Generalized Lagrangian model for buoyant jets in current. *Journal of Environmental Engineering,* 116(6), pp. 1085-1106.

Maia, L., Bezerra, M., Pinheiro, L. & Redondo, J., 2011. Application of the Cormix model to assess environmental impact in the coastal area: an example of the ocean disposal system for sanitary sewers in the city of Fortaleza (Ceará, Brazil). *Journal of Coastal Research,* Volumen 64, pp. 922-926.

MIT, 2004. *Vertical coordinates,* Cambridge, U.S.: Massachusetts Institute of Technology.

Morelissen, R., Kaaij, v. d. & Bleninger, T., 2013. Dynamic coupling of near field and far field models for simulating effluent discharges. *Water Science and Technology,* 67(10), pp. 2210-2220.

Morton, B., Taylor, G. & Turner, J., 1956. Turbulent gravitational convection from maintained and instantaneous sources. *Proceedings of the Royal Society of London, Series A, Mathematics and Physical Sciences,* 234(1196).

Moses, E., Giovanni, Z. & Libchaber, A., 1993. An experimental study of laminar plumes. *Journal of Fluid Mechanics,* Volumen 251, pp. 581-601.

Moses, E., Zocchi, G., Procaccia, I. & Libchaber, A., 1991. The dynamics and interaction of laminar thermal plumes. *Europhysics Letters,* 14(1), pp. 55-60.

Muhammetoglu, A., Yalcin, O. & Ozcan, T., 2012. Prediction of wastewater dilution and indicator bacteria concentrations for marine outfall systems. *Marine Environmental Research,* Volumen 78, pp. 53-63.

Nakayama, A. & Nizamani, Z., 2016. Simulation of near field mixing process in marine disposal of treated sewer water. *ARPN Journal of Engineering and Applied Sciences,* 11(4), pp. 2006-2016.

Neumann, B., Vafeidis, A., Zimmermann, J. & Nicholls, R., 2015. Future coastal population growth and exposure to to sea level-rise and coastal flooding - A global asssessment. *PLoS One,* 10(3).

Novoa, W., 2015. *Aforo de velocidades de corrientes marinas. Emisario submarino de Cartagena,* Cartagena, Colombia: Prepared for: Aguas de Cartagena.

Oliver, C., Davidson, M. & Nokes, R., 2008. k-epsilon Predictions of the initial mixing of desalination discharges. *Environmental Fluid Mechanics,* Volumen 8, pp. 617-625.

Oliver, C., Davidson, M. & Nokes, R., 2013. Removing the boundary influence on negatively buoyant jets. *Environmental Fluid Mechanics,* Volumen 13, pp. 625-648.

Palomar, P. y otros, 2012a. Near field brine discharge modelling part 1: Analysis of commercial tools. *Desalination,* Volumen 290, pp. 14-27.

Palomar, P., Lata, J. & Losada, I., 2012b. Near field brine discharge modeling part 2: Validation of commercial tools. *Desalination,* Volumen 290, pp. 28-42.

Panamerican Health Organization, 2006. *Sewage disposal of coastal cities submarine outfalls.* [Online]
Available at: www.bvsde.paho.org/bvsaca/i/dispagua.html
[Accessed 15 August 2016].

Papakonstantis, I., Christodoulou, G. & Papanicolaou, P., 2011b. Inclined negatively buoyant jets 2: concentration measurements. *Journal of Hydraulic Research,* 49(1), pp. 13-22.

Papanikonstantis, I., Christodoulou, G. & Papanicolaou, P., 2011a. Inclined negatively buoyant jets 1: geometrical characteristics. *Journal of Hydraulic Research,* 49(1), pp. 3-12.

Pera, L. & Gebhart, B., 1975. Laminar plume interactions. *Journal Fluid Mechanics,* 68(2), pp. 259-271.

Pincine, A. & List, E., 1973. Disposal of brine into an estuary. *Water Pollution Control Federation,* 45(11), pp. 2335-2344.

Pope, S., 1978. An explanation of the turbulent round-jet/plane-jet anomaly. *AIAA Journal ,* 16(3), pp. 279-281.

Ramaprian, B. & Chandrasekhara, M., 1989. Measurements in vertical plane turbulent plumes. *Journal of Fluids Engineering,* Volumen 111, pp. 69-77.

Roberts, P., 1979. Line plumes. *Journal of Hydraulic Engineering,* 105(4), pp. 313-330.

Roberts, P., 1999. Modeling Mamala Bay outfall plumes. I: Near field. *Journal Hydraulic Engineering,* 125(6), pp. 564-573.

Roberts, P., 2003. *Dilution modeling for the Cartagena ocean outfall,* Atlanta, Georgia: Aguas de Cartagena.

Roberts, P., 2013. Ocean outfalls. En: H. Fernando, ed. *Handbook of Environmental Fluid Dynamics, Volume Two.* Boca Raton: CRC Press/Taylor and Francis Group, LLC., pp. 229-241.

Roberts, P. & Carvalho, J., 2000. *Modeling of ocean outfall for Cartagena, Colombia,* Cartagena: s.n.

Roberts, P., Ferrier, A. & Daviero, G., 1997. Mixing in inclined dense jets. *Journal of Hydraulic Engineering,* 123(8), pp. 693-699.

Roberts, P. y otros, 2010. *Marine wastewater outfalls and treatment systems.* London, UK: IWA Publishing.

Roberts, P. et al., 2010. *Marine wastewater outfalls and treatment systems.* London, UK: IWA Publishing.

Roberts, P., Snyder, W. & Baumgartner, D., 1989a. Ocean outfall I: Submerged wastefield formation. *Journal of Hydraulic Engineering,* 115(1), pp. 1-25.

Roberts, P., Snyder, W. & Baumgartner, D., 1989c. Ocean outfalls. III: Effect of diffuser design on submerged wastefield.. *Journal of Hydraulic Engineering,* 115(1), pp. 49-70.

Roberts, P. & Synder, W., 1993a. Hydraulic model for the Boston outfall. I: Riser configuration. *Journal of Hydraulic Engineering,* 119(9), pp. 970-987.

Roberts, P. & Synder, W., 1993b. Hydraulic model study for the Boston Outfall. II: Environmental performance. *Journal of Hydraulic Engineering,* 119(9), pp. 988-1002.

Roberts, P., Synder, W. & Baumgartner, D., 1989a. Ocean outfalls. I: Submerged wastefield formation.. *Journal Hydraulics Engineering,* 115(1), pp. 1-25.

Roberts, P., Synder, W. & Baumgartner, D., 1989b. Ocean outfalls. II: Spatial evolution of submerged wastefield.. *Journal of Hydraulic Engineering,* 115(1), pp. 26-48.

Roberts, P. & Toms, G., 1987. Inclined dense jets in flowing current. *Journal of Hydraulic Engineering,* 113(3), pp. 323-340.

Roberts, P. & Villegas, B., 2006. *Three-dimensional modeling of bacterial transport for the Cartagena ocean outfall,* Atlanta, USA: Prepared for Aguas de Cartagena.

Robinson, D., Wood, M. & Piggott, M. &. G. G., 2015. CFD modelling of marine discharge mixing and dispersion. *Journal of Applied Water Engineering and Research.*

Salas, H., 2000b. *Emisarios submarinos: Enfoque general, conceptos básicos de diseño y requerimiento de datos para América Latina y el Caribe.,* s.l.: Centro Panamericano de Ingeniería Sanitaria y Ciencias de Ambiente.

Salas, H., 2000. *Submarine outfalls: A viable alternative for sewage discharge of coastal cities in Latin America and the Caribbean,* s.l.: Pan American Center for Sanitary Engineering and Environmental Sciences (CEPIS).

Shao, D. & Law, A., 2010. Mixing and boundary interactions of 30° and 45° inclined dense jets. *Environmental Fluid Mechanics,* Volumen 10, pp. 521-553.

Shih, T. y otros, 1995. A new k-epsilon eddy viscosity model for high Reynolds number turbulent flows. *Computers Fluids,* 24(3), pp. 227-238.

Tang, H., Joongcheoal, P., Sotiropoulos, F. & Khangaonkar, T., 2008. Three dimensional numerical modeling of initial mixing of thermal discharges at real life configurations. *Journal of Hydraulic Engineering,* 134(9), pp. 1210-1224.

Tate, P., Scaturro, S. & Cathers, B., 2016. Marine outfall . En: M. Dhanak & N. Xiros, edits. *Springer Handbook of Ocean Engineering.* s.l.:Springer, pp. 7-36.

Tate, P., Scaturro, S. & Cathers, B., 2016. Marine outfalls. En: M. Dhanak & N. Xiros, edits. *Springer Handbook of Ocean Engineering.* s.l.:Springer International Publishing.

Tian, X. & Roberts, P., 2003. A 3D LIF system for turbulent buoyant jet flows. *Experiments in fluids,* Volumen 35, pp. 636-647.

Tian, X., Roberts, P. & Daviero, G., 2004a. Marine wastewater discharges from multiport diffusers I: unstratified stationary water.. *Journal of Hydraulic Engineering,* 132(4), pp. 1147-1155.

Tian, X., Roberts, P. & Daviero, G., 2004b. Marine wastewater discharges from multiport diffusers. II: Unstratified flowing water. *Journal of Hydraulic Engineering,* 130(12), pp. 1147-1155.

UN Atlas of the Oceans, 2016. *Human Settlements on the Coast.* [Online] Available at: http://www.oceansatlas.org/subtopic/en/c/114/#:~:text=44%20%25%20of%20the%20world's%20population,within%20200km%20of%20a%20coastline.
[Accessed 29 11 2020].

UNESCO, 1980. *Background papers and supporting data on the international equation of state,* UNESCO: Technical Report 38.

UNESCO-IOC, 2015. *Marine Pollution.* [Online] Available at: http://www.unesco.org/new/en/natural-sciences/ioc-oceans/priority-areas/rio-20-ocean/blueprint-for-the-future-we-want/marine-pollution/
[Accessed 10 November 2015].

United Nations Environment Programme, 2015. *Land-based Sources of Pollution.* [Online] Available at: http://www.unep.org/regionalseas/issues/landactivities/default.asp
[Accessed 3 November 2015].

United Nations, 1999. *Protocol concerning pollution from land-based sources and activities to the convection for the protection and development of the marine environment of the wider Caribbean region,* s.l.: United Nations.

United Nations, 2008. *Percentage of total population living in coastal areas.* [Online] Available at: http://www.un.org/esa/sustdev/natlinfo/indicators/methodology_sheets/oceans_seas_coasts/pop_coastal_areas.pdf
[Accessed 3 November 2015].

Valero, D. & Bung, D. B., 2016. Sensitivity of turbulent Schmidt number and turbulence model to simulations of jet in cross-flow. *Environmental Modelling & Software,* Volumen 82, pp. 218-228.

Versteeg, H. & Malalasekera, W., 2007. *An introduction to computational fluid dynamics. The fine volume method..* Second ed. Harlow, Essex: Pearson Education Limited.

Wilcox, D., 1998. *Turbulence Modeling for CFD,* La Canada, California: DCW Industries, Inc..

Woods, A., 2010. Turbulent plumes in nature. *Annual Review of Fluid Mechanics,* Volumen 42, pp. 391-412.

World Bank, 2014. *Restauración del ambiente costero de Cartagena, Colombia,* Washington, DC: World Bank.

World Health Organization, 2003. *Guidelines for safe recreational water environments. Volume I: Coastal and freshwaters,* Geneva: World Health Organization.

Xue, W. et al., 2014. Numerical simulation of initial mixing of marine wastewater discharge from multiport diffusers. *Engineering Computations: International Journal for Computer-Aided Engineering and Software,* 31(7), pp. 1379-1400.

Yeh, S.-C.y otros, 2011. Optimal expansion of a coastal wastewater treatment and ocean outfall system under uncertainty (I): simulation analysis. *Civil Engineering and Environmental Systems,* 28(1), pp. 19-38.

Yimer, I., Campbell & Jiang, L., 2002. Estimation of the turbulent Schmidt number from experimental profiles of axial velocity and concentration for high Reynolds number jet flows. *Canadian Aeronautics and Space Journal,* 48(3), pp. 195-200.

Zeitoun, M., 1970. *Conceptual designs of outfall systems for desalination plants,* s.l.: Office of Saline Water, U.S. Dept. of Interior.

Zhang, S., Jiang, B., Law, A. & Zhao, B., 2016. Large eddy simulations of 45° inclined dense jets. *Environmental Fluid Mechanics,* Volume 16, pp. 101-121.

Zhang, S., Law, A. W.-K. & Jiang, M., 2017. Large eddy simulations of 45° and 60° inclined dense jets with bottom impact. *Journal of Hydro-environment Research,* Volumen 15, pp. 54-66.

Zhang, X. & Adams, E., 1999. Prediction of near field plume characteristics using a far field circulation model. *Journal of Hydraulics Engineering,* 125(3), pp. 233-241.

Zhao, L., Chen, Z. & Lee, K., 2011. Modelling the dispersion of wastewater discharges from offshore outfalls: a review. *Environmental Reviews,* Volumen 19, pp. 107-120.

Zhao, L., Chen, Z. & Lee, K., 2011. Modelling the dispersion of wastewater discharges from offshore outfalls: a review. *Environmental Reviews,* Volume 19, pp. 107-120.